Search for Doubly-charged Higgs Boson Production in the Decay $H^{++}H^{--} \rightarrow \mu^+\mu^+\mu^-\mu^-$ with the DØ Detector at $\sqrt{s} = 1.96$ TeV

A Dissertation Presented

by

Marian Zdražil

to

The Graduate School

in Partial Fulfillment of the Requirements

for the Degree of

Doctor of Philosophy

in

Physics

Stony Brook University

August 2004

State University of New York
at Stony Brook

The Graduate School

Marian Zdražil

We, the dissertation committee for the above candidate for the Doctor of Philosophy degree, hereby recommend acceptance of the dissertation.

Professor Michael M. Rijssenbeek
Dissertation Advisor, Department of Physics and Astronomy

Professor Robert L. McCarthy
Chairman of Defense, Department of Physics and Astronomy

Professor George F. Sterman
Committee Member, Department of Physics and Astronomy

Professor Thomas K. Hemmick
Committee Member, Department of Physics and Astronomy

Dr. Srinivasan Rajagopalan
Outside Member, Brookhaven National Laboratory

This dissertation is accepted by the Graduate School.

Dean of the Graduate School

Abstract of the Dissertation
Search for Doubly-charged Higgs Boson Production in the Decay $H^{++}H^{--} \rightarrow \mu^+\mu^+\mu^-\mu^-$ with the DØ Detector at $\sqrt{s} = 1.96$ TeV

by

Marian Zdražil

Doctor of Philosophy

in

Physics

Stony Brook University

2004

This work presents a search for the pair production of doubly-charged Higgs Bosons in the process $p\overline{p} \rightarrow H^{++}H^{--} \rightarrow \mu^+\mu^+\mu^-\mu^-$ using inclusive dimuon events. These data correspond to an integrated luminosity of about 113 pb^{-1} and were recorded by the DØ experiment between August 2002 and June 2003. In the absence of a signal, 95% confidence level mass limits of $M(H_L^{\pm\pm}) > 118.6$ GeV/c^2 and $M(H_R^{\pm\pm}) > 98.1$ GeV/c^2 are set for left-handed and right-handed doubly-charged Higgs boson, assuming 100% branching into muons and hypercharge $|Y| = 2$ and Yukawa coupling $h_{\mu\mu} > 10^{-7}$. This is the first search for doubly-charged Higgs bosons at hadron colliders. It significantly extends the previous mass limit of 100.5 GeV/c^2 for a left-handed doubly-charged Higgs boson measured in the muon final states by the OPAL collaboration.

Contents

List of Figures

List of Tables

Acknowledgments

First of all, I would like thank all the members of the DØ Collaboration both for their hard work building and operating the detector and for putting up with me for the past years.

Special thanks go to my colleagues and friends, Stefan Söldner-Rembold and Avtandyl (Avto) Kharchilava, for their help, support and advice in many aspects of the analysis as well as my career decisions.

Thanks to John Hobbs, Nikos Varelas, Suyong Choi, Qizhong Li, Jae Yu, Andre Turcot and others in the Higgs group and the Higgs group as a whole for many valuable suggestions.

Thanks to many friends I have made here, who helped me in numerable ways: Aurelio Juste, Slava Kulik; Ia Iashvilli.

Many thanks to colleagues from the SMT and CFT hardware crowd, Aurelio Juste, Petros Rapidis, Eric Kajfasz, Marcel Demarteau, Alan Bross, Fred Borcherding, Drew Alton; Global Tracking Group, Gastón Gutierrez, Herb Greenlee, Harry Melanson; Offline Calibration Database group, Taka Yasuda, Vladimir Sirotenko. It was an honor for me to belong to a group of people who can build, operate, write programs for and finally understand such a complicated system as the high-energy physics detector.

Thanks to all those DØ Collaborators who take care of the clued0 system.

Special thanks go to my advisor, Michael Rijssenbeek, for reading early drafts of pieces of this thesis and helping me to give my writings the final shape.

I would like to thank Peter Bock (Heidelberg) and Thomas Junk (Ur-

bana) for helping us with the limit setting programs and Michael Spira (PSI) for providing the next-to-leading order cross-sections for the doubly-charged Higgs boson production.

Finally, warmest thanks to my parents for all they did for me, and to my friends Viktorie and Iva Reichova.

Chapter 1

Introduction

Even though the standard model of the strong and electroweak interactions has proven enormously successful, it need not be the case that a single Higgs-doublet field is responsible for giving masses to the weakly interacting vector bosons and the fermions. This thesis presents a detailed account of the search for an exotic doubly-charged Higgs boson in the muon final states at DØ . This thesis presents a detailed account of the search published in [1].

The general layout is as follows. In Chapter 2 we explore the phenomenology of models which contain doubly-charged Higgs bosons, describe its properties, production and decay channels and review several measurements that set a limit on doubly-charged Higgs bosons. Chapter 3 discusses the experimental apparatus used for this analysis, the DØ Run II detector. Chapter 4 describes how was the dimuon data sample was selected, while Chapter 5 describes the Monte Carlo simulation of signal and background samples. Calculation of reconstruction efficiencies needed to normalize Monte Carlo samples to the data and their time dependence is summarized in Chapter 6. The comparison of the data and Monte Carlo is made in Chapter 7. It also ex-

plains all corrections that have to be applied to fix track transverse momenta and smear them in Monte Carlo. The most important part of the analysis [1] is to understand the like-sign background. This is why a discussion of major contributing backgrounds is given in Chapter 8. No search analysis can be made without optimization of selection cuts, an overview is provided in Chapter 9. Chapter 11 applies like-sign backgrounds from Chapter 8 and candidate events from Chapter 10 to calculate the limit on doubly-charged Higgs boson mass by taking into account systematic uncertainties listed in Chapter 12. Results and conclusions of this thesis are briefly summarized in Chapter 13. Finally, appendices A, B, C, D and E present some of the studies made before and in the course of performing this analysis. They are included because they all made this search possible. SMT and CFT cluster efficiency studies, CFT cluster position and uncertainty calculations in the framework of the DØ event reconstruction code, development of the SMT offline calibration database, and $Z \to \mu^+\mu^-$ mass resolution are presented in a great level of detail there. An attractive extension of the standard model is the left-right symmetric model of weak interactions. These models require in the Higgs sector a bidoublet Φ and two left-right symmetric triplets $\Delta_{L,R}$. It was shown that introducing of L-R Higgs triplets provides an opportunity to understand smallness of neutrino masses. This possibility is in detail discussed in appendix F.

Chapter 2

Phenomenology of a doubly-charged Higgs boson

Doubly-charged Higgs bosons (Δ^{++}/Δ^{--})[1] arise in many scenarios extending the weak interaction beyond the Standard Model (SM) and can be relatively light. This chapter reviews the theoretical motivation for these states and presents current limits from different experiments. A special attention is paid to the Fermilab Tevatron searches.

2.1 Doubly-charged Higgs Bosons in extensions of Standard Model

Doubly-charged Higgs bosons appear in left-right symmetric models [2, 3], in Higgs triplet models [4] and in Little Higgs models [5].

[1] Doubly-charged Higgs is denoted as Δ^{++}/Δ^{--} in the theoretical literature, it is usually named H^{++}/H^{--} in the experimental papers.

It is well known [4] that models with only Higgs $SU(2)_L \otimes U(1)_Y$ doublets provide the most straightforward extensions of the SM that satisfy constraints deriving from $\rho \equiv M_{\rm W}^2/\cos^2\theta_W M_{\rm Z}^2 \approx 1$ and the absence of flavor-changing neutral currents. However, there are many more complicated possibilities. For instance, conventional left-right-symmetric models are often constructed using a Higgs sector containing several triplet representations [3]. In those models, it is necessary to assign a very small vacuum expectation value ($v.e.v.$) to the neutral member of the left-handed triplet in order to avoid unacceptable corrections to the $W-Z$ mass ratio. However, it is certainly not necessary to go to left-right-symmetric extensions of the SM in order to consider Higgs-triplet fields. Large tree-level deviations of the electroweak ρ parameter from unity can be avoided by two means:

- the neutral triplet fields can be given $v.e.v.$ that are much smaller than those for the neutral doublet fields
- or, the triplet fields and the $v.e.v.$ of their neutral members can be arranged so that a custodial $SU(2)$ symmetry is maintained.

Only the latter type of models are further considered. By custodial $SU(2)$ symmetry at the tree level is meant that the hypercharges Y and $v.e.v.$ of all Higgs multiplets are chosen so that $\rho = 1$ is maintained.

A number of models with custodial $SU(2)$ symmetry, have been proposed in the literature [6]. For example, a Higgs doublet representation with $Y = -3$ contains a doubly-charged Δ^{--} and a singly charged Δ^{-}. If part of a multiplet with a neutral member, a Δ^{--} would immediately signal the presence of a Higgs representation with total isospin $T = 1$ or higher. Most

popular are the complex $Y = -2$ triplet Higgs representations, such as those required in left-right symmetric models, that contain a Δ^{--} , a Δ^{-} and Δ^{0}.

In assessing the attractiveness of a Higgs sector model containing a Δ^{--} many constraints need to be considered. For a triplet and higher representations containing a neutral member, limits on the latter's $v.e.v.$ required for $\rho = 1$ at tree-level are generally severe. Models with $T = 1$ and $T = 2$ can have $\rho = 1$ at tree-level by combining representations. However, such models generally require fine-tuning, in order to preserve $\rho = 1$ at one-loop. The simplest way to avoid all ρ problems is to either consider representations that simply do not have a neutral member (e.g. a $Y = -3$ doublet or a $Y = -4$ triplet representation), or else models in which the $v.e.v.$ is precisely zero. We will only consider models of this type in what follows [4].

Further constraints on Higgs representation arise if we require unification of the coupling constants without intermediate scale physics. In the SM, unification is possible for a relatively simple Higgs sector that includes a single $|Y| = 2$ triplet in combination with either one or two $|Y| = 1$ doublets (the preferred number of doublets depends upon the precise value of $\alpha_s(m_Z)$). In the case of minimal supersymmetric extension of the Standard Model ($MSSM$) [7, 8, 9, 10, 11], precise unification requires exactly two doublet Higgs representations; any extra doublet representations or any number of triplet or higher representations would destroy unification.

In short, the popular two-doublet $MSSM$ need not be nature's choice. We should be on the look-out for signatures of exotic Higgs representations, the clearest of which would be the existence of a doubly-charged Higgs Boson. Thus it is important to understand how to search for and study such a

particle.

Naturally, the phenomenology of the Δ^{--} derives from its couplings. Trilinear couplings of the type $W^-W^- \to \Delta^{--}$ are not present in the absence of an enabling non-zero $v.e.v.$ for the neutral member (if present) of the representation, and $q'\bar{q}\Delta^{--}$ couplings are obviously absent. There are always couplings of the form $Z/\gamma \to \Delta^{--}\Delta^{++}$. In addition, and of particular interest, there is the possibility of lepton-number-violating $l^-l^- \to \Delta^{--}$ couplings in some models. For $Q = T_3 + \frac{Y}{2} = -2$ the allowed cases are

$$\begin{aligned} l_R^- l_R^- &\to \Delta^{--} \ (\ T = 0,\ T_3 = 0,\ Y = -4\ ), \\ l_L^- l_R^- &\to \Delta^{--} \ (\ T = \frac{1}{2},\ T_3 = -\frac{1}{2},\ Y = -3\ ), \\ l_L^- l_L^- &\to \Delta^{--} \ (\ T = 1,\ T_3 = -1,\ Y = -2\ ). \end{aligned} \tag{2.1}$$

Note that the above cases do not include the $T = 3$, $Y = -4$ representation that yields $\rho = 1$, nor the $T = 1$, $Y = -4$ triplet with no neutral member, but do include the $T = 1/2$, $Y = -3$ doublet representation with no neutral member, and the popular $T = 1$, $Y = -2$ triplet representation.

In left-right symmetric (LR) electroweak theory [12, 13, 14, 15] the doubly-charged Higgs boson is a member of a triplet Higgs representation which plays a crucial part in the model. The gauge symmetry $SU(2)_L \otimes SU(2)_R \otimes U(1)_{B-L}$ of the LR model is broken to the SM symmetry $SU(2)_L \otimes U(1)_Y$ due to a triplet Higgs Δ_R, whose neutral component acquires a non-vanishing $v.e.v.$. The Δ_R, called the 'right-handed' triplet, transforms according to $\Delta_R = (1, 2, 3)$, and it consists of the complex fields Δ_R^0, Δ_R^+ and Δ_R^{++}. If the Lagrangian is assumed to be invariant under a discrete $L - R$ symmetry, it must contain, in addition to Δ_R, also a 'left-handed' triplet $\Delta_L =$

$(\Delta_L^0, \Delta_L^+, \Delta_L^{++}) = (3, 1, 2)$. Hence the LR model predicts two kinds of doubly charged particles with different interactions. They are both with $|Y| = 2$. Phenomenologies of the right-handed and left-handed isospin triplets are completely different [16]. In contrast with Δ_R, the existence of Δ_L is not essential from the point of view of the spontaneous symmetry breaking of the gauge symmetry. The $v.e.v.$ of its neutral member is actually quite tightly bound by the ρ parameter, i.e. by the measured mass ratio of the ordinary weak bosons (see discussion above).

In the case of a $|Y| = 2$ triplet representation the lepton-number-violating coupling to left-handed leptons is specified by the Langrangian form [17]

$$\mathcal{L}_Y = i\ h_{L,ij}\ \psi_{iL}^T\ C\tau_2\ \Delta_L\ \psi_{jL} + i\ h_{R,ij}\ \psi_{iR}^T\ C\tau_2\ \Delta_R\ \psi_{jR} + h.c. \qquad (2.2)$$

where $i, j = e, \mu, \tau$ are generation indices, the ψ's are the two-component left-handed (right-handed respectively) lepton fields ($\psi_{lL,R} = (\nu_l, l^-)_{L,R}$), and Δ is the 2×2 matrix of Higgs fields [6]

$$\Delta_{L,R} = \begin{pmatrix} \Delta_{L,R}^-/\sqrt{2} & \Delta_{L,R}^{--} \\ \Delta_{L,R}^0 & -\Delta_{L,R}^-/\sqrt{2} \end{pmatrix}. \qquad (2.3)$$

From the point of view of phenomenology a very important fact is that the $U(1)_{B-L}$ symmetry prevents quarks from coupling to Δ_R and Δ_L [18]. In the process that involve hadrons the triplet Higgses appear therefore only through higher-order corrections.

The Yukawa Lagrangian form 2.2 leads to large Majorana mass terms of the form $h_{R,ij} < \Delta_R^0 \nu_{iR} \nu_{jR}$ for the right-handed neutrinos [19]. These give rise to the see-saw mechanism [19, 20], which provides the simplest explanation

to the lightness of ordinary neutrinos, if neutrinos do have a mass. This subject is discussed in more detail in Appendix F.

Apart from the question of neutrino mass, the LR model is more satisfactory than the SM also because it gives a better understanding of parity violation and it maintains the lepton-quark symmetry in weak interactions. Nevertheless, so far there has been no direct evidence of left-right symmetry in weak interactions. This also sets a lower bound to the energy scale of the breaking of that symmetry.

Decays of a Δ^{--} are generally quite exotic [2, 3, 6]. At the Tevatron, the two production mechanisms with potentially larger cross section are pair (Drell-Yan process) production, $p\bar{p} \to \gamma/Z^0 \; X \to \Delta^{--}\Delta^{++} \; X$ or single production via WW fusion, $p\bar{p} \to \mathrm{W}^-W^- \; X \to \Delta^{--} \; X$. However, existing phenomenological and theoretical constraints can be only easily satisfied if the $\mathrm{W}^-W^- \to \Delta^{--}$ coupling is vanishing. This is why in this analysis we consider the discovery reach for $\Delta^{--}\Delta^{++}$ pair production only.

For a vanishing $\Delta^{--} \to W^-W^-$ coupling, the only two-body decays that might be important are $\Delta^{--} \to \Delta^-W^-$, $\Delta^{--} \to \Delta^-\Delta^-$ and, if the lepton coupling is present, $\Delta^{--} \to l^-l^-$. Typically, the Δ^{--} and Δ^{++} have similar masses, in which case $\Delta^{--} \to \Delta^-\Delta^-$ is likely to be disallowed. Thus, the focus is on the Δ^-W^- and l^-l^- final states. Decays into $\Delta^{\pm}$ would only be relevant if the singly-charged Higgs boson is lighter than the doubly-charged Higgs boson. In many models, it is possible for the Δ^{--} to couple to like-sign lepton pairs, l^-l^-. If the $W^-W^- \to \Delta^{--}$ coupling is vanishing (or very small), it is then very likely that the doubly-charged Higgs will dominantly decay to like-sign leptons via the lepton-number-violating coupling.

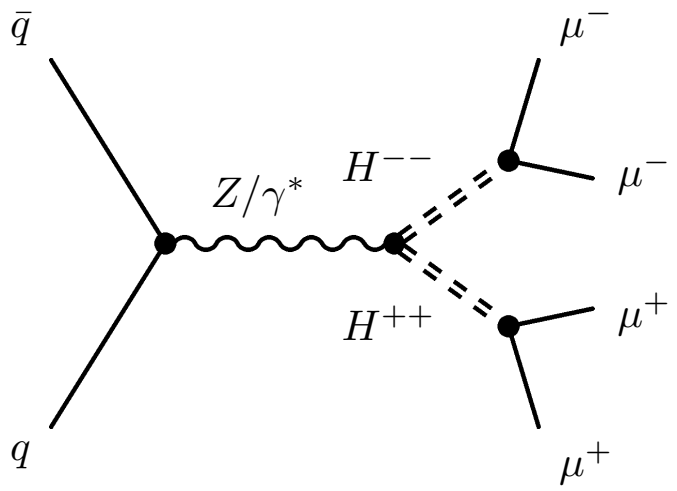

Figure 2.1: Leading-order diagram for the pair production of doubly-charged Higgs bosons in $p\overline{p}$ scattering, where both Higgs bosons decay into muons.

The possible decay modes are decays in the e, μ and τ channel. Since these decays violate lepton flavor conservation, decay modes with mixed lepton flavor (e.g. $\Delta^{\pm\pm} \rightarrow e^{\pm}\mu^{\pm}$) are also possible. An exact measurement of the branching ratio for this kind of decay process gives a very impressive limit on the coupling constant.

For a $T = 1$, $Y = -2$ triplet we find [2, 3, 6]

$$\Gamma^{\Delta^- W^-}_{\Delta^{--}} = \frac{g}{16\pi} \frac{M^3_{\Delta^{--}} \beta^3}{m^2_W} \tag{2.4}$$

$$\Gamma^{l^- l^-}_{\Delta^{--}} = \frac{\mid h_{ll} \mid^2}{8\pi} M_{\Delta^{--}} [\ 1 - \frac{2m^2_l}{M^2_{\Delta^{--}}}\ ] [\ 1 - \frac{4m^2_l}{M^2_{\Delta^{--}}}\ ]^{1/2} \tag{2.5}$$

where β is the usual phase space suppression factor, and h_{ll} stands for

$$| h_{ll} | \equiv c_{ll} \, m^2_{\Delta^{--}} \tag{2.6}$$

with c_{ll} a dimensionless coupling constant to be estimated from the experiment. These constants are the subject of a further discussion in this paper. Their relative ratio provides an insight into the branching ratios of $\Delta^{--} \to l^- l^-$ into $l = e$, μ or τ.

Alternatively, if the $\Delta^{--} \to l^- l^-$ and $\Delta^{--} \to W^- W^-$ couplings are both vanishing or very small, then the Δ^{--} can have a sufficiently long lifetime that it will decay outside the detector. Identification of the $\Delta^{--}\Delta^{++}$ pair via the associated dE/dx distributions in the tracker would then be possible (if the detector design allows to do that).

2.2 Experimental limits on the doubly-charged Higgs bosons

In this section we consider contribution of a doubly-charged Higgs boson Δ^{--}/Δ^{++} exchange in several physics processes. It was demonstrated that the effective Hamiltonian that is typically used to interpret the results of muonium-antimuonium oscillation experiments also describes the t-channel exchange of a Δ^{--} [17]. And a limit on the existence of the Δ^{--} can be extracted from the most recent muonium oscillation results [16]. The effect of Δ^{--} exchange on high-energy Bhabha scattering is discussed, and a limit is extracted from the published cross sections of several experiments at SLAC, DESY, as well as LEP searches at OPAL and L3 [16]. The case of a non-diagonal coupling of the Δ^{--} to the charged leptons (non-diagonal

in lepton flavor) is considered. A limit is extracted from the result of the most recent search for the rare decay $\mu \rightarrow 3e$ [16]. Finally, the contribution to the anomalous magnetic moment of the muon $(g-2)_\mu$ is discussed and the limit is derived from very recent measurement published by the Muon $(g-2)$ Collaboration in Brookhaven [21]. These measurements represent indirect searches for a doubly-charged Higgs boson, it is possible however, to search for Δ^{--} directly. Limits from LEP experiments are given [22, 23]. This thesis presents a direct search for a doubly-charged Higgs in the muon channel at DØ.

2.2.1 Indirect signals

Low-energy bounds on the doubly-charged Higgs can be derived from the good agreement between theory and experiment in many process expected in the Standard Model, and from non-observation of reactions which are forbidden or suppressed in the SM. These processes represent indirect signals for a doubly-charged Higgs, from their results are derived present low-energy bounds on the doubly-charged Higgs couplings and mass.

A. Muonium-Antimuonium transitions

The origin of the apparent family structure of all known fermions is a complete mystery. It has been known since the discovery of the kaon that the weak eigenstates of the quark sector do not respect this family structure. However, no analogous behavior has ever been observed in the lepton sector. Most searches for lepton-flavor violation have concentrated upon processes

which change lepton flavor L_f by one unit (e.g. $K \to \mu e$ or $\mu \to e\gamma$)[2]. There have been relatively few searches done for those processes that change lepton flavor by two units.

An example of such a transition is the process $e^+e^- \to \mu^-\mu^-$, or the transformation of muonium ($\mu^+e^- \equiv M$) into antimuonium ($\mu^-e^+ \equiv \bar{M}$). The latter process is the exact analog of neutral kaon mixing. There is a number of physical models that incorporate lepton-flavor-changing processes. Feynman diagrams for three processes that mediate the conversion of muonium into antimuonium are shown in Figure 2.2.

Figure 2.2(a) represents the second-order exchange of ordinary massive Dirac neutrinos. Since the external (lepton) masses are at least as large as the internal (neutrino) masses, this process is more analogous to $B^0 - \bar{B}^0$ mixing than to neutral-kaon mixing. Several authors have calculated the effective Hamiltonian for B-meson mixing. Changing quark labels to lepton labels, we can write that the effective Hamiltonian for second-order neutrino exchange is given by the expression [24]

$$\begin{aligned} \mathcal{H}_{eff} \quad = \; & \tfrac{G_A}{\sqrt{2}}\, \bar{\psi_\mu}\gamma^\alpha \,(\, 1+\gamma_5 \,)\, \psi_e \; \bar{\psi_\mu}\gamma_\alpha \,(\, 1+\gamma_5 \,)\, \psi_e + \\ & \tfrac{G_B}{\sqrt{2}}\, \bar{\psi_\mu}\, \gamma^\alpha \,(\, 1-\gamma_5 \,)\, \psi_e \; \bar{\psi_\mu}\, \gamma_\alpha \,(\, 1-\gamma_5 \,)\, \psi_e + h.c. \end{aligned} \tag{2.7}$$

where the coupling constants G_A and G_B are complicated functions of lepton masses, neutrino masses and mixing angles.

The process presented in Figure 2.2(b) is quite similar to that represented by Figure 2.2(a) except that Majorana neutrinos are exchanged instead of

[2]A change of lepton flavor ΔL_f is defined as the change in lepton number for *each* species of lepton.

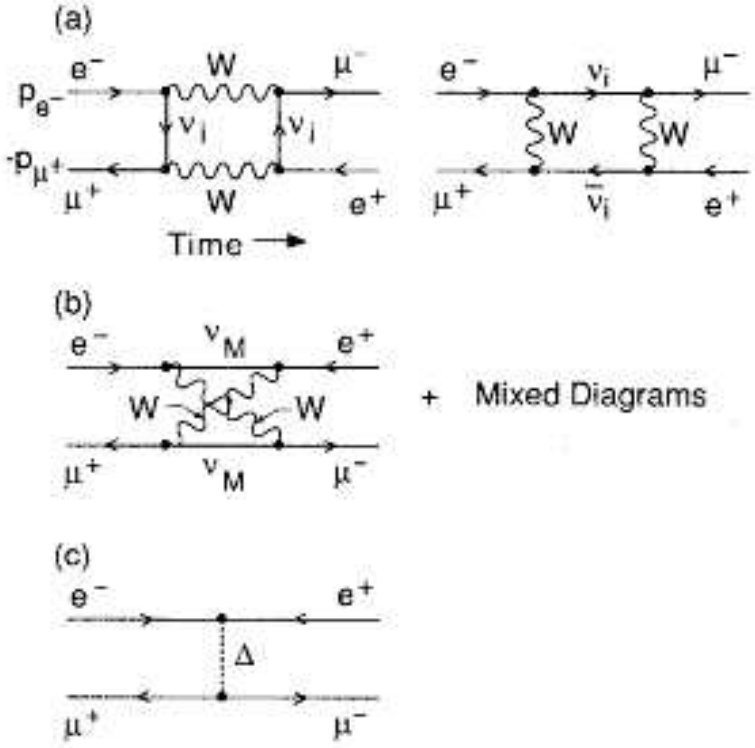

Figure 2.2: Three possible subprocesses for muonium to antimuonium conversion. (a) represents a second-order exchange of ordinary Dirac neutrinos. (b) is a similar process but with Majorana neutrinos instead. (c) represents the t-channel exchange of a doubly-charged Higgs boson. All diagrams can be reordered to describe the process $e^-e^- \to \mu^-\mu^-$.

Dirac ones. The limit on the coupling constant can be derived from the absence of neutrinoless double-beta decay [25].

The third process shown in Figure 2.2(c), involves the t-channel exchange of a doubly-charged Higgs boson.

The mass of the doubly-charged Higgs boson M_Δ is certainly large on the scale of the momentum transfer that is associated with muonium to antimuonium oscillation. The effective Hamiltonian for $M - \bar{M}$ conversion can therefore be written as [17]

$$\mathcal{H}_\Delta = \frac{g_{ee}\ g_{\mu\mu}}{8M_\Delta^2}\ \bar{\psi_\mu}\ \gamma^\alpha\ (\ 1+\gamma_5\ )\ \psi_e\ \bar{\psi^\mu}\ \gamma_\alpha\ (\ 1+\gamma_5\ )\ \psi_e + h.c. \tag{2.8}$$

with the coupling constant defined as

$$G_{M\bar{M}} \equiv \frac{g_{ee}\ g_{\mu\mu}}{4\sqrt{2}M_\Delta^2} = \frac{g_{ee}\ g_{\mu\mu}}{g^2}\ [\ \frac{m_W}{M_\Delta}\ ]^2\ G_F \tag{2.9}$$

where g is the $SU(2)$ coupling constant and m_W is the W boson mass.

Using Equation 2.9, the current limit on $G_{M\bar{M}}$ can be converted into a limit on the ratio of couplings to M_Δ^2 (at 90% CL) [26]

$$\frac{g_{ee}\ g_{\mu\mu}}{M_{\Delta^{++}}^2} \leq 5.8 \times 10^{-5}\ GeV^{-2}. \tag{2.10}$$

Processes that exhibit lepton flavor violation may be the most spectacular to contemplate but are not necessarily the most sensitive ones to use in experimental searches.

B. Bhabha scattering

The doubly-charged Higgs boson could contribute to both Bhabha and Møller scattering, even if they were too heavy to be directly produced at the given

collider energy. They can therefore be detected via deviations from the SM expectations for the total cross sections and angular correlations. In the presence of off-diagonal flavor couplings, they may even produce states which are not expected in the realm of the standard model.

Doubly-charged scalar Higgs boson contribution to Bhabha scattering at the tree level, shown in Figure 2.3, involves the t-channel exchange

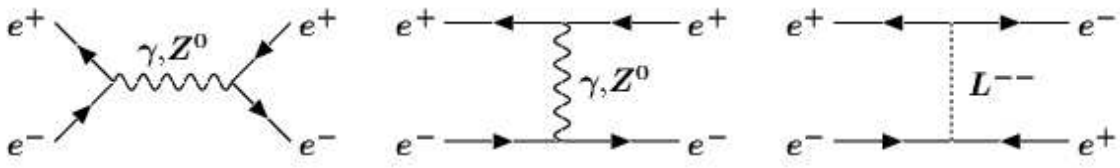

Figure 2.3: Lowest order Feynman diagrams contributing to $e^+e^- \rightarrow e^+e^-$ scattering. The contribution from doubly-charged Higgs is given in the third diagram.

of a Δ^{--} . Møller scattering involves the s-channel exchange which is experimentally less interesting.

If we assume that M_Δ is large as compared with the center-of-mass energy of the scattering process, the effective Hamiltonian for Bhabha scattering process can be written as [27]

$$\mathcal{H}_{Bhabha} = \frac{g_{ee}^2}{2\ M_\Delta^2}\ \bar{\psi}_{eR}\ \gamma^\alpha\ \psi_{eR}\ \bar{\psi}_{eR}\ \gamma_\alpha\ \psi_{eR} + h.c. \tag{2.11}$$

where we have chosen to express all fields as chiral fields. From Equation (2.11) is trivial to extract the cross section for unpolarized Bhabha scattering [27]

$$\begin{aligned}\sigma_{Higgs}(cos\theta) &\equiv \frac{d\sigma}{d(cos\theta)} \\ &= \frac{\pi\ \alpha^2}{4s}\ [\ 4\ A_0 + A_-(\ 1 - cos\theta\ )^2 \\ &+\ A_+\ (\ 1 + cos\theta\ )^2\ ],\end{aligned} \tag{2.12}$$

where the coefficients A_0, A_- and A_+ are defined as

$$\begin{aligned}A_0 &= [\ \frac{s}{t}\ ]^2\ |\ 1 + \frac{g_r g_l}{e^2}\frac{t}{t_z}\ |^2, \\ A_- &= |\ 1 + \frac{g_r g_l}{e^2}\frac{s}{s_z}\ |^2, \\ A_+ &= \frac{1}{2}\ |\ 1 + \frac{s}{t} + \frac{g_r^2}{e^2}\ [\ \frac{s}{s_z} + \frac{s}{t_z}\ ] + \frac{2 g_{ee}^2 s}{e^2 M_\Delta^2}\ |^2 \\ &+ \frac{1}{2}\ |\ 1 + \frac{s}{t} + \frac{g_l^2}{e^2}\ [\ \frac{s}{s_z} + \frac{s}{t_z}\ ]\ |^2\ .\end{aligned} \tag{2.13}$$

The various quantities used in Equation 2.12 are defined as follows: θ is the scattering angle in the center of mass (c.m.) frame; s is the square of the c.m. frame energy; $t\ =\ -s\ (\ 1 - cos\theta\ )/2$; $s_Z = s - M_Z^2 + iM_Z\Gamma_Z$ (M_Z and Γ_Z are the mass and decay width of the Z^0 boson, respectively); $t_Z = t - M_Z^2 + iM_Z\Gamma_Z$ (M_Z and Γ_Z are the mass and decay width of the Z^0 boson, respectively); $g_r = e\ tg\ \theta_W$ (e and θ_W are the electric charge and electroweak mixing angle, respectively); and $g_l = -e\ cotg\ 2\theta_W$.

Equation 2.12 is valid only for the case $M_\Delta^2 \gg s$. If s is comparable to or larger than M_Δ^2, the coefficient A_+ must be modified to account for effect of the Δ^{--} propagator.

From the Bhabha scattering cross-section at SLAC [28, 29] and DESY [30, 31] the following bound on the g_{ee} was established

- at 90% confidence limit:

$$\frac{g_{ee}^2}{M_{\Delta^{++}}^2} \leq 8.0 \times 10^{-6}\ GeV^{-2} \tag{2.14}$$

- at 95% confidence limit:

$$\frac{g_{ee}^2}{M_{\Delta^{++}}^2} \leq 9.7 \times 10^{-6}\ GeV^{-2} \tag{2.15}$$

LEP experiments have searched for pair production of doubly-charged Higgs Bosons in e^+e^- scattering. From this search, mass limits of $M(\Delta_L^{\pm\pm}) > 100.5$ GeV/c^2 and $M(\Delta_R^{\pm\pm}) > 100.1$ GeV/c^2 were obtained by OPAL [32] and a limit of $M(\Delta_{L(R)}^{\pm\pm}) > 99.4$ GeV/c^2 by L3 [33], for 100% branching ratio into muons[3].

C. Muon decays

Many of the best limits on lepton-flavor violation come from searches for rare decay modes of the muon [34]. If the coupling of the doubly-charged Higgs is purely diagonal in the lepton flavor as described in Equation 2.2, the Δ^{--} does not mediate muon decay at the tree level.

We consider the case when the doubly-charged Higgs boson couples non-diagonally to the charged-lepton sector [35, 36]. In such a case, the doubly-charged Higgs can mediate the decay $\mu \rightarrow e^-e^+e^-$. This process is shown in Figure 2.4.

A very stringent coupling constant limit can be obtained from an existing limit on branching ratio for the $\mu \rightarrow 3e$ process [37].

The non-diagonal coupling can be defined by the following Lagrangian form [38]

[3]All limits in this note are given at 95% CL, unless specified otherwise.

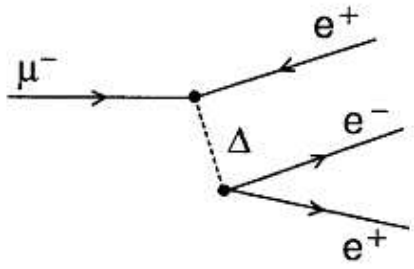

Figure 2.4: The decay $\mu \to e^- e^+ e^-$ mediated by a Δ^{--} .

$$\mathcal{L} = \frac{g_{e\mu}\ g_{ee}}{8M_\Delta^2}\ \bar{\psi}_\mu\ \gamma^\alpha\ (\ 1+\gamma_5\ )\psi_e \bar{\psi}_e \gamma_\alpha (\ 1+\gamma_5\ )\ \psi_\mu + h.c. \tag{2.16}$$

where the coupling constant $g_{e\mu}$ is presumably suppressed by the sine of a mixing angle as compared to the regular diagonal coupling constants.

Equation 2.16 can be used to calculate the $\mu \to 3e$ branching ratio [17]

$$BR(\mu \to 3e) \equiv \frac{\Gamma(\mu^+ \to e^- e^+ e^-)}{\Gamma(\mu^- \to e^- \nu_\mu \bar{\nu}_e)} = \tag{2.17}$$
$$= \frac{g_{e\mu}^2\ g_{ee}^2}{16\ G_F^2\ M_\Delta^4}\ =\ 2\ [\ \frac{g_{e\mu}\ g_{ee}}{g^2}\ ]^2\ [\ \frac{M_W}{M_\Delta}\ ]^4.$$

The best published limit on the branching ratio of $\mu \to 3e$ is $BR(\mu \to 3e) < 6.8 \times 10^{-13}$ at 90% confidence level [40]. The limit on $g_{e\mu} g_{ee}/M_\Delta^2$ can be found using Equation 2.18 [41]

$$\frac{g_{e\mu}\ g_{ee}}{M_{\Delta^{++}}^2} \leq 3.2 \times 10^{-11}\ GeV^{-2} \tag{2.18}$$

This appears to be the most stringent limit on the existence of doubly-charged Higgs boson.

Another interesting lepton-flavor violating process is the radiative muon decay, $\mu \to e\gamma$ [42, 43, 44, 45]. This process is forbidden in the SM, but it can be mediated at the one-loop level by doubly-charged Higgs boson as depicted in Figure 2.5.

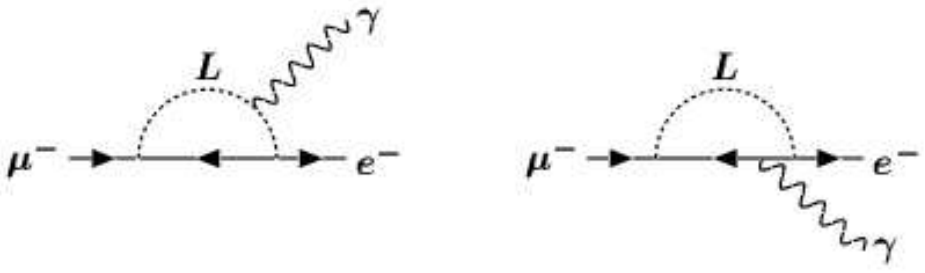

Figure 2.5: The radiative muon decay $\mu \to e\gamma$ mediated by $\Delta^{\pm\pm}$ (labeled as L because contribution from a singly-charged Higgs (L=$\Delta^{\pm\pm}$ or $\Delta^{\pm}$) is possible too).

The branching ratio of the radiative decay is indeed constrained to be very small [46]

$$BR(\mu \to e\gamma) \leq 4.0 \times 10^{-11} \tag{2.19}$$

However, one should keep in mind that being this a one-loop process, the matrix element is suppressed by a factor $(1/4\pi)^2$. This is why decay $\mu \to 3e$ gives a stronger bound. Nevertheless, $\mu \to e\gamma$ applies to different combinations of generation indices, because one can observe any lepton flavor in the loop. That makes this process to be equally interesting.

From non-observation of this decay follows [40, 41]

$$\frac{g_{e\mu}\, g_{\mu\mu}}{M^2_{\Delta^{++}}} \leq 2.0 \times 10^{-10}\ GeV^{-2}. \tag{2.20}$$

D. Anomalous magnetic moment of the muon

The anomalous magnetic moment of the electron and the muon are two of the most accurately measured quantities in physics. The Muon (g-2) Collaboration in Brookhaven [47] has measured the anomalous magnetic moment of the negative muon $a_{\mu^-} = (g-2)/2$ to a precision of 0.7 parts per million (ppm) at the Brookhaven Alternating Gradient Synchrotron (AGS).

The measurement is based on muon spin precession in a magnetic storage ring with electrostatic focusing [48, 49, 50, 51, 52]. Protons from AGS are sent on a fixed target, where pions are produced dominantly. They decay into muons in-flight ($c\tau$ of a pion is 6.7 m). Muons are fed into a uniform, doughnut-shaped magnetic field and travel in a circle (central orbit radius is 7.11 m). After each circle, muon's spin axis changes by 12^o, and it keeps on precessing in the same direction (precession period is 4.37μs). After circling the ring many times, muons spontaneously decay to electron (plus neutrino) in the direction of the muon spin.

Inside the ring, there are 24 scintillating counter detectors on the inside of the ring. The $(g-2)_\mu$ parameter is then azimuthal angle measured between electron direction of flight and muon momentum orientation, divided by the magnetic field $B = 1.45$ T the muon is traveling through in the ring.

The $(g-2)_\mu$ value of the negative muon magnetic anomaly was announced on January 8, 2004.

The published experimental value is [21]

$$\begin{aligned} a_{\mu^-}(BNL\ 2001) &= 11659214(8)(3) \times 10^{-10}\ (0.7\ ppm) \\ a_{\mu^-}(exp) &= 11659208(6) \times 10^{-10}\ (0.5\ ppm) \end{aligned} \tag{2.21}$$

in which the total uncertainty consists of 5×10^{-10} (0.4 ppm) statistical uncertainty and 4×10^{-10} (0.3 ppm) systematic uncertainty.

SM prediction for a_μ consists of QED, hadronic and weak contributions. The uncertainty on the SM value is dominated by the uncertainty on the lowest-order hadronic vacuum polarization. The same can be determined indirectly using hadronic τ decay data [53]. In principle, the τ data should even improve the precision of a_μ(had) measurement. However, discrepancies between the τ and the e^+e^- results exist. These two data sets do not give consistent results for the pion form factor. Using the annihilation of e^+e^- to hadrons data gives the corresponding theoretical value [54]

$$a_{\mu^-}(SM) = 11659181(8) \times 10^{-10}\ (0.7\ ppm) \tag{2.22}$$

The number deduced from τ decay is larger by 15×10^{-10}. The difference between the experimental determination of a_μ and the SM theory using the e^+e^- or τ data for the calculation of the hadronic vacuum polarization is 2.7σ and 1.4σ, respectively [21].

The new physics contribution could be of the order of

$$\delta(a_{\mu^-}(exp) - a_{\mu^-}(SM)) = 2.7\ \sigma = 2.7 \times 10^{-9}. \tag{2.23}$$

As we will see, these constraints are not particularly strong. The $(g-2)/2$ unlike other low energy bounds are square of a coupling constant.

There are two one-loop Feynman diagrams mediated by doubly-charged Higgs that could contribute to $(g-2)$. They are given in Figure 2.6.

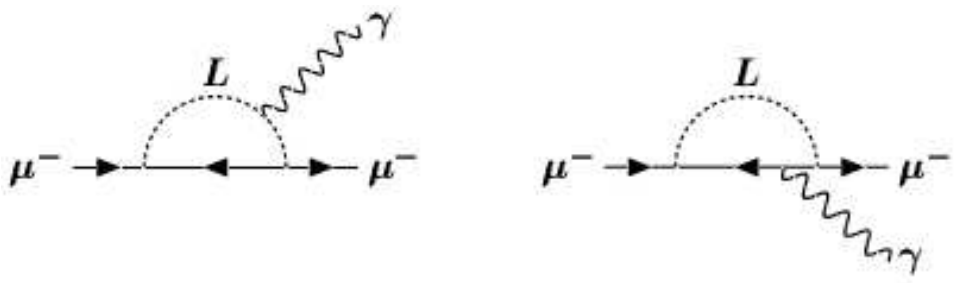

Figure 2.6: One-loop diagrams mediated by doubly-charged Higgs bosons that contribute to $(g-2)$ (labeled as L because contribution from a singly-charged Higgs is easily possible too).

The contribution of both diagrams has been evaluated [38]. They contribute to a_{μ^-} as [39]

$$a_{\mu^-} = -\frac{3\ h_{\mu\mu}^2\ m_\mu^2}{16\pi M_{\Delta^2}} \tag{2.24}$$

If one assumes that the total discrepancy between the SM and $(g-2)$ measurement is caused by extra contribution from $\Delta^{\pm\pm}$ bosons, the limit on the coupling is the following

$$\frac{g_{\mu\mu}^2}{M_{\Delta^{++}}^2} \leq 4.0 \times 10^{-6}\ GeV^{-2}. \tag{2.25}$$

2.2.2 Direct signals

The limits on the existence of doubly-charged Higgs bosons that are obtained from the study of virtual processes have the property that the limit on the

mass M_Δ is correlated with the size of the coupling g_{ll}. This correlation can be taken off by searching for the production of real Δ^{--} Δ^{++} pairs. The direct signal process $e^+e^- \rightarrow \Delta^{++}\Delta^{--}$ would produce rather spectacular four-lepton events (such as μ^- μ^- μ^+ μ^+ combinations). This section reviews coupling-independent limits from published measurements of the process $e^+e^- \rightarrow 4l$ (by LEP experiments) and it provides an insight into calculating of the NLO cross-section for the doubly-charged Higgs boson production at Tevatron and LHC.

A. Limits from $e^+e^- \rightarrow \Delta^{++}\Delta^{--} \rightarrow 4\ l$ searches at LEP

The tree level differential cross section for the process $e^+e^- \rightarrow \Delta^{++}\Delta^{--}$ is given by the expression [6]

$$\frac{d\sigma}{d(cos\theta)} = \frac{\pi\ \alpha^2\ Q_\Delta^2}{4s}\ sin^2\theta\ )\ [\ 1 - \frac{4M_\Delta^2}{s}\ ]^{3/2}, \tag{2.26}$$

where $\sqrt{s}$ is the total center of mass frame energy of the e^+e- system; θ is the polar angle of the outgoing Δ^{--} with respect to the incident electron direction; and Q_Δ is the charge of the Higgs boson ($Q_\Delta = 2$). The total cross section for the process can therefore be written as [17]

$$\sigma = \frac{4\pi\alpha^2}{3s}\ [\ 1 - \frac{4M_\Delta^2}{s}\ ]^{3/2}. \tag{2.27}$$

In the limit $M_\Delta/s \rightarrow 0$, the total cross section is equal to the cross section for the production of muon pairs.

Each of the Higgs bosons then decays into a same-sign pair of leptons with a characteristic decay width $\Gamma^{l^\pm l^\pm}$ that is described by Equation 2.5. For a mass $M(\Delta^{\pm\pm})$ of about 100 GeV/c^2, Yukawa couplings of $h_{\mu\mu} < 0.5$

are still allowed. The requirement that the $\Delta^{\pm\pm}$ is not stable and decays within $\simeq 1$ cm then according to Equation 2.5 corresponds to $h_{\mu\mu} > 10^{-7}$.

The lower limit for left- or right-handed doubly-charged Higgs bosons decaying via any single lepton channel $\Delta^{\pm\pm} \to ll$ ($\ell = \tau, \mu, \mathrm{e}$), assuming a 100% branching ratio in that channel, is $M(\Delta^{\pm\pm}) > 98.5$ GeV/c^2(OPAL) and 97.3 GeV/c^2(L3). DELPHI [22] has searched in the channel $\Delta^{\pm\pm} \to \tau^{\pm}\tau^{\pm}$, obtaining a limit of $M_{\Delta^{\pm\pm}} > 97.3$ GeV/c^2.

OPAL has also searched for the production of single doubly-charged Higgs bosons, which constrains the Yukawa coupling to electrons, h_{ee}, to be less than 0.071 for $M(H^{\pm}) < 160$ GeV/c^2 [23].

B. Doubly-charged Higgs searches at Tevatron and LHC

At hadron colliders, the lowest order (LO) partonic cross section for doubly-charged Higgs boson pair production is given by

$$\hat{\sigma}_{LO}(q\bar{q} \to \Delta^{++}\Delta^{--}) = \frac{\pi\alpha^2}{9Q^2}\,\beta^3\,[\,e_q^2 e_\Delta^2 + \frac{e_q e_\Delta v_q v_\Delta (1 - M_Z^2/Q^2) + (v_q^2 + a_q^2)v_\Delta^2}{(1 - M_Z^2/Q^2)^2 + M_Z^2\Gamma_Z^2/Q^4}] \tag{2.28}$$

with $v_q = (2\ I_{3q} - 4e_q s_W^2)/(2s_W c_W)$, $a_q = 2\ I_{3q}/(2s_W c_W)$ and $v_\Delta = (2\ I_{3\Delta} - 2e_\Delta s_W^2)/(2s_W c_W)$, where $I_{3q}(I_{3\Delta})$ denotes the third isospin component and $e_q(e_\Delta)$ the electric charge of the quark q (doubly-charged Higgs boson Δ^{--}) and $s_W = sin\theta_W$, $c_W = cos\theta_W$. Q^2 is the squared partonic center of mass frame energy, α is the QED coupling evaluated at the scale Q, M_Z the Z boson mass and Γ_Z the Z boson width. The Higgs velocity is defined as $\beta = \sqrt{1 - 4M_\Delta^2/Q^2}$.

The hadronic cross sections can be obtained from convoluting the partonic

cross section with the corresponding (anti)quark densities of the (anti)protons

$$\sigma_{LO}(pp/p\bar{p} \to \Delta^{++}\Delta^{--}) = \int_{\tau_0}^{1} d\tau \sum_q \frac{d\mathcal{L}^{q\bar{q}}}{d\tau}\ \hat{\sigma}_{LO}(Q^2 = \tau s) \tag{2.29}$$

where $\tau_0 = 4M_\Delta^2/s$ with s being the total hadronic center of mass energy squared, and $\mathcal{L}^{q\bar{q}}$ denotes the $q\bar{q}$ parton luminosity.

Next-to-leading order (NLO) QCD corrections to the $\Delta^{++}\Delta^{--}$ pair production cross-section have recently been calculated [55]. Both at the Tevatron and the LHC, QCD corrections are found to be of moderate size. They increase the LO cross section by about $20-30\%$. The residual theoretical uncertainties are of the order of $10-15\%$ which is sufficient for experimental searches for these particles at the Tevatron and LHC.

The standard QCD corrections are: virtual gluon splitting, gluon emission and quark emission. They are identical to corrections applied in case of the Drell-Yan process.

The LO cross section is modified as follows [55]

$$\begin{aligned}
\sigma &= \sigma_{LO} + \Delta\sigma_{q\bar{q}} + \Delta\sigma_{qg} \\
\Delta\sigma_{q\bar{q}} &= \frac{\alpha_s(\mu_R)}{\pi} \int_{\tau_0}^{1} d\tau \sum_q \frac{d\mathcal{L}^{q\bar{q}}}{d\tau} \int_{\tau_0/\tau}^{1} dz\ \hat{\sigma}_{LO}(Q^2 = \tau z s)\omega_{q\bar{q}}(z) \\
\Delta\sigma_{q\bar{g}} &= \frac{\alpha_s(\mu_R)}{\pi} \int_{\tau_0}^{1} d\tau \sum_q \frac{d\mathcal{L}^{q\bar{g}}}{d\tau} \int_{\tau_0/\tau}^{1} dz\ \hat{\sigma}_{LO}(Q^2 = \tau z s)\omega_{q\bar{g}}(z)
\end{aligned} \tag{2.30}$$

where the coefficient functions can be expressed as [56]

$$\begin{aligned}
\omega_{q\bar{q}}(z) &= -P_{qq}(z)\ ln\frac{\mu_F^2}{\tau_s} + \frac{4}{3}\left\{ \left[\frac{\pi^2}{3} - 4 \right] \delta(1-z) + 2\,(1+z^2)\left(\frac{ln(1-z)}{1-z} \right)_+ \right\} \\
\omega_{qg}(z) &= -\frac{1}{2}\ P_{qg}(z)\ ln\left(\frac{\mu_F^2}{(1-z)^2\ \tau s} \right) + \frac{1}{8}\left\{ 1 + 6z - 7z^2 \right\}
\end{aligned} \tag{2.31}$$

and where μ_F denotes the factorization scale, μ_R the renormalization scale and P_{qq}, P_{qg} the splitting functions [57]

$$\begin{aligned} P_{qq}(z) &= \frac{4}{3}\left\{ \frac{1+z^2}{(1-z)_+} + \frac{3}{2}\,\delta(1-z) \right\} \\ P_{qg}(z) &= \frac{1}{2}\left\{ z^2 + (1-z)^2 \right\}. \end{aligned} \tag{2.32}$$

The numerical results were calculated by Margarete Mühlleitner and Michael Spira using CTEQ6L1 (CTEQ6M) parton densities at (next-to-)leading order with the strong coupling α_s adjusted accordingly, i.e. $\alpha_s^{LO}(M_Z) = 0.130$, $\alpha_s^{NLO}(M_Z) = 0.118$. The electroweak quantum numbers of the doubly-charged Higgs boson Δ^{--} have been chosen to be isospin $I_{3\Delta} = -1$ and charge $Q_\Delta = -2$.

The NLO cross section at the Tevatron for the left- and right-handed states, and the ratio between the NLO and LO cross-section (K-factor) as a function of $M(\Delta^{\pm\pm})$ are shown in Figure 2.7.

The renormalization and factorization scale has been chosen as $\mu_F^2 = \mu_R^2 = Q^2$ which is the natural scale choice for Drell-Yan like processes.

For comparison, Figures 2.8 and 2.9 show the cross section and K-factor ($K = \sigma_{NLO}/\sigma LO$) as function of doubly-charged Higgs mass. The curve for the Tevatron is truncated at $M_\Delta = 500$ GeV/c^2, since the cross section gets too small above and it thus phenomenologically irrelevant.

The QCD corrections increase the LO cross section by $20-30\%$ which can be inferred from Figure 2.9. The residual renormalization and factorization scale dependence at NLO amounts to about $5-10$ % and it serves as an estimate of the theoretical systematical uncertainty in this analysis. This uncertainty is comparable to NNLO corrections. The uncertainties of the

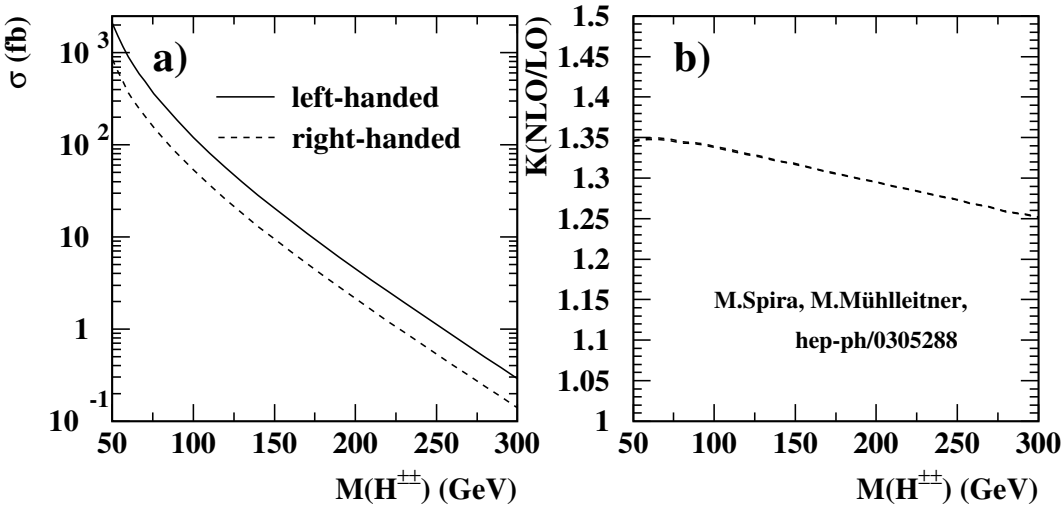

Figure 2.7: Tevatron: (a) NLO cross-sections and (b) ratio of the NLO to LO cross-sections as a function of the mass of the doubly-charged Higgs boson, $M(\Delta^{\pm\pm})$ [55].

parton densities have to be added. This why the final theoretical uncertainty on the NLO cross section amounts to $10 - 15$ % [55].

The pair production cross-section for left-handed doubly-charged Higgs bosons in the mass range $100 < M(\Delta^{\pm\pm}) < 200$ GeV/c^2 is about a factor two larger than for the right-handed states due to different coupling to the intermediate Z boson.

The search for doubly-charged Higgs boson decaying into muons via the process $q\overline{q} \rightarrow \gamma^*/Z \rightarrow \Delta^{++}\Delta^{--} \rightarrow \mu^+\mu^+\mu^-\mu^-$ is presented in this thesis. The leading-order diagram is shown in Figure 2.1.

Using dimuon events with muons of opposite charge, which originate mainly from $Z \rightarrow \mu^+\mu^-$ decays, we first study the experimental sensitivity to a possible $\Delta^{\pm\pm}$ signal. This data sample is also used to determine muon

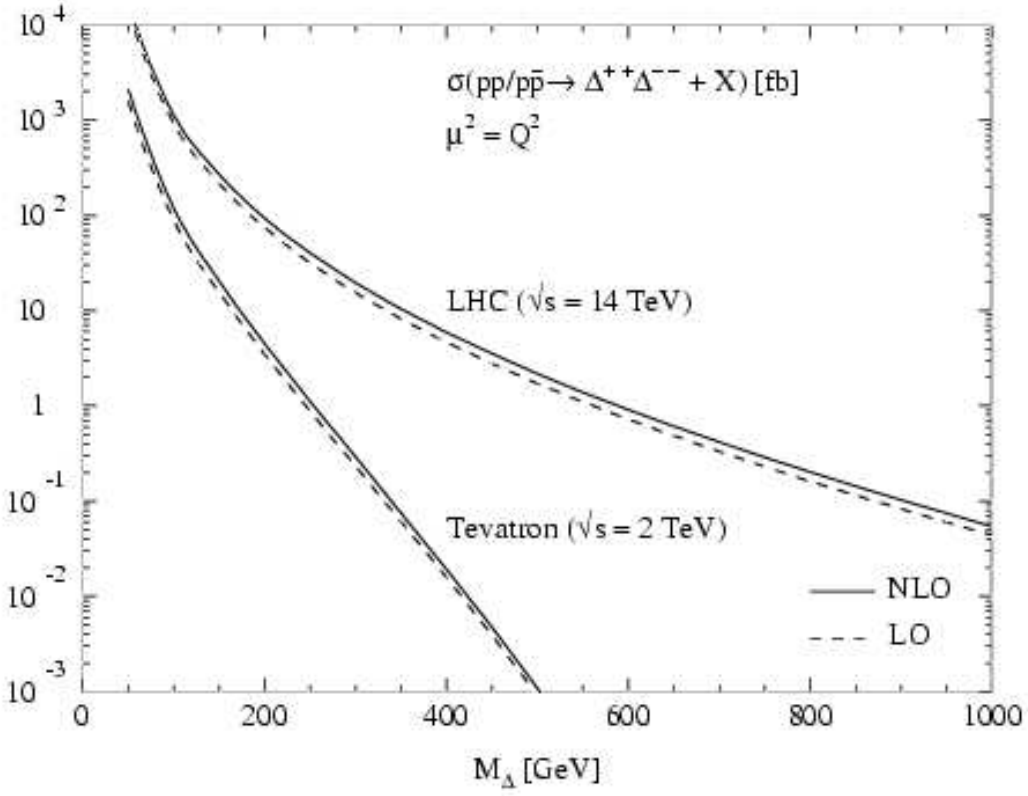

Figure 2.8: Production cross sections of doubly-charged Higgs pair production at the Tevatron and the LHC as a function of its mass [55].

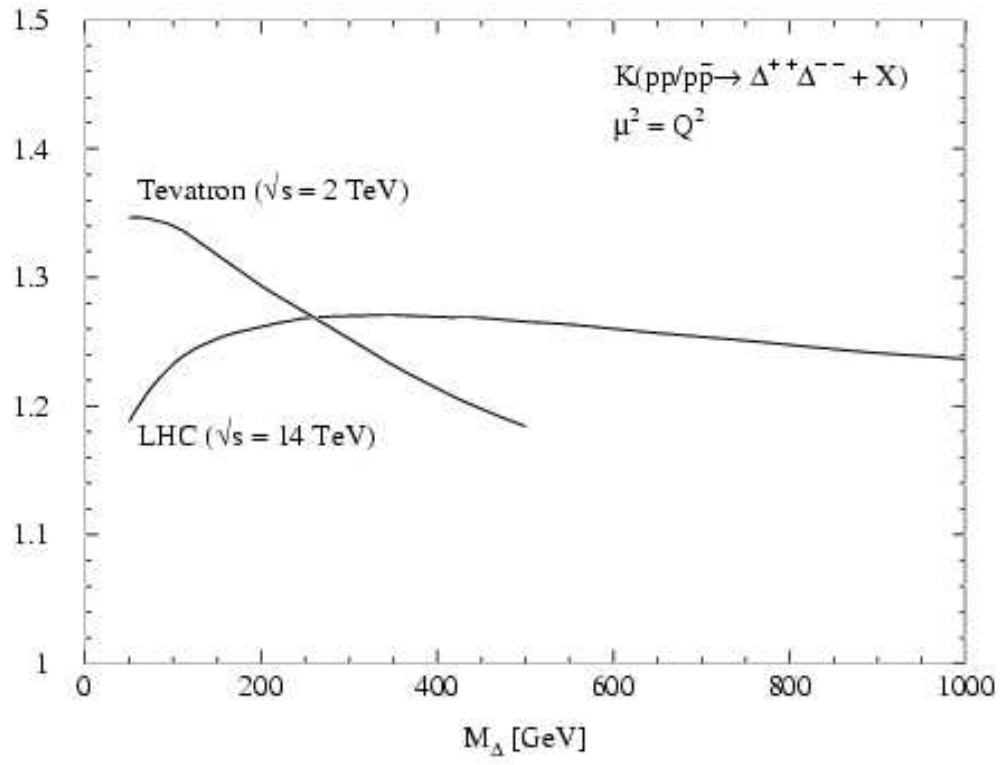

Figure 2.9: K-factors of doubly-charged Higgs pair production at the Tevatron and the LHC as a function of its mass [55].

reconstruction efficiencies and to study the description of the experimental resolutions by the Monte Carlo simulation. A search for doubly-charged Higgs production in muon final states is then performed by selecting events that contain like-charged muon pairs.

Chapter 3

Experimental apparatus

DØ Run II detector is a large, multipurpose detector for studying $p\bar{p}$ collisions which has been operating at the Fermilab Tevatron since March 2001. The design was optimized for the study of high-p_{T} physics and high mass states, and stresses the identification and measurement of electrons and muons, the measurement of the direction and total energy of high-p_{T} jets, and the determination of missing transverse energy. Emphasis is also placed on identifying and tracking individual particles within jets.

Detectors for colliding beam experiments are composed of several different particle-detection devices. They all have their specific strengths and weaknesses. The general layout is optimized however, to achieve optimal efficiency of detecting products of high-energy collisions inside the detector. This is naturally dictated by the physics processes governing the interaction of different particles with the material.

The tracking system is the closest to the interaction point. These devices are designed to measure with a high efficiency and a great accuracy the three-dimensional trajectories of particles passing through them. The tracking

detectors are immersed in a magnetic field. This permits a determination of the momentum of the charged particle using the curvature (its bending radius) in the magnetic field.

The tracking system is surrounded by the calorimetry. Calorimeters are detectors that measure the energy of a particle that is passing through them. An ideal calorimeter should be so thick that it will absorb all the energy of incident particles. The energy of a particle is measured through the energy deposit in the active material of the calorimeter. This is somewhat inconsistent with the tracking detectors. They should contain as little material as possible in order to minimize effects like multiple scattering and energy loss. Both effects alter the precision with which the calorimeter can estimate energy of an incident particle. Additionally, it complicates reconstruction of particle energies because one has to take into account the energy deposit prior to the calorimeter (that is not read out). A calorimeter is typically made thick enough to stop all known particles except for muons and neutrinos.

Muons are identified by the use of the tracking system outside the calorimeter. Any charged particles that penetrate the calorimeter are likely to be muons. Their momentum is measured using the toroidal field created in the muon system. Neutrinos are not detected at all. Their presence is however inferred from an imbalance in the total detected momentum perpendicular to the beam.

The the DØ detector is illustrated in Figure 3.1. In DØ Run I detector the central magnetic field was absent. The absence of a magnetic tracker implied the need for an excellent calorimeter. DØ uses a liquid argon sampling calorimeter made with depleted uranium absorber plates. The DØ Run II

detector combines both, a very good calorimetry and a precise momentum measurement using a solenoidal magnetic field. In addition, the extensive muon system is installed surrounding the calorimeter. Measurement of the muon momentum is provided by magnetized iron toroids that is placed between the first two muon tracking layers.

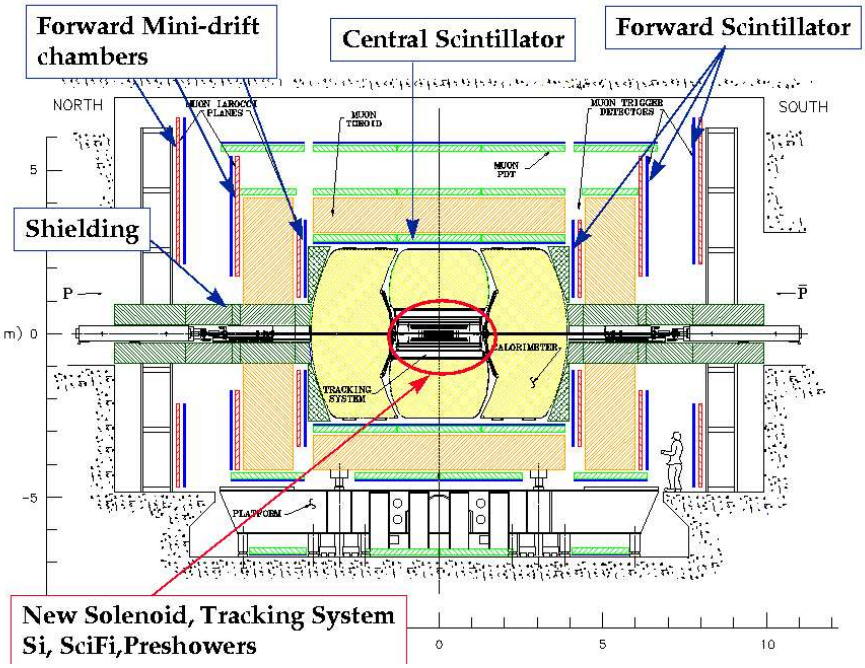

Figure 3.1: Cross sectional view of the Run II DØ detector.

The DØ detector is about 13 m high × 11 m wide × 17 m long with a total weight of about 5,500 tons [58, 59]. The entire detector assembly rests on rollers so that it can be rolled from the assembly area to the collision hall. The platform provides rack space for detector electronics and other support services.

The electronic noise and grounding is an issue at DØ . In order to minimize the electronic noise, most of the clocked devices are kept out of platform. They are moved to the Movable Counting House (MCH), where the analog signals are brought. The MCH contains the digitization electronics, Level 1 trigger, high-voltage power supplies and distribution boxes, etc. The MCH also moves with the detector when rolling in to reduce the length of cables needed to read out the detector. The detector data cables are lead out into the second floor of MCH, into so-called fixed counting house.

The DØ detector was constructed to study high mass and high-p_{T} phenomena, such as super-symmetric squarks, gluons and charginos, top physics, the b-sector, properties of the W boson, searches for the Standard Model Higgs boson and beyond. The detector has performed extraordinarily well in Run I. The top discovery and other published physics results are a living reminder of that.

In preparation for Run II both collider experiments have undergone significant upgrades to improve their physics performance and make them compatible with high luminosity running. The major change to the accelerator affecting the operation of the experiments was an increase in the number of bunches from 6 to 36, with a corresponding decrease in bunch crossing time to 396 ns.

With the improvement in the Tevatron luminosity and the experience gained in operating the DØ detector and in analyzing the data from Run I, the DØ collaboration has upgraded the detector to insure the fullest exploitation of the physics opportunities for the Tevatron Run II.

The upgrade of the DØ experiment includes:

- A large area silicon microstrip vertex detector
- A 2 Tesla superconducting solenoid magnet
- Eight layers of scintillating fiber tracking with axial and $\pm 3^{\circ}$ stereo readout
- A preshower detector surrounding the solenoid and in the forward regions, to improve e/γ identification
- Muon pixel counters in both the central and forward regions
- A new forward muon system
- Adapted calorimeter electronics to match the reduced bunch crossing interval and improvements to the trigger and DAQ systems (front-end electronics)

The DØ detector is comprised of the following main elements.

3.1 Tracking system

The most important part of the upgrade is the central tracking system, shown in Figure 3.2. It has been entirely replaced. The 2 T axial magnetic field is provided by a ~ 2.6 m long superconducting solenoid magnet with ~ 0.5 m inner radius. The solenoid encloses a scintillating fiber tracker and a silicon microstrip tracker.

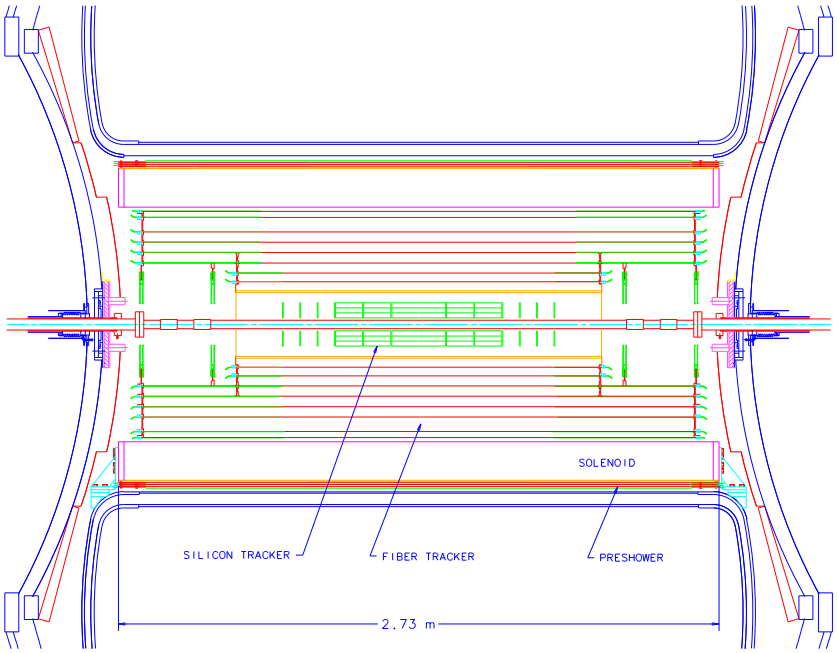

Figure 3.2: Cross sectional view of the DØ tracking system.

3.1.1 Silicon Microstrip Tracker

The SMT has 792,576 individual strips (6,192 readout chips), with typical pitch of $50 - 80$ μm, and a design optimized for tracking and vertexing capability at $|\eta| < 3$ [1]. The system has a six-barrel longitudinal structure, each with a set of four layers arranged axially around the beam pipe, and interspersed with 16 radial disks.

The basic philosophy of the DØ silicon tracker is to maintain track and vertex reconstruction over the full η acceptance of DØ . This task, however, is complicated by the Tevatron environment. In a machine with a point source luminous region the interaction point could be surrounded by detectors in a roughly spherical geometry. This would allow all tracks to intersect the detector planes at approximately normal incidence and provide optimal resolution. The upgraded Tevatron, however, is has the following parameters:

- Luminosity of $10^{32}\,\mathrm{cm}^{-2}\mathrm{s}^{-1}$.

[1] *Rapidity*, Y, is a variable used commonly for particle behavior description in inclusive reactions.

$$Y = \frac{1}{2} \cdot \ln \frac{E + p_{\mathrm{L}}}{E - p_{\mathrm{L}}} \tag{3.1}$$

where E and p_{L} are the energy and momentum component parallel to the beam axis. Rapidity distributions are Lorentz invariant.

Pseudorapidity, η, is used to approximate the rapidity when the mass and momentum of a particle are not known, and equals Y when $\beta = 1$ (massless particle). It is defined as

$$\eta = -\ln(\tan(\theta/2)) \tag{3.2}$$

where θ is the polar angle between the particle direction and the beam axis.

- Length of interaction region $\sigma_z \approx 25\,\text{cm}$.
- Initial crossing interval of 396 ns.
- Beam transverse sigma of less than $50\,\mu\text{m}$.

Each of the machine parameters has an effect on the silicon design. The luminosity sets a scale for the radiation damage expected over the life of the detector, which in turn dictates the operating temperature. The length of the interaction region sets the length scale of the device. With a long interaction region it is difficult to deploy detectors such that the tracks are generally perpendicular to detector surfaces for all η. This requirement led to a hybrid system, with barrel detectors measuring primarily the r-φ coordinate and disk detectors which measure r-z as well as r-φ. Thus vertices for high η particles are reconstructed in three dimensions by the disks, and vertices of particles at small values of η are measured in the barrels. The crossing interval sets the design parameters for the electronics and readout as well as the probability that multiple interactions occur in a single crossing. Finally the small beam radius compared to a typical B track impact parameter of $300\,\mu\text{m}$ means that fast impact parameter triggers can be contemplated, such as Silicon Tracker Trigger (STT) and Central Tracker Trigger (CTT).

Given all constraints and design considerations, to be discussed in more detail below, the following design was adopted. There are six barrels in the central region. Each barrel has four silicon readout layers, numbered one through four. The four most central barrels employ only double sided silicon. Layers 1 and 3 have axial and 90° stereo readout; layers 2 and 4 have axial and 2° stereo readout. The outermost two barrels, the barrels at high $|z|$,

employ single sided silicon with axial readout only in layers 1 and 3. Layers 2 and 4 have, as in the central four barrels, double sided silicon with axial and 2° stereo readout. The SMT barrel geometry is shown in Figure 3.4.

Each barrel is capped with a disk of wedge detectors, called the "F-disks". The F-wedges are double sided silicon wafers with trapezoidal shape, with the edges at $\pm 15°$ with respect to the symmetry axis of the wafer. The strips run parallel to one edge, giving an effective stereo angle of 30°. There are twelve wedges mounted on a disk. To provide further coverage at intermediate $|\eta|$, the central silicon system is completed with a set of three F-disks on each side of the barrel. Each disk is rotated by 7.5° with respect to its more central disk.

In the far forward and backward regions two large diameter "H-disks" provide tracking at high $|\eta|$. Each H-wedge consists of two single sided silicon detectors, glued back-to-back. The strips run at 7.5° with respect to the symmetry axis of the wafers, giving an effective stereo angle of 15°. A total of 24 wedges are mounted on one H-disk. Figure 3.3 shows an isometric view of the silicon tracker.

Given the limited radial space available, the four layer silicon detector design was chosen. In this geometry, disks at fixed locations in z provide an additional space point on a track, which give great aid in pattern recognition and track finding. In such a system the disk separation must be kept small to minimize extrapolation errors. However, each plane of disks also represents a dead region between the barrels which lowers the overall efficiency of the detector. Thus, there is a compromise between vertex resolution at large η (1/disk spacing) and efficiency at small values of η.

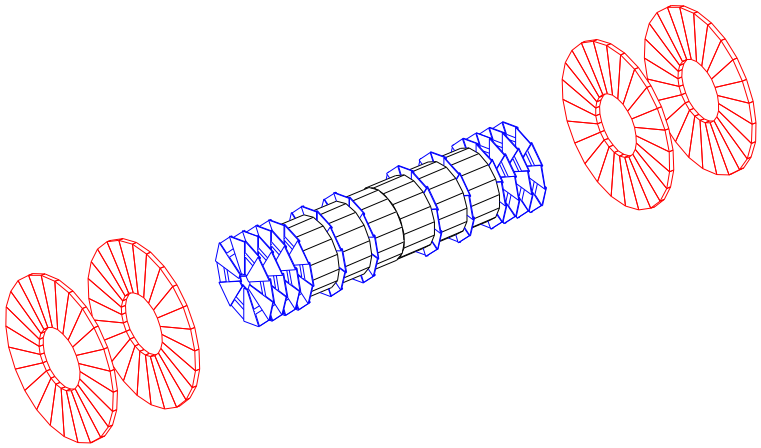

Figure 3.3: Isometric view of the DØ silicon tracker.

This design clearly puts a premium on a minimal gap between barrel sections. In the design adopted, this gap is minimized in several ways:

1. Inboard mounting of the electronics. The readout electronics and their supports are mounted on top of the active detector surface. This means that extra inter-barrel space is not needed for "ears".

2. Inboard routing of cables. Cables which supply power, control, and readout bus signals are routed to the outer radius between detector layers rather than off the ends of the ladders.

3. Thin disk modules. The disk detectors are designed to be as thin as possible consistent with mechanical rigidity. In these modules the electronics is mounted outboard of the silicon with flexible jumpers to bring the signals to the readout chips.

The 12 cm long barrel segments are separated by 8 mm gaps containing F-disks at $|z| = 12.487$, 25.300 cm and 38.113 cm. A set of three more F-

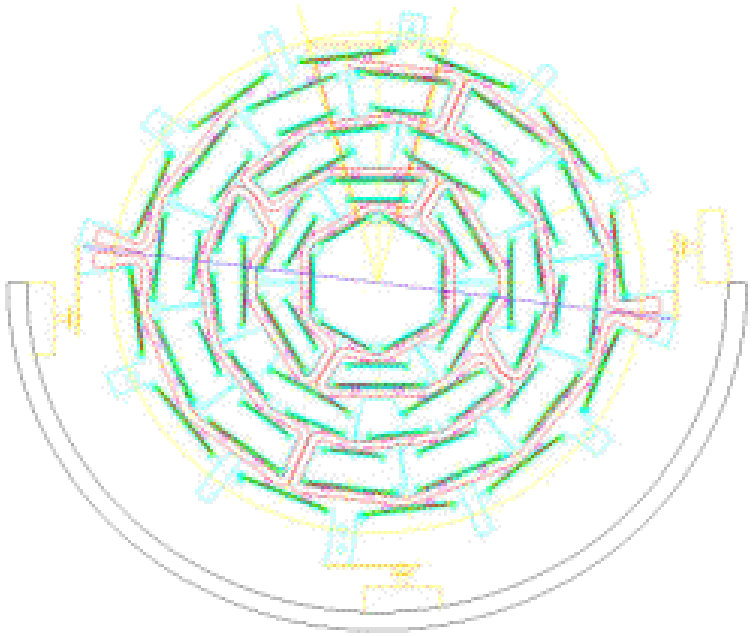

Figure 3.4: SMT barrel geometry.

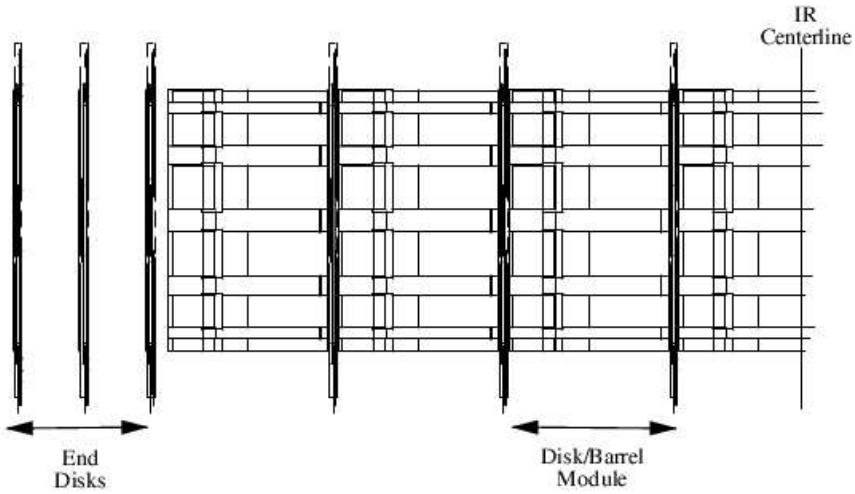

Figure 3.5: Side view of one half of the central silicon detector.

	Barrels	F-disks	H-disks
Channels	387,072	258,048	147,456
Modules	432	144	96 pairs
Si area	$1.3m^2$	$0.4m^2$	$1.3m^2$
Inner radius	$2.7cm$	$2.6cm$	$9.5cm$
Outer radius	$9.4cm$	$10.5cm$	$26cm$

Table 3.1: SMT numbers (module means ladder or wedge).

Location	Module type	Stereo angle (°)	Pitch (μm)	# of modules	#chips /mod	# of HDIs
Barrel layers:						
L1,L3 (outer)	SS	0	50	72	3	72
L1,L3 (inner)	DSDM	0/90	50/150	144	3/3=6	144
L2,L4	DS	0/±2	50/60	216	5/4=9	216
Disk wedges:						
F	DS	±15	50/60	144	8/6	288
H	SS	±7.5	50/50	96	6/6	192

Table 3.2: SMT detector types (module means ladder or wedge).

disks is located at each end of the central barrel section, at $|z| = 43.113$ cm, 48.113 cm and 53.113 cm, as shown in Figure 3.5. The disks greatly increase the coverage at high $|\eta|$.

Tables 3.1 and 3.2 summarize some SMT design numbers.

Readout

The silicon detectors are read out using the SVXIIe chip [61], which is fabricated in the UTMC radiation hard 1.2 μm CMOS technology. Each chip

consists of 128 channels, each including a preamplifier, a 32 cell deep analog pipeline and an 8 bit ADC. It features 53 MHz read out speed, sparsification, downloadable ADC ramp, pedestal and bandwidth setting.

Input charge is integrated on the preamplifier for a train (typically 36) of beam crossings and is reset during inter-bunch gaps. This charge is delivered to a 32-cell analog pipeline. Upon a Level 1 accept sampling is performed on the appropriate cells and this analog information is fed to a parallel set Wilkenson ADCs. Digitization utilizes both edges of a 53 MHz clock. It provides 8 bits of analog information in 2.4 μs. Readout is half as fast. Typical noise performance is 490e + 50e/pF.

In order to achieve a geometry with 2 mm gaps between the barrels and the disks, the electronics and cabling have to be mounted inboard of the detectors. Therefore, the SVXIIe chips and associated circuitry are mounted on a double-sided, 0.2 mm pitch, kapton based flex circuit, the so called High Density Interconnect (HDI). The HDI is laminated onto a 300 μm thick Berilium substrate (heat spreaders) and glued to the silicon sensor. In case of double-sided silicon, the HDI is wrapped around one silicon edge to serve both ladder surfaces. The flexible long tail of the HDI allows the routing of the cable to the outer side of the barrel region. It is through the HDI tail that the control and readout of the SVXIIe chip take place. In addition, the analog and digital chip voltages, as well as high voltage for silicon bias are provided. As an example a double sided 2° ladder with 9 readout chips is shown in Figure 3.6.

Figure 3.7 shows a sketch of how the read out of the SMT is set up. The HDIs are connected through 2.5 m long Kapton flex cables to Adaptor Cards

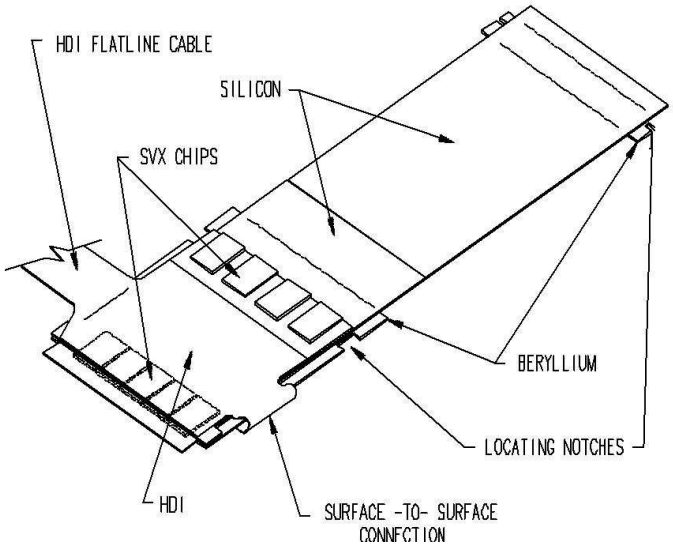

Figure 3.6: A double sided 2° ladder with 9 readout chips.

(ACs) located on the face of the Central Calorimeter. The ACs transfer the signals and power supplies of HDIs to 10 m long high mass cables which connect to Interface Boards (IBs). The IBs supply and monitor power to the SVXIIe chips, distribute bias voltage to the sensors and refresh data and control signals traveling between the HDIs and the Sequencers. The Sequencers control the operation of the chips and convert their data into optical signals carried over 1 Gb/s optical links to VME Readout Buffer (VRB) boards. Data is read out from the chips, transfered in the VRBs through the Sequencers whenever a Level 1 accept is issued and held pending a Level 2 trigger decision.

The trigger information is received via the SCL (Serial Command Link) by the sequencer crate controller. The SVX sequencer provides timing and control signals for eight chains of SVX chips. These signals are regenerated

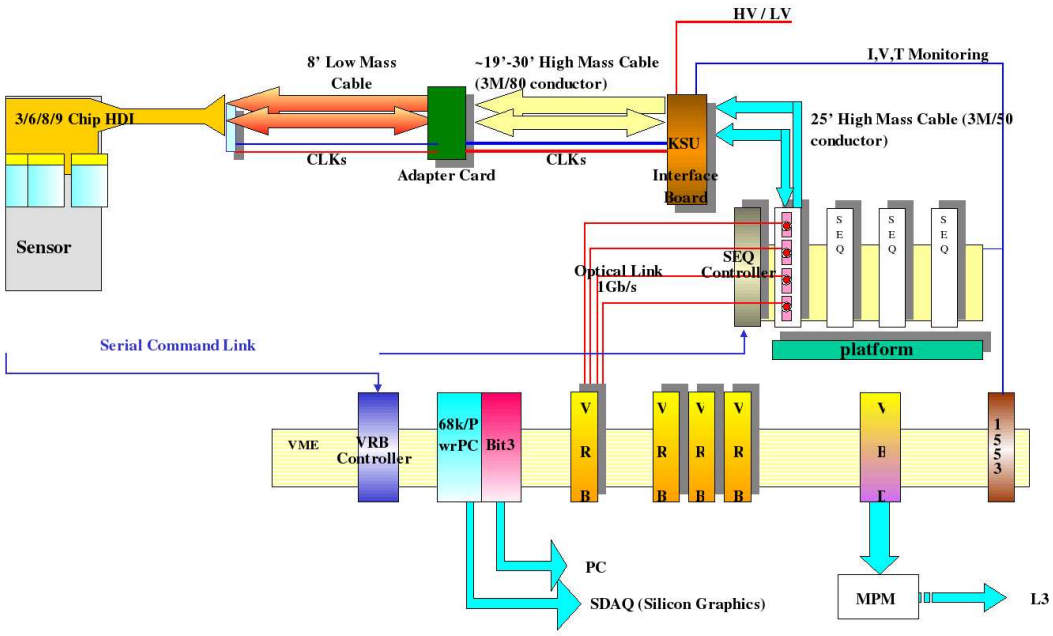

Figure 3.7: SMT read out chain.

by interface cards located on the side of the central calorimeter cryostat. The interface cards also control power and bias for the SVX chips, provide interfaces to the monitoring systems, and individual HDI circuit temperature and current trips.

Data from the HDI strings are sent from the sequencers to VRB (VME Readout Buffer) buffer memories located in the moving counting house via optical fibers. The VBE/MPM readout to Level 3 was replaced by single board computers in all DØ crates. A second single board computer is resident in the readout crate to collect and process detailed diagnostic information. Downloads and slow control is provided by a MIL-1553 control system.

A large scale "10% Test" was organized to test major detector components with the production versions of final readout components. This test

was crucial for debugging readout hardware, testing termination schemes, and adjusting sequencer timings. Bugs were found in the SVX chip that caused pedestal jumps and readout errors. Additional initialization states were added to the SVX control sequence to solve these problems.

The test started as a small scale test but gradually grew in complexity and scale. At the end of the test we were able to reach our goal to successfully read out one tenth of the silicon detector ($\sim$ 80k readout channels) in the final readout configuration. Hence the name "10% Test". The aim of the test was twofold: (a) to test the readout chain from the SVXIIe chips to Level3 trigger system and (b) to certify as many produced assemblies (barrels and disks) as possible before they were installed at DØ . The work was rather challenging due to both the complexity of the readout system and the scope of the whole project: commissioning of the readout system with bit error rates down to the 10^{-14} level, certification of different assemblies built (barrel and disks), ensuring the existence of adequate control and monitoring tools, etc. During this period, many problems were uncovered and solved in every single readout component, including the SVXIIe chips. During this period, we got an opportunity to read-out two different barrels ($\sim$ 55.3 and 69.1k channels), one F-disk ($\sim$ 21.5k channels) and one H-disk ($\sim$ 36.9k channels) and finally a barrel+disk combination ($\sim$ 90.6k channels). The readout system was fully exercised, achieving the desired level of performance in terms of data integrity, noise and, in general, robustness. During that period we also performed a cosmic ray test, observing for the first time tracks in one of the barrels, which allowed us to exercise the offline reconstruction chain. A first-pass alignment with the cosmic ray tracks was performed.

From the measured residuals it was deduced that all ladders were installed within their alignment tolerances and that the overall alignment of the barrel was within the specifications. All this served as a solid ground for a successful commissioning of the SMT later on in the assembly hall at DØ .

Clock, power, and signal quality and timing are critical to proper operation of the SVXIIe chip. The DØ SMT is read out using low mass kapton flex cables within the detector volume followed by high quality 50 and 80 conductor "pleated foil" cables on the outside. Both types of cables carry both power and digital signals. Cable runs range from $15 - 20$ meters. A pair of coaxial cables carries the differential clock. The small intermodule gap ($\sim$ 1 mm) is made possible by routing the HDI readout "tail" cables between ladders in the barrel. These are trimmed to length and coupled to a "card edge" style Hirosi connector on the low mass cables. Low mass cables are routed along the half-cylinder and coupled to the 80 conductor pleated foil cables at a ring of adaptor cards located between the calorimeter cryostat (on a so-called "horse shoe").

Performance Considerations

The details of the design of the silicon tracking detector were mainly driven by requirements with regard to the momentum and vertex resolution, the precision on the $r - z$ measurement and pattern recognition. The first two motivations are discussed below in more detail since they are important for this analysis.

Momentum Resolution

The momentum resolution of the tracker is determined by the strength of

the magnetic field, its maximum radius, the accuracy of the measurement of the helix, and the amount of multiple scattering. An overall figure of merit can be defined as the inverse measurement error ($1/\sigma$) times the field integral ($B \cdot L$) in the $r - \varphi$ dimension times the lever arm (L), i.e. BL^2/σ. The silicon provides an accurate measurement of the track angle at small radius, but the measurement of the sagitta and outer points in the central rapidity region are performed in the fiber tracker. The silicon serves to anchor the track at the inner radius. The number and detailed location of the silicon layers does not have a major effect on the momentum resolution.

A plot of the momentum resolution as a function of η for a 1 GeV/c p_{T} track originating at $z = 0$ is shown in Figure 3.8. The solid line shows the resolution for the tracker excluding the H-disks. As $|\eta|$ increases beyond 1.8, tracks begin to miss the last fiber tracker layer and the effective value of BL^2 decreases, rapidly destroying the momentum resolution. Momentum resolution can only be maintained if the detector resolution also improves as $1/L^2$ as $L \to 0$. We have attempted to preserve momentum resolution in the forward direction by adding the large area H-disks, with 10 micron resolution, which cover radii less than 26 cm. These disks do not need to have low mass and can be made at a lower cost compared to the more delicate ladders and F-disks. In the region covered by the H-disks the resolution is comparable to the fiber tracker for radii $r > \sqrt{(0.5\mathrm{m})^2 \times \frac{10\,\mu\mathrm{m}}{120\,\mu\mathrm{m}}} = 14\,\mathrm{cm}$. The effect of the silicon vertex detector on the resolution including the H-disks is shown in the dashed line in Figure 3.8.

Vertex Resolution

Vertex resolution considerations can be understood by considering a simple

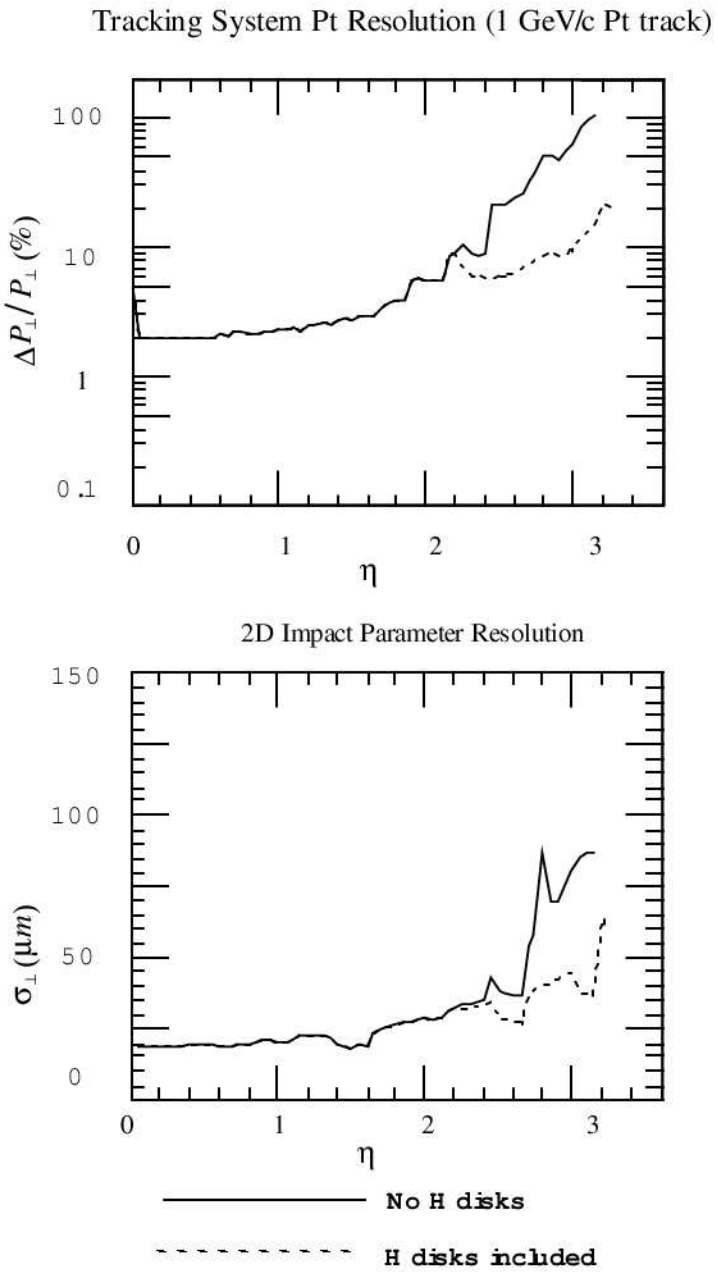

Figure 3.8: Momentum resolution and impact parameter resolution versus pseudo-rapidity.

two layer silicon system with identical resolution at the inner and outer radii, r_1 and r_2. The impact parameter resolution is given by

$$\sigma = \sigma_{meas} \left\{ \frac{\sqrt{1 + (r_1/r_2)^2}}{1 - (r_1/r_2)} \right\}.$$

A similar formula holds for disks where r_1 and r_2 are the radii of the first and last hits on a track passing through several disks. We see that the impact parameter resolution is dependent on the ratio of inner to outer radii of the detector. The cost depends strongly on the outer radius.

Given the above considerations we have decided on a compact system with the inner ladders as close to the beam pipe as is mechanically comfortable and with an outer radius which is consistent with deploying four layers of detectors. The size of the beam is less than 50 μm.

Vertex resolution is also affected by the detector resolution, σ_{meas}. This is primarily a function of the detector strip pitch, which is constrained by existing interconnect and amplifier technology. Our strip readout pitch is chosen to be 50 μm.

Naively the resolution is the pitch/$\sqrt{12}$. In a system where pulse height information is available the resolution is improved by the sharing of charge among two or more readout strips. These charge sharing effects can reduce the resolution from 14 μm (i.e. 50 μm/$\sqrt{12}$) to 5–10 μm, depending on the amount of sharing. The effective strip pitch can also be reduced by intermediate strips at smaller pitch (25 μm) which couple capacitively to the instrumented strips.

Disks are used to provide full three dimensional vertex reconstruction. The disk design, with $\pm 15^\circ$ stereo double-sided detectors, was chosen after careful analysis of the trade off between resolution and mechanical complex-

ity.

3.1.2 Central Fiber Tracker

The Central Fiber Tracker (CFT) consists of scintillating fibers mounted on eight concentric cylinders. The fibers are constructed in ribbons each 128 fibers wide composed of two singlet layers. These singlet layers are formed into the 'doublet' layers which form the ribbon by placing the fiber of one of the singlet layers in the space between the fibers of the other singlet layer. Eight axial layers are aligned along the beam axis. Another eight stereo layers are divided into two groups of four layers: U and V stereo fibers make a 3° angle with the beam axis.

The light from the fibers is converted into electrical pulses by visible light photon counters (VLPCs). These small silicon devices which have an array of eight photo sensitive areas, each 1 mm in diameter on their surface. They operate at temperatures from 6 to 15 Kelvin, which enables them to achieve a quantum efficiency (Q.E.) value well over 80% and a gain from $20,000$ to $50,000$ photo electrons.

The detector is divided into 80 sectors in φ. Each pie shaped slice have 896 fibers and the entire detector has $71,680$ channels. The axial fibers, which are half of all fibers, are used to form a fast Level 1 hardware trigger. All CFT fibers are read out on a Level 1 trigger accept and are used for the Level 2 trigger.

Figure 3.9 shows the design of the Central Fiber Tracker.

The baseline design of the CFT calls for scintillating fibers completely covering eight concentric support cylinders occupying the radial space of

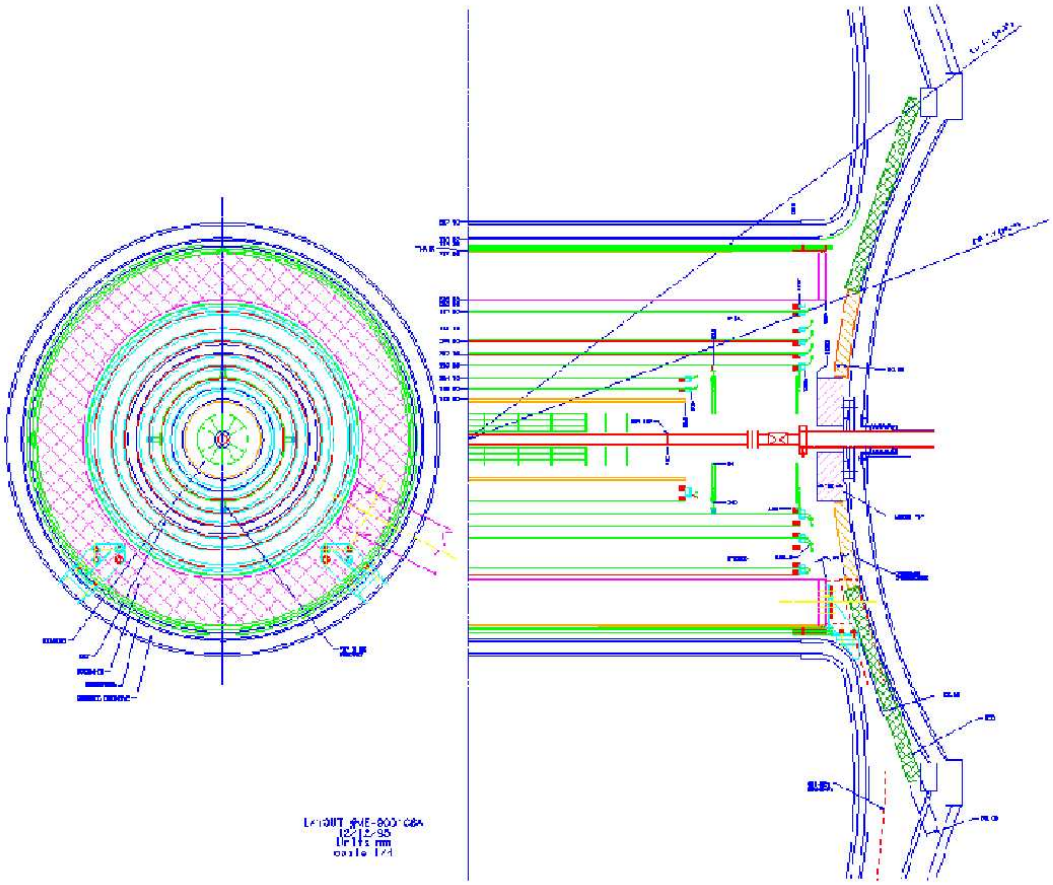

Figure 3.9: Design of the Central Fiber Tracker.

20 to 50 cm. A fiber doublet layer oriented with the fibers in the axial direction is mounted on each of the eight support cylinders. An additional doublet layer oriented in either the u or v stereo angle of approximately 3° is mounted on successive cylinders. The orientation is then: xu-xv-xu-xv-xu-xv-xu-xv. The diamater of scintillating fibers is 835 microns, 775 microns is the active volume diameter. The length of fibers ranges from 166 to 252 cm. Each scintillating fiber is mated, through an optical connector, to a clear fiber waveguide which pipes the scintillation light to a VLPC. The clear fiber waveguides vary in length between approximately 8 to 12 meters.

The details of the central fiber tracker design are given in Table 3.3.

The small fiber diameter, only 835 microns, gives the fiber tracker an inherent doublet layer resolution on the order of 100 microns, which combined with the silicon tracker in the axial view gives the DØ good momentum resolution for charged particles. In order to preserve this resolution capability, the location of all individual fibers must be known to an accuracy better than 50 microns in the (r, φ) plane.

The most important factor for the high-p_{T} tracking is the momentum resolution. It is dominated by multiple scattering of charged particles. To minimize this effect, the material budget of the CFT is kept at its minimum. On the other hand, it is necessary to preserve the rigidity of the system and roundness of the cylinders, to position precisely scintillating fibers.

The small fiber diameter and a large channel count give the tracker sufficient granularity both to find tracks and to trigger in the complex DØ Run II environment. A high doublet layer cluster/hit efficiency is essential to the CFT performance. The mean number of detected photoelectrons per fiber

Layer	Radius (cm)	no. of fibers per sector	no. of fibers per layer	no. of fiber ribbons	fiber pitch (μm)	active length (m)
A	19.99	16	1,280	10.0	979.3	1.66
AU	20.15	16	1,280	10.0	987.2	1.66
B	24.90	20	1,600	12.5	975.8	1.66
BV	25.60	20	1,600	12.5	982.1	1.66
C	29.80	24	1,920	15.0	973.4	2.52
CU	29.97	24	1,920	15.0	978.6	2.52
D	34.71	28	2,240	17.5	971.7	2.52
DV	34.87	28	2,240	17.5	976.2	2.52
E	39.62	32	2,560	20.0	970.4	2.52
EU	39.78	32	2,560	20.0	974.4	2.52
F	44.53	36	2,880	22.5	969.5	2.52
FV	44.69	36	2,880	22.5	972.9	2.52
G	49.43	40	3,200	25.0	968.7	2.52
GU	49.59	40	3,200	25.0	971.8	2.52
H	51.43	44	3,520	27.5	916.1	2.52
HV	51.59	44	3,200	27.5	919.0	2.52

Table 3.3: Design parameters of the Central Fiber Tracker.

must exceed 2.5 for a minimum ionizing particle. Indeed, this number is a product of of the intrinsic photo yield of the scintillator, the light transmission properties of the fiber and all connectors, and the Q.E. of the VLPC.

Only the fibers themselves are susceptible to any radiation damage. It was indicated in earlier studies that no more than 30% reduction in light yield is expected for the innermost fiber cylinder. Other layers are going to be damaged correspondingly less.

Due to the fiber tracker's fast response time, the total time of the collection of signals from the central fiber tracker from one interaction is considerably shorter than the 396 ns bunch spacing in Run II. This enables the fiber tracker to participate in the DØ Level 1 trigger without contributing any dead time. The trigger is implemented using field programmable gate arrays, FPGA's. First, the signals from singlet axial laers are combined into hits. Coincidence between eight hits form tracks. The tracks are combined with central preshower clusters to form an electron trigger, and with muon detectors to form a muon trigger. However, in order to perform this operation in the 4 μs time allowed for Level 1 processing, the tracker has to be divided into 80 equal azimuthal sectors for parallel processing.

CFT overlap

As it can be observed in Table 3.3, the first two cylinders are shorter than the remaining six cylinders by about 86 cm, to allow for the CFT support structure. Additionally, the region above $|\eta| > 1.63$ is called CFT overlap. Tracks that originate in the geometrical center of the DØ detector, will cross fewer CFT layers with $|\eta|$ increasing, and as a result, the track fit is going

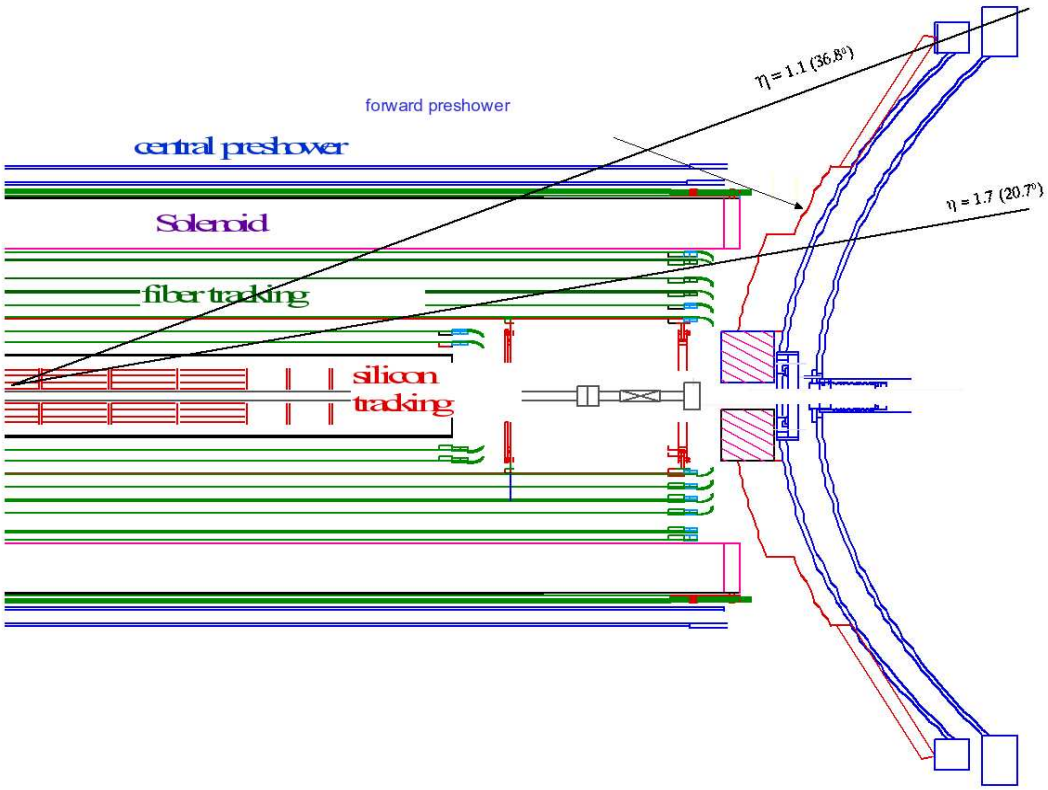

Figure 3.10: Overlap region of the Central Fiber Tracker, $|\eta| > 1.63$.

to be worse and worse. The momentum resolution degrades in this region significantly, this can be observed in Figures 3.8 and 3.12. This is particularly important for high-p_{T} tracks and especially for the curvature q/p_{T} measurement.

Figure 3.10 shows the overlap region of the Central Fiber Tracker. Tracks crossing the CFT overlap region contribute more frequently to the like-sign muon background through charge mis-identification of one of the muon tracks than tracks measured in the central region of the tracker, i.e. $|\eta| < 1.6$.

Readout electronics

The CFT readout electronics are contained on three sets of printed circuit boards which are located at three different places: (a) VRB boards, (b) Port Card Board and (c) Stereo/Trigger Boards. The front end boards digitize the signals and form the trigger tracks. These boards are mounted directly on the VLPC cassettes and come in two varieties, stereo and trigger boards. The Port Card Boards read out the digitized values from the SVX chains and transmit them via fast optical link to the third set of boards, the VME Readout Buffers (VRB). The Port Card Boards are located in the center platform of the detector in the collision hall and the VRBs are located in the moving counting house. Both the Port Card Boards and VRBs are identical to boards used by the silicon tracker electronics. The front end boards receive the analog electrical signals from the VLPC cassettes split them and store one part of the signal in a 32 deep pipeline buffer. On receipt of a Level 1 accept one of the stored events is digitized using the SVXIIe chip and transferred over a fast serial link to the moving counting house where it is available to the DAQ system. On the trigger boards the other part of the analog signal is discriminated using the SIFT-IIb chip and the discriminated outputs are used to form a pre Level 1 axial track list. This list is transmitted to other detector parts for use in Level 1 triggers and is also pipelined for transmission to the Level 2/3 on a Level 1 accept.

The VLPC cassette contains $1,024$ channels of VLPC readout and is divided into 8 modules of 128 channels each which are interchangeable and repairable. Figure 3.11 shows the full cassette with readout boards attached. Since the VLPCs operate at cryogenic temperatures, a liquid Helium cryosys-

tem is required. The VLPCs share the Helium refrigerator with the solenoid magnet and the VLPC cassette cryostats operate off a separate control dewar. Two cryostats, each accomodating up to 51 VLPC cassettes, house the entire VLPC system. Two cryogens are used in the system. Liquid Helium from the control dewar allows for VLPC operation at about 6 K and liquid Nitrogen cools an intermediate heat intercept in the VLPC cassette in order to reduce the heat load to the liquid Helium. The cassette cold end sits in a stagnant gaseous Helium volume. Conduction through the gas cools the VLPCs.

Each VLPC cassette holds two front end boards which are slightly different versions of the same board. The board mounted on the right side of the cassette when viewed from the front is called the Right Hand Board (RHB) and the one on the left the Left Hand Board (LHB). Each front end board supports 512 channels of signal from the cassette. The RHB interfaces to the cryogenic power and control systems for each cassette. Each front end board interfaces to the bias voltage supply and return for the VLPCs.

The CFT is divided into eighty equal wedges in azimuth known as sectors. The channels from each sector are input into two front end boards. The channels from the stereo fibers are input into the stereo boards. The channels from the axial fibers are input into the trigger boards which also contain the logic which forms the Level 1 axial trigger tracks. While each board supports 512 input channels the CFT does not use them all, the Central Preshower detector (CPS) uses the rest.

In the analog signal line from VLPC, after the coupling capacitor, is placed the SIFT chips. It was developed for a fast logical output needed

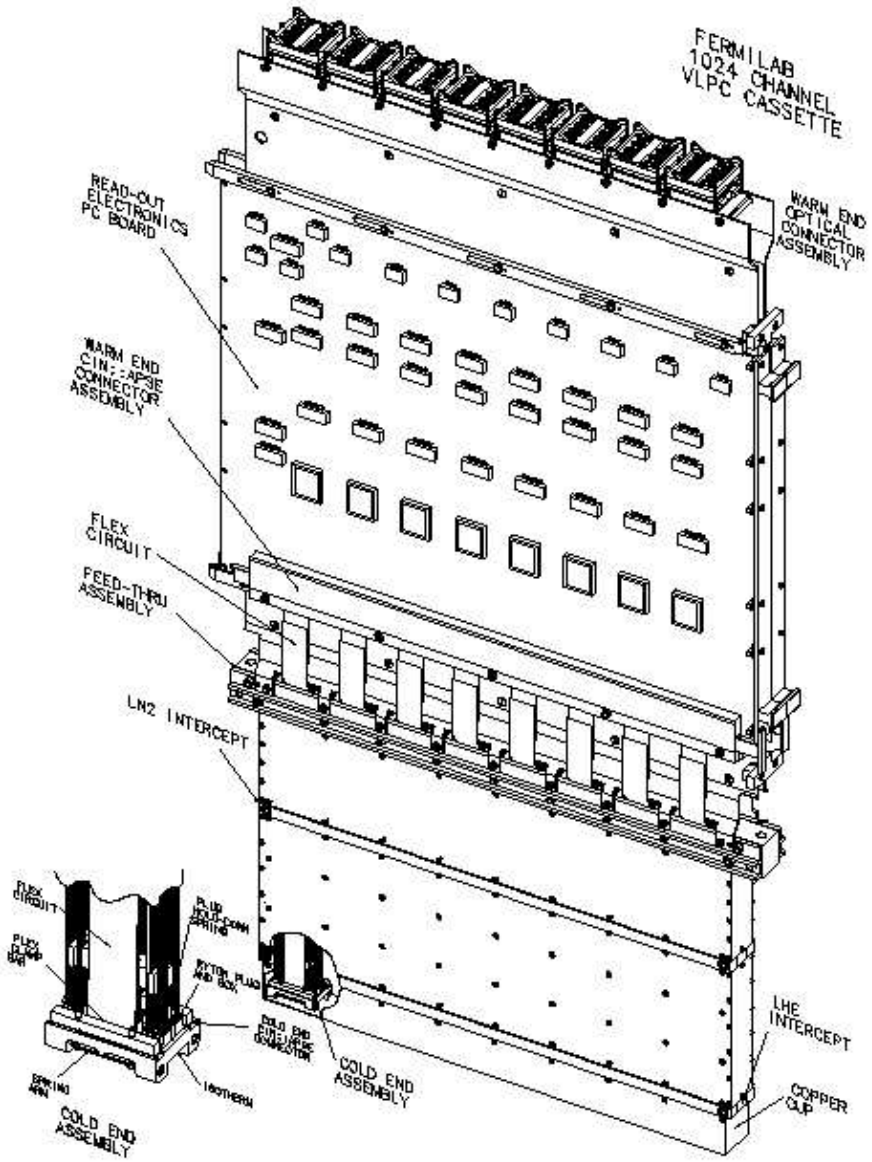

Figure 3.11: The VLPC cassette with readout electronics board attached.

for Level 1 trigger. Each SIFT chip has 16 input channels and a common threshold. The chip first amplifies the signal and then buffers it. It outputs a 3.3 V single ended output for those channels above threshold. The SIFT chip outputs an analog signal to the SVXIIe for digitization. The SVXIIe chip functionality is described in [61]. It was designed for the silicon tracker readout but is well suited to the fiber tracker readout as well. The signal amplitude and shape as well as the effective detector capacitance out of the VLPC or SIFT within range of the SVXIIe chip. Detailed information on the silicon tracker read out system can be found in several places [62, 100] and does not have to be repeated here.

Momentum resolution

The expected transverse momentum resolution for the DØ tracking system is shown in Figure 3.12.

The calculation was performed with the following parameters: (a) the resolution of the scintillating fiber doublet is 100 microns, (b) the resolution of the silicon barrels is 10 microns, (c) the thickness of the barrels supporting the scintillating fibers is 0.086 g/cm^2 for barrels 3 and 4 and 0.065 g/cm^2 for all other barrels, (d) the radial distribution of the non-active material in the silicon detectors is taken into account, (e) and the interaction vertex is known with a precision of 35 microns.

The transverse momentum resolution at pseudorapidity $\eta = 0$ is parametrized as

$$\frac{\sigma_{p_{\mathrm{T}}}}{p_{\mathrm{T}}} = \sqrt{0.015^2 + (0.0014 \cdot p_{\mathrm{T}})^2}. \tag{3.3}$$

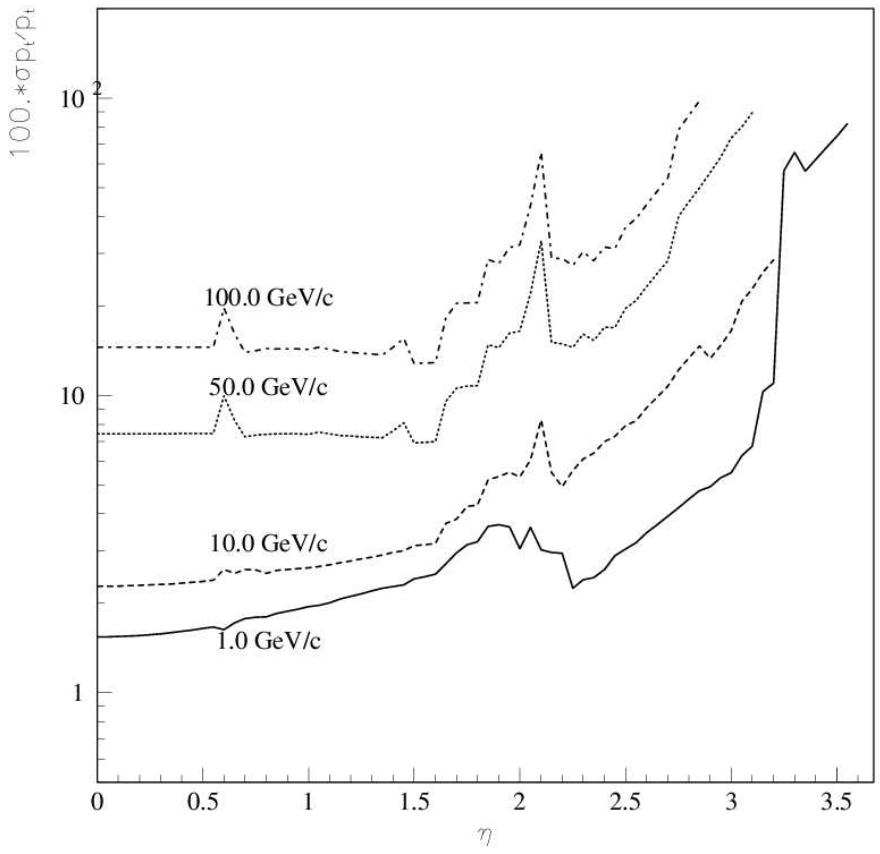

Figure 3.12: Momentum resolution as a function of pseudo-rapidity, assuming 35 micron primary vertex resolution.

3.1.3 Preshower Detectors

Central and forward preshower detectors located just outside of the superconducting coil (in front of the calorimetry) are constructed of several layers of extruded triangular scintillator strips that are read out using wavelength-shifting fibers and VLPCs.

3.2 Calorimetry

Calorimeters are used to determine the energies of particles, both charged as well as neutral, by total absorption in the calorimeter medium. In fact, the calorimeter is a block of matter which intercepts the primary particles and due to its size causes them to interact and deposit all their energy inside the calorimeter volume. The deposited energy is transformed into the subsequent cascade of secondary particles, a so called *shower*. Such a cascade of secondary particles is a flow of low-energy particles. Most of the incident energy is unfortunately dissipated and appears in the form of heat. A rather small fraction of the deposited energy is detectable in the form of a signal.

Calorimeters offer many attractive capabilities:

- they are sensitive to charged and neutral particles
- the energy degradation through the shower development is a statistical process. The average number of secondary particles $\langle N \rangle$ is therefore proportional to the energy of an incident particle. This significant property causes that the uncertainty in the energy measurement is governed by statistical fluctuations of N and hence the energy resolution σ/E improves as $1/\sqrt{N} \sim 1/\sqrt{E}$.

- the required length of the calorimeter for total absorption increases logarithmically with particle energy E.
- thanks to the detector segmentation, the shower development allows a precise measurement
- different response to electron and hadrons can be used for particle identification
- their fast response allows them to operate with fast trigger techniques and rapid online event selection.

Calorimeters can be logically split into two groups in view of their different purposes

- electromagnetic calorimeters:

  They are designed to measure the energy of photons and electrons. Photons interact predominantly via pair production in the vicinity of a nucleus. Electrons loose their energy mainly through Bremsstrahlung which is an interaction with a Coulomb field of an atom. Photons of high energies are produced in Bremsstrahlung. Indeed, daughter particles, again photons, electrons and positrons, might undergo interactions themselves. An electromagnetic shower is started that way. It developes until the energy of particles lowers to the level of critical energy (energy at which the showering process stops).

- hadronic calorimeters:

  Their purpose is to measure energy of the hadronic shower, to identify

jets, estimated missing transverse energy $E_{\mathrm{T}}^{\mathrm{miss}}$ and perform measurement of low-energy muons.

The jets are the natural objects at hadron-collider experiments because of the high c.m.s. energy. The individual particles can be hardly seen in the calorimeter. Only the energy flows might be measured in some angular *tower* of the calorimeter. Quantum Chromodynamics can reliably calculate only the energy flow of partons in a definite angular cone. This is not the disadvantage however. Quarks and gluons coming from the reaction convert into observable hadrons after the collision. This process is called hadronization and it is not possible to describe it in detail theoretically. There are several models which are invented to describe these collisions. Their fundamental assumption is that the energy flow calculated on the level of partons is almost equal to the energy flow of measured hadrons. This significant property gives *jets* physical sense. Jets are angularly collimated streams of hadrons which are interpreted as "traces" of original quarks or gluons. The jet energy is estimated by measuring the energy deposited in a cone of opening angle ΔR around the jet axis (average direction):

$$\Delta R = \sqrt{\Delta^2\eta + \Delta^2\phi} \tag{3.4}$$

This equation makes the backbone of the "jet finding algorithm". There are also several intrinsic limitations for jet calorimetry (especially for $E_{\mathrm{T}}^{\mathrm{miss}}$ and jet energy measurement), such as fragmentation effects (they depend on the nature of jets), magnetic field sweeping of charged particles (the opening of the cone and low momentum fragments), gluon

radiation and energy losses to non-interacting particles, such as neutrinos or even muons (they are minimum-ionizing particles).

Due to the high luminosity, a special attention must be paid to the pile-up energy from minimum-bias events which also becomes important. Minimum-bias events are soft-scattering events which are superimposed during the same crossing and which are dependent on the luminosity. There are on average 0.7 minimum bias events at current luminosity ($10^{32} cm^{-2} s^{-1}$).

The development of hadronic showers in matter is very complicated, this is why an analytical treatment is unfortunately not available.

Hadron production is sensitive to the energy carried by the incident particle and to the type of a projectile. In average the multiplicity increases very slowly with the mass number of the target material. About half of the energy is carried by leading particles. One third of the pions, that are produced by the collision in the calorimeter medium, are the neutral pions. Their energy is dissipated in the form of electromagnetic showers because of their electromagnetic decay into two gammas. They will therefore propagate without further nuclear interactions. The average fraction is [71]

$$\langle f_{\pi_0} \rangle \; = \; 0.11 \cdot \ln E[GeV/c^2] \tag{3.5}$$

in the energy range of several hundred GeV/c^2. The size of the π^0 component is determined by the production in the first interaction.

A fraction of the total energy is dissipated in ionizations by electrons

and charged hadrons. This energy fluctuates from event to event. Therefore this is the most important and the largest contribution to the energy resolution. Another problem is that the largest fraction of energy is not seen. The energy which is going either in breaking nuclei (binding energy) or in low energy neutrons is invisible.

Many of the low energy particles (gammas, protons of few MeV) which are produced in deexcitations of nuclei are badly sampled because of saturation effects in the active matter. A large fraction of the nuclear excitation goes into fast protons and neutrons. Finally, muons and neutrinos emitted in the decay of pions escape from the calorimeter. These muons and neutrinos are direct products of the charged pion decay. As it has pointed out earlier, neutrinos will remain undetected. They will not leave any trace in the detector. Muons however, are minimum ionizing particles, which means that muons are particles that find themselves in the minimum of the ionization loss curve $\frac{1}{\rho}\frac{dE}{dx}$, and hence their energy losses are about 2 MeV/g$\cdot$cm^{-2} and they are nearly independent of muon transverse momentum. This is why an average muon energy loss in the DØ calorimeter can be approximated by about 2.3 GeV/c^2.

There are two important interaction phases during the hadronic shower development [71]:

- *High-energy cascade phase:*

  Secondary particles are produced due to high energy of incident hadrons which are taking part in the interactions with the nucleus of the active material. Most of the secondary particles are natu-

rally pions. Protons, neutrons, heavy fragments and other heavy particles can be also produced if the incident energy is big enough to fulfill the kinematical conditions allowing their production. The secondary particles have rather high energies after their creation and hence they can later interact too.

– *Nuclear deexcitation phase:*

The excited nucleus decreases its energy by emission of slow neutrons and by γ-transitions. The energy spent breaking up nuclei will not be visible. This is quantified by the e/π ratio, i.e. ratio of the calorimeter responses to electrons and pions. Uranium is used to correct this ratio, its nuclei can be easily broken up by slow neutrons, which will in result, produce particles that can be detected and this additional energy will compensate for energy losses due to slow neutrons and γ-transitions.

The nuclear deexcitation and pion, muon decays will affect the shower composition, which has a very different response. The hadronic shower has a characteristic longitudinal and transverse profile. The longitudinal distribution is scaled in units of absorption length λ_{abs}, which has the meaning of the mean distance between two inelastic collisions of hadrons with nuclei [72, 73]. The transverse distribution depends on the longitudinal depth. The core of a shower is rather narrow, it is increasing with the shower depth. The collimated core, which consists of high-energy particles, is surrounded by lower-energy particles. The main part of them extends away from the shower axis, the 95 % containtment is required in a cylinder of radius $R \sim 1\ \lambda_{\text{abs}}$ [74].

There are many approaches in calorimeter construction. In principal, two are the most distinct ones: homogeneous calorimeters where the absorber is also an active material (lead glass, NaI or BGO), or the sampling calorimeters. This approach interleaves layers of a dense, inert absorber with layers of a material which is sensitive to particles passing through it, such as liquid Argon, scintillators, etc. Most of the energy is deposited in the passive material and only a small fraction of the incident energy is read out from the active medium.

3.2.1 Calorimeter geometry

The DØ calorimeter is a sampling calorimeter. The depleted uranium, with copper and stainless steel in the outer regions, is used as a primary absorber. The liquid argon (LAr) is used as the ionization medium. The electron recombination is very low for inert gases, this is why the signal to noise ratio is going to be rather high. The calorimeter is rather compact because of the high density of uranium.

The calorimeter is divided into a large number of modules. Each of them consists of a stack of interleaved absorber plates and signal boards. A schematic view of one calorimeter cell is shown in Figure 3.13. The absorber plates are separated from signal boards by liquid argon gap of 2.3 mm. The signal board consists of a copper pad sandwiched between two 0.5 mm thick pieces of G10. The outer surfaces of these boards are coated with a resistive epoxy coating. The absorber plates are grounded. The positive voltage of $2.0 - 2.5$ kV is applied to the resistive coatings. Charged particles from e.m. or hadronic shower cross the LAr gap and leave a trail of ionization. The

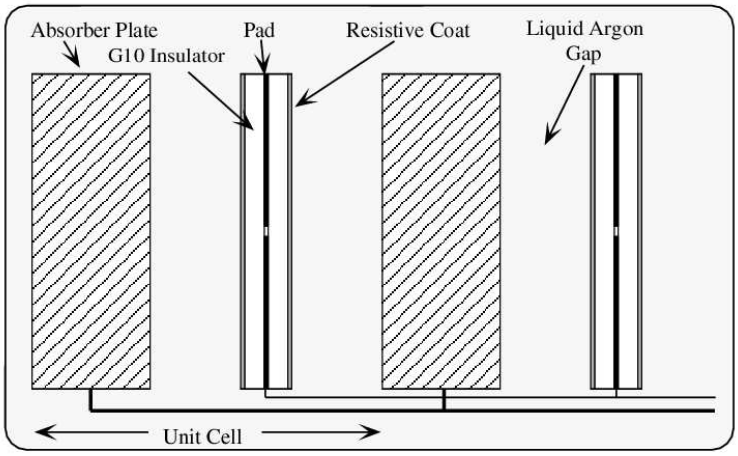

Figure 3.13: A schematic view of a calorimeter cell [58].

ionization electrons drift towards the signal board where they are collected. The drift time is approximately 450 ns. They induce a signal on the copper pad via capacitive coupling. The readout pads are subdivided into smaller cells so that the transverse position of showers can be measured. The corresponding cells in adjacent signal boards are ganged together in depth to form readout cells.

Figure 3.14 shows the DØ calorimeter design. The calorimeter is placed in the cryostat because of the liquid argon used as a sensitive medium. The calorimeter is divided into three major assemblies, each sits in its own cryostat. This way is secured access to the tracking system. There is a central calorimeter (CC) and two end-cap calorimeters (EC).

The central calorimeter provides coverage up to pseudorapidity of about 1.2. It is roughly toroidal, and it consists of three concentric layers of modules. The inner layer has 32 electro-magnetic (EM) modules. They are thick

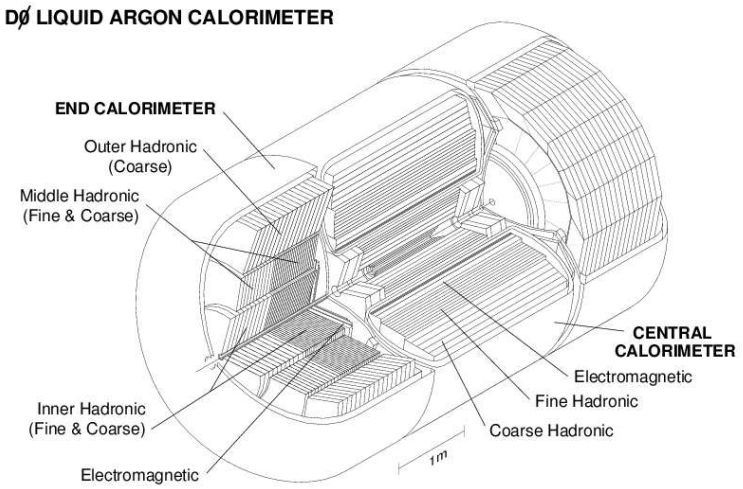

Figure 3.14: The DØ calorimeter [75].

enough to contain most e.m. showers. It is approximately 20.5 radiation length, where one radiation length is a distance on which energy of a particle degrades down to $1/e$ of the incident energy in a given medium. The middle layer consists of 16 fine hadronic (FH) modules, which measure showers due to hadronic particles (96 radiation lengths). The final layer consists of 16 coarse hadronic (CH) modules, which measure any leakage of energy out of the back of the calorimeter into the muon system, so called punch through [2]. The parameters of the CC modules are given in [58, 75].

The two end-caps provide additional coverage on each side of the CC from a pseudorapidity of about 1.3 out to about 4. End-caps are composed of three concentric layers of modules, they are divided into e.m., fine and coarse hadronic types. The center of the EC consists of a disk-shaped e.m. module, back to it, there are cylindrical fine and coarse inner hadronic mod-

[2]Punch through effect was estimated to be less than 1% [130].

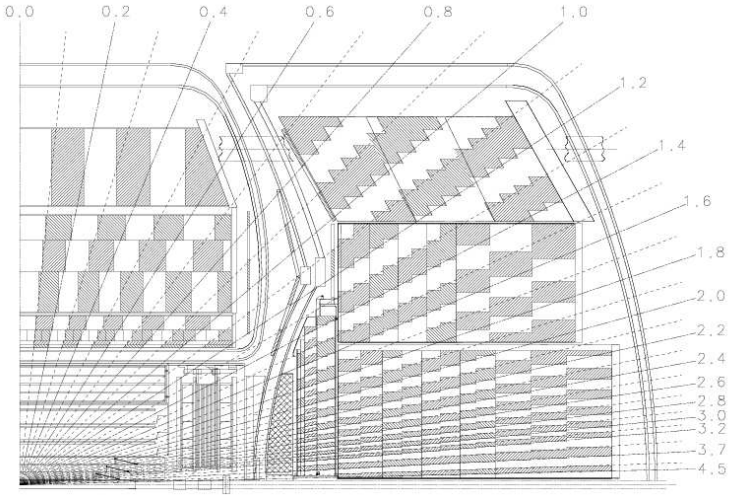

Figure 3.15: Side view of the calorimeters [75].

ules. The fine and coarse middle hadronic modules are arranged in a ring around the central core. Finally, the last ring is built out of coarse outer hadronic modules.

The area in (η, φ) plane is covered by readout cell of size 0.1×0.1. In the third layer of EM modules, where a shower deposits most of its energy, cells have areas of 0.05×0.05. In addition, cells with $|\eta| > 3.2$ have a φ size of 0.2 and are somewhat larger in η as well. The calorimeter segmentation is shown in Figure 3.15.

In a transition region between CC and EC ($0.8 < |\eta| < 1.4$), there is a relatively large amount of uninstrumented material. This space is left out because of cryostat walls and the support structures for the calorimeter modules. There are two devices used in this region: (a) massless gaps (MG) and (b) the intercryostat detector (ICD). The MG are rings of two signal boards mounted on the end plates of the CCFH, ECMH and ECOH modules.

The ICD is a ring of scintillation counters mounted on the exterior of the EC cryostats. Both devices have a segmentation of 0.1×0.1.

3.2.2 Calorimeter readout

The signals induced on the readout pads are pulses with widths of the order of 450 ns [75]. Signals are led out through four ports in the cryostats to charge sensitive preamplifiers mounted on top of the cryostats. The signal is then passed to the base line subtractor (BLS) boards located on the platform below the detector. The BLS modules perform analog shaping and split the signal into two paths. One is used for trigger purposes. Signals from all EM and fine hadronic cells within a 0.2×0.2 tower are summed. These signals form the input to the Level 1 calorimeter trigger.

The other path is used for the data readout. The incoming signal is sampled just before the beam crossing and again about 300 ns later. The difference between these two samples is a DC voltage which is proportional to the collected charge. The difference is then sent to the ADCs where, if the event is accepted by the Level 1 trigger, the signals are digitized and sent to the Level 2 trigger.

3.3 Muon system

The Run II DØ muon system [76] will enable DØ to trigger, identify and measure muons in the new high rate environment [77]. The luminosity in Run II has increased up to 2×10^{32} cm^{-2}s^{-1} and the beam spacing changes from 2.5 μs to 396 ns. This change indeed requires a corresponding upgrade

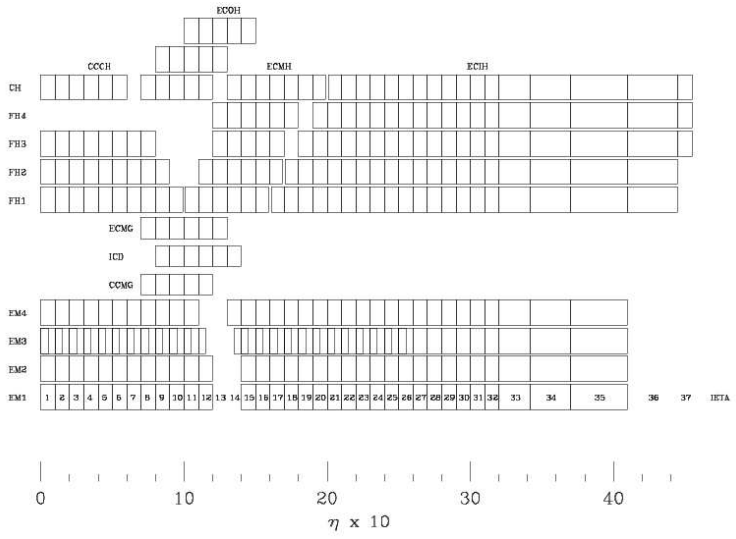

Figure 3.16: Layout of calorimeter channels in depth and η [59].

of the DØ detector [78, 79]. The central muon system has been supplemented with additional scintillator layers for triggering, cosmic ray rejection, and low momentum muon measurements. New shielding has been added to decrease background rates. The muon trigger has been redone to accommodate the high trigger rate and increased number of interactions per beam crossing. The upgraded central tracking system consisting of the Central Fiber Tracker and the Silicon Microstrip Tracker improves the momentum measurements of muons as well as other charged particles.

The DØ muon detector has three subsystems: (1) Proportional Drift Tubes (PDTs), (2) Mini-Drift Tubes (MDTs) and (3) trigger scintillation counters. The PDTs were used in the $1992 - 1996$ data taking run and provide tracking coverage for pseudorapidity $|\eta| \leq 1.0$. The forward muon tracking system, new for Run II, uses planes of mini-drift tubes and extends muon detection to $|\eta| = 2.0$. Scintillation counters are used for trigger-

ing and for cosmic muon and accelerator backgrounds rejection. Toroidal magnets and special shielding complete the muon system. All subsystems interact with three levels of triggers. Level 1 generates trigger information synchronously with the beam crossing, Level 2 operates asynchronously with a maximum decision time of 0.1 ms. All three muon detector subsystems use a common readout system based on a 16-bit fixed point digital signal processor, which buffers the data from the front-end, re-formats the data if accepted by Level 2 and sends it to the Level 3 trigger system, which is a farm of Linux workstations running software trigger filters. Muon triggers accepted by Level 3 are written to tape for offline reconstruction.

Geographically, the muon system can be divided between Central Muon Detectors and Forward Muon System.

3.3.1 Central Muon Detectors

The central muon tracking system, with pseudorapidity coverage $|\eta| \leq 1.0$, consists of 94 proportional drift tube chambers built for Run I [80]. The A layer is between the calorimeter cryostat and the 2 T muon toroid magnet. The A layer chambers on the top and sides have 4 decks to help in rejecting backgrounds, while those on the bottom only have 3 decks due to space constraints. The B and C layers outside the toroid have three decks each. Figure 3.17 shows the layout of the muons system. The chambers are rectangular aluminum tubes with 5.7 cm by 10 cm cells. The drift distance resolution is about 1 mm. The momentum resolution from the PDTs is about 30% for muons with $p_{\mathrm{T}} = 100$ GeV/c, where p_{T} is the momentum transverse to the beam direction. But when the muon track is matched with

tracks from the DØ central tracking system, the resolution is improved for all central muons. For muons with $p_{\mathrm{T}} = 100$ GeV/c, the resolution using central tracking is about 15%.

Layers of scintillator, called the Cosmic Gap, on the top and upper sides of the central muon detector were used in Run I to help reject cosmic rays. Coverage was completed for Run II when Cosmic Bottom counters were added. A new layer of scintillators, called the $A\varphi$ counters, was added between the A layer and the calorimeter [81]. These counters have φ segmentation of 4.5 degrees. The $A\varphi$ counters are used for muon triggering, rejection of out-of-time scattered particles and identifying low-p_{T} muons.

3.3.2 Forward Muon System

The Forward Angle Muon Detection System, which consists of mini-drift tubes (MDTs) and pixel scintillators, is entirely new for Run II. The Run I forward toroids are used, and new shielding has been added. The MDT system covers the region $1.0 \leq |\eta| \leq 2.0$ [82]. The mini-drift tubes have 8 cells of 1 $cm \times 1$ cm cross section, and are made of aluminum extruded combs and plastic sleeves. The A layer chambers are in front of the forward toroid magnet and the B and C layers are behind it. The layers are divided into octants. The length of each tube depends on its position in the octant. As in the central region, the MDT A-Layer has four decks of drift tubes and the B and C Layers have three decks each. The coordinate resolution is 0.7 mm/deck. The momentum resolution is 20% for low momentum tracks.

The Muon Forward Scintillator Pixel system covers the same η region [83]. The φ segmentation of 4.5 degrees matches the segmentation of the Central

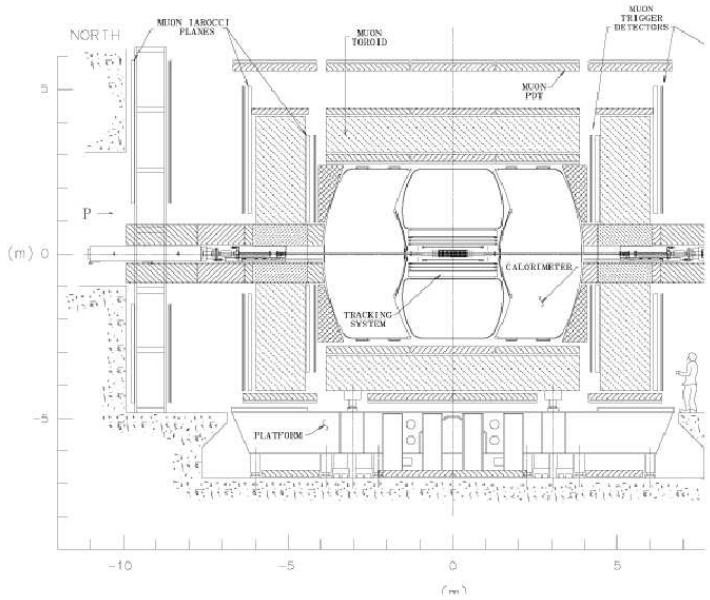

Figure 3.17: The Run II DØ Muon Detector [76].

Fiber Tracker. The η segmentation is 0.1. The typical size is 20 cm $\times$ 30 cm. The counters are made out of Bicron 404A scintillator. Kumarin WLS bars are used for light collection into PMTs. The scintillators are used for triggering and track reconstruction.

Large backgrounds in the forward direction in Run I were mainly due to the interaction of beam jets with the forward elements of the DØ detector and the accelerator hardware. Shielding was built in several large movable sections. These extend from the end cap calorimeters and contain the low-β quadrupole magnet inside a case of 20 inches of iron, 6 inches of polyethylene and two inches of lead.

3.3.3 Triggers and electronics upgrades

The DØ Run II Muon Trigger System consists of 3 levels [84]. Level 1 is a pipelined hardware stage. It processes information from individual subdetectors in Field Programmable Gate Arrays (FPGA) with a decision time of 4.2 μs. The decision is based on preliminary information from tracking, calorimetry, and muon systems. The trigger accept rate, which is an output from Level 1, and input to Level 2, is 10 kHz. Level 2 is a second hardware stage using Dec Alphas. It refines Level 1 information and adds more information if available with preprocessors for each subdetector. A global processor combines information from the subdetectors. Level 2 has a maximum decision time of 100 μs. The accept rate out of Level 2 is 1 kHz. Level 3 has two stages: a custom-built data acquisition system and a Linux farm of processors which makes the final trigger decisions. The farm does partial online event reconstruction and uses filters to accept or reject events. The decision time depends on the number of farm nodes, and is about 50 ms for the beginning of the run. The sustained trigger rate out of Level 3 is 20 Hz, with an output event size of 250 kB.

To be able to keep up with an increased input data rate, the front-end electronics of all the muon subsystems was upgraded. Digital signal processors (DSPs) are used to buffer and reformat the data [85]. The DSPs make muon stubs from hits and buffer the Level 1 accepted data from the front-end readout, while a Level 2 decision is pending. If the trigger is accepted by Level 2, the DSPs reformat the data and send it to the Level 3 trigger system.

The muon trigger has three levels, plus one extra trigger level between

Level 1 and Level 2 called SLICs (Second Level Input Computers) [86]. Level 1 triggers uses wire positions, scintillator hits in the A, B and C layers and central, north and south octants to define and/or trigger terms. The SLICs use 80 DSPs to find muon stubs in from nearby hits in a single layer. Level quality values are calculated for all muon candidates. Level 3 uses muon hits, makes muon segments and combines them into muon tracks which are matched with central tracks and calorimeter information. Events passing the trigger requirements are written to tape.

3.4 Luminosity counters and Forward Proton Detector

Luminosity is measured using plastic scintillator arrays located in front of the EC cryostats, covering $2.7 < |\eta| < 4.4$. A forward-proton detector, situated in the Tevatron tunnel on either side of the interaction region, consists of a total of 18 Roman pots used for measuring high-momentum charged-particle trajectories close to the incident beam directions.

Chapter 4

Data set selection

The events are read out from the DØ detector in form of a 'raw data' event. It is given as set of quantities such as digitized counts in a calorimeter cell, ADC counts for the silicon or central fiber tracker, and so on.

In order to obtain variables interesting from the physics point of view such as kinematical parameters of physics objects, the event has to be reconstructed. It means that all digitized counts have to be turned into description of objects as leptons and jets. This process is carried out by a set of computer programs (packages) called `d0reco`. The reconstruction program consists of following consecutive steps

- *Hit finding* - raw data is unpacked and converted into 'hits'.
- *Clustering and tracking* - hits that are close to each other are formed into objects called clusters. Tracking part of the code builds clusters into 'tracks', this part is called track finding and track fitting. In the calorimeter, clusters are grouped together into jets.
- *Vertexing* - vertexing code combines tracks and finds their common

crossing - a vertex. Primary vertices and secondary vertices are found.

- *Particle identification* - information from all parts of the detector is combined to produce collections (lists) of objects which are candidates for tracks, electrons, photons, jets or muons. At this level, criteria to build all these objects are very loose so that no potentially interesting objects are lost at this stage.

The pre-selection cuts are supposed to select a set of data that is particularly interesting for a given analysis. When performing an analysis, the researcher typically decides for much tighter selection criteria defining his/her data set. All the cuts, reconstruction, pre-selection, selection and analysis cuts, are described in detail in what follows.

4.1 Data set definition

The analysis is based on the data taken by the DØ experiment between August 2002 and June 2003 in the run range 162012 to 178310. The selection uses the single-muon data set skimmed by the WZ group [87]. This skim requires at least one loose muon with transverse momentum (p_{T}) greater than 8 GeV/c. The transverse momentum of the muon is measured using central tracking system, if the central track was found, or by the muon system in case no central track was matched to the track reconstructed in the muon system. This skim is intentionally very loose. Users are expected to apply further cuts which can be tailored to suit the particular analysis being carried out.

Every physics data taking run at DØ is graded based on its quality. This

is performed to guarantee the highest quality of data intended for various physics analyses. Data quality is evaluated on several levels, both online and offline. Each of the subdetector systems grades quality of the run online, just after the data taking is stopped. Part of the evaluation is carried out offline, e.g. jets and missing transverse energy evaluation.

All runs labeled as 'bad' for SMT, CFT, muon system or calorimeter (only runs with a calorimeter crate missing from the readout) are rejected with the decision based on the information from the Run Quality Database [88], where the run quality evaluation is stored.

Not all luminosity blocks that enter the calculation of the total integrated luminosity for a given trigger are good. In case of problems, bad luminosity blocks are labeled as 'bad'. All events corresponding to 'bad' luminosity blocks are later removed from the data sample. The list of bad luminosity blocks is obtained using a modified version of the lm_access package [89]. The list is created when the program calculates the total integrated luminosity for triggers of interest. The list of bad luminosity blocks serves as an input to the analysis, all events that belong to bad luminosity blocks are rejected while the analysis program is executed.

Only the dimuon trigger `2MU_A_L2M0` is used in this analysis. This trigger is defined as follows [90]

- *Level 1* - this trigger is based on Level 1 $mu2ptxatxx\_ncu1$ trigger. It means that
  - this trigger is defined in a all muon region, see Section 3.3.
  - it is based on scintillator hits only, i.e. no tracking is involved at this level.

– calorimeter readout is not unsuppressed.

- *Level 2* - Events with at least one muon, that means medium quality (=2) [91], must be found. There is no p_{T} or region requirement except that the muons must get through the iron (transverse momentum must be more than 3 GeV/c)

- *Level 3* - All events pass at Level 3, i.e. all trigger bits are set to *true* in the event record. Technically speaking, the passing fraction is equal to one at Level 3.

The run ranges 174207−174217 and 172359−173101 are excluded because of well-known problems with the dimuon trigger [92].

The data are reconstructed with the p13.04, p13.05 and p13.06 versions of the event reconstruction code and they exist in the form of thumbnail files. Thumbnails have the format of reconstructed data, where the original Data Summary Tape (DST), which contains a full information about the event in all phases of reconstruction process, raw data including, is compressed into thumbnail format by dropping information that is not needed from physics analysis perspective, e.g. all hit or cluster information in the tracking system. That is economic from the point of view of a disk space, however, some information that is useful or needed for a detailed understanding of some effects is lost that way.

A good example are studies discussed in Appendix E: the p13.xx track reconstruction suffered from high-p_{T} track transverse momentum reconstruction problems due to the residual misalignment in the central fiber tracker (CFT). This effect was small and it was caused by CFT sagging due to the

gravity, but it turned out to be crucial for high-p_{T} tracks since their curvatures (bent radius) are large and any misalignment will make the tracks seem to be more curved than they actually are. As a result, the Z boson resolution measured with the tracker was by factor of two worse than in Monte Carlo [93].

The momentum correction for the misaligned CFT geometry has been applied to calculate the invariant mass of the dimuon system [93], see Section 5. This correction was not performed on the level of pre-selection however.

Dimuon events were obtained in the form of raw data from SAM, and also reconstructed with the p14 event reconstruction code. This provides an opportunity for a comparison of both reconstruction codes.

Sequential data Access via Meta-data (SAM) is a file based data management and access layer between the Storage Management System and the data processing layers. The goal of this SAM is to optimize the use of data storage and delivery resources, such as tape mounts, drive usage, and network bandwidth. In order to facilitate this goal, the primary objectives are

- Clustering the data onto tertiary storage in a manner corresponding to access patterns
- Caching frequently accessed data on disk or tape
- Organizing data requests to minimize tape mounts, and
- Estimating the resources required for file requests before they are submitted and, with this information, making administrative decisions concerning data delivery priority.

In addition, it is desired to unload the burden of individual file tracking from the analysis physicists, and place it onto the data management system. This is an added bonus integrated into the SAM system.

The integrated luminosity for this selected data set, using the trigger `2MU_A_L2M0` is determined with the lm_access package [89] is 119 ± 12 pb^{-1}.

4.2 Preselection

The preselection starts from the single-muon data set, see Section 4.1. In earlier runs, between December 19, 2002 and January 2, 2003 (it corresponds to runs $169521 - 170008$), the data was reconstructed with the wrong set of calibration constants (p13.04 and p13.05 reconstruction versions) corresponding to the first CFT super-sector, see Section 3.1.2. These events were later reconstructed with p13.06 reconstruction code using the correct set of CFT calibration constants. Some events were therefore reconstructed twice. In fact, there were $35,408,215$ events available at the time of a preselection, of which $2,643,491$ were reconstructed twice. Events reconstructed with wrong calibration constants were subsequently removed from the data sample.

The modified version of the *higgs_skim* package [94] was used to perform the dimuon skim. All luminosity blocks that belong to events from a single muon skim were stored for luminosity calculating.

In this analysis, we used the *MuoCandidate* code [95], p13-br-04 version `v1.2`. For the dimuon skim, the following criteria are applied on muons offline:

- All muons must pass the 'loose' muon quality criteria [96]. A loose

muon being defined by at least two out of the following three requirements:

1. At least two wire hits, and at least one scintillator hit in the A layers
2. At least two wire hits in the BC layers.
3. At least one scintillator hit in the BC layers.

- Event must have two loose muons, or one loose muon and a global track with a MIP trace in the calorimeter. The quality of a muon is determined within the *MuoCandidate* code.
- Each muon has $p_T > 8$ GeV, momentum measurement comes from the matching of a global track [97] to a central muon.
- Veto on cosmics rays is used directly in *MuoCandidate*. A cosmic ray muon which penetrates the entire detector will leave hits in the muon chambers on both sides of the interaction region. Such an event can be rejected based on the timing cut of those two measurements. Times measured from the beam crossing in *A*- and *BC*-stubs on both sides of the muon system are subtracted and the ≤ 10 ns cut on this value is applied. Some background events survive this selection, and the reason why as well as their nature is summarized in Section 6.6.

The dimuon skim contains $157,514$ events, out of $35,178,151$, which is the total number of events in the WZ group single-muon skim.

4.3 Dimuon event selection

The event selection is performed in two steps. First, we select dimuon candidates consistent with $Z \to \mu^+\mu^-$ production (selections S1 and S2).

The $Z \to \mu^+\mu^-$ events are used to study detection efficiency, experimental resolution, and systematic uncertainties. We also use this sample to demonstrate the sensitivity of the analysis to a doubly-charged Higgs signal.

The following selections are applied in the first step

S1 The event must fulfill the trigger condition `2MU_A_L2M0`. This requires a dimuon scintillator trigger at Level 1 and at least one with medium quality at Level 2 [98].

Offline all muons must pass the 'loose' muon quality criteria, i.e., fulfill at least two out of the three criteria listed in Section 4.2.

In the subsequent analysis, with an exception of the section on tracking efficiencies, all loose muons also have to be matched to a track from the tracking detectors (SMT and CFT), defined as having more than 9 hits in the Central Fiber Tracker (CFT) [99] and at least three hits in the Silicon Microstrip Tracker (SMT) [100]. These requirements are very weak as can be seen in Figure 4.1.

This requirement reduces background from badly reconstructed tracks. The momentum of the muon is taken from the measurement in the central tracker (CFT and SMT), i.e., the momentum measured with the toroids is not used. There must be at least two loose muons with a transverse momentum p_T of more than 15 GeV/c, and the invariant mass of the two muons is required to be greater than 30 GeV/c^2. If an

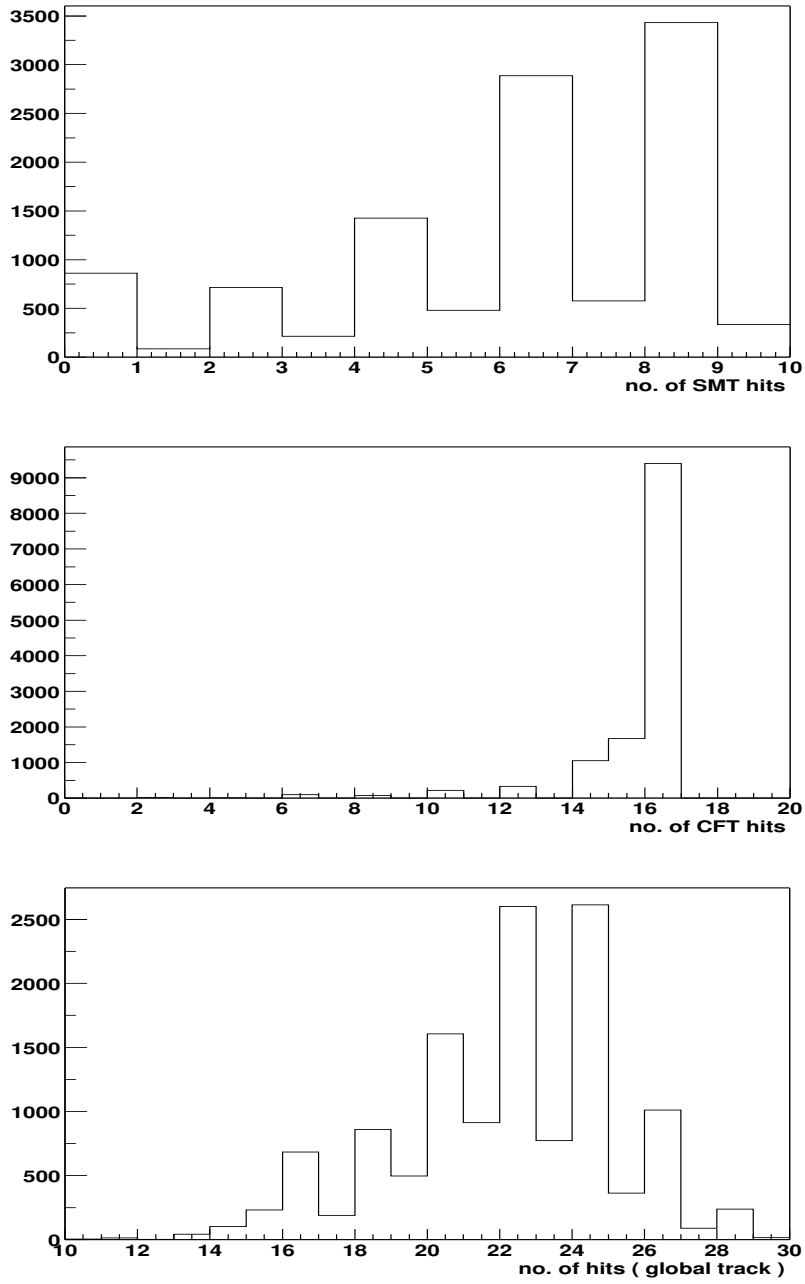

Figure 4.1: Number of SMT, CFT and (SMT+CFT) hits associated with global tracks, before the track quality criterion is imposed on the number of SMT and CFT hits.

event contains more than two muons, the two muons with highest p_{T} are used to calculate the invariant mass, independent of their charge.

S2 Isolation criteria based on calorimeter and tracking information [101] are applied to reject background mainly from muons originating from semi-leptonic b decays.

The sum of the transverse energies of the cells in a halo around the muon direction is required to be

$$\sum_{cells,i} E_{\mathrm{T}}^{i} < 2.5 \text{ GeV, for } 0.1 < R < 0.4, \tag{4.1}$$

where $R = \sqrt{\Delta\phi^2 + \Delta\eta^2}$. A similar condition is defined for the sum of the transverse momenta of all tracks other than the muon in a cone of $R = 0.5$ around the muon direction,

$$\sum_{tracks,i} p_{\mathrm{T}}^{i} < 2.5 \text{ GeV, for } R < 0.5. \tag{4.2}$$

The event has to contain at least two isolated muons.

The second step, using selections S3 and S4, is designed to reduce the background from $\mathrm{Z} \rightarrow \mu^+\mu^-$ in the dimuon data:

S3 The angle $\Delta\phi$ between the two muons with highest p_{T} is required to be less than $4\pi/5$. This is used in events with only two reconstructed muons, and rejects background from $\mathrm{Z} \rightarrow \mu^+\mu^-$ events, for the situation when the charge of one of the two muons is mis-measured, and

from remaining semi-leptonic decays of b quarks in jets that were not removed by the isolation requirement S2. This also removes background from cosmic muons.

S4 At least one pair of muons in the event is required to be of like-sign charge.

Selections S2 and S3 (so-called isolation and $\Delta\varphi$ cuts) were optimized in order to achieve the optimal performance. Details of the performance study are given in Section 9.

Chapter 5

Monte Carlo Simulation

This chapter summarizes the generation of the signal Monte Carlo sample, as well as of the expected physics backgrounds that contribute to the data sample. The same-sign lepton decay modes contain low Standard Model backgrounds. It provides a clean environment for new physics searches, the signature is a spectacular four muon final state. The dominant backgrounds in the four muon mode, where at least 2 same-sign muons are accepted, arise from electroweak processes where real high-p_{T} muons are created from W or Z decays along with either fake muons or muons from heavy flavor decays (semi-leptonic b decays, for instance, where the same-charged muons come from B-hadron mixing). The backgrounds are diboson production: $ZZ \to 4\mu$, $WZ \to 3\mu + \nu$ or $WW \to 2\mu + 2\nu$; $t\bar{t}$ production: $t\bar{t} \to \mu^+\nu b\mu^-\bar{\nu}\bar{b}$; $b\bar{b}$ production production: $b\bar{b} \to \mu^+\nu c\mu^-\bar{\nu}\bar{c}$; $Z \to \tau\tau$: τ decays into muons; $Z \to \mu\mu$ production (charge mis-identification may occur); and boson plus jets: W + jets, Z+jets where $W \to \mu\nu$, $Z \to \mu^+\mu^-$ and the jets produce real or fake muons.

The signal and backgrounds are simulated with PYTHIA 6.2 [102]. The

events are then fed to a DØ GEANT-based simulation of the detector [103]. Both programs, the detector GEANT simulation `d0gstar` [104] as well as the read-out electronics simulation `d0sim` are integral part of the framework program package named `mc_runjob` [105] that allows to generate Monte Carlo events, run them through full-detector simulation and reconstruct them in one go. These packages can be run stand-alone however, if necessary. That gives the simulation process desired flexibility, if sample re-reconstruction is required.

The `v05-00-17` version of `mc_runjob` has been used to generated most of the Monte Carlo samples considered in this analysis.

All Monte Carlo samples are simulated using the p13 version of the DØ event reconstruction code, except for the $Z/\gamma^* \rightarrow \mu^+\mu^-$ sample, which has been simulated with the p14 version on the Monte Carlo computing farms. There is a difference of about two percent between the overall muon reconstruction efficiencies of these two versions, which is adequately taken into account in the analysis.

5.1 Signal Monte Carlo simulation

PYTHIA Monte Carlo allows process:

$$p\bar{p} \rightarrow Z^0/\gamma X \rightarrow H^{--}H^{++}X, \tag{5.1}$$

with the $H^{\pm\pm}$ forced to decay to like-sign muon pairs.

The signal is generated using the CTEQ4L parton distribution functions of the proton [108] in steps of 10 GeV/c for the mass range $80 < M_{H^{\pm\pm}} < 200$ GeV/c^2. The NLO cross section for the left- and right-handed states

are taken from [55]. The integrated luminosity of signal samples ranges from 7 fb^{-1} to $M_{\text{H}^{\pm\pm}} = 80$ GeV/c^2 and 450 fb^{-1} for $M_{\text{H}^{\pm\pm}} = 200$ GeV/c^2. All signal samples were generated privately, on `clued0` (cluster of Linux machines at DØ).

5.2 Background Monte Carlo simulation

The background Monte Carlo samples are given in Table 5.1. NLO cross sections are used for the normalization of the generated samples [15-17].

Process	NLO Cross-section	$\mathcal{L}$ [fb^{-1}]
$\text{p}\overline{\text{p}} \rightarrow \text{Z}/\gamma^* + \text{X} \rightarrow \mu^+\mu^- + \text{X}$	252 pb [109]	1.03
$\text{p}\overline{\text{p}} \rightarrow \text{Z}/\gamma^* + \text{X} \rightarrow \tau^+\tau^- + \text{X}$	252 pb [109]	0.71
$\text{p}\overline{\text{p}} \rightarrow \text{t}\overline{\text{t}} + \text{X} \rightarrow \mu\mu + \text{X}$	108 fb [110]	250
$\text{p}\overline{\text{p}} \rightarrow \text{W}W + \text{X} \rightarrow \mu\nu\mu\nu + \text{X}$	143 fb [111]	138
$\text{p}\overline{\text{p}} \rightarrow \text{WZ} + \text{X} \rightarrow \mu\nu\mu\mu + \text{X}$	13 fb [111]	192
$\text{p}\overline{\text{p}} \rightarrow \text{ZZ} + \text{X} \rightarrow \mu^+\mu^-\mu^+\mu^- + \text{X}$	1.9 fb [111]	1,315

Table 5.1: Background Monte Carlo samples used in the analysis with cross sections and integrated luminosities corresponding to the number of generated events.

5.2.1 $\text{Z} \rightarrow \mu\mu$ background

The $\text{Z} \rightarrow \mu\mu$ background sample was generated on the farms. The generation of Z decays includes the Drell-Yan contribution. The generation is broken into smaller mass windows so that a sufficient statistics/luminosity is ob-

mass range [GeV/c^2]	$\mathcal{L}$	BR $\times$ cross section
2-15	769 nb^{-1}	26 nb
15-60	44 pb^{-1}	438 pb
60-130	1.1 fb^{-1}	244 pb
130-250	4.4 fb^{-1}	2.3 pb
250-500	128 fb^{-1}	150 fb
above 500	1,618 fb^{-1}	6.2 fb

Table 5.2: Properties of the Z $\rightarrow \mu\mu$ background sample.

tained even for the tails of the mass distribution. The entire sample consists of 6 sub-samples. Their properties are listed in Table 5.2. The NNLO[1] cross section is used to normalize the $Z \rightarrow \mu^+\mu^-$ sample [112].

It is well known that PYTHIA does not describe the jet multiplicity in Z+jet events very well [113]. The independent observation of this statement is demonstrated in Figure 5.1.

The jet multiplicity n_{jet} in Z events is measured using the DØ Run II cone algorithm with a radius $R = \sqrt{(\Delta\eta)^2 + (\Delta\phi)^2} = 0.5$ for minimum jet transverse momenta of 15 GeV/c [114]. Version 4.1 of the JetCorr package was used [115]. Since the kinematic distributions used in this analysis are expected to be sensitive to the number of jets, the Z/$\gamma^* \rightarrow \mu^+\mu^-$ Monte Carlo events are re-weighted to reproduce the jet multiplicity distribution observed in the data. The calculated jet multiplicity in Z events depends on the choice of the jet transverse momentum cut. The dependence of jet multiplicity on the p_{T} cut is neglected in this correction however. The higher is the cut

[1]NNLO stands for next-to-next-to-leading order cross section

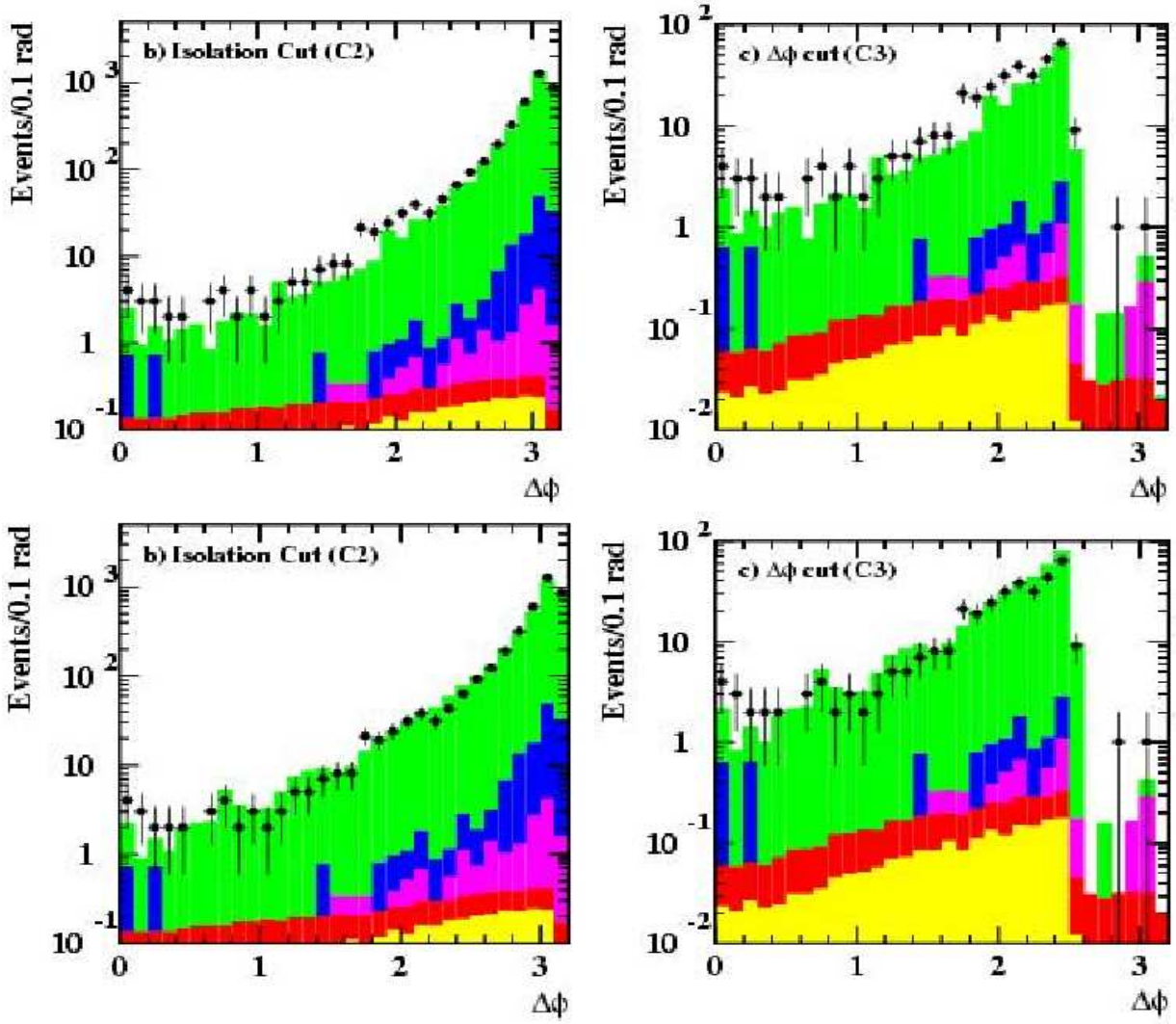

Figure 5.1: The acolinearity distributions before (top) and after (bottom) re-weighting Monte Carlo Z+jet events to better describe jet multiplicity observed in dimuon events in data. The acolinearity distribution is shown after the isolation cut (S2) (left) and after the $\Delta\varphi$ cut (S3) (right).

on jet transverse momentum, the larger is the discrepancy between Monte Carlo and data in terms of jet multiplicity in Z events. The alternative way around is the production of Z+njet samples for $n_{jet} = 0, 1, 2$ and 3 with the ALPGEN generator [106] (PYTHIA is unable to produce Z+njets *exclusive* samples, only *inclusive* Z+jets sample, i.e. Z + one and more jets) and combine them based on the measured cross section. The calculation of the background normalization is based on the fact that the background jet multiplicity spectrum for radiative QCD processes falls nearly exponentially; i.e.,

$$\frac{number\ of\ l + \geq n_{jet}\ events}{number\ of\ l + \geq (n_{jet} - 1)\ events} \approx const. \tag{5.2}$$

Roughly speaking, each additional jet adds an extra factor of the strong coupling α_s to the cross section. This was suggested on theoretical grounds [107] and has been shown to work well empirically for small n_{jet} ($n_{jet} \leq 5$) for Monte Carlo $Z \rightarrow \mu\mu$ and the data in Figure 5.2. This effect is also well-known as the so-called 'Berends scaling'.

The corresponding weights are 0.87(2), 1.08(3), 1.95(5) and 2.71(9) for $n_{jet} = 0, 1, 2$ and 3, respectively [116]. The total number of events before and after re-weighting must remain the same, which is the important cross-check that all coefficients were derived correctly. The contribution from events with $n_{jet} > 3$ is negligible, this is why the weight factor remains equal to one.

5.2.2 Z $\rightarrow \tau\tau$ background

The Z $\rightarrow \tau\tau$ background is not the type of background that contributes to like-sign backgrounds significantly. However, similarly to $Z \rightarrow \mu\mu$ sample,

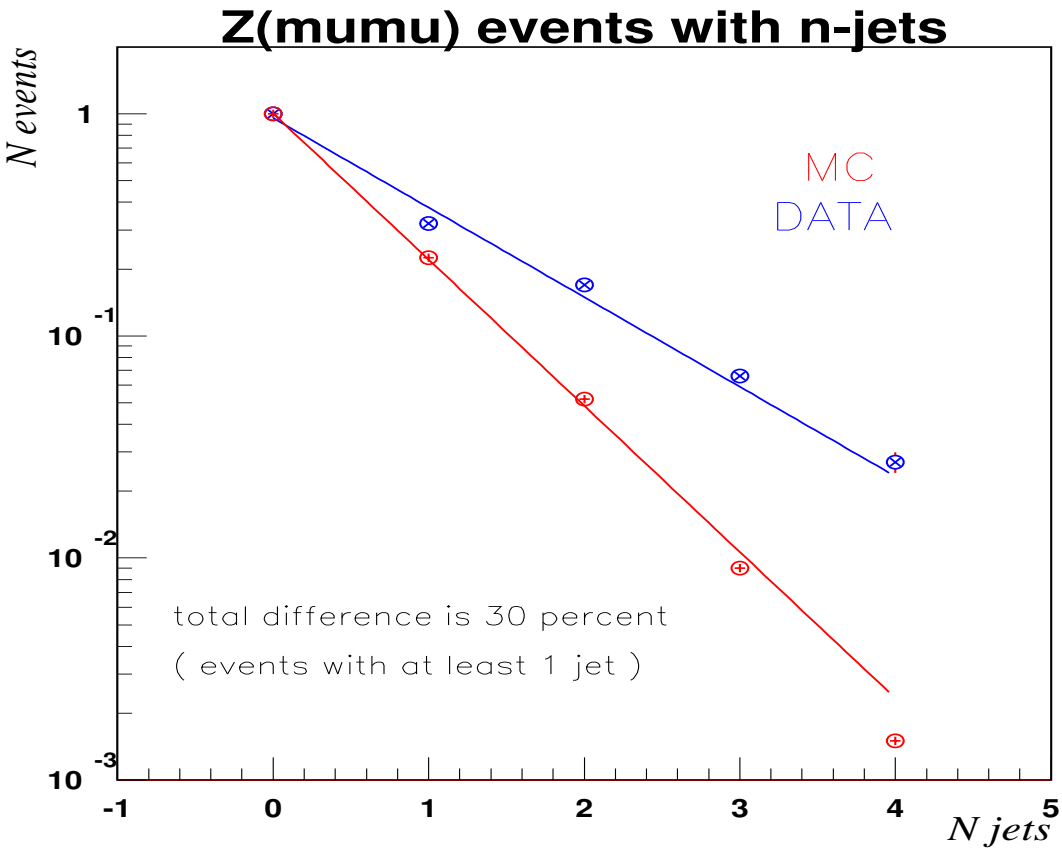

Figure 5.2: The so-called Berends scaling - jet multiplicity in $Z(\rightarrow \mu\mu)$+jets events - both for an uncorrected Monte Carlo $Z \rightarrow \mu\mu$ sample and data using Run II cone algorithm with a radius $R = \sqrt{(\Delta\eta)^2 + (\Delta\phi)^2} = 0.5$ to define jets with transverse momenta greater than 15 GeV/c^2 [114].

some of the events might contain a high-p_{T} track that is ill reconstructed with the opposite sign of the charge. An event that was generated as an opposite-sign event is, in such a case, considered to be the same-sign event and it therefore contributes to the same-charged background. The transverse momentum distribution of muons in this sample is obviously much softer than in $Z \to \mu\mu$ events due to the 3-body decay of τ-leptons. Thus the invariant mass of $Z \to \tau\tau$ peaks sooner (in lower masses) and falls down to zero much faster than in case of the $Z \to \mu\mu$ background.

In order, to study properties of $Z \to \tau\tau$ background properly, a large statistics are needed. This is a motivation for simulating much larger $Z \to \tau\tau$ sample than the one currently available. In the new sample, all τ-leptons are free to decay naturally, however only $Z \to \tau\tau$ events with 2 generated muons, each with a true transverse momentum greater than 8 GeV/c, are picked from the entire generated sample. Invariant mass of these events must be greater than 15 GeV/c. In order to select only high-p_{T} dimuon events, `d0_mess` program [117] is used. This package allows to choose and reconstruct only those events (out of all generated by PYTHIA) that pass a certain set of selection criteria. This sample was generated privately because of its specific nature. The cross section times branching ratio for a process $p\bar{p} \to Z/\gamma^* \to \tau\tau \to \mu\mu X$, where both muons have transverse momenta greater than 8 GeV/c, is 3.8 pb, after NLO corrections have been applied. The total number of $40,000$ events with properties listed in this section was used in this analysis.

5.2.3 $t\bar{t}$ and diboson backgrounds

These samples were generated by the Monte Carlo group on the DØ offline computing farms. Only final states with 2 and more muons are considered. Properties of $t\bar{t}$ and diboson samples are listed in Table 5.1.

5.2.4 $b\bar{b}$ background

The $b\bar{b}$ production is an important background because it is the natural source of a large like-sign dimuon background. Like-sign muon pairs in these events are produced through neutral B-hadron mixing. The $b\bar{b}$ background is important for many searches, e.g. doubly-charge Higgs, ZH ($H \rightarrow \mathrm{b\overline{b}}$), SUSY searches, WW cross section measurement etc. Simulation of this background with PYTHIA did not give satisfactory results in the past. However, it is a goal of this paragraph to demonstrate that it is possible to achieve a nice agreement with data using the PYTHIA generator with certain tuning. The direct comparison of a generated dimuon sample which is one of the final states of the $b\bar{b}$ production is given below. It is interesting to compare a generated $b\bar{b} \rightarrow \mu\mu X$ sample with data in terms of production cross section (expected rates respectively) and variables that are the main focus in this analysis, i.e. invariant mass and acolinearity.

$b\bar{b}$ production and its tune-up to data

In hadron collisions, heavy quark production at leading order is manifested through:

- $q\bar{q}$ annihilation ($q\bar{q} \rightarrow Q\bar{Q}$)

- gluon fusion in s- and t-channels

Each of the processes dominates a different region in phase-space. The quark-antiquark annihilation is a major process near the $Q\bar{Q}$ threshold and large p_{T}, whereas gluon fusion processes dominate at low transverse momenta. At Tevatron, the $b\bar{b}$ production is governed by gluon fusion. The leading order $b\bar{b}$ production in PYTHIA is well described by the `MSEL=5` process. This process is also known as 'flavor creation'. There is a sufficiently good agreement between the shape of the integrated b-quark p_{T} distribution observed in the data and the one predicted in NLO QCD [118, 119]. However, the rate measured in data is by a factor of more than two higher with respect to the NLO QCD prediction. The next-to-leading order (NLO) depends on the choice of parton density functions (PDF), but the gluon density has not yet been measured for the values of x probed at the Tevatron. The NLO b-quark cross section also indicates a strong dependence on the factorization and renormalization scales used in the calculation.

PYTHIA 6.203 is also used to estimate the $b\bar{b}$ background from semi-leptonic b decays into muons [120]. To produce a large $b\bar{b}$ sample we use inclusive QCD production: $q + q \rightarrow q + q$ (where $q = u, d, s, c, b, g$) with MSEL parameter set to one. It is generally accepted that it is important to have a good leading order QCD Monte Carlo model predictions of collider observables. The leading-order QCD Monte Carlo model gives an estimate of a base line that serves the purpose of comparison to other calculations. It is a consensus that the QCD should be able to describe heavy quark production quantitatively and qualitatively, similarly to what has been already achieved in light quark and gluon production. It is important to realize

that one measures hadrons and leptons, not quarks or gluons. This is why the leading-order Monte Carlo has to incorporate fragmentation via 'string fragmentation', 'cluster fragmentation' or 'FF fragmentation' [121, 122] that produce final state hadrons and/or leptons. The sources of b quark production are:

- **flavor creation**

  Flavor creation corresponds to the production of a $b\bar{b}$ pair by gluon fusion or by annihilation of light quarks. Leading order flavor creation production rate is by a factor of four below data [118]. The flavor creation represents only about 30% of the entire $b\overline{b}$ production however.

- **flavor excitation**

  Flavor excitation corresponds to the scattering of b or $\bar{b}$ quark out of the initial state into the final state by a gluon or by a light quark/anti-quark. It is extremely sensitive to the number of b quarks within a proton, i.e. to the structure functions.

- **shower/fragmentation (i.e. gluon splitting)**

  The $b\bar{b}$ pair is created within a parton shower or during the fragmentation process of a gluon or a light quark/anti-quark. The QCD hard-scattering 2-to-2 subprocess involves gluons and light quarks and anti-quarks. This process is color-enhanced. The Monte Carlo model predictions differ significantly for 'shower/fragmentation' contribution. It is not a big surprise because ISAJET [123] uses independent fragmentation, while HERWIG [124] and PYTHIA do not. HERWIG and PYTHIA modify the leading order of parton showers to include color coherence effects. ISAJET does not do that.

All three sources are important at the Tevatron. There are two processes considered in this analysis: `MSEL=5` (flavor creation only) and `MSEL=1` (flavor creation, flavor excitation and gluon splitting). Two independent samples are produced to provide a comparison, the outcome of this study is presented in this thesis as well as in [120].

The `MSEL=5` process is known to have a cross section by a factor of more than four smaller than the b quark cross section measured by collider experiments at DØ and CDF [118]. Also the invariant mass and acolinearity are known to differ from the data. That can be best viewed in Figure 5.3. `MSEL=5` underestimates the contribution of collinear $b\bar{b}$ pairs. They are mainly produced by gluon splitting which is a dominant process in that region, see the bottom plot in Figure 5.3. Since they are produced by a gluon splitting production process, their transverse momentum is going to be soft. As a result, majority of these events is removed by the muon transverse momentum cut applied offline. In other words, these events will not pass the first selection criterion in this analysis (S1).

Additionally, the full 'Tune A' is turned on in production card files, and CTEQ4L (current default for PDFCODE in `mc_runjob`). 'Tune A' was originally tuned using CTEQ5L, this is why it can be slightly inconsistent with other tunes done with CTEQ4L. However, simulations presented in this thesis reproduce the data very well, this is why the choice of CTEQxL version probably does not play a crucial role.

It has been observed earlier, e.g. at HERA [118], that `PARP(67)=1` does not describe well the p_{T} spectra in events with at least 3 jets. In the QCD analysis [125, 126], studying the $\Delta\varphi$ between jets, it is also seen that

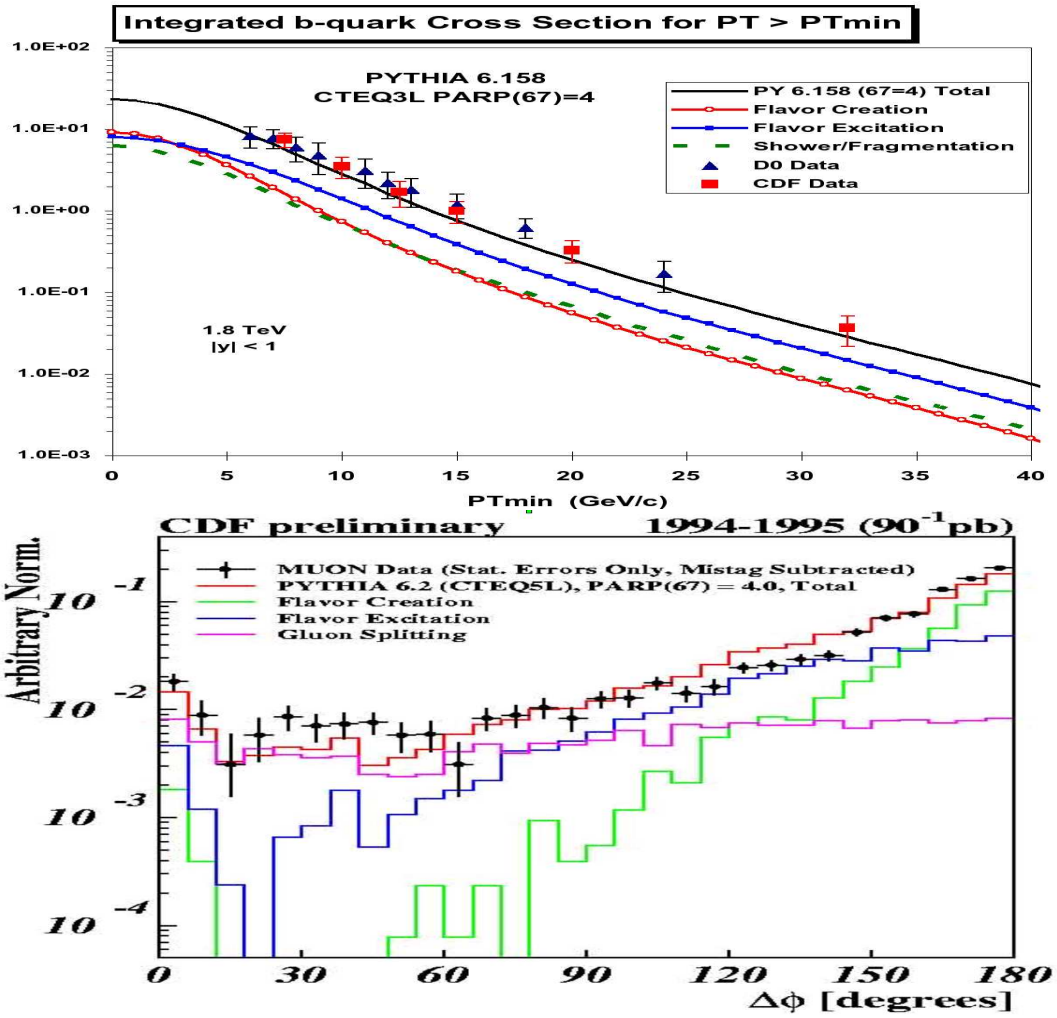

Figure 5.3: The agreement between `MSEL=5`, `MSEL=1` and DØ / CDF Run I data [118]. The upper plot shows contribution of flavor creation, flavor excitation and gluon splitting to the total b quark inclusive production cross section. The bottom plot demonstrates how important are flavor excitation and gluon splitting for a correct description of the data (CDF Run I data) in terms of acolinearity between two produced b quarks. `MSEL=5` is unable to describe neither the cross section (top) nor the acolinearity in a region of small $\Delta\varphi$ (bottom).

PARP(67)=4 describes the data much better than PARP(67)=1. In order to achieve a better description of azimuthal angle $\Delta\varphi$ between b and $\bar{b}$ quarks, the PARP(67) parameter is set to 4. The PARP(67) parameter is a scale factor that governs the amount of large angle initial state radiation (ISR). The larger is the value of PARP(67), the more large angle ISR there is mixed in to the event. A large sample generated by accident with MSEL=1 and PARP(67)=1 is available. That provides a unique opportunity for a comparison of $b\bar{b}$ samples produced with PARP(67)=1 and PARP(67)=4 and its effect on acolinearity distributions. This effect can be observed in Figure 5.4.

Choice and consequences of a parton level p_{T} cut

The $b\bar{b}$ simulation is not an easy task however, since it represents a major challenge due to its huge cross section. This is a reason why minimum transverse momentum of 30 GeV/c is required for the generated partons, $p_{\mathrm{T}}^{\mathrm{min}} = 30$ GeV/c. The PYTHIA parameter CKIN(3) is set to 30 and the d0_mess package [117] is used to select only those events that contain at least two muons with true $p_{\mathrm{T}}^{\mu} > 12$ GeV/c (a safety margin of 3 GeV/c is allowed). The generated number of events corresponds to an integrated luminosity of about 2.7 fb^{-1}.

The value of the minimum transverse momentum on the parton level has been decided based on the following reasoning: the optimal scenario would be to set this cut as low as possible (not to use it at all, respectively), it is however not possible because the CPU time needed to generate such a big sample would increase beyond limits acceptable and achievable given clued0 computation resources. It is clear that such a task reaches far beyond

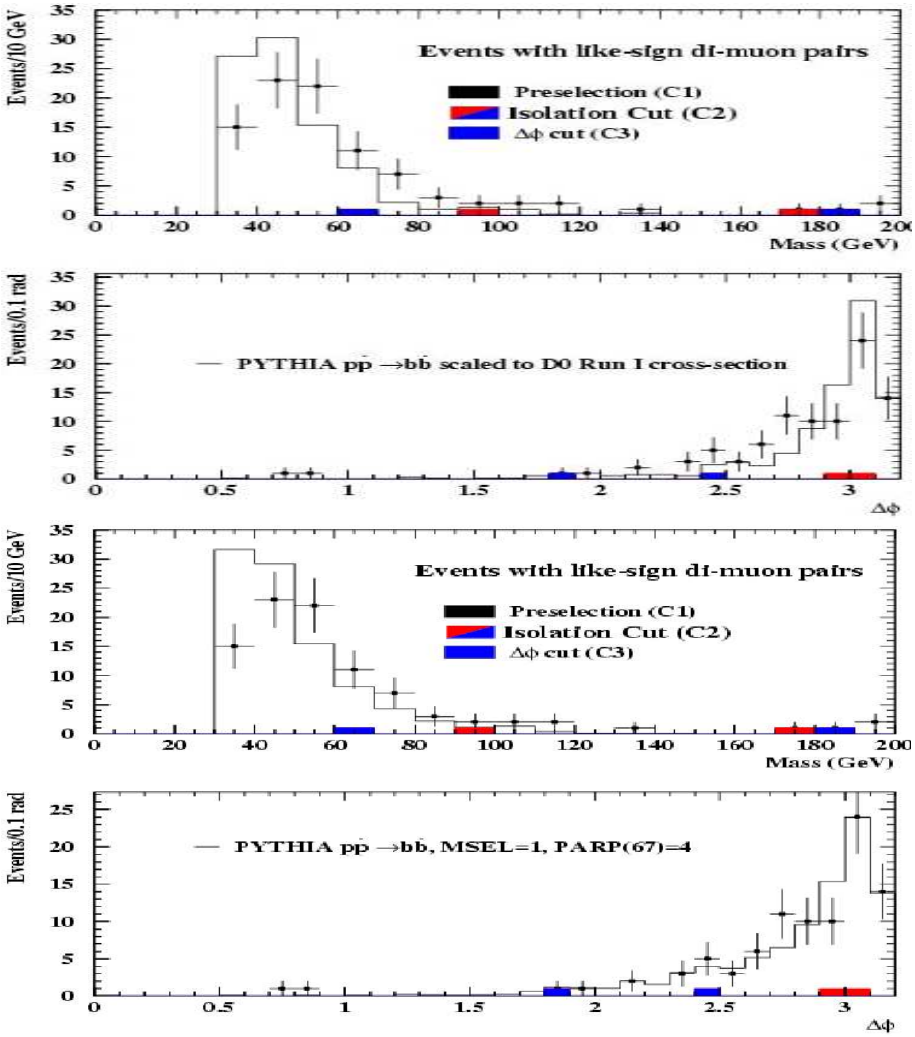

Figure 5.4: Invariant mass and acolinearity distributions for like-sign events. Both samples are generated with `MSEL=1`, upper two plots with `PARP(67)=1` and bottom two plots with `PARP(67)=4`. The Monte Carlo sample generated with `PARP(67)=4` describes the data better in terms of $\Delta\varphi$ distribution. There is almost no effect of this parameter on the invariant mass distribution (compare the first plot with the third plot from the top).

present capability. That is why a modest transverse momentum cut has to be introduced. The b quark decay is, in principal, a 3-body decay. The offline requirement on the reconstructed muon transverse momentum in this analysis is 15 GeV/c. This is why a cut of about 10 GeV/c is probably safe in this perspective. Since there are 3 particles produced in the b quark decay ($b \to \mu\nu c$, $b \to c \to \mu\nu s$), each of them carries away 1/3 of the generated parton transverse momentum, 30 GeV/c cut on the parton level should not represent any harm to the analysis. Everything goes for its price however, even a moderate cut like this raises a question if any bias of a generated muon transverse momentum distribution can be involved. And this question has to be addressed adequately. One should also not forget that the produced b quark looses its energy through final state radiation (FSR) effects and that lowers b quark transverse momentum as well. Any bias due of the true muon transverse momentum distribution due to the kinematic selection is rather unlikely, even if one looks as low as 12 GeV/c in the p_{T}^{μ} distribution. There is no (or really small) p_{T}^{μ} bias introduced by this cut on a parton level. That can be observed in Figure 5.5.

If there was any bias, it should demonstrate itself as a dull turn-on (instead of a sharp cut off of a falling exponential) close to the minimum p_{T}^{μ} (12 GeV/c). This part of the p_{T}^{μ} spectrum is cut off later on in the analysis by the preselection cut, this is why any bias of this kind would not affect the measurement anyway. There is an important feature of the parton level p_{T} cut however: the minimum transverse momentum cut on the parton level can be 'misplaced', i.e. it is not necessarily placed on the generated b or $\bar{b}$ quark. It might be applied to some other parton produced in PYTHIA (e.g.

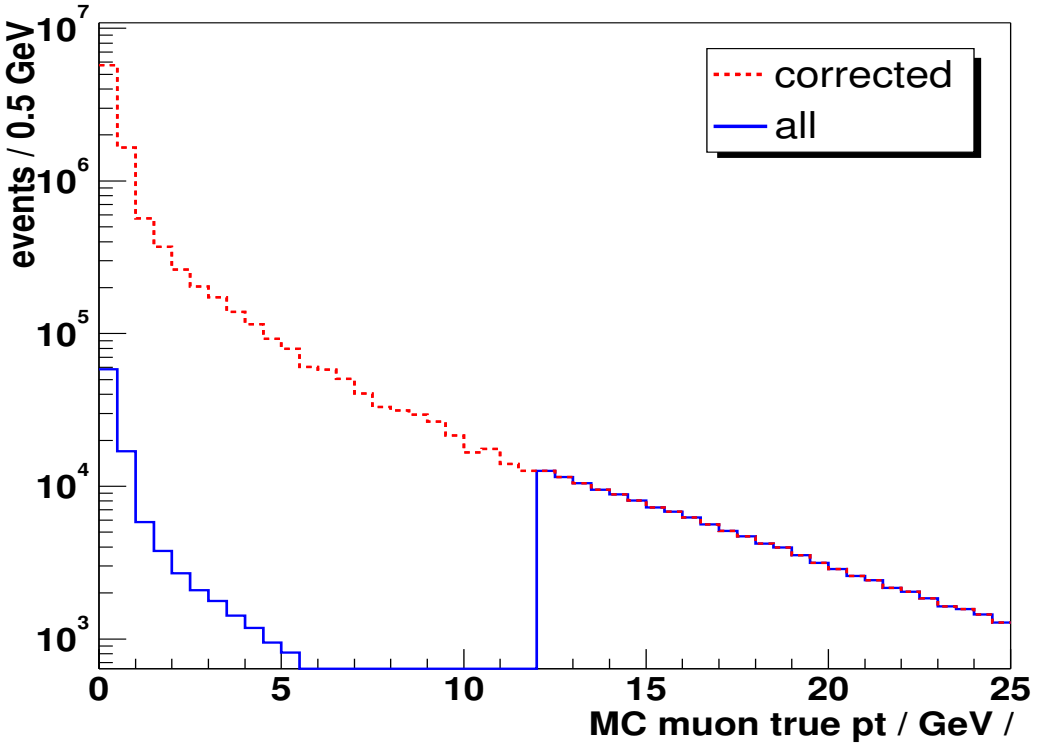

Figure 5.5: If there is any bias due to the parton level p_{T} cut, one should observe a deviation from the falling exponential. This figure shows the Monte Carlo muon true p_{T}^{μ} distribution (solid/blue histogram). The sharp edge at $p_{\mathrm{T}}^{\mu} = 12$ GeV/c is due to the `d0_mess` preselection (i.e. 2 generated muons are required, each with true $p_{\mathrm{T}}^{\mu} > 12$ GeV/c). Muons below 12 GeV/c are additional muons, they can serve as representatives of an unbiased spectrum. In the dashed/red histogram the additional muons spectrum (that are below 12 GeV/c) is scaled up so that these two spectra are normalized at 12 GeV/c bin. One can see that these two spectra match very well in terms of slopes in the vicinity of 12 GeV/c. This indicates, that the bias due to the parton level cut is indeed rather small.

to a gluon in gluon splitting). In fact, that is even better for us. In case of flavor excitation or gluon splitting, the parton level $p_{\mathrm{T}}^{\mathrm{min}}$ cut is even softer than it was originally planned. This effect creates a small bias toward low p_{T}^{μ} in case of the `MSEL=5` process, i.e. only flavor creation is involved. That can be seen if Figure 5.7, the first plot from the top. The parton level $p_{\mathrm{T}}^{\mathrm{min}}$ cut acts upon b or $\bar{b}$ quark and as a result it might be a little bit too hard for a small fraction of events. One should keep in mind that 2-to-2 process (e.g. flavor creation) happens in 20 % of cases only. The rest are 2-to-3 processes (flavor excitation and gluon splitting), for those the parton level $p_{\mathrm{T}}^{\mathrm{min}}$ cut is essentially harmless.

b quark production cross section in data and PYTHIA Monte Carlo

The distribution most commonly studied by hadron collider experiments is the b-quark transverse momentum distribution in a fixed pseudorapidity region

$$\sigma(p_{\mathrm{T}} > p_{\mathrm{T}}^{min}) = \int_{|\eta|<|\eta_{max}|} d\eta \int_{p_{\mathrm{T}}>p_{\mathrm{T}}^{min}} dp_{\mathrm{T}} \; \frac{d\sigma^2}{d\eta \; dp_{\mathrm{T}}} \tag{5.3}$$

Figure 5.6 shows the inclusive b quark production cross section as a function of the minimum transverse momentum $p_{\mathrm{T}}^{\mathrm{min}}$ of the b quark, as measured in the Run I data [127]. The inclusive b quark production cross section $\sigma^{\mathrm{b}}(p_{\mathrm{T}}^{\mathrm{b}} > 30$ GeV/c) is measured by DØ to be (54 ± 20) nb in the rapidity interval $|y^{\mathrm{b}}| < 1$ which is in good agreement with the PYTHIA cross section of 58 nb at $\sqrt{s} = 1.8$ TeV. The production cross section measured in Run I data was scaled to the whole rapidity coverage $|y^{\mathrm{b}}| < 4.2$ and $\sqrt{s} = 1.96$ TeV in Tevatron Run II.

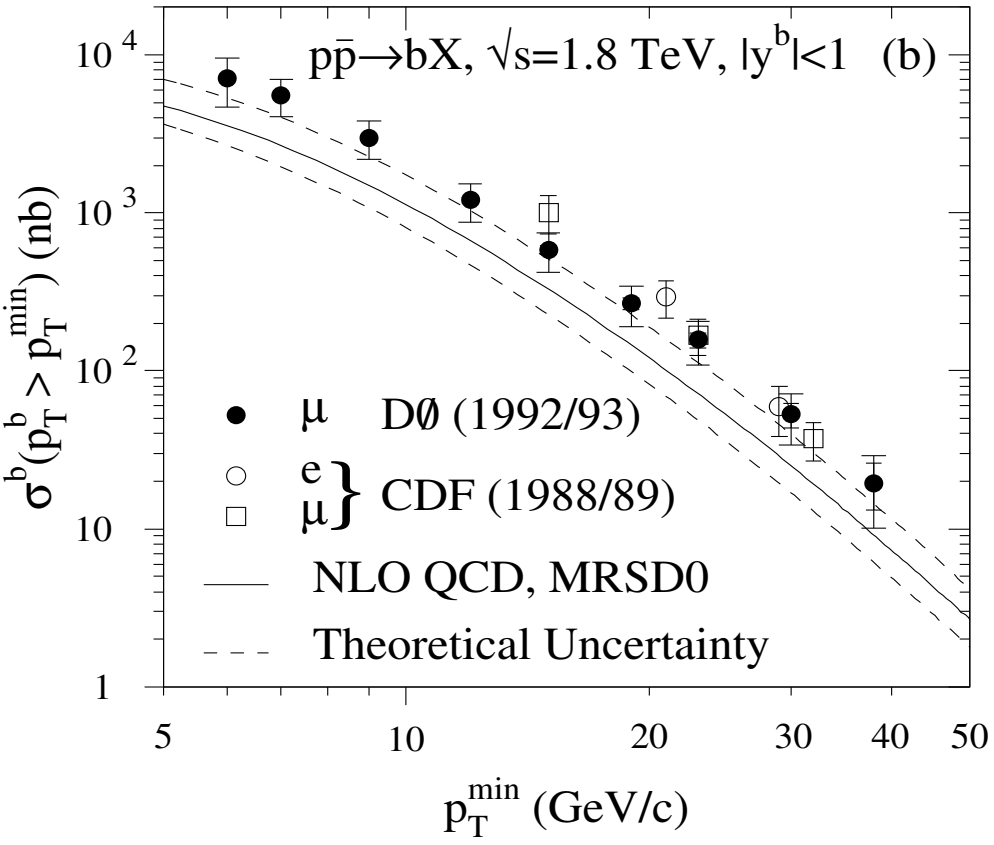

Figure 5.6: The b quark production cross section measured by DØ [127] using Run I data compared to a NLO QCD prediction.

Comparison of `MSEL=1` and `MSEL=5` processes

The PYTHIA (CTEQ4L) inclusive b quark production cross sections estimated in a rapidity range $|y^{\mathrm{b}}| < 1$, with `PARP(67)=4`, are

- `MSEL=5` at $\sqrt{s} = 1.8$ TeV

$$\sigma^{\mathrm{b}}(p_{\mathrm{T}}^{\mathrm{b}} > 30 \text{ GeV/c}) = 9 \text{ nb}$$

- `MSEL=5` at $\sqrt{s} = 1.96$ TeV

$$\sigma^{\mathrm{b}}(p_{\mathrm{T}}^{\mathrm{b}} > 30 \text{ GeV/c}) = 11 \text{ nb}$$

- `MSEL=1` at $\sqrt{s} = 1.8$ TeV

$$\sigma^{\mathrm{b}}(p_{\mathrm{T}}^{\mathrm{b}} > 30 \text{ GeV/c}) = 58 \text{ nb}$$

- `MSEL=1` at $\sqrt{s} = 1.96$ TeV

$$\sigma^{\mathrm{b}}(p_{\mathrm{T}}^{\mathrm{b}} > 30 \text{ GeV/c}) = 85 \text{ nb}$$

The statistical uncertainties on these values are $10 - 20$ %. The direct comparison of invariant mass and acolinearity calculated for a `MSEL=5` and `MSEL=1` samples is given in Figure 5.7.

Cross section of the generated $b\bar{b} \to \mu\mu$ sample

The $b\bar{b}$ sample is produced in the following consecutive steps:

- QCD inclusive process without any parton level cut

$$\sigma^{\mathrm{b}}(no\ p_{\mathrm{T}}^{\mathrm{b}}\ cut) = 40 \text{ mb}$$

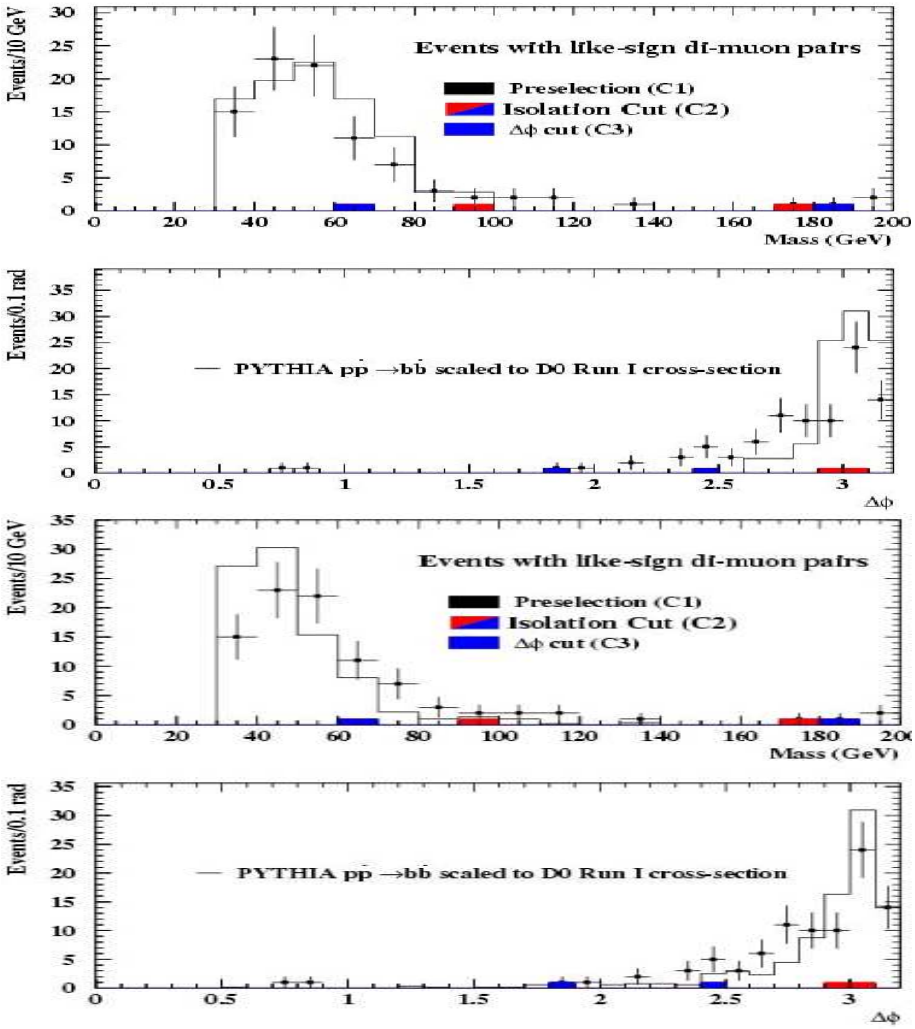

Figure 5.7: Invariant mass and acolinearity distributions for like-sign events. Both samples are generated with `PARP(67)=4`, upper two plots with `MSEL=5` and bottom two plots with `MSEL=1`. The Monte Carlo $b\bar{b}$ sample generated with `MSEL=1` describes the data better in terms of $\Delta\varphi$ distribution. There is an obvious bias at low masses in the invariant mass plot (first plot from the top) due to the cut on parton transverse momentum $p_{\mathrm{T}}^{\mathrm{min}}$.

- QCD inclusive process with $p_{\mathrm{T}}^{\mathrm{b}} > 30$ GeV/c parton level cut [2]

$$\sigma^{\mathrm{b}}(p_{\mathrm{T}}^{\mathrm{b}} > 30 \text{ GeV/c}) = 5.1 \ \mu\mathrm{b}$$

- QCD inclusive process with a $p_{\mathrm{T}}^{\mathrm{b}} > 30$ GeV/c parton level cut, B hadrons, which are a product of b quark hadronization, are forced to decay into muons

$$\sigma^{\mathrm{b}}(p_{\mathrm{T}}^{\mathrm{b}} > 30 \text{ GeV/c}, b \to \mu) = 2.52 \text{ nb}.$$

The splitting rate of $b \to \mu$ estimated using PYTHIA is $\epsilon_{QCD \to b\bar{b}} = 5$ %, the branching ratio of $b \to \mu$ is approximately 10.5 %. This is why the $b\bar{b}$ cross section estimated for a full rapidity range $|y^{\mathrm{b}}| < 4.2$ is

$$\sigma^{\mathrm{b}}(p_{\mathrm{T}}^{\mathrm{b}} > 30 \text{ GeV/c}, \ b\bar{b}) = 252 \text{ nb}.$$

All B hadrons are forced in the PYTHIA decay table to decay semi-leptonically into muons, all other processes are forbidden. This is a reason why $b \to c \to \mu$ cascade decays are not present in this sample. They are more complicated to produce. However, the transverse momenta of muons produced in cascade decays are soft. This component of a generated $b\bar{b}$ sample would be filtered out by the p_{T}^{μ} cut anyway, as it has been already discussed in Section 5.2.4.

- `d0mess` selection

At least 2 generated muons, each with a true $p_{\mathrm{T}}^{\mu} > 12$ GeV/c are required to be present in each event. The estimated passing rate, which

[2] It is assumed here that $p_{\mathrm{T}}^{\mathrm{b}}$ and $p_{\mathrm{T}}^{\mathrm{min}}$ are the effectively same cuts. As it has been pointed out earlier, that is not always the situation.

can be calculated based on the `d0mess` printout, is 1.2(1) %.

$$\sigma^{\mathrm{b}}(p_{\mathrm{T}}^{\mathrm{b}} > 30 \text{ GeV/c},\ b \to \mu,\ 2\ muons,\ p_{\mathrm{T}}^{\mu} > 12\ GeV/c) = 29.7 \text{ pb}.$$

127 million events are generated by QCD inclusive process. Only about 74 thousand events pass the selection criteria in `d0mess`.

Comparison of simulated $b\overline{b}$ sample with data

To normalize Monte Carlo samples to data, we estimate from data all reconstruction efficiencies: track, muon identification, isolation, trigger and matching. The procedures applied to calculate all considered efficiencies are described in a great level of detail in Section 6. Until now, we have silently assumed that trigger, muon identification and track reconstruction efficiencies are independent of transverse momentum of the reconstructed muon. This is the correct approach when dealing with high-p_{T} muons that create a hard core of the studied data sample, but it is a wrong assumption for lower p_{T} muons that originated from b decays, for instance. Production processes like flavor excitation and gluon splitting produce a sample of muons with significantly softer transverse momenta.

Thus any reconstruction efficiency turn-on will have a significant impact on the shape of the invariant mass distribution for this kind of events. The same impact can be observed in transverse momentum distribution. The track reconstruction efficiency is already flat and saturated in the region above 15 GeV/c, unlike the trigger and muon identification (loose muon) efficiencies.

- **trigger turn-on measured in $Z \to \mu\mu$ events**

  The trigger turn-on for the `2MU_A_L2M0` trigger is measured using the

method described in Section 6.4 as a function of muon transverse momenta p_{T}. The trigger turn-on was separately measured for the leading, sub-leading and all muons in the event, see Figure 5.8.

The same variable can be shown as a function of reconstructed invariant mass, Figure 5.9.

The function chosen to fit the dependence of `2MU_A_L2M0` trigger efficiency on the reconstructed invariant mass of the dimuon system is tangent hyperbolic, it can be approximated by

$$\epsilon(m_{\mu\mu}) = 0.713 \ \tanh(\ 0.074\ m_{\mu\mu} - 1.622\ ). \tag{5.4}$$

Figure 5.10 shows the effect of trigger turn-on correction on the invariant mass and acolinearity distributions.

A clear difference in the shape of the invariant mass distribution, in the region of lower masses, can be observed in Figure 5.10. It is obvious that in absence of any p_{T} bias, the invariant mass for $b\bar{b}$ events should be a falling exponential. That can be observed in the first plot from the top. As soon as any trigger/muon identification turn-on is introduced, it is likely that some events with the low invariant mass are going to be rejected due to the trigger/muon identification inefficiency. This results in a deflection from the falling exponential. And this is an effect that occurs in like-sign dimuon data. The Monte Carlo $b\bar{b}$ sample distributions must be convoluted with this kind of detector response in order to achieve an optimal agreement with the data.

- **muon identification turn-on measured in $Z \to \mu\mu$ events**

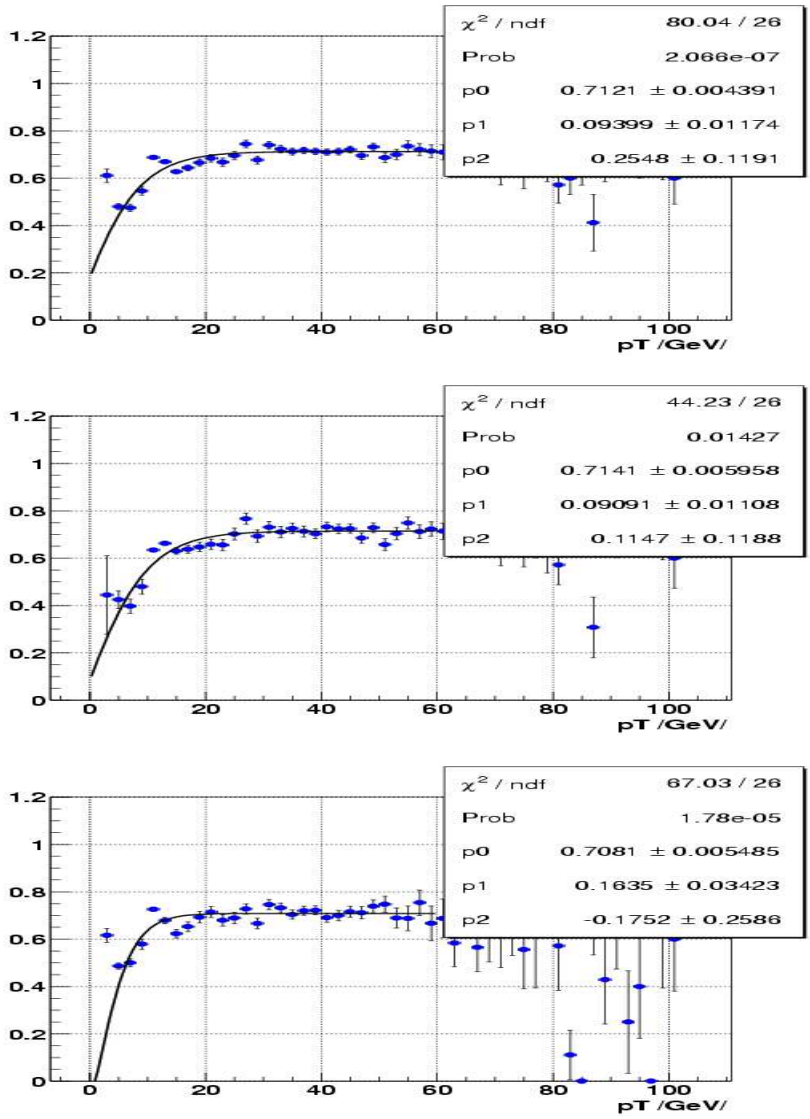

Figure 5.8: `2MU_A_L2M0` trigger efficiency as a function of muon transverse momenta, for all muons (top), leading muon p_{T} (center) and sub-leading muon p_{T} (bottom). The fitted function is a tangent hyperbolic.

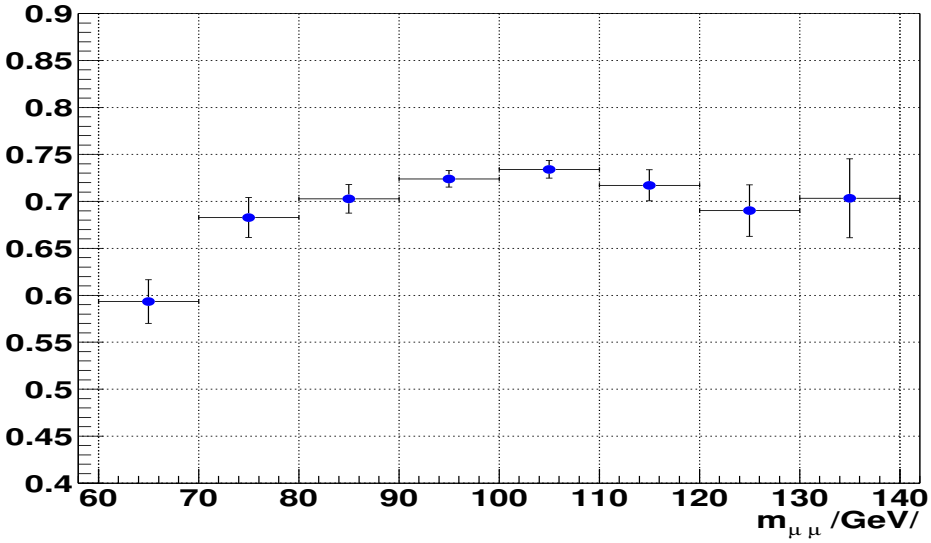

Figure 5.9: 2MU_A_L2M0 trigger efficiency as a function of the reconstructed invariant mass. The behavior is assumed to be tangent hyperbolic.

Yet another contribution to the final shape of the invariant mass distribution comes from the muon identification turn-on. The measurement of a muon identification efficiency, e.g. the efficiency to reconstruct a loose muon, as a function of muon transverse momentum p_{T} can be parametrized by a form

$$\epsilon(p_{\mathrm{T}}) = 0.97 \ \tanh(\ 0.066\ p_{\mathrm{T}} - 0.378\ ). \tag{5.5}$$

Similar result was obtained in [128].

The total correction that contributes to the normalization of Monte Carlo to data can be then expressed as:

$$\epsilon_{tot}^{trig,\ \mu-ID}(m_{\mu\mu}) = \epsilon^{trig}(m_{\mu\mu})\ [\ \epsilon_{tot}^{\mu-ID}(m_{\mu\mu})\ ]^2 = 0.765\ \tanh(\ 0.027\, m_{\mu\mu} - 0.606\ ). \tag{5.6}$$

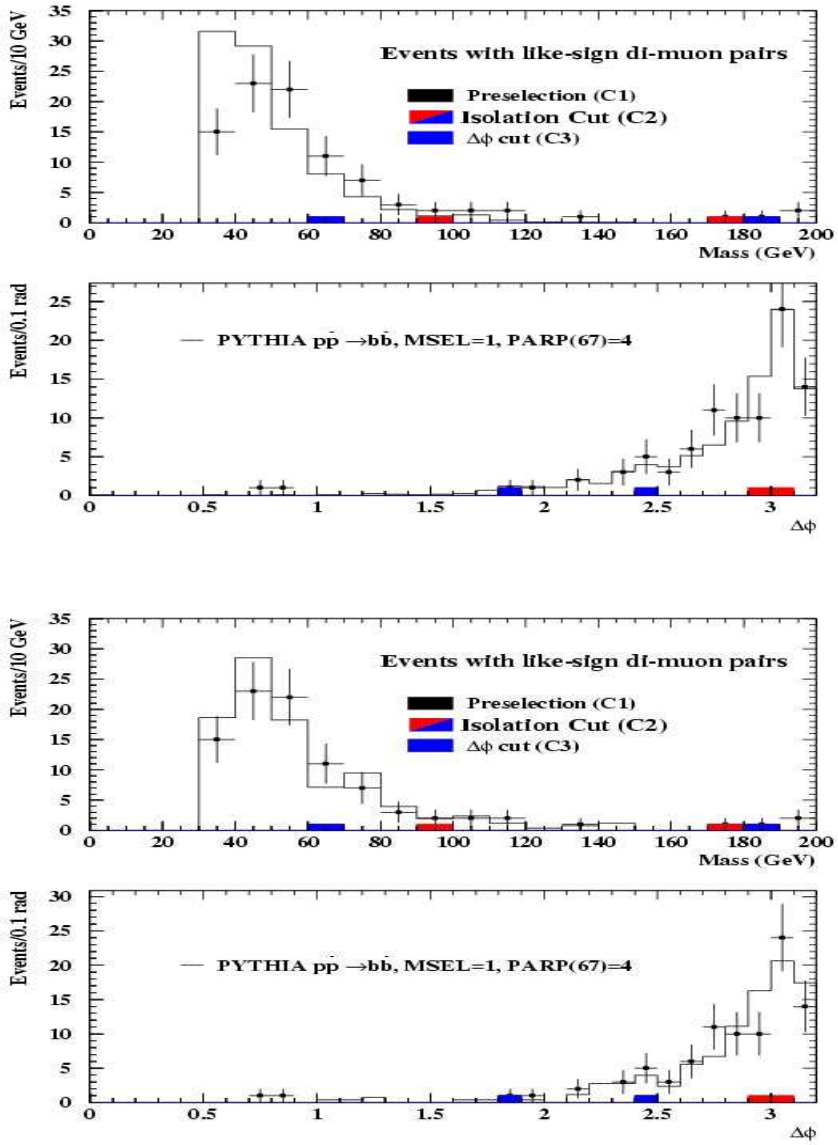

Figure 5.10: The effect of trigger turn-on on the invariant mass and acolinearity distributions for like-sign dimuon events. The upper two plots show both variables before the trigger turn-on correction is applied, the bottom two plots after it its application.

The improvement after applying the loose muon reconstruction efficiency corrections is shown in Figure 5.11.

To have even better agreement between Monte Carlo and data, all dependencies of reconstruction efficiencies on p_{T} and angular variables should be accounted for. We do not do that in this analysis since the contribution from other effects than those described in this section are of a much smaller magnitude. Nevertheless, all residual discrepancy could be explained by that.

5.2.5 W+jets background

In many analyses that involve isolated muon final states, the question arises on whether the current DØ Monte Carlo can reliably predict the background rates from $W(\rightarrow \mu\nu)+X$ processes, where the additional muon(s) comes from the jet fragmentation, punch-through, etc. [130]. Only one muon is isolated, whereas the other one is not. This background is particularly relevant for doubly-charged Higgs searches in muon final states.

W+jets background estimated from data

While the problem described above is an interesting project on its own, the ultimate answer should, at this time, come directly from the data. The current study is an attempt to address this issue. No detailed and/or dedicated analysis of this problem has been performed at DØ yet. This is why the following study serves the specific goal of this analysis and it does not attempt to give a general answer to this problem.

The aim of this study is to estimate from data the isolated dimuon rates for muons with $p_{\mathrm{T}} > 15$ GeV/c that specifically come from W+jets produc-

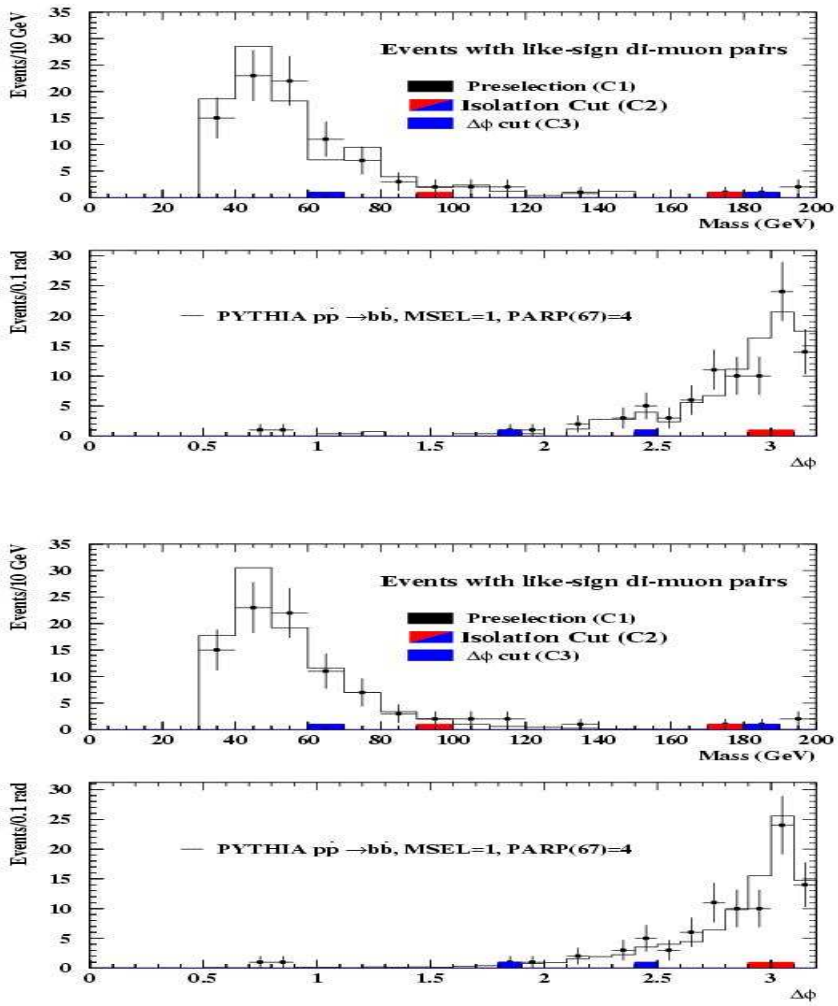

Figure 5.11: The improvement of an agreement between Monte Carlo and data in terms of invariant mass and acolinearity distributions for like-sign dimuon events. The upper two plots show both variables after the trigger efficiency turn-on correction is applied, the bottom two after the loose muon reconstruction efficiency turn-on and the trigger efficiency turn-on corrections are both accounted for.

tion.

The $W \rightarrow \mu\nu$ inclusive sample was selected and analyzed by Peter Tamburello. The details of his analysis and event selections are documented in [131].

In his analysis $W \rightarrow \mu\nu$ candidates are selected using the following cuts:

- $E_t^{missing} > 20$ GeV/c^2
- $p_{\mathrm{T}}^{\mu} > 8$ GeV/c
- $|\eta^{\mu}| < 2$.

The events selected this way are from more than 90 % the W candidates. The dominant background comes from QCD $b\bar{b}$ production. In order to reduce this contribution, the additional cut on the W transverse mass of $m_t^W > 30$ GeV/c^2 is applied. The QCD $b\bar{b}$ rates are estimated separately, thus the eventuality of double counting must be avoided.

The transverse momentum distribution of the second muon in these events is shown in Figure 5.12. One can clearly see the two components of this spectrum - an exponentially falling distribution that is taken over by the $Z \rightarrow \mu\mu$ production at around $p_{\mathrm{T}} \sim 10$ GeV/c.

The transverse momentum spectrum of the second muon is fitted in various p_{T}^{μ} intervals to evaluate systematic uncertainties: $2 - 9$ GeV/c, $3 - 9$ GeV/c and $2 - 8$ GeV/c. The fit is extrapolated to the transverse momentum region above 15 GeV/c and the expected number of like-sign dimuon events is calculated from the fit extrapolation. It is assumed that these muons represent $W(\rightarrow \mu\nu) + X(jet \rightarrow \mu)$ background in this analysis. The number of events with dimuons from $Z + X$ background processes is estimated

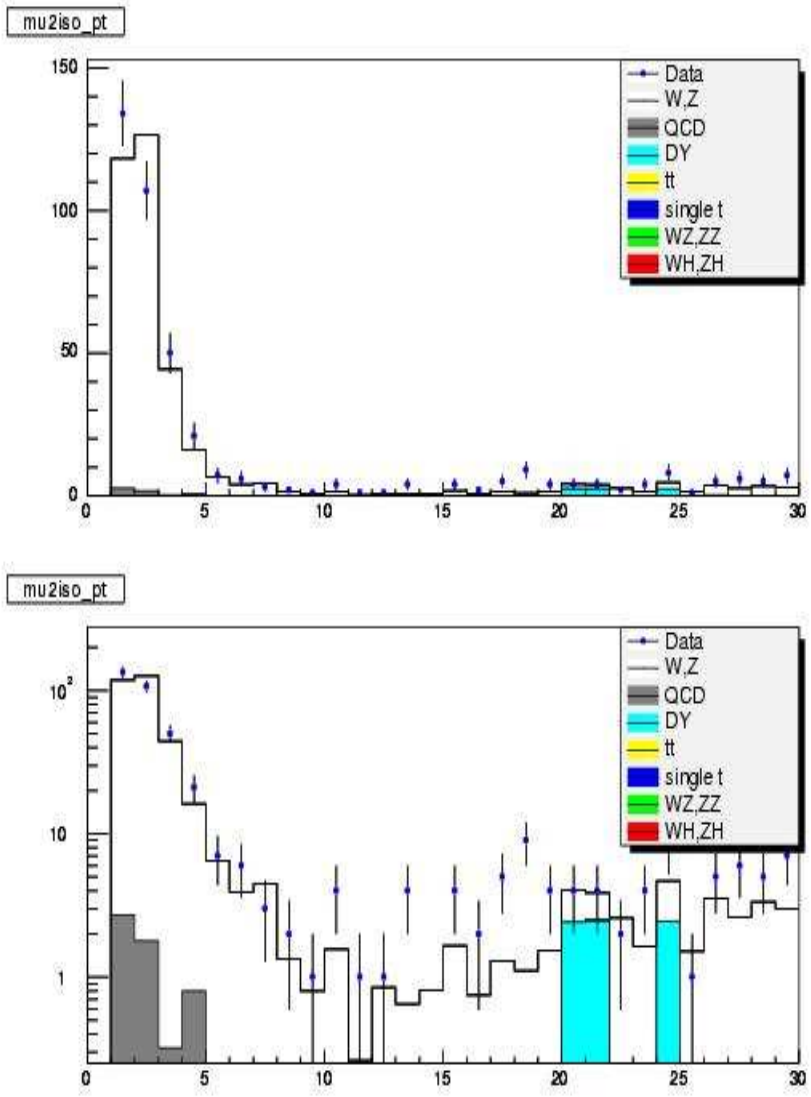

Figure 5.12: The transverse momentum spectrum of the second muon in the event. This muon is most of the time inside a jet. The lower plot is the same plot as the upper one, except that the y-axis is in a logarithmic scale. Both plots are courtesy of Peter Tamburello.

separately.

Several inputs are required to interpret the outcome of the previous fit as the contribution of like-sign dimuon events from $W(\rightarrow \mu\nu) + X(\rightarrow \mu)$ processes to the total background in this analysis. The following scaling factors are very conservative; in favor of larger expectation rates.

- The integrated luminosity of the $W(\rightarrow \mu\nu)$ inclusive sample is 150 pb^{-1}. The scaling factor on the size of the data sample is:

$$f_1 = \frac{\int \mathcal{L}(H^{++}\ analysis)}{\int \mathcal{L}(W\rightarrow\mu\ analysis)} = \frac{113\ pb^{-1}}{150\ pb^{-1}} = 0.75$$

- The scaling factor on trigger efficiency for dimuon events. The ratio of dimuon and single muon trigger efficiencies.

$$f_2 = \frac{\epsilon(H^{++},\ dimuon\ trigger)}{\epsilon(W\rightarrow\mu,\ single\ muon\ triggers)} = 1.5$$

- The scaling factor on dimuon event selection efficiencies. The second muon selection criteria are identical in both cases, e.g. isolation requirement.

$$f_3 = \frac{\epsilon(H^{++}\rightarrow\mu\mu)}{\epsilon(W+X\rightarrow\mu\mu)} = 1.5$$

- The expected number of events above $p_{\mathrm{T}} > 15$ GeV/c in the entire $W + X$ sample is $r = 0.007$. Finally, the expected contribution from the $W + X$ processes to the same-charged dimuon background in this analysis is

$$r_{tot} = r \cdot f_1 \cdot f_2 \cdot f_3 = 0.007 \cdot 0.75 \cdot 1.5 \cdot 1.5 = 0.012 \text{ events.}$$

The expected number of events is consistent with the Monte Carlo prediction derived from the $W + X \rightarrow \mu\mu$ background, next subsection gives details of this calculation.

The systematic error due to the fit was included. It comes from the extrapolation into the transverse momentum region above 15 GeV/c. The final expectation rate from $W + X \rightarrow \mu\mu$ background can be estimated as:

$$rate\ (W + X \rightarrow \mu\mu) = 0.012 \pm 0.004\ (stat.)\ ^{+0.16}_{-0.012}\ (sys.) \qquad (5.7)$$

The conclusion is that the contribution from W+jets background to the total background in the analysis is rather small and as such can be neglected.

W+jets background estimated from Monte Carlo

Properties of W+jets and Z+jets samples considered in this analysis are summarized in Table 5.3. The number of events passing the last cut before and after normalization to the luminosity of the data sample is given in the third, fourth column, respectively.

The W+jets sample has been analyzed. The results is given in Table 5.3. Only 5 events pass the preselection cut (S1). They are all removed by the isolation cut (S2). While the muon from the W is isolated, the other muon is inside a jet. This is why the second muon does not pass the isolation criterion.

The W+jets background is also estimated from the dimuon data set. With looser cuts, one can see a clear Jacobian peak from muons that originated from W decays. However, the background from the Z decays in this dimuon sample is overwhelming.

sample	# of events	last cut	normalized to luminosity	σ	generator
Z (incl.)	1 fb^{-1}	4 events	0.31 events	252 pb	Pythia
Z+1jet	150k	2 events	0.10 events	54 pb	Alpgen
Z+2jets	188k	7 events	0.06 events	44.5 pb	Alpgen
$Zb\bar{b}$	97k	87 events	0.03 events	0.35 pb	Alpgen
W+1jet	115k	0 events	0.00 events	758 pb	Alpgen
W+jets (incl.)	617k	0 events	0.00 events	1.9 nb	Pythia
$Wb\bar{b}$	33k	47 events	0.03 events	2.3 pb	Alpgen

Table 5.3: Summary of W+jet(s) and Z+jet(s) Monte Carlo samples studied in this analysis.

The following alternative way to estimate contribution from the W+jet background using Monte Carlo is investigated:

- Require an isolated muon with $p_{\mathrm{T}} > 15$ GeV/c in every event considered. It is a muon that originates from the W decay.
- Examine the transverse momentum distribution of the sub-leading muon, i.e. p_{T} spectrum of a muon inside a jet. For this muon, the p_{T} requirement has been lowered down to 8 GeV/c in order to gain more statistics. This muon is very likely not isolated.

Table 5.4 gives (the first and second column) the number of events expected after the following selection is made:

- event has at least one isolated muon with $p_{\mathrm{T}} > 15$ GeV/c

- there must be another muon with $p_{\mathrm{T}} > 8$ GeV/c (first column) or $p_{\mathrm{T}} > 15$ GeV/c (second column)

The last column gives number of expected events normalized to the luminosity of the data sample.

sample	events	$p_{\mathrm{T}} > 8$ GeV/c	$p_{\mathrm{T}} > 15$ GeV/c	normalized to lum.
W+1jet sample	115k	42 events	8 events	5.96 events
W+jets sample	617k	70 events	17 events	5.95 events

Table 5.4: Number of expected events from W+jet(s) Monte Carlo sample. The selection criteria is described in the text.

Results for these two samples are consistent with each other. This can be inferred from the number of expected events normalized to the luminosity (last column). In other words, these two samples can be combined.

The plot of sub-leading muon p_{T} is shown in Figure 5.13. The sub-leading muon is required to be isolated. At the same time, the isolation/p_{T} requirement on the muon coming from the W decay is dropped. The total number of events is then given in Table 5.5.

sample	events	$p_{\mathrm{T}} > 8$ GeV/c	$p_{\mathrm{T}} > 15$ GeV/c
W + 1 jet	115k	8 events	3 events
W + jets	617k	6 events	1 event

Table 5.5: Number of expected events from W+jet(s) Monte Carlo sample. The sub-leading muon is required to be isolated, the leading muon (muon from the W decay) is not required to be isolated.

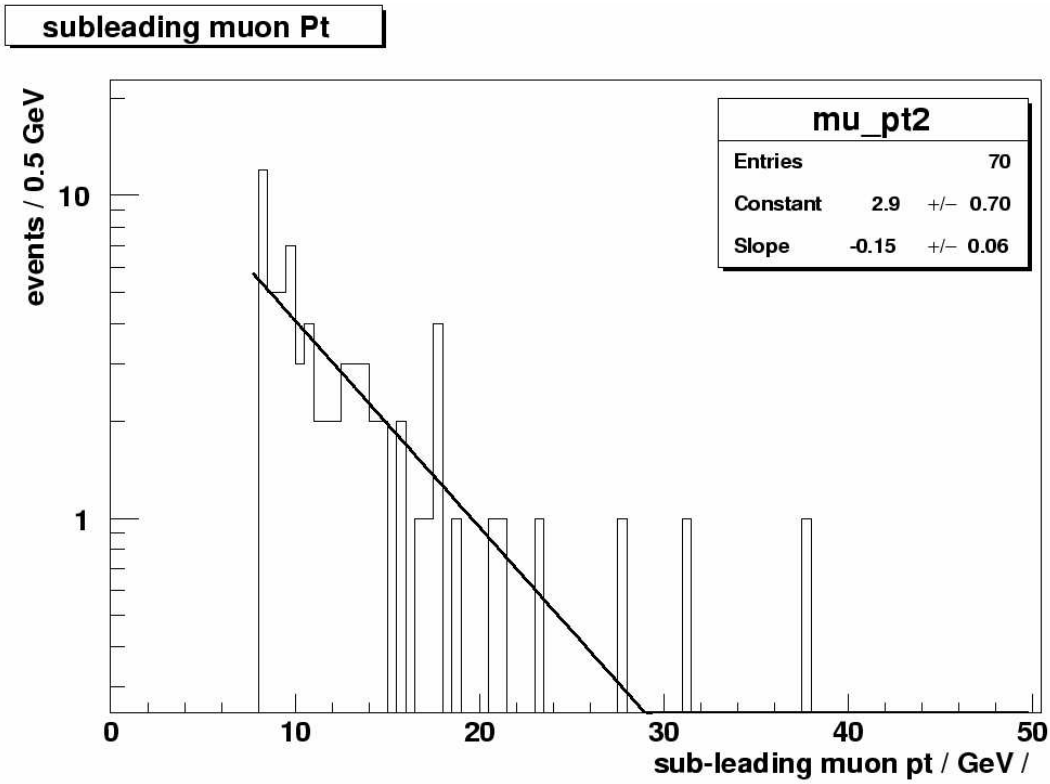

Figure 5.13: Sub-leading muon transverse momentum. This muon comes most likely from a jet.

The statistics is reduced significantly. The total expected number of events from these two samples, after they are combined, is 1.8 events. The acolinearity (S3) and like-sign (S4) cuts are not applied yet. The isolation/p_{T} requirement on the muon that comes from the W decay has been lowered, which is the reason why the rate is somewhat higher. It is safe to assume that the like-sign cut lowers the total number of expected events by one half. To conclude, the dimuon like-sign background from W+jets sample is much less than one event. To give a more precise estimation, at least a million of W+jet events needs to be generated.

A large W+jets inclusive Monte Carlo sample with at least two muons per event, both with true $p_{\mathrm{T}} > 8$ GeV/c, was generated with PYTHIA. This selection has been performed with the `d0mess` program. The `d0mess` package allows to pick events with two muons in a certain p_{T} range directly on the generator level. That boosts efficiency of the entire simulation process greatly. The total event count of the generated sample is $26,420$ events. The production cross section corresponding to this sample is (446 ± 53) fb, the corresponding luminosity is then (59 ± 9) fb^{-1}. The correction for the next-to-leading order corrections has been applied.

The cut flow table for this background is given in Table 5.6. The total number of events after the last cut is:

$$r\ (W + X \to \mu\mu) = 0.013 \pm 0.002\ (stat.) \tag{5.8}$$

That is in a good agreement with what has been calculated using the $W \to \mu\nu$ inclusive data sample, Equation 5.7.

selection	no. of events expected
preselection (S1)	0.448
isolation (S2)	0.104
acolinearity (S3)	0.041
same-charge (S4)	0.013

Table 5.6: Number of W+jets events normalized to the luminosity of the data sample after each cut in this analysis.

Chapter 6

Reconstruction efficiencies

All efficiencies are determined with the $Z \rightarrow \mu^+\mu^-$ data sample, and the same methods are applied to Monte Carlo samples. Only statistical uncertainties on the efficiencies are taken into account.

6.1 Tracking efficiency

The tracking efficiency is determined using dimuon events with one "tight" muon [96] and one "loose" muon triggered through `2MU_A_L2M0`.

A tight muon is defined by requiring that all of the loose criteria (Section 4.3) are fulfilled and, in addition, that the fit to a muon track converges. All quality definitions are inclusive, i.e. all tight muons are contained in the loose sample.

The track reconstruction efficiency depends on several aspects discussed in detail further in the text.

6.1.1 Combination of tracker and toroid measurements

The invariant mass of the two muons is required to lie in the range $60 < M_{\mu\mu} < 120$ GeV/c^2. The invariant mass $M_{\mu\mu}$ is determined using the momentum measured in the DØ tracking system (SMT and CFT) for the tight muon, and the toroid system for the loose muon.

A tight muon is always required to have a matched global track. The tracking efficiency is then determined from the ratio of the number of events where the loose muon has a matched track to the total number of events in the mass window.

The requirement on number of hits measured with SMT and CFT is applied, as it was stipulated in Section 4.

The tracking efficiencies for data and Monte Carlo (MC) are determined as follows (all uncertainties are statistical only):

- for $p_{\mathrm{T}} > 15$ GeV/c, based on the toroids (loose muon):

$$\epsilon_{\mathrm{data}}^{\mathrm{track}} = (77.8 \pm 0.6)\% \tag{6.1}$$

$$\epsilon_{\mathrm{MC}}^{\mathrm{track}} = (85.2 \pm 1.1)\% \tag{6.2}$$

- for $p_{\mathrm{T}} > 30$ GeV/c, based on the toroids (loose muon):

$$\epsilon_{\mathrm{data}}^{\mathrm{track}} = (78.2 \pm 0.8)\% \tag{6.3}$$

$$\epsilon_{\mathrm{MC}}^{\mathrm{track}} = (86.3 \pm 1.5)\% \tag{6.4}$$

The dependence of track reconstruction efficiency on pseudorapidity η and azimuth angle φ of the muon is shown in Figures 6.2 for data and Monte

Carlo. There is a clear drop of the track reconstruction efficiency in a region $2. < \varphi < \pi$ which is caused by CFT problems that extend over several runs. This has to be investigated further. Figure 6.3 shows the reconstructed invariant mass for all dimuons in the entire data sample with different requirements on transverse momentum of a loose muon (measured using a toroid system) and track matching requirement. The transverse momentum cut has been decided based on a local minimum in the transverse momentum distribution measured with the toroid system. It can be seen in Figure 6.1.

6.1.2 Using only muon information from toroids

The invariant mass of the two muons is required to lie inside the range $60 < M_{\mu\mu} < 120$ GeV/c^2. The invariant mass $M_{\mu\mu}$ is determined using momentum measured in the muon toroid system in order to obtain an unbiased estimate of tracking efficiency.

Unlike Section 6.1.1, the tight muon is required to have a matching central track. The tracking efficiency is then calculated as a ratio of the number of events where the loose muon has a matched track to the total number of events for which the invariant mass lies inside the mass window specified above.

The requirement on number of SMT and CFT hits associated to a track is applied, this requirement was described in Section 4.

The estimated values of tracking efficiencies in data are (errors are statistical only):

- for $p_{\mathrm{T}} > 15$ GeV/c, based on toroid system measurement (loose muon):

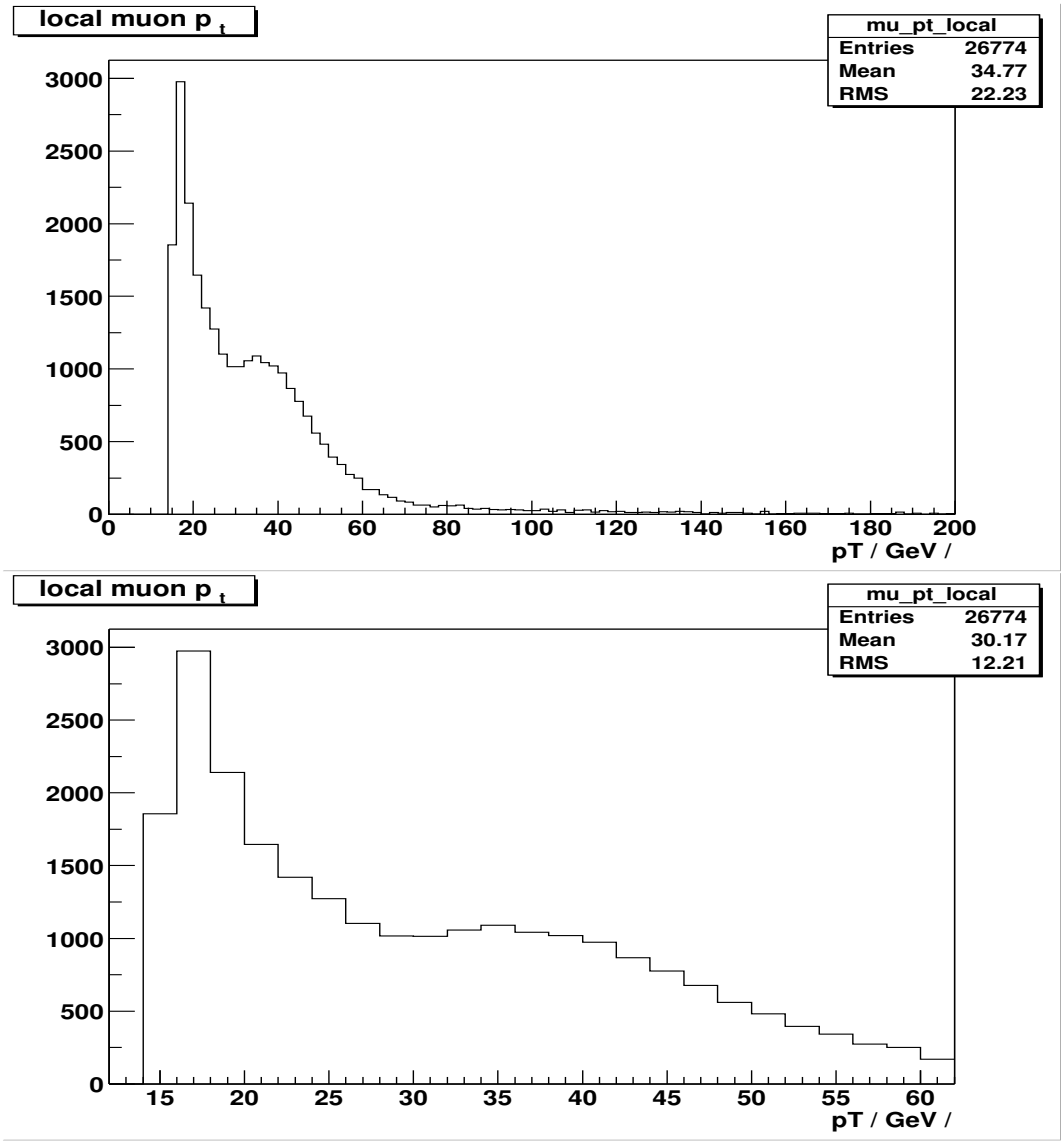

Figure 6.1: Transverse momentum distribution for muons based on toroid system. The possibility for using a harder cutoff to define the loose muon p_{T} is investigated. The applied value of $\sim$ 30 GeV/c is based on the dip observed at $\sim$ 30 GeV/c. The bottom plot is a zoom-in of the upper one.

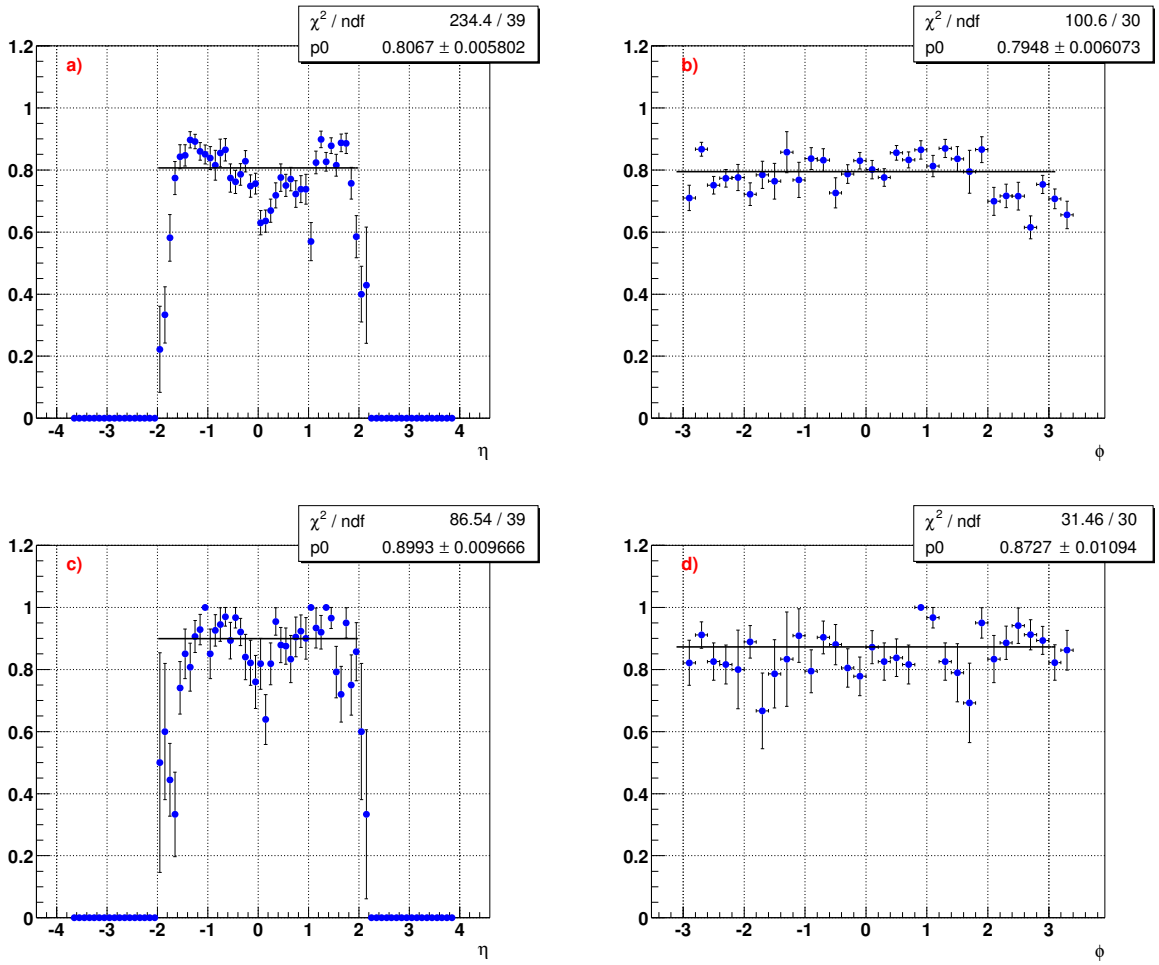

Figure 6.2: Tracking efficiency determined for data (a,b) and Monte Carlo (c,d) as a function of pseudorapidity η and azimuth angle φ of the muon. The distributions are based on combined global tracking and toroid information.

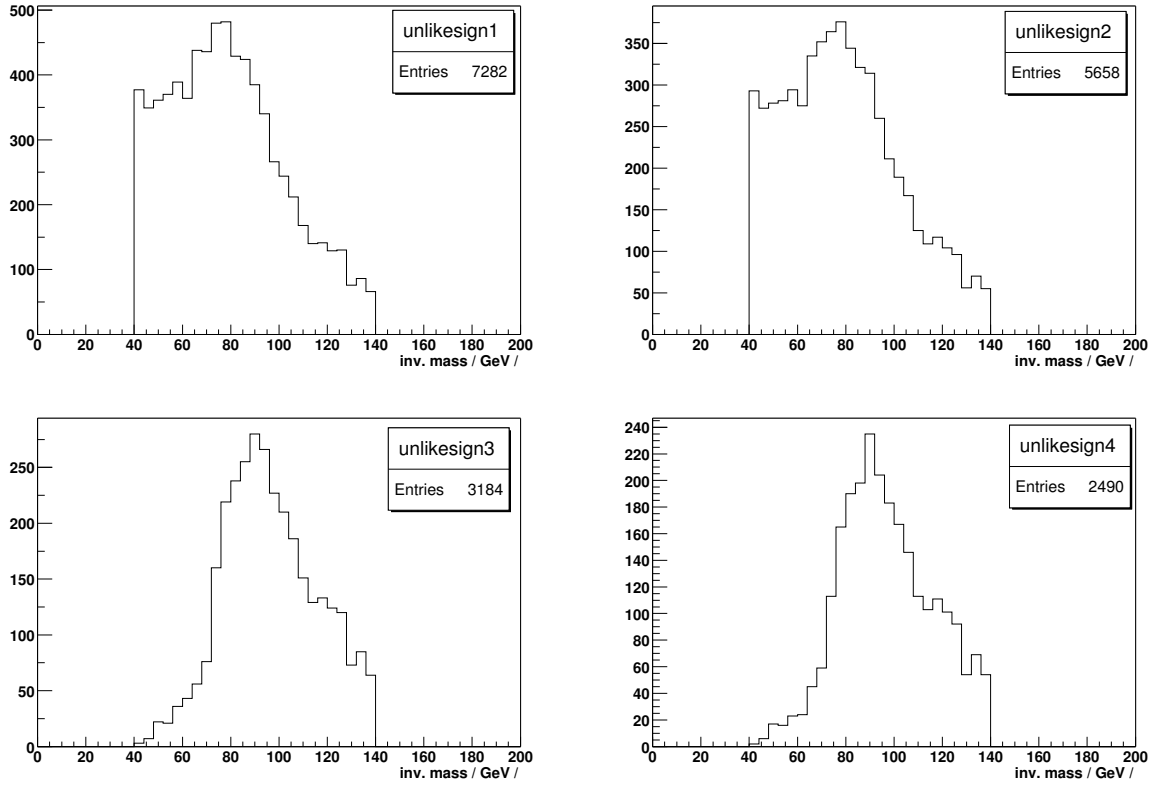

Figure 6.3: Invariant mass of dimuons calculated using combined information from central tracker (tight muon) and toroid system (loose muon), both for toroid muon $p_{\mathrm{T}} > 15$ GeV/c (top), and toroid muon $p_{\mathrm{T}} > 30$ GeV/c (bottom plot). A match of the muon to a central track is required on the left and this requirement is dropped on the right.

$$\epsilon_{\text{data}}^{\text{track}} = (76.8 \pm 0.6)\% \tag{6.5}$$

- for $p_{\text{T}} > 30$ GeV/c, based on toroid system measurement (loose muon):

$$\epsilon_{\text{data}}^{\text{track}} = (78.9 \pm 0.7)\% \tag{6.6}$$

The dependence of tracking efficiency on the pseudorapidity η and azimuth angle φ of the muon is shown in Figure 6.4 and 6.5 for data and Monte Carlo. There is a clear drop of the track reconstruction efficiency in the CFT super-sector 3, i.e. in a region $2. < \varphi < \pi$. This problem requires a further investigation. Figure 6.6 shows the reconstructed invariant mass for events with a track matched to a toroid muon and all selected dimuons in the sample for a p_{T} cutoff placed on transverse momentum at 15 GeV/c and 30 GeV/c.

The matching efficiency is part of the track reconstruction efficiency, and it is estimated to be about 99%.

The purity of the sample can be best demonstrated on a difference of scintillator times in A layers both for tight and loose muons. This difference is shown in Figure 6.7, in both upper plots. The same variable is shown for tight and loose muons traversing layers BC in the two bottom plots.

6.2 Efficiency to reconstruct loose muons

The efficiency to reconstruct a loose muon can be determined using dimuon events where one of the two muons is required to be a tight muon matched to a 'central' track measured in the tracking detectors (SMT and CFT) and

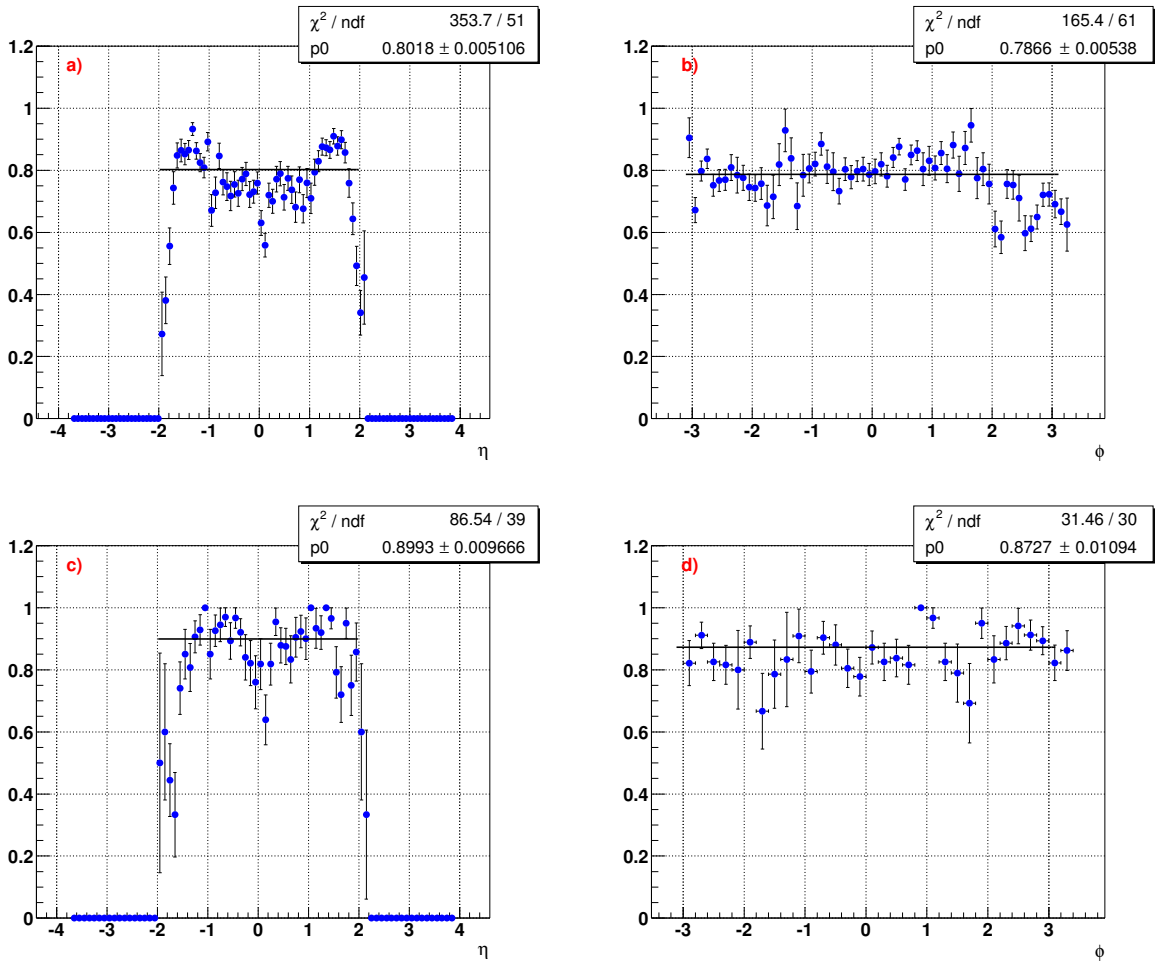

Figure 6.4: Tracking efficiency determined for data (a,b) and Monte Carlo (c,d) as a function of pseudorapidity η and azimuth angle φ of the muon. Muon information is based on toroid measurement only for loose muons with $p_{\mathrm{T}} > 15$ GeV/c.

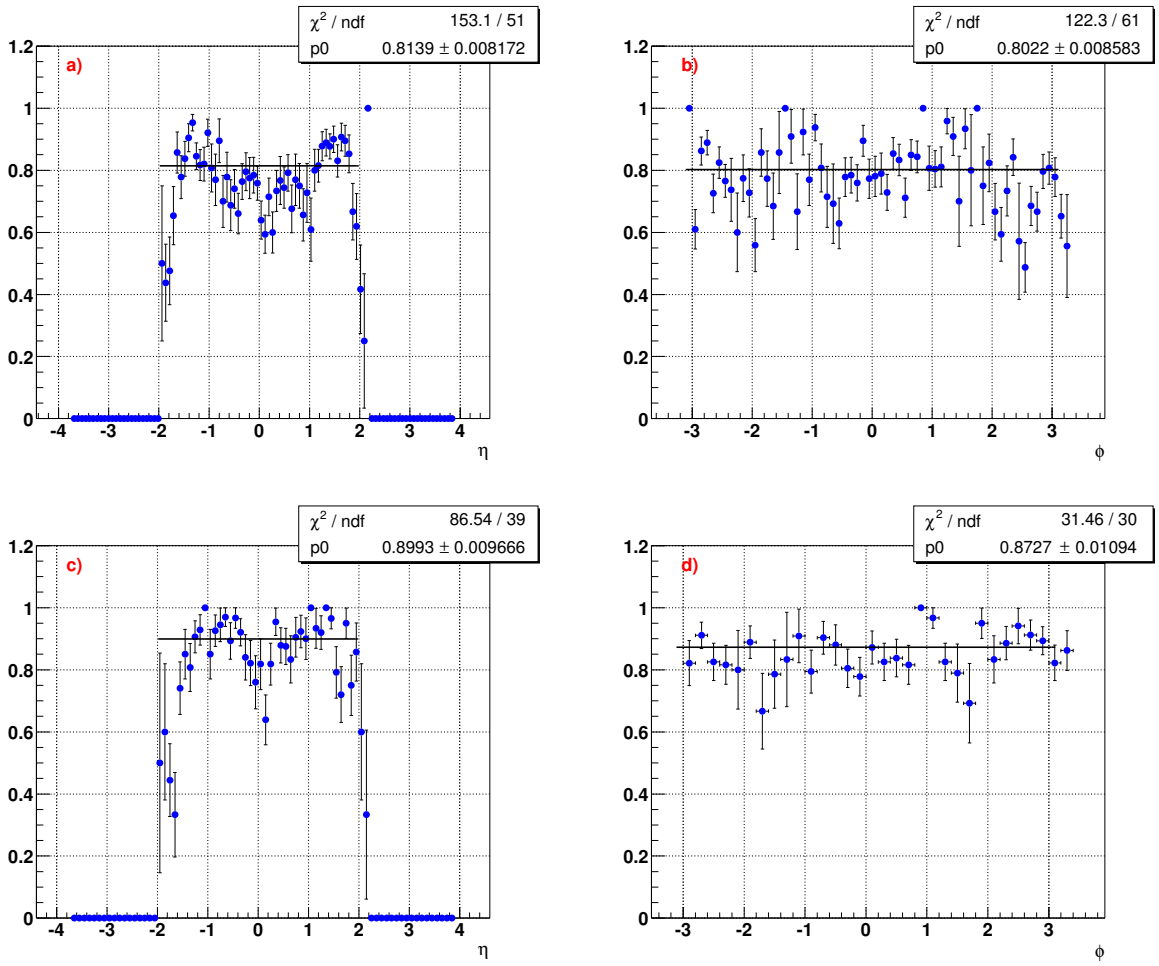

Figure 6.5: Tracking efficiency determined for data (a,b) and Monte Carlo (c,d) as a function of pseudorapidity η and azimuth angle φ of the muon. Muon information is based on toroid measurement only for loose muons with $p_{\mathrm{T}} > 30$ GeV/c)

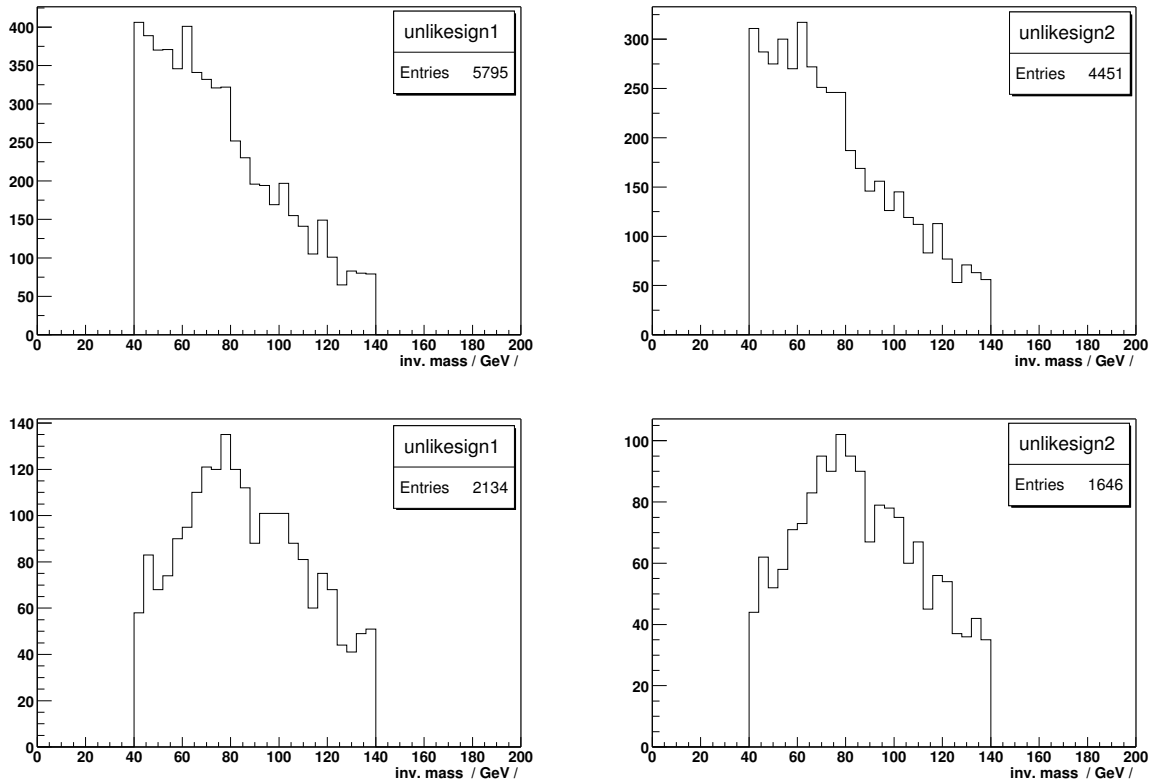

Figure 6.6: Invariant mass calculated from the toroid system muon information, with muon $p_{\mathrm{T}} > 15$ GeV/c (top), and muon $p_{\mathrm{T}} > 30$ GeV/c (bottom). There is no track matching requirement on the left and a track matched to a loose muon is required on the right.

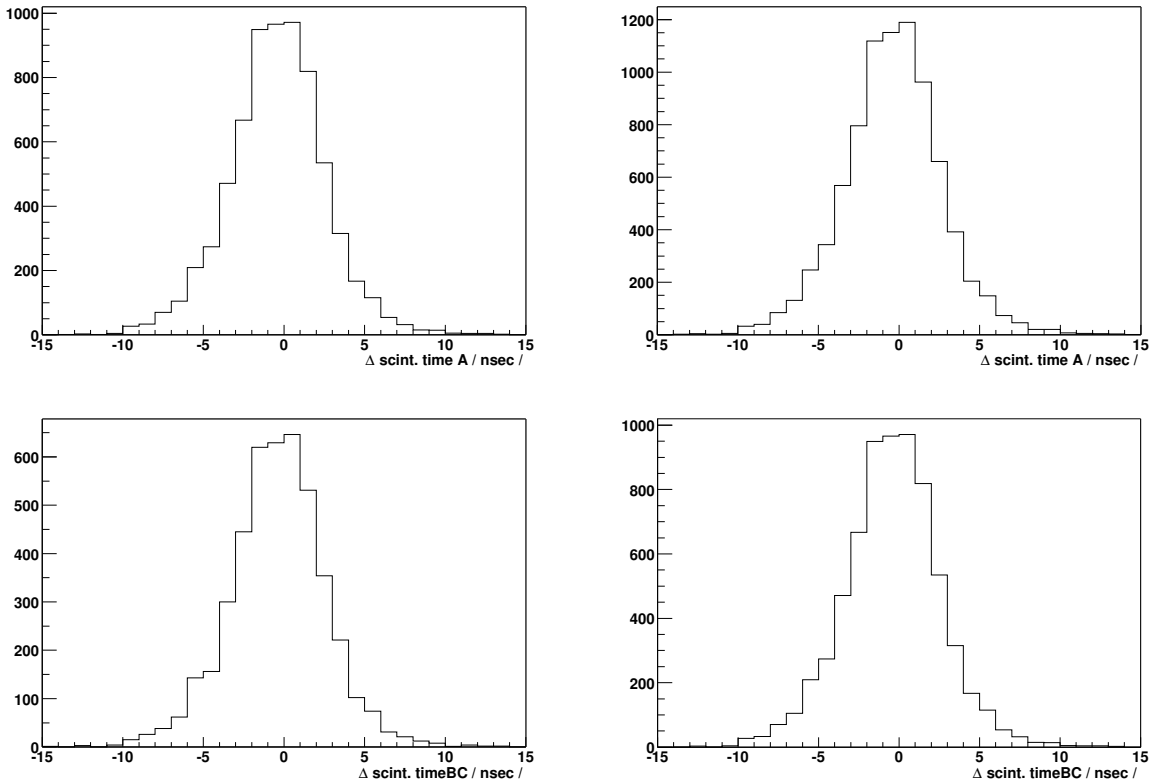

Figure 6.7: Difference of scintillator times for both types of (tight and loose) muons in A layers of the muon system (top), and BC layers (bottom) for muons with matched tracks (left) and all dimuons (right), the requirement of a track matched to a loose muon is dropped here.

the other muon is required to be a central track within the kinematic and geometric acceptance. There is no trigger requirement.

The kinematic and geometric acceptance is defined by requiring at least two muons with a minimum transverse momentum p_{T} of 15 GeV/c within a pseudorapidity range $|\eta| < 2.0$, but not within the hole in the muon system at the bottom of the detector.

The 'hole' at the bottom of the muon system is excluded, i.e., all tracks with

- $|\eta| < 1.25$, and
- $\varphi >$ -2.0 and $\varphi <$ -1.1

are removed from the consideration.

The invariant mass of the two muons calculated using central tracks must be in the range $60 < M_{\mu\mu} < 120$ GeV/c^2. The loose muon efficiency is determined as a ratio of events where the second muon consists of a central track matching a loose muon to the total number of events. Only central tracks with a minimum ionizing particle (MIP) trace in the calorimeter are considered in this section. Such an energy deposit in the calorimeter is of the order of a few GeV.

The efficiency to reconstruct a loose muon yields

$$\begin{aligned} \epsilon_{\mathrm{data}}^{\mathrm{loose}} &= (97.0 \pm 0.2)\% \\ \epsilon_{\mathrm{MC}}^{\mathrm{loose}} &= 100\% \end{aligned} \tag{6.7}$$

Figure 6.8 shows the comparison of invariant mass distribution obtained

for all dimuons to the distribution calculated with those dimuons for which the second muon is a loose muon matched to a central track.

6.3 Isolation efficiency

The efficiency of the isolation cut is determined by requiring that both muons are isolated, as it is defined in Section 4.3. By counting the number of $Z \to \mu\mu$ events in this sample that fall into a mass window $60 < M_{\mu\mu} < 120$ GeV/c^2, the following per event efficiencies are obtained

$$\begin{aligned} \epsilon_{\rm data}^{\text{two isolated } \mu'\text{s}} &= \epsilon_{\rm data}^{\text{isolation}} = (82.5 \pm 0.4)\% \\ \epsilon_{\rm MC}^{\text{two isolated } \mu'\text{s}} &= \epsilon_{\rm MC}^{\text{isolation}} = (83.1 \pm 0.1)\%. \end{aligned} \tag{6.8}$$

Both invariant mass distributions are shown in Figure 6.9. The isolation efficiency for having one muon isolated only is

$$\begin{aligned} \epsilon^{\text{one isolated } \mu} &= \sqrt{\epsilon^{\text{ two isolated } \mu'\text{s}}} \\ \epsilon_{\rm data}^{\text{one isolated } \mu} &= (90.8 \pm 0.4)\% \\ \epsilon_{\rm MC}^{\text{one isolated } \mu} &= (91.2 \pm 0.1)\%, \end{aligned} \tag{6.9}$$

and finally, the efficiency to have at least one muon isolated is

$$\begin{aligned} \epsilon^{\text{at least one isolated } \mu} &= 2\ \epsilon^{\text{one isolated } \mu} - (\epsilon^{\text{one isolated } \mu})^2 \\ \epsilon_{\rm data}^{\text{at least one isolated } \mu} &= (99.2 \pm 0.5)\% \\ \epsilon_{\rm MC}^{\text{at least one isolated } \mu} &= (99.2 \pm 0.1)\%. \end{aligned} \tag{6.10}$$

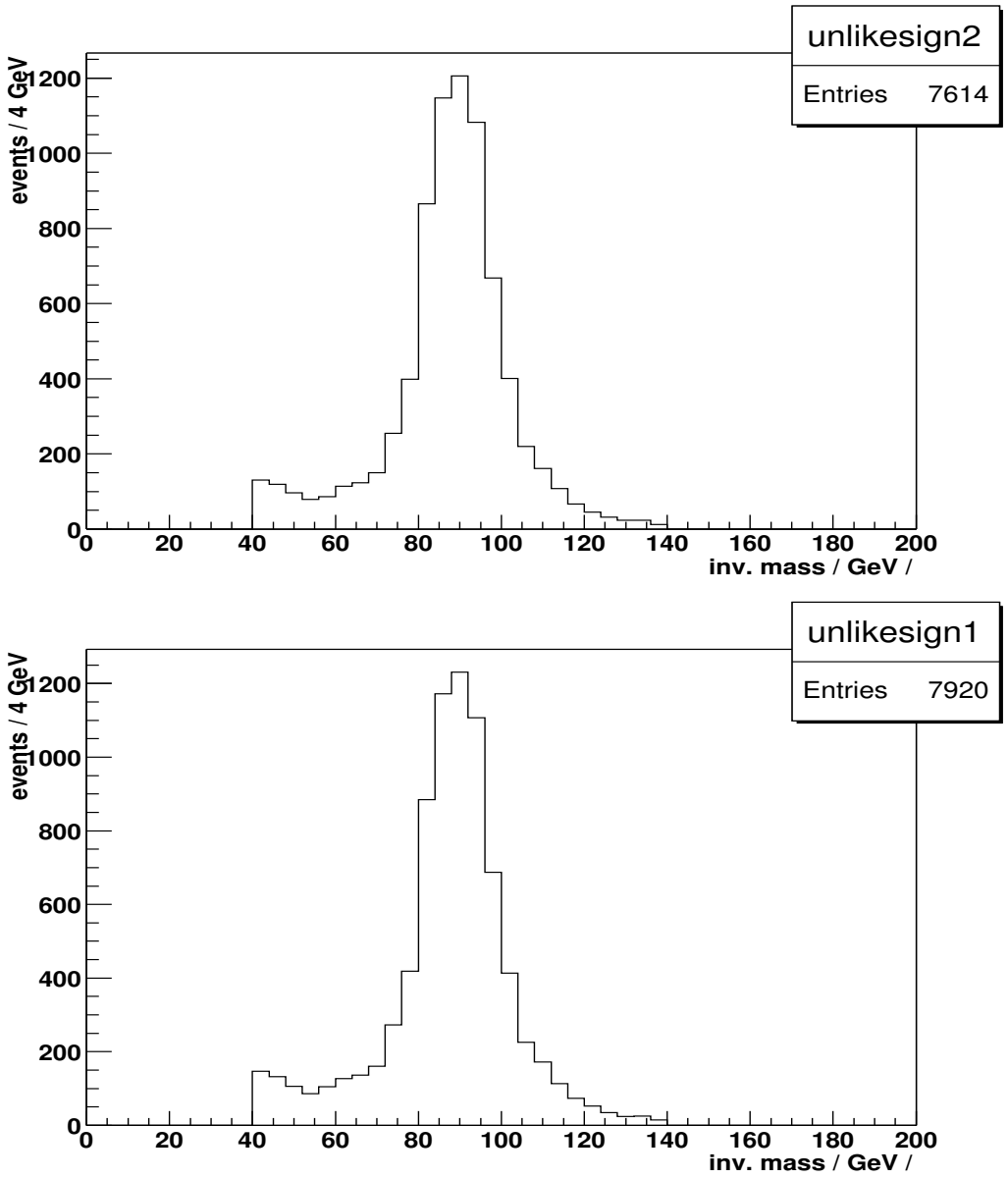

Figure 6.8: Invariant mass calculated for tracks matched to a local muon (top) and all dimuon events (bottom). The mass window is defined as $60 < M_{\mu\mu} < 120$ GeV/c^2.

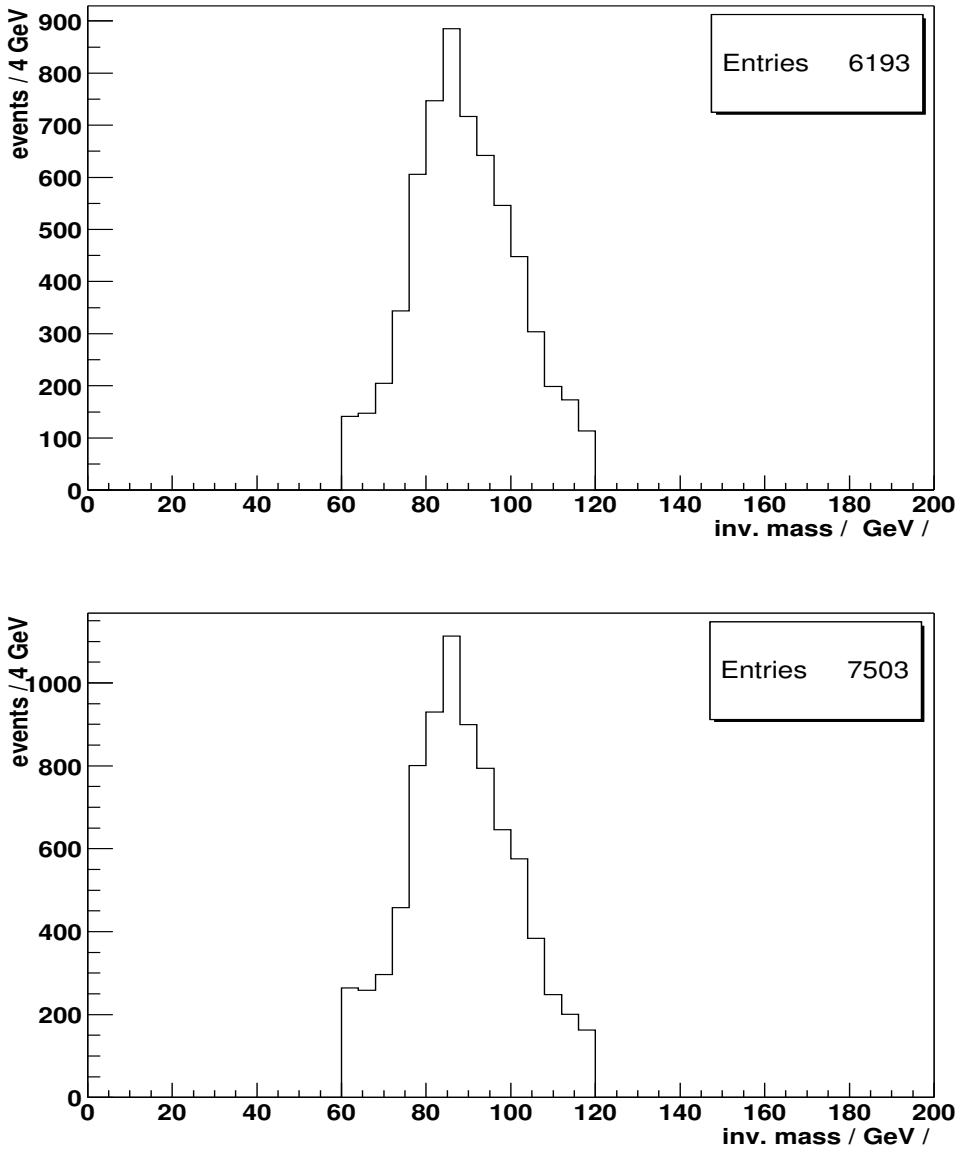

Figure 6.9: Invariant mass calculated for events where both muons are isolated (top) and all events with two muons (bottom).

If one extends the mass window to the entire invariant mass region (invariant mass must be above 30 GeV/c^2), the isolation cut efficiency is

$$\epsilon_{\text{data}}^{\text{isolation}} = (77.8 \pm 0.6)\%. \tag{6.11}$$

The explanation for this discrepancy is the physics content of this sample. The majority of events are $Z \rightarrow \mu\mu$ events, but the data also contains $b\bar{b}$ events from semi-leptonic b-quark decays. That is the reason why this sample is not a pure sample of isolated muons from $Z \rightarrow \mu\mu$, it contains a significant fraction of non-isolated muons, i.e. muons inside jets. About 415 $b\bar{b}$ events are expected in this data sample. The non-isolated muons are the cause of a discrepancy between data and Monte Carlo which amounts to about 5%. As soon as the mass window around the Z mass peak is defined, the discrepancy is all gone. The isolation efficiency for non-isolated muons can be estimated from a like-sign dimuon sample because majority of the like-sign events after preselection cut are $b\bar{b}$ events. The $b\bar{b}$ events are charge democratic, i.e. one quarter of all $b\bar{b}$ events (both b quarks branching into muons) are like-sign muon pairs. The isolation efficiency for non-isolated muons is

$$\epsilon_{\text{data}}^{\text{isolation}} = (5.0 \pm 2.2)\%. \tag{6.12}$$

It means that 5% of $b\bar{b}$ events might be mistakenly identified as a pair of isolated muons.

6.4 Trigger efficiency

The trigger efficiency was determined by selecting events with two loose muons with $p_{\mathrm{T}} > 15$ GeV/c, and by requiring that any EM trigger fires. In addition, runs for which the 2MU_A_L2M0 trigger was prescaled, i.e. the prescale factor obtained from Run Database [132] is different from one, are removed. The efficiency of the trigger 2MU_A_L2M0 to fire on $Z \to \mu\mu$ like events is calculated from the ratio of events

$$\epsilon^{\mathrm{trig}} = \frac{N(\mathtt{EM} \wedge \mathtt{2MU\_A\_L2M0})}{N(\mathtt{EM})} \tag{6.13}$$

and it is found to be $(76.5 \pm 1.6)\%$. The invariant mass of events that enter the trigger efficiency calculation must fall into the mass window defined as $60 < M_{\mu\mu} < 120$ GeV/c. This requirements improves purity of the sample. Figure 6.10 shows the invariant mass reconstructed when the dimuon trigger condition is required and with no trigger requirement.

The trigger efficiency should be estimated before and after the '$fast\_z$' trigger was removed, this change occured before the run 173351, since the dimuon trigger efficiency has significantly improved. New look up tables were encoded to the trigger firmware. The trigger efficiency before run 173351 was estimated to be

$$\epsilon^{\mathrm{trig}} = (71.5 \pm 2.2)\% \tag{6.14}$$

and it has improved to

$$\epsilon^{\mathrm{trig}} = (77.7 \pm 1.9)\% \tag{6.15}$$

by approximately 6%.

Whereas the data sample used to determine the trigger efficiency is dominated by $Z \to \mu\mu$ events (dimuon events), the trigger efficiency for the signal sample will be much higher since there are 3 muons reconstructed on average. Figure 6.11 shows the multiplicity of reconstructed muons in signal Monte Carlo sample. In 69% of analyzed signal events there are 3 muons reconstructed that pass our quality selection criteria.

For events with three and more muons, assuming that the di-muon permutations are not correlated, the trigger efficiency can be estimated as

$$\epsilon_{\text{signal}} = \epsilon^3 + 3\epsilon^2(1-\epsilon) + 3\epsilon(1-\epsilon)^2 \tag{6.16}$$

to be $\epsilon^{\text{trig}} = (98.4 \pm 2.2)\%$. The signal trigger efficiency is in fact lower because the dimuon permutations, for which we have calculated the trigger efficiency, are never uncorrelated. In alternative language, if one of the muons cannot be triggered on (e.g. out of fiducial volume of the detector), at least two other dimuon permutations that include the same muon cannot be triggered on either.

In order to get a more realistic estimate on signal trigger efficiency, the trigger simulation package `d0trigsim` [133] is run on signal H^{++} Monte Carlo events. The muon trigger efficiencies at Level 1 in the trigger simulation are adjusted so that there is a good agreement between the data and Monte Carlo trigger efficiencies for $Z \to \mu^+\mu^-$ events. At Level 1 the `2MU_A_L2M0` trigger is based on scintillator hits only, for details see Section 4.1. This is why by giving each hit certain probability to be missed during the detector trigger response simulation changes the trigger efficiency at this level, but

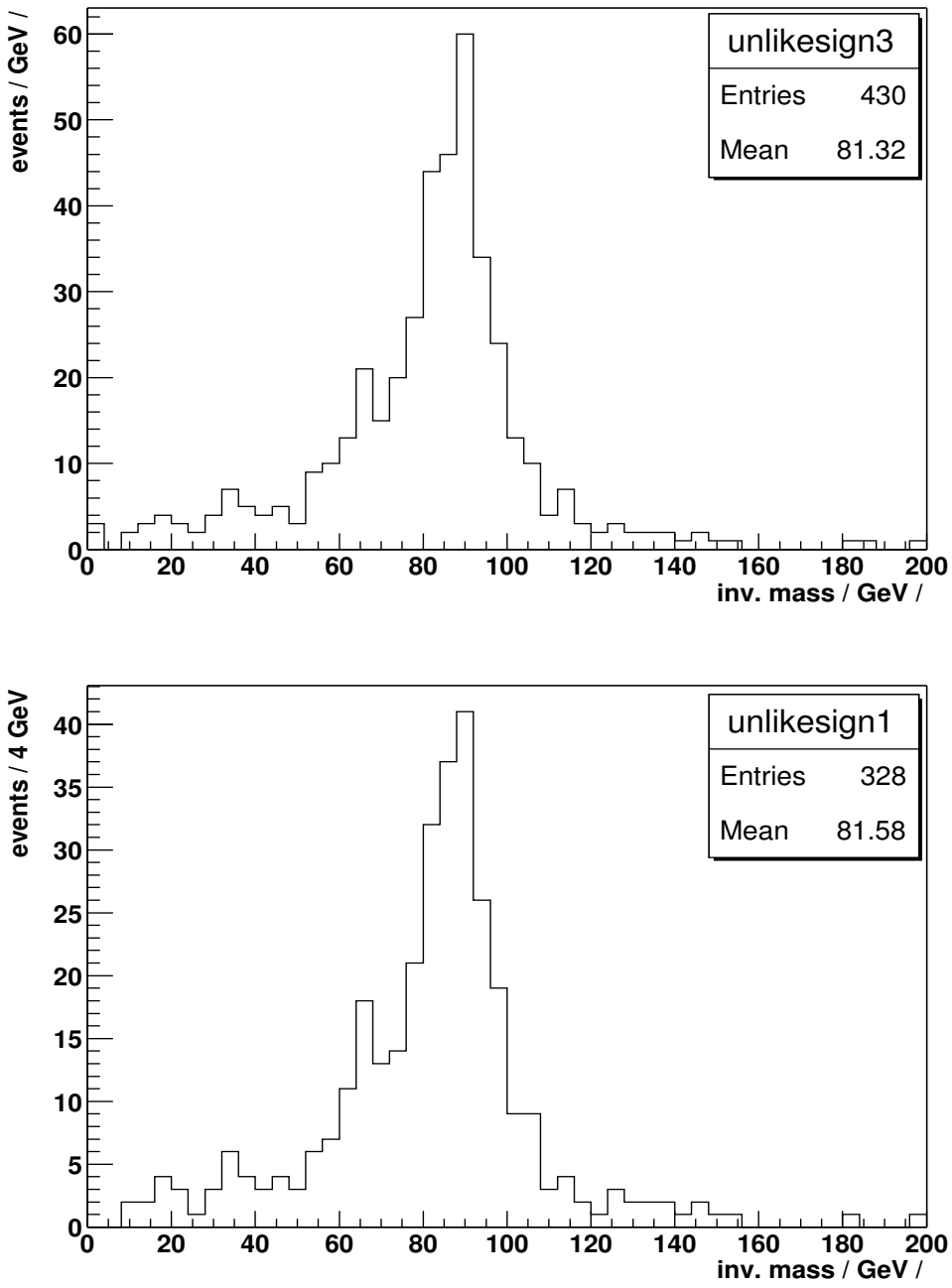

Figure 6.10: Invariant mass calculated for events with and without 2MU_A_L2M0 trigger requirement.

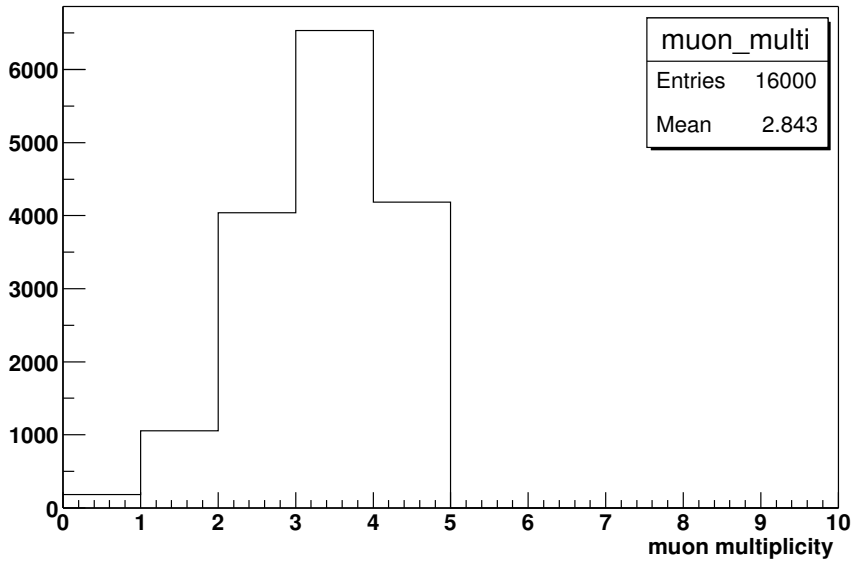

Figure 6.11: Reconstructed muon multiplicity in signal H^{++} Monte Carlo

all other correlations in later stages are automatically preserved. This is in fact the way the existing `d0trigsim` has been modified. The probability for a scintillator hit to be missed at Level 1 has been calculated from the difference in trigger efficiency measured in Monte Carlo and the data. It ranges between $5-10\%$ based on the type of Level 1 trigger (single muon or dimuon respectively) which is part of the `2MU_A_L2M0` trigger definition.

After encoding the adjustment described above, the signal trigger efficiency is then determined to be

$$\epsilon^{\text{trig}}_{\text{signal}} = (91.6 \pm 0.2)\%. \tag{6.17}$$

6.5 Kinematic and geometric acceptance

The kinematic and geometric acceptance is determined from the Monte Carlo simulation by requiring the two muons to have a minimum transverse momentum p_{T}^{μ} of 15 GeV/c, to be within a pseudorapidity range $|\eta| < 2.0$ and by removing the hole in the muon system in the bottom of the detector. The kinematic and geometric acceptance for the $\mathrm{Z} \to \mu\mu$ events is found to be

$$\epsilon_{\mathrm{Z}\to\mu\mu}^{\mathrm{acc}} = (42 \pm 1)\%. \tag{6.18}$$

The kinematical and geometrical acceptance for signal events is

$$\epsilon_{\mathrm{signal}}^{\mathrm{acc}} = (75 \pm 1)\%. \tag{6.19}$$

The reconstruction efficiency for $Z \to \mu\mu$ events is given by

$$\epsilon_{\mathrm{Z}} = \epsilon^{\mathrm{acc}} \epsilon^{trig} \epsilon^{iso} \left(\epsilon^{track} \epsilon^{loose} \epsilon^{match} \right)^2 . \tag{6.20}$$

By inserting all measured reconstruction efficiencies in this section to Equation 6.20, we obtain

$$\epsilon_z = (13.8 \pm 0.7)\%. \tag{6.21}$$

All uncertainties on the efficiency measurements are statistical only.

The $\mathrm{Z} \to \mu\mu$ cross-section can be factorized as

$$\sigma_z = \frac{C_{DY} \times N_{\mathrm{Z}\to\mu\mu}}{\epsilon_z \ \times \ \int \mathcal{L}} \tag{6.22}$$

where $C_{DY} = 87.5\%$ is the fraction of $\mathrm{Z} \to \mu\mu$ events in the simulated Monte Carlo sample that includes Drell-Yan pairs in the final state. The

measured value of $Z \rightarrow \mu\mu$ cross-section is

$$BR \times \sigma_z = (252 \pm 22)\ pb. \tag{6.23}$$

The main contribution to the cross-section uncertainty comes from the error on luminosity. The luminosity uncertainty is 6.5% [89].

6.6 Cosmics

The dimuon sample was investigated for a presence of cosmic muon events. These events can be of eminent danger for search oriented analyses because they can successfully mimic the $Z \rightarrow \mu\mu$ events and they will contribute to the background that is hard to describe. Cosmic muons can have a very high transverse momentum, this is why their invariant mass can be also rather high. Due to their high p_T, a charge flip on one of the tracks matched to a local muon might occur and such an event is then considered to be a like-sign event. The charge flip happens more likely for high-p_T tracks because the curvature (q/p_T) is small and any effect due to spatial resolution or misalignment is going to increase probability for the track to flip a charge. The charge of a track is derived directly from the sign of a track curvature. This is why any contamination of data with cosmic muons has to be avoided.

The cosmic events are supposed to be removed on the level of preselection, see Section 4.2, by using a certified *MuoCandidate* code which provides a method allowing to turn on cuts on scintillator times measured both in A and BC layers:

$$-10\ nsec\ \leq\ t_A^{scint}\ \leq 10\ nsec \tag{6.24}$$

$$-15\ nsec\ \leq\ t_{BC}^{scint}\ \leq 10\ nsec. \tag{6.25}$$

Both distributions, t_A^{scint} and t_{BC}^{scint}, are shown in Figure 6.7. Most of the events pass the criteria listed above. However, as it was found, this cut does not always remove all cosmic muon events. There is no trigger requirement in the preselection. When analyzing this sample, 95 events were found to be fully consistent with cosmic events. They were separated from the rest of data and various studies are performed with them, mainly to understand how to remove any cosmic muon events from the data set. They are called cosmic muon candidate events further in the text. The cosmic muon candidates display the following features:

- they are back-to-back in φ and η, Figure 6.13 shows these distributions
- the z-displacement from the detector center is ≥ 0.5 cm
- muons have typically a balanced transverse momentum
- majority of these cosmic muon candidates are unlike-sign muon pairs, due to the CPT theorem.
- majority of them comes from the top of the detector (top left and right corner respectively, due to the geometrical acceptance of the muon system, see Section 6.2)
- one of the muons is loose, another one is tight

- all events pass the scintillator time cut, despite of the fact that there are 3 out of 4 possible time measurements available (loose muons can fail one of the conditions in Section 4.2, one scintillator time measurement can be missing)

The purity of the entire dimuon sample after the preselection cut can be quantified as

$$\epsilon_{cosm} = (98.4 \pm 0.6)\%. \tag{6.26}$$

Figure 6.13 shows the acolinearity of cosmic muon candidate events as well as the sum of both muon's η measurements ($\eta_1 + \eta_2$). Because they are all back-to-back, the following cut on the sum of their η can be placed to remove the remaining cosmic muons.

$$|\eta_1 + \eta_2| > 0.01 \tag{6.27}$$

This cut has a great discriminating power. The only potential danger of this cut is that besides the cosmic muon events it also removes a small fraction (less than 0.5%) of $Z \rightarrow \mu\mu$ like events. Most of the Z candidate events are back-to-back in either azimuth angle φ or pseudorapidity η, to be back-to-back in both variables at the same time happens really rarely due to the boost of the Z in one direction.

However, an analysis oriented on searches should be extremely cautious about using this kind of cut, or any similar cuts.

An alternative to a cut suggested above is to require the `2MU_A_L2M0` dimuon trigger. Figure 6.12 shows the reconstructed invariant mass with and without the `2MU_A_L2M0` trigger requirement fulfilled. This comparison

was made on the sample of events described above in detail, they are labeled as cosmic muon candidates. Majority of these events is rejected by using the dimuon trigger. Events that pass the dimuon trigger requirement are consistent with $Z \rightarrow \mu\mu$ events.

The purity of the entire dimuon sample when the dimuon trigger is required is then 100%. It means that after the dimuon trigger is required, on the top of the timing cuts applied to every dimuon event directly in the `MuoCandidate` code, no cosmic muon candidate is present in the data sample.

6.7 Time dependence of efficiencies

The dimuon sample described in Sections 4.1 and 4.2 has been ordered on a run-by-run and event-by-event basis and broken into 16 subsequent sub-samples with approximately 10k events each. Run ranges of every sub-sample are specified in Table 6.1.

The integrated luminosity of each sample, together with a track reconstruction, loose muon, isolation and trigger efficiencies are measured for each sample. The results are summarized in Table 6.2.

All efficiencies versus time are shown in Figure 6.14. The x-axis is label as time in arbitrary units, i.e. each point corresponds to a sub-sample defined above and thus to a certain period of data taking.

The time dependence of the final product, of the $Z \rightarrow \mu\mu$ cross section, is shown in Figure 6.15.

The time dependence of reconstruction efficiencies can be used for a precise understanding of the dimuon data set as well as a feed back for data reconstruction and detector teams as an important data quality monitoring

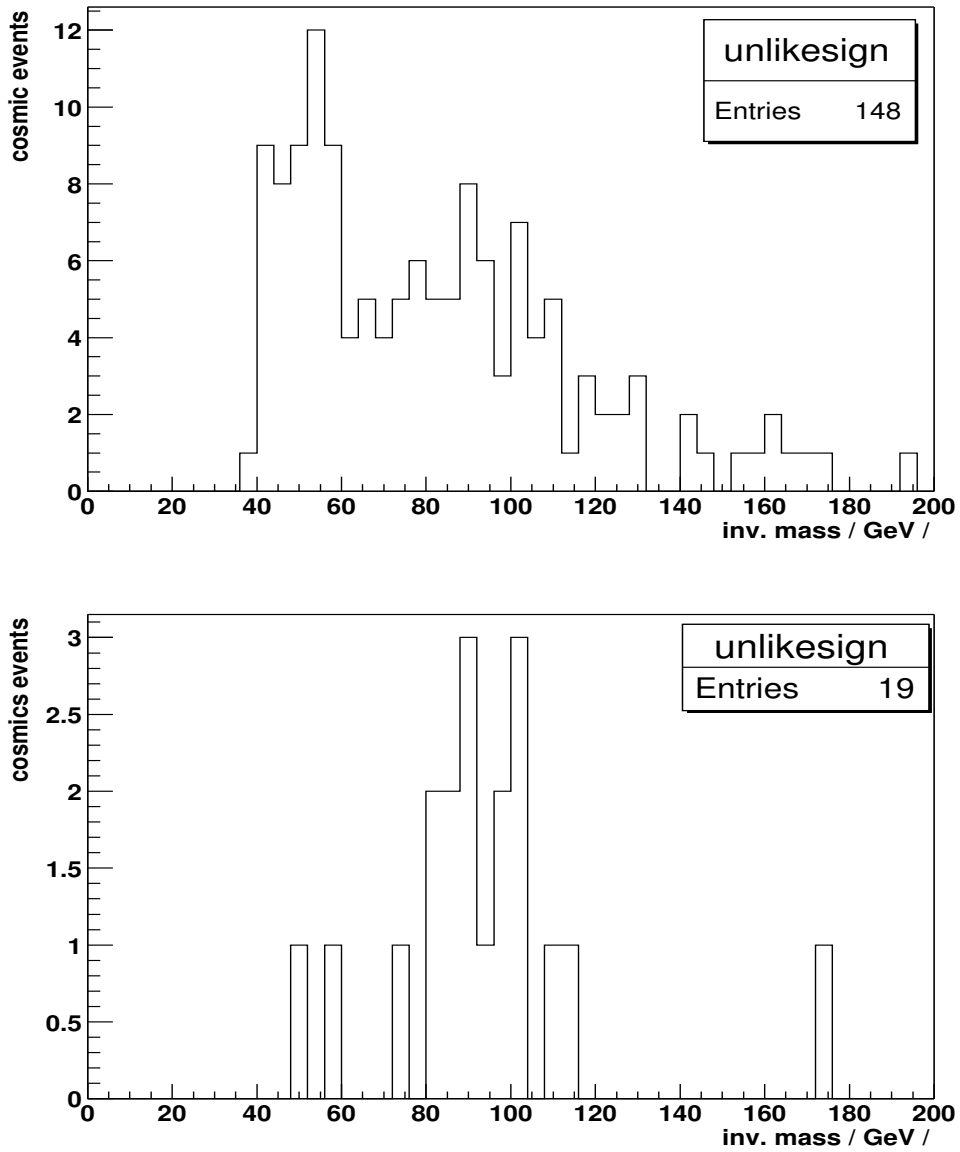

Figure 6.12: Invariant mass calculated for cosmics events selected out of the dimuon skim, the invariant mass with no trigger requirement (top), the `2MU_A_L2M0` trigger required (bottom).

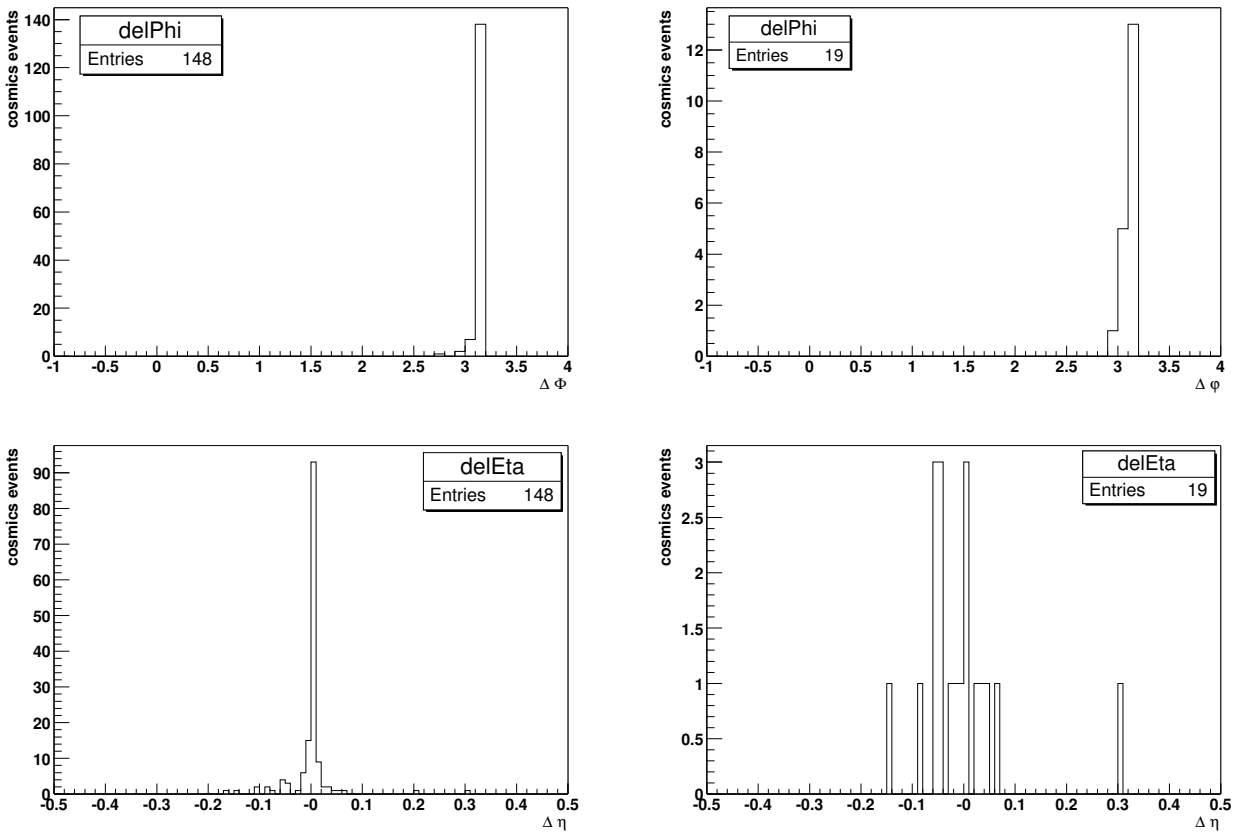

Figure 6.13: Cosmic candidate events: acolinearity distribution (top) and $(\eta_1^\mu + \eta_2^\mu)$ distribution (bottom) with (right) and without (left) the `2MU_A_L2M0` trigger requirement.

sample	first run	last run
1	151831	164041
2	164041	165775
3	165775	167012
4	167012	168389
5	168389	169794
6	169794	172482
7	172482	174305
8	174305	174801
9	174801	175517
10	175517	175870
11	175870	176474
12	176474	176677
13	176677	176970
14	176970	177277
15	177277	178119
16	178119	178310

Table 6.1: Run ranges for time-ordered sub-samples of the dimuon data set. All bad SMT, CFT, muon system and calorimeter runs are removed. Runs with the bad dimuon trigger and events that correspond to bad luminosity blocks are removed from the sample too.

sample #	track eff. (%)	trigger eff. (%)	isolation eff. (%)	loose eff. (%)	# of Z candidates	$\int \mathcal{L}$ (pb^{-1})	# events	good/bad luminosity blocks (%)
1	78.5	78.0	76.6	97.4	251	7.5	10,003	77.9
2	83.4	70.2	75.3	97.0	278	8.0	10,000	97.8
3	77.3	65.6	79.8	97.7	271	9.1	10,000	97.7
4	75.1	58.3	74.3	96.6	305	9.0	10,000	98.7
5	75.9	69.9	76.2	96.4	309	8.9	10,000	96.7
6	78.5	73.3	80.0	96.6	308	8.8	10,029	96.6
7	71.5	80.4	78.1	94.5	186	7.1	10,000	97.8
8	77.9	68.2	78.5	96.9	257	6.4	10,000	98.3
9	81.9	78.7	79.4	97.4	294	6.9	10,000	92.2
10	75.9	81.3	78.7	97.4	286	6.8	10,000	98.4
11	80.6	85.0	78.1	96.6	265	6.7	10,000	99.3
12	71.9	74.6	70.8	95.1	236	5.9	10,000	98.8
13	78.3	71.5	74.3	97.8	151	4.4	10,000	80.3
14	80.1	72.5	81.4	97.2	242	5.4	10,000	99.5
15	79.2	91.1	78.0	96.2	261	6.2	10,000	99.5
16	78.2	88.4	79.3	97.8	233	6.0	9,512	99.7
total	78.1	76.5	77.8	97.0	4,133	112.8	159,544	94.7

Table 6.2: Track reconstruction, trigger, isolation and loose muon efficiencies (%), number of Z-candidates, integrated luminosity (pb^{-1}), number of preselected events and a percentage of good luminosity blocks in each of the sub-samples.

tool. These results were used to understand a larger width of the Z mass peak using the data reconstructed with p13 version of the tracking code [93].

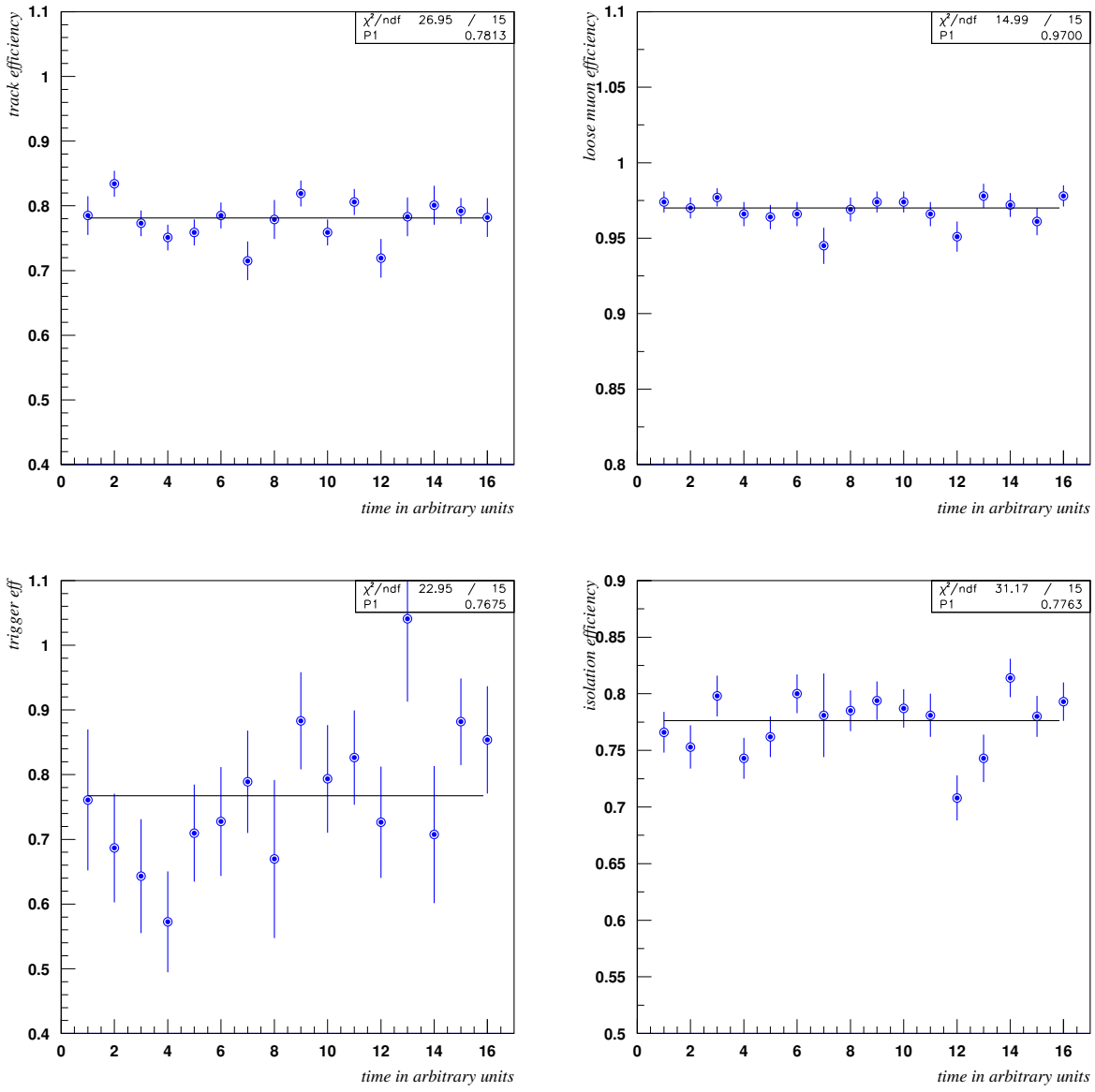

Figure 6.14: Reconstruction efficiencies (track, loose muon, trigger and isolation) versus time.

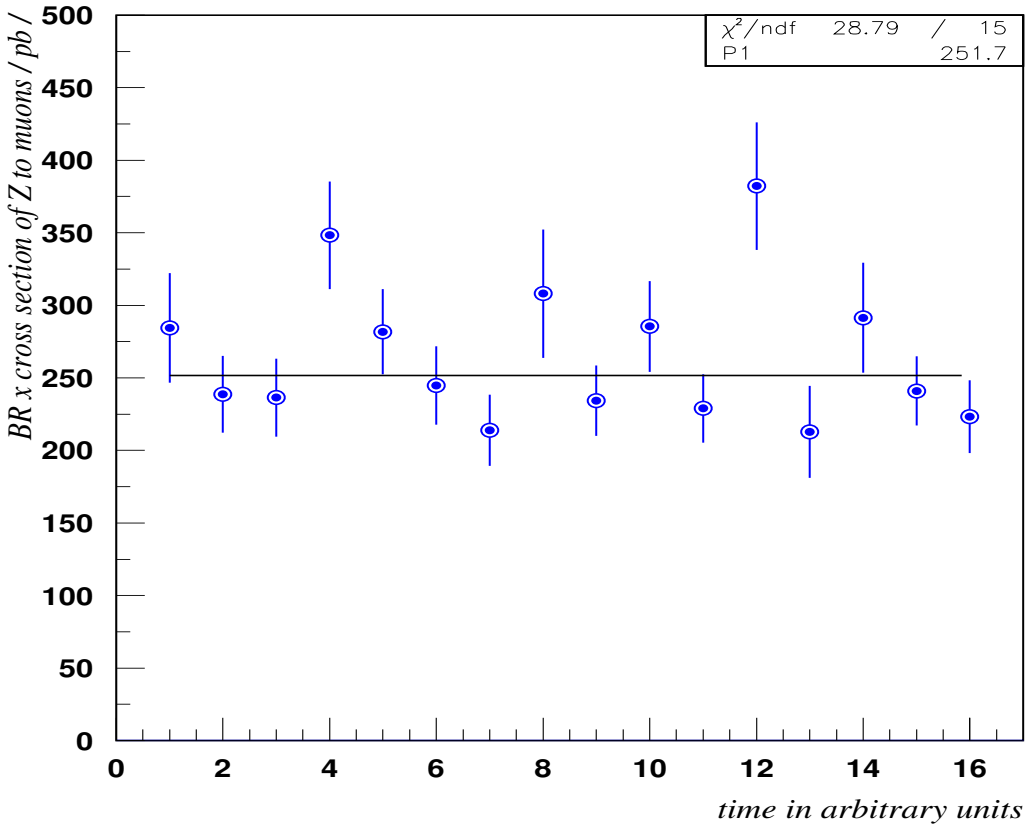

Figure 6.15: Z $\rightarrow \mu\mu$ cross section versus time, $BR \times \sigma_z = (252 \pm 22)$ *pb*.

Chapter 7

Comparison of data and MC

The goal of this chapter is to describe the normalization of Monte Carlo to the data, comment on their agreement after each cut applied in this analysis, demonstrate their agreement in terms of the invariant mass and acolinearity distributions as well as properties of candidate events, e.g muon multiplicity, jet multiplicity, topology etc. This is an important piece of the analysis. In any search analysis, one has to demonstrate the understanding of backgrounds. One has to show not only that all relevant backgrounds are taken into account; none of them is missing or underestimated, but also the adequate understanding of all cuts has to be demonstrated. Both aspects can be understood from a cut flow tables for all dimuon combinations (Table 7.1) and like-sign dimuon combinations (Table 8.1). Any inadequate description of the data with Monte Carlo shows up in the cut flow table as a discrepancy between the number of events expected for a given simulated physics background sample, and/or the sum of background samples, and the number of events measured in the data. It can be obvious from the difference in number of events after each cut, or, in contrary, after one of the cuts only. Therefore,

one has to decide, whether a missing contribution to the background, the physics nature of the generated Monte Carlo sample, some detector related issue or the normalization are to be blamed. The normalization procedure is described in Section 7.1.

It is important to compare not only the total numbers of events after each cut, but also shapes of distributions for variables/distributions used in this analysis to set a limit on doubly-charged Higgs boson mass. There are two most important variables in this analysis: the invariant mass and the acolinearity between the two produced muons. The invariant mass and acolinearity distributions are described in a great level of detail in Section 7.5.

Finally, all other properties of events other than the invariant mass and acolinearity should be subject of further investigation. For instance, the multiplicity of muons and jets in selected events. This is particularly important for candidate events, since these are the kind of events that contribute to the limit calculation and one has to be absolutely certain that they are adequately described with simulated Monte Carlo backgrounds. These issues are described in Section 7.7.

7.1 Normalization of Monte Carlo to data

The Monte Carlo efficiencies are scaled to the efficiencies measured with data in Section 6 using the following normalization factor

$$\epsilon_{adjust} = \frac{\epsilon_{data}}{\epsilon_{MC}} = \frac{\epsilon^{data}_{track} \times \epsilon^{data}_{match} \times \epsilon^{data}_{loose}}{\epsilon^{MC}_{track} \times \epsilon^{MC}_{match} \times \epsilon^{MC}_{loose}}. \quad (7.1)$$

The reconstruction efficiencies plugged into the formula are presented in Equations 6.2 -6.11. The values of ϵ_{adjust} applied in this analysis are:

- Normalization of p14 Monte Carlo samples to data (p13)

$$\epsilon_{adjust} = 0.835 \tag{7.2}$$

- Normalization of p13 Monte Carlo samples to data (p13)

$$\epsilon_{adjust} = 0.878 \tag{7.3}$$

Each selected Monte Carlo muon is assigned a probability not to pass the selection criteria which reflects the inefficiency of reconstructing the central track, finding a matched central track or identification of a muon at all. The number between 0 and 1 is generated and if it lies in the interval $< \epsilon_{adjust}, 1 >$, the muon is rejected from the list of selected muons. In other words, the adjustment to efficiencies observed in data is made on a muon-by-muon basis. This method is also known as the *acceptance-rejection method*.

The isolation is a specific variable. It can be understood from Equations 6.8 in Section 6 that no additional adjustment needs to be done. There is one specific sample however, that has a need for an adjustment of similar nature as the one applied above for tracking, matching and muon identification efficiencies. It is the $b\overline{b}$ sample which contains non-isolated muons only, i.e. muons that are inside b jets. The Monte Carlo does not describe the data sufficiently in terms of isolation variables. All muons in the $b\overline{b}$ sample are found to be non-isolated and as such rejected from the list, i.e. that none of the $b\overline{b}$ events survives the isolation cut. That is not what has been observed in the data. The probability for a non-isolated muon to be reconstructed as an isolated muon is derived from the data, the value is given in Equation 6.12.

The remaining factor that also contributes to the Monte Carlo normalization is the trigger efficiency. The Monte Carlo samples are corrected for the trigger efficiency on event-by-event basis. A different trigger efficiency is applied for the background and signal Monte Carlo sample, since the trigger efficiency depends strongly on number of muons present in the event. The trigger efficiency measurement has been discussed in Section 6.4 in detail. The background Monte Carlo samples are treated for the trigger turn-on, the correction is performed using Equation 5.6 derived in Section 5.2.4. The event is kept/rejected by making a decision based on a randomly generated value between 0 and 1, and the trigger efficiency value calculated using the reconstructed invariant mass in the event. Signal Monte Carlo samples are treated in a different way. Unlike in the background samples, the trigger efficiency in signal samples is assumed to be flat in transverse momentum, i.e. no trigger turn-on dependence is taken into account. There are several reason for this assumption:

- there are 3 muons reconstructed on average in the signal sample. It means that the trigger efficiency must be very high. It will therefore depend much less on the p_{T} of reconstructed muons.

- transverse momentum of reconstructed muons is as hard, or as a matter of fact, even harder than the one of muons that come from Z decays. One should keep in mind that $\mathrm{H}^{\pm\pm}$ bosons are typically Lorentz boosted. This is why p_{T} of muons from $\mathrm{H}^{\pm\pm}$ boson decays is higher.

- the trigger efficiency in signal sample has been estimated using modified `d0trigsim` program. This procedure has been fully described in Section 6.4. Any transverse momentum dependence is therefore very hard

to guess. By doing so, one would take the same risk as by neglecting it completely.

Apart from the trigger turn-on dependence, the trigger efficiency is applied in signal Monte Carlo samples on event-by-event basis, in a similar fashion as the one described above for other background samples.

Normalized number of events $N^{norm}_{S\{i\}}$ remaining in each sample after every selection $S\{i\}$, where $i = 1, ..., 4$, is normalized to the data as follows

$$N^{norm}_{S\{i\}} = \frac{N_{expected}}{N_{generated}} \times N_{S\{i\}}. \tag{7.4}$$

In this formula, $N_{expected} = \sigma \times \int \mathcal{L} \times \epsilon_{adjust}$ is the total number of expected events given the integrated luminosity of the data sample, the cross section of the sample and the adjustment factor given in Equation 7.1; $N_{generated}$ is the total number of simulated events in Monte Carlo sample and $N_{S\{i\}}$ is the total number of events that pass a given selection $S\{i\}$, $i = 1, ..., 4$.

The number of expected Monte Carlo events is based on the NLO (NNLO if possible) cross sections for all processes given in Table 5.1 and the integrated luminosity of the data sample $\int \mathcal{L}$.

The background contribution from $t\bar{t}$ and diboson (WZ, ZZ and WW) production is also estimated by Monte Carlo simulation. The NLO cross section is used for $t\bar{t}$ events [110]. Higher-order QCD corrections to diboson production are approximated by multiplying the LO cross section given in PYTHIA by the K-factor [136]

$$K = 1 + (8/9)\pi\alpha_s. \tag{7.5}$$

The K-factor is equal to 1.34 at $\sqrt{s} = 1.96$ TeV/c^2.

7.2 Correction of track q/p_T in data

It is well known that there is a big discrepancy in Z mass resolutions measured in data and the $Z \rightarrow \mu\mu$ + Drell-Yan Monte Carlo sample in p13 DØ event reconstruction code. The discrepancy is more than factor of two. It was found that the central fiber tracker is probably sagging due to the gravity with respect to the silicon vertex detector. The shift is estimated to be approximately 125 microns. After the new alignment geometry was calculated, the Z mass resolution has improved, without any additional correction needed. This analysis is however using an older version of the event reconstruction code (p13 as compared to an improved p14 code), this is why corrections described in Appendix E.7 have to be applied in order to achieve a better transverse momentum resolution.

After applying transverse momentum corrections in the data, Equations 5.22 and 5.23 in Appendix E.7, the Z mass resolution is comparable to what is observed in Monte Carlo. Residual misalignment and cluster efficiency effects, which originate from the 20 ADC cut applied on the ADC information read out from each fiber, are responsible for the remaining discrepancy. It is less than 1.5 GeV/c^2 however. The same result is obtained using the new aligned geometry of the central fiber tracker implemented into the p14 event reconstruction code.

7.3 Smearing of MC track momentum

The correction of track transverse momenta outlined in Appendix E.7 is applied in this analysis. The remaining difference between the Monte Carlo

and data Z mass resolution is about 1.5 GeV/c^2. The transverse momentum of Monte Carlo tracks must be smeared in order to compensate for this effect, so that the same mass resolution is achieved. The correction to track transverse momentum is applied. The smeared $(1/p)'$ is generated using Gaussian probability distribution with the mean at $(1/p)$ and σ calculated as follows:

$$\sigma = \frac{\sqrt{A^2 \cosh \eta + B^2 p^2}}{p}, \tag{7.6}$$

where $A = 0.015$ and $B = 0.0018$. Factor A represents the multiple scattering term and B the resolution term. The smeared transverse momentum is calculated from $(1/p)'$ using azimuthal angle φ.

7.4 Cut flow tables

In the following two sections is discussed an agreement between the data and Monte Carlo simulation for the normalization, number of events remaining after each selection and for the shape of the dimuon mass and $\Delta\varphi$ distributions.

The number of events remaining in each sample after each selection (cut) is shown in Table 7.1, it is also being referred to as a 'cut flow table' further in the text.

There is a good agreement between the data and Monte Carlo in terms of number of events expected after each selection. It is important that the sum of all Monte Carlo background samples agrees with the data well. If there was any discrepancy, it would automatically mean that there is either some missing background that has to be added or that the Monte Carlo sample

	data	MC (sum)	$Z \to \mu^+\mu^-$	$b\overline{b}$	$Z \to \tau^+\tau^-$	$t\overline{t}$	ZZ	WZ	WW
S1	5168	5254 ± 47	4816 ± 46	391 ± 7.3	40 ± 3	3.04	0.09	0.57	3.51
S2	4133	4113 ± 43	4055 ± 43	18.4 ± 1.4	34 ± 1	2.13	0.08	0.50	3.14
S3	378	368 ± 14	359 ± 14	3.0 ± 0.5	2.4 ± 0.4	1.50	0.07	0.37	1.87
S4	3	1.5 ± 0.4	0.3 ± 0.1	0.8 ± 0.4	< 0.1	0.11	0.05	0.23	< 0.01

Table 7.1: Number of events remaining after each selection and the expected background from Monte Carlo simulation. The errors are only statistical uncertainties from Monte Carlo generation. The contribution from $Wb\overline{b}$ and $Zb\overline{b}$ final states is negligible. The contribution from $W(\to \mu\nu)$+jets background is less than 0.1 events after (S4); calculation of the estimate is described in Section 5.2.5.

is not normalized properly (some of the reconstruction efficiencies is biased, for instance). There is no indication of that, which means that all important backgrounds are taken into account properly. An agreement is achieved even after the last two selections (S3 and S4), which are rather restrictive. This is not trivial, because any problem with understanding the data and/or Monte Carlo samples would result in a statistically significant discrepancy. A good example of such a problem is re-weighting of $Z \to \mu\mu$ events, see Section 5.2.1 for details. Since PYTHIA does not provide a good description of the jet multiplicity in Z+jet events, the $\Delta\varphi$ distributions are very sensitive to the number of jets in an event. Without re-weighting the simulated $Z \to \mu\mu$ events, there would be almost 30% discrepancy between the data and Monte Carlo after the acolinearity selection (S3).

The primary idea of this analysis is to develop a set of cuts that is able to

remove all Standard Model and instrumental backgrounds and to keep the signal efficiency as high as possible at the same time, so that the doubly-charged Higgs sensitivity stays high. It can be seen in Figures 7.1 and 7.2 that while the backgrounds are removed more and more with each selection applied, the signal efficiency decreases slowly.

The production of W bosons decaying into $\mu\nu$, in association with jets, is yet another source background mainly at low dimuon mass. The W+jets background is missing in Table 7.1. By extrapolating to $p_{\mathrm{T}} > 15$ GeV/c the steeply falling p_{T} spectrum of muons that fail the isolation requirements in dimuons from a sample of $W \to \mu\nu$+jets data, the contribution is estimated to be less than 0.1 events. The expected background rate, as determined from the data, is in agreement with the Monte Carlo simulation. This calculation is discussed in a great level of detail in Section 5.2.5.

7.5 Invariant mass and acolinearity distributions

The distribution of the dimuon mass and of $\Delta\varphi$ are shown in Figure 7.1 and Figure 7.2, respectively. The data are compared to the sum of Monte Carlo contributions from different background processes. In events with more than two muons, the invariant mass and $\Delta\varphi$ are calculated only for the two muons with highest transverse momentum. There is a good agreement between data and the Monte Carlo simulation, both for the normalization and for the shape of the dimuon mass and the $\Delta\varphi$ distributions after each selection. The fact, that the invariant mass as well as $\Delta\varphi$ distributions agree, is the best argument

that no important background contribution is neglected. Should there be some missing background, it would manifest as a discrepancy between the number of events and shapes expected in the data and Monte Carlo.

Discrepancies in $\Delta\varphi$ distributions between Monte Carlo and data

There are 3 minor discrepancies in $\Delta\varphi$ and invariant mass distributions that are worth of further investigating and explanation.

- The first observed discrepancy is a bump in the $\Delta\varphi$ distribution of the $b\overline{b}$ background at around 1.0, in Figure 7.1. The possible 'explanations' of what is the $b\overline{b}$ bump at about 1 rad in $\Delta\varphi$ caused by are given here:

    1. It is not statistically significant. One can see that there are only about 5 events that cause this discrepancy. It means that the error is about 2 events. If there were only 3 events, nobody would probably consider an existence of a bump in the $\Delta\varphi$ distribution at all. The bump is really small. As a matter of fact, it looks like the data shows the same behavior. Here, of course, due to a poor statistics, it is hard to tell. This is one possible answer; but it is too simple to blame the statistics for this kind of behavior.

    2. There is another explanation: let's think for a moment that indeed it is a real physics effect. Given the fact that the data seems to indicate the same behavior, one can think a little bit along the lines of how does the azimuthal distribution look like for $b\overline{b}$ events, where B hadrons decay into muons.

       It can be seen in Rick Field's study from CDF [118], it is shown in Figure 5.3 in Section 5.2.4. There is a turn-on in low $\Delta\varphi$ region

from gluon splitting into $b\overline{b}$. In other words, it means that the 2 muons produced this way are very close to each other in φ, they are almost parallel. These muons have a lower transverse momentum as compared to the LO flavor creation process, muons produced via flavor creation are in contrary mainly back-to-back. There is no effect like the one just described in $\Delta\varphi$ plots 7.2 produced in this analysis; but there is none for a good reason ! This effect is taken off by the requirement that both muons have $p_{\mathrm{T}} > 15$ GeV/c. Once this cut is dropped/lowered, it actually is possible to see the collinear muons from $b\overline{b}$ decays in Monte Carlo. Muons produced via gluon splitting into $b\overline{b}$ are obviously much softer in transverse momentum, this is why a relatively hard p_{T} cut will remove them completely. The only part of the $\Delta\varphi$ that remains, is the beginning of the turn-on towards lower $\Delta\varphi$ values.

If the p_{T} cut on muon transverse momentum was hardened, to say 20 GeV/c, the bump in the $b\overline{b}$ acolinearity distribution would not exist at all. The bump probably is a continuous turn-on from gluon splitting that is truncated on one side by our choice of the cut on muon transverse momentum. All that is left over from a turn-on is a bump at around 1 rad, it corresponds to 60° in Rick Field's plots 5.3.

Indeed, this explanation might be wrong, it only is a possible idea of what happens.

- Another minor discrepancy can be observed in the $\Delta\varphi$ distribution of the $b\overline{b}$ background in a region close to 0., in Figure 7.2. There is clear

deficit of events in the $b\overline{b}$ sample in this region. It is understood from the description of $b\overline{b}$ sample simulation in Section 5.2.4, that the low-p_T muon contribution is neglected in this sample. Muons from cascade processes are not generated. This is a reason why the $b\overline{b}$ sample can be used only for the purpose of describing the high-p_T dimuons. It is possible that low mass resonances like Υ (and/or others) cause the raise of the distribution towards zero in the $\Delta\varphi$ distribution. These dimuon events are removed by the p_T cut on muons, but probably not completely. The remaining events cause the increase in the data in $\Delta\varphi$. Since these events are not simulated in the Monte Carlo sample, it results in a small discrepancy as compared to the data in the low $\Delta\varphi$ region.

- In Figure 7.1 can be observed a clear mass resolution discrepancy between the Monte Carlo $Z \rightarrow \mu\mu$ sample and the data in the region above ~ 150 GeV/c^2. The Monte Carlo is additionally smeared, see Section 3, to describe the data better. The smearing factors in Equation 7.6 are optimized so that the mass resolution measured in $Z \rightarrow \mu\mu$ Monte Carlo events agrees with the mass resolution obtained in the data in the mass window $60 - 120$ GeV/c^2. There is no guarantee that the same smearing factors are able to describe the mass resolution in the tails of the invariant mass spectrum. An improved smearing formula has to be introduced in order to get an adequate description in the entire region of invariant masses in this analysis. This effect might go away in the next iteration of the analysis with an improved event reconstruction code (p14) applied in the data.

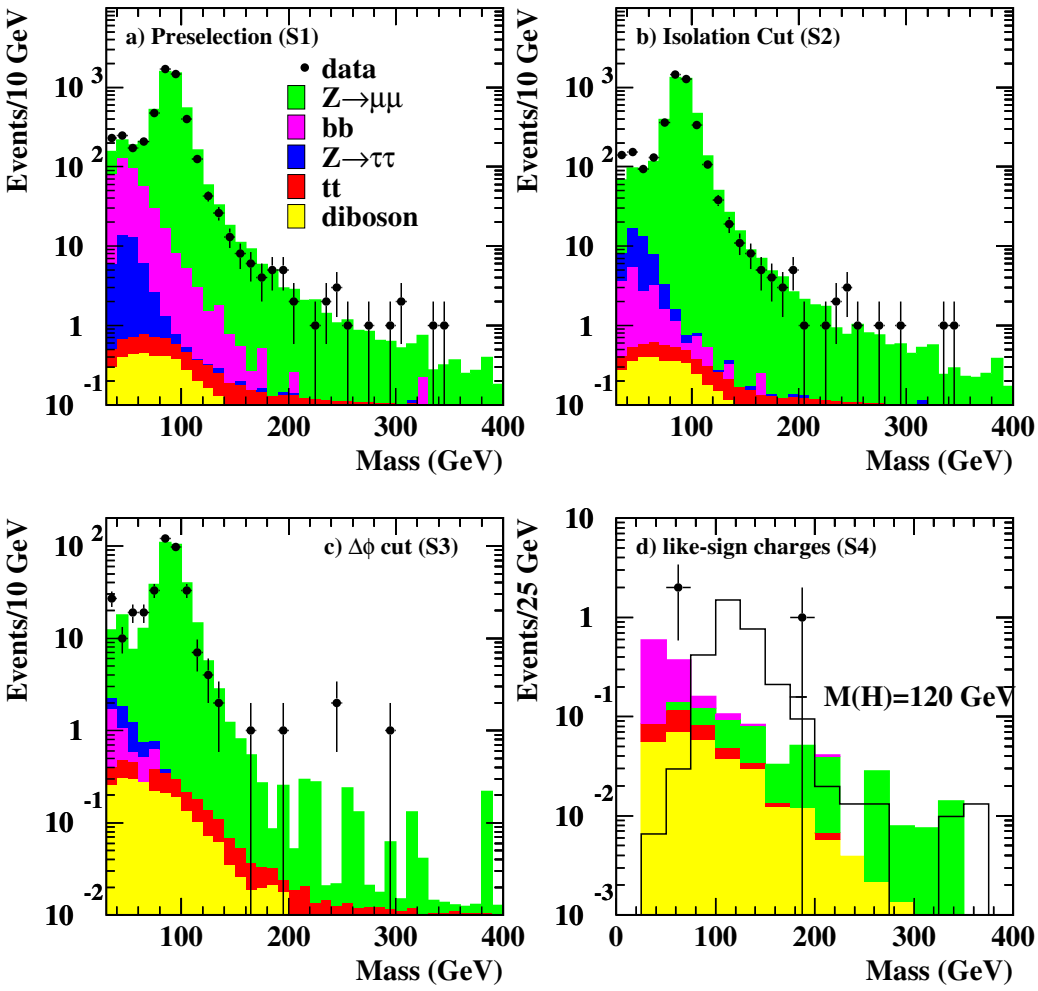

Figure 7.1: Distributions in the di-muon mass for data compared to the sum of Monte Carlo background processes: a) after preselection (S1); b) after the isolation requirement (S2); c) after the $\Delta\varphi$ requirement (S3); d) after the like-sign requirement (S4). The signal expected for a left-handed $H^{\pm\pm}$, with $M(H^{\pm\pm}) = 120$ GeV/c^2, is also shown by the open histogram.

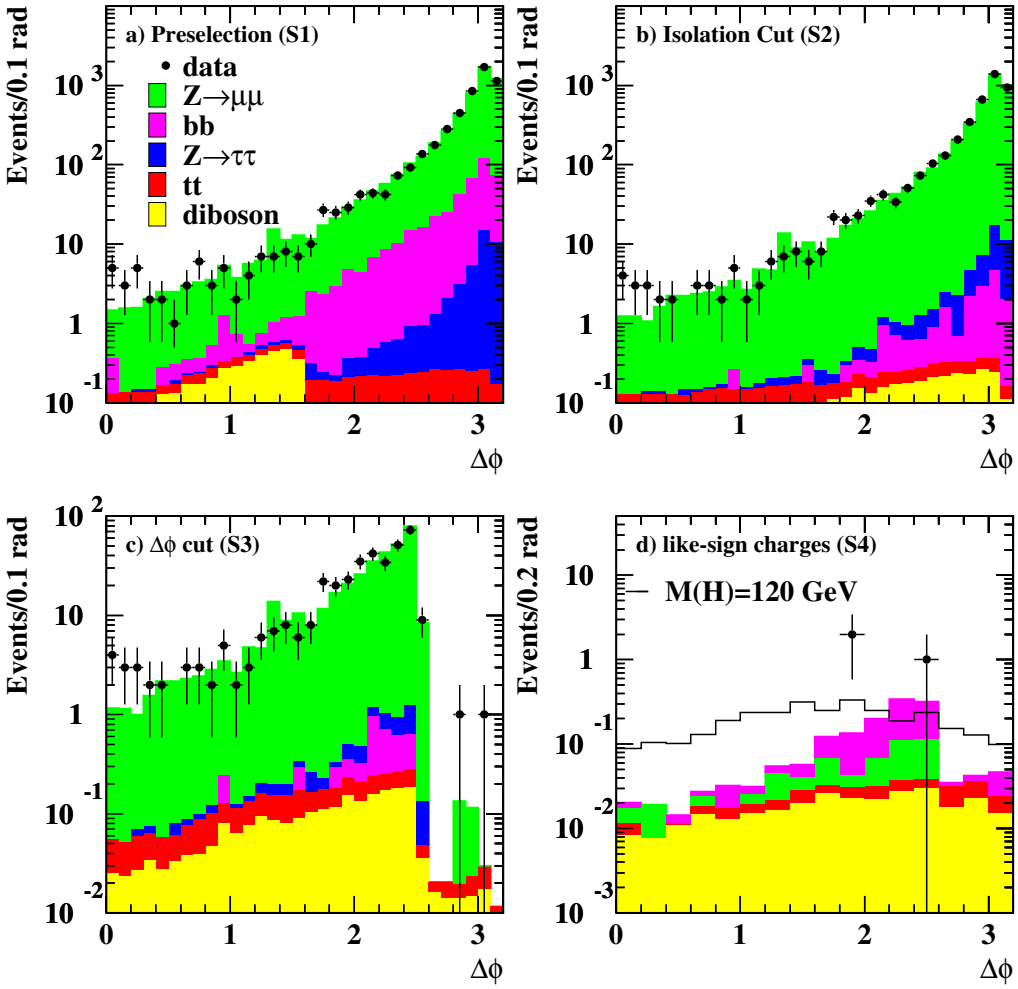

Figure 7.2: Distribution in $\Delta\varphi$ between the two muons for data compared to the sum of Monte Carlo background processes: a) after preselection (S1); b) after the isolation requirement (S2); c) after the $\Delta\varphi$ requirement (S3); d) after the like-sign requirement (S4). The signal expected for a left-handed $H^{\pm\pm}$, with $M(H^{\pm\pm}) = 120$ GeV/c^2, is also shown by the open histogram.

7.6 Remaining events

After the final selection (S4), requiring the presence of at least one pair of like-sign muons in the event (S4), only three candidate events remain. The invariant mass is calculated for the pair of like-sign muons with the highest p_{T}. The event with the highest like-sign mass in Figure 7.1d is at 83 GeV/c^2 and contains a second pair of oppositely charged muons with a higher invariant mass. Since only the highest mass of all possible pairings is plotted in an event, this event appears at $M = 252$ GeV/c^2 in Figure 7.1c. The pair of events in the same mass bin (Fig. 7.1d) is not the same as the pair of events in the same $\Delta\varphi$ bin (Fig. 7.2d). The two entries in Figures 7.1d and 7.2d which are entered in the same bin are not from the same event.

Most muons from Z decays are collinear, i.e., $\Delta\varphi \approx \pi$, and are removed by the $\Delta\varphi$ requirement. Since it is applied to events with only two muons, a few events remain at $\Delta\varphi > 4\pi/5$.

An interesting check of understanding the backgrounds after the final selection is comparing muon multiplicity and jet multiplicity in Monte Carlo and data.

In the data, there are 2 three-muon events and 1 two-muon event. Two out of 3 remaining events in data have jets in them, only one is without jets at all. It is believed that one event is the case of charge mis-identification in data, see Section 10.2.3 for details.

In Monte Carlo, there are two main sources of three-muon events: $Z \rightarrow \mu\mu$ + Drell-Yan and diboson ($ZZ/WZ/WW$) backgrounds. The expected number of three-muon events from $Z \rightarrow \mu\mu$ + Drell-Yan background is 0.23 events after the last selection (S4). From diboson backgrounds, one expects

0.17 events. The total number of three-muon events in Monte Carlo is more than 0.40 events, we did not take into account other backgrounds. They contribute little however given their small total production rate.

The comparison of number of three-muon events in the data and Monte Carlo is then 2 data events compared to more than 0.40 Monte Carlo events. This is not a bad agreement if one keeps in mind that the total number of events in the data and the sum of Monte Carlo, which is 3 data events *versus* 1.5 Monte Carlo events. The $Z \rightarrow \mu\mu$ background is the main contribution to the background, in the entire Monte Carlo sample, there are 3 three-muon events and only one two-muon event found. All four $Z \rightarrow \mu\mu$ Monte Carlo events have jets. The kinematic variables of these events are given in Table 7.2. Event (2) is a charge mis-identification event, the leading muon is assigned the transverse momentum and the charge that are mis-reconstructed in the central tracker. This track traverses the CFT in a region with less than 16 layers, this region is called the CFT overlap, see Section 3.1.2 for reference.

	$M(\mu^{\pm}\mu^{\pm})$ (GeV/c^2)	$\Delta\varphi$	$p_{\mathrm{T}}(1)$ (GeV/c)	$p_{\mathrm{T}}(2)$ (GeV/c)	$p_{\mathrm{T}}(3)$ (GeV/c)	no. of jets
(1)	61.2	2.19	58.1	49.5	17.	1
(2)	173.6	2.46	105.7	18.0	–	1
(3)	42.9	1.60	56.0	36.6	21.	1
(4)	62.2	3.08	74.0	21.0	17.	1

Table 7.2: Kinematic variables of four $Z \rightarrow \mu\mu$ Monte Carlo events that pass the final selection (S4). The invariant mass, $\Delta\varphi$, transverse momentum of all muons and number of jets in an event are given in the Table.

7.7 Signal distributions

In Figures 7.1d and 7.2d, the distributions for a doubly-charged Higgs signal with a mass $M(\mathrm{H}^{\pm\pm}) = 120$ GeV/c^2 are shown, with the normalization given by the NLO cross section, and for the experimental efficiencies. The number of expected signal events after each selection is shown in Table 7.7 for different masses. The efficiencies lie in the range $45\% - 52\%$, and they are nearly independent of mass. The total signal efficiency, i.e. signal efficiency times kinematic and geometric acceptance, for the event selection in this analysis is $(47.5 \pm 2.5)\%$. The geometric and kinematic acceptance is taken from a GEANT-based [103, 104, 137] simulation of the detector, see Section 6.5.

Muons from doubly-charged Higgs decays are boosted. This is why the mean of the $\Delta\varphi$ distribution is at around $1.7 - 2.0$ for Higgs masses below 200 GeV/c^2. The average muon multiplicity of signal events is 3. This is also a reason why the acolinearity selection (S3) does not alter signal efficiency too much (Table 7.7, selections (S3) and (S4)).

The mass resolution changes from 7.6 GeV/c^2 for $M_{\mathrm{H}^{\pm\pm}} = 80$ GeV/c^2 to 30 GeV/c^2 for $M_{\mathrm{H}^{\pm\pm}} = 200$ GeV/c^2. This effect has to be taken into account when calculating the mass limit on the doubly-charged Higgs boson, see Section 11.

M (GeV/c^2)	80	100	120	140	160	180	200
$N = \sigma L$	32.8	13.6	6.4	4.5	1.68	0.91	0.51
S1	22.0	9.4	4.4	2.3	1.17	0.65	0.35
S2	19.8	8.5	4.0	2.1	1.05	0.58	0.31
S3	17.2	7.5	3.5	1.9	0.95	0.53	0.29
S4	15.0	6.5	3.0	1.7	0.81	0.46	0.25
$\epsilon(\pm 1\%)$	45%	48%	47%	52%	48%	50%	48%
$\hat{\sigma}_1$ (GeV/c^2)	7.6 ± 0.1	11.0 ± 0.2	11.9 ± 0.3	17.7 ± 0.4	19.8 ± 0.5	23 ± 1	30 ± 1

Table 7.3: Number of expected signal events after each cut and efficiency for each mass point. The first row gives the number of expected events using the NLO cross section for left-handed $H^{\pm\pm}$ boson. The value of $\hat{\sigma}_1$ at each mass point is the width of the narrower of two Gaussians fitted to the reconstructed mass distribution. The simulation is done in 10 GeV/c^2 mass steps, but only every second mass point is shown. Only statistical uncertainties are given in the Table.

Chapter 8

Like-sign background

This chapter gives details about the like-sign background in this analysis. The idea is to construct a set of selection criteria, or 'cuts', which should preferentially select the doubly-charged Higgs boson signal over the background processes. Any statistically significant excess could be evidence for a doubly-charged Higgs boson signal. The result of this analysis, in the form of a set of data events which pass the cuts and the expected background samples, also form the input for the mass limit calculation.

8.1 Like-sign events after preselection

When the requirement of having at least one pair of like-sign muons is applied before the preselection (S1), most of the background from Z decays is removed. Only 101 like-sign events remain after that in the data. The number of expected events after each selection is given in Table 8.1. Since no isolation criterion is imposed at this stage, the most probable background is due to $b\overline{b}$ production, with both b quarks decaying semi-leptonically.

	data	MC (sum)	$b\bar{b}$	$Z \to \mu^+\mu^-$	$Z \to \tau^+\tau^-$	$t\bar{t}$	ZZ	WZ
S1	101	96.6 ± 3.3	95.1 ± 3.3	0.9 ± 0.3	< 0.1	0.24	0.06	0.29
S2	5	5.4 ± 1.9	4.4 ± 1.9	0.6 ± 0.2	< 0.1	0.11	0.05	0.27
S3	3	1.5 ± 0.4	0.8 ± 0.4	0.3 ± 0.1	< 0.1	0.11	0.05	0.23

Table 8.1: Number of events with at least one like-sign muon pair remaining after each selection and the number expected background events from the Monte Carlo simulation. The uncertainties are the statistical uncertainties from the Monte Carlo. The procedure used to estimate the number of $b\bar{b}$ events is described in the text. There is no contribution from WW events.

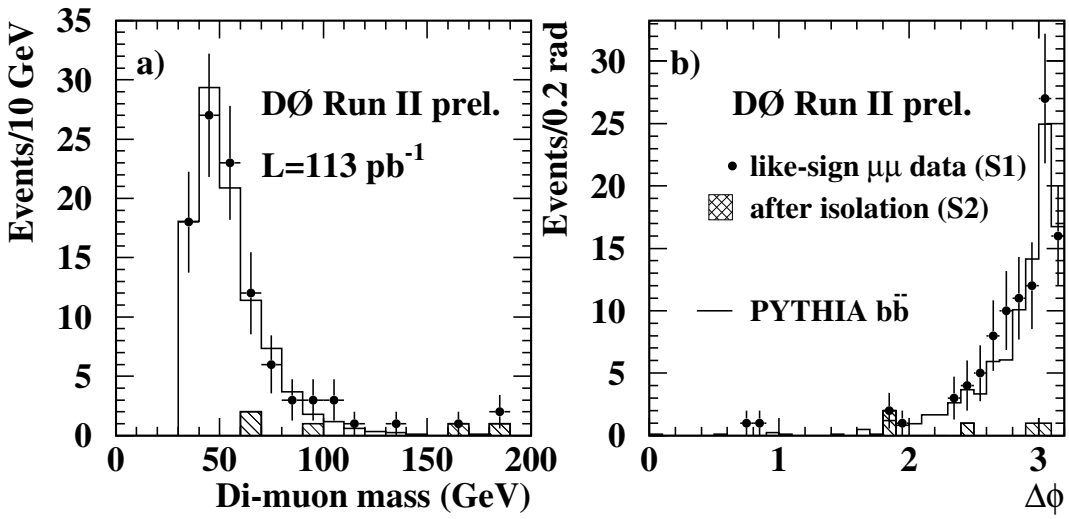

Figure 8.1: Invariant mass and $\Delta\phi$ distributions for the 101 like-sign events remaining in data after the preselection (points with error bars), compared to PYTHIA simulation (histogram). The five (three) events remaining after the isolation (or $\Delta\phi$) selection are shown separately.

The expected number of $b\overline{b}$ background events, given in Table 8.1, is calculated from the PYTHIA $b\overline{b}$ sample using efficiencies derived from data. Since the Monte Carlo sample is generated without trigger simulation, the p_T dependent trigger efficiency is folded in with the p_T distribution. The muon reconstruction efficiency applied to this sample is corrected for any residual difference between data and Monte Carlo [128]. This procedure was described in Chapter 7.

Figure 8.1 shows the invariant mass for like-sign dimuons and their $\Delta\varphi$ distributions in the data and Monte Carlo. The shapes, as well as event rates, are well reproduced with the $b\overline{b}$ simulation performed in this analysis, it is described in Section 5.2.4.

Out of 101 preselected (S1) events, 5 remain after applying the isolation requirement (S2), while 16 events remain after applying only the $\Delta\varphi$ requirement. Assuming that all events have originated from $b\overline{b}$ processes, the isolation and $\Delta\varphi$ selection efficiencies are 5% and 16%, respectively. Using these the background from $b\overline{b}$ production in the final sample is expected to be approximately 0.9 events.

8.2 Charge mis-identification background

There are two sources of charge mis-identification. The first source is charge mis-identification for tracks with $|\eta| > 1.63$ due to the smaller number of CFT layers in the CFT overlap region. Tracks in this region have less than 16 CFT hits, see Section 3.1.2. The second source of charge mis-identification are very high-p_T tracks where the uncertainty on the measured curvature and a possible residual mis-alignment can cause a charge flip. These effects are

included in the Monte Carlo simulation but they might be underestimated. The p14 version of Monte Carlo did not include an 'as-built' detector geometry, i.e. the geometry that is obtained from the data (detector survey + alignment) is used instead of an ideal geometry. This is why all effects from mis-alignment of the central tracker are not included. The charge mis-identification rate is much larger in the data. The number of background events due to both effects can also be estimated using the data. Assuming that the charge mis-identification efficiency is independent of the $\Delta\phi$ requirement, the charge mis-identification rate is given by the ratio of like-sign to opposite-sign events after selection (S2), numbers can be obtained from Tables 7.1 (opposite-sign) and 8.1 (like-sign),

$$S3(like) = \frac{S2(like) \times S3(opposite)}{S2(opposite)} \tag{8.1}$$

and it is 0.12%. Since 378 data events remain before the selection of like-sign pairs (S4), a background rate of 0.45 events is expected due to charge mis-identification.

An alternative way of putting an upper limit on charge mis-identification rate is to assume that all like-sign events after the final selection (S4) originate from charge mis-identification. In such a case, the rate for charge mis-identification can be expressed as

$$r_{mis-id} = 3/(2 \times 5,168) \sim 3 \times 10^{-4}. \tag{8.2}$$

The charge mis-identification rate is of the order of 10^{-4}, i.e. approximately one out of ten thousand tracks is mis-reconstructed and assigned a wrong charge.

An important piece of analysis could be to describe the dependence of charge mis-identification on the jet multiplicity, p_{T} of the track/jet and acolinearity ($\Delta\varphi$ angle between muons). It is obvious that there are dependencies like that, it follows from the dependence of $\Delta\varphi$ on the jet multiplicity and jet transverse momentum. The size of the data sample does not allow to have a systematic study like this at the moment. It is going to be possible in the future since more than 0.5 fb^{-1} is going to be available by the end of year 2004.

8.2.1 Charge mis-identification rate using Monte Carlo with 'as-built' detector geometry

Another approach towards estimation of the $Z \to \mu\mu$ charge mis-identification is to simulate it by using the newest version of the simulation code that has implemented an 'as-built' detector geometry. The new version is p15, the draw back of doing so is that this version has not yet been fully tested at the time this analysis was performed. This is why results from this study were not used for publication purposes. A large 270k events $Z/\gamma \to \mu\mu$ sample has been generated with p15.05(06) Monte Carlo simulation version. It turns out that the Z mass resolution in the data is very close to what is observed in this sample, $\sigma(M_Z) = 7.9$ GeV/c^2. It is 6.0 GeV/c^2 in the p14 Monte Carlo sample used in this analysis, this is why additional smearing (Equation 7.6) is necessary. Also the hit resolution in SMT and CFT is much closer to what is observed currently in the data. There still is a residual difference, but that can be explained by effects described in Appendix E. This comparison with the data shows that p15.05 is very promising and it describes the data

much better than any previous version of the DØ event reconstruction. Running the analysis code on this sample gives the following results: 7 events are expected after preselection, 5.3 events after isolation selection and 1.4 pass the final (like-sign) cut (S4). Based on results from this sample, 1.4 like-sign events are expected in $Z \rightarrow \mu\mu$ Monte Carlo. This is significantly closer to what was obtained from the data. Interesting variables to plot are the physics η of leading p_{T} tracks in charge mis-identification events and the number of CFT hits associated to charge mis-identified tracks, it is shown in Figure 8.2.

The distributions in Figure 8.2 show that the charge mis-identification events in Monte Carlo are mainly due to fewer CFT hits that are associated to the track when it is traversing the central tracker in a $|\eta|$ region above 1.63. It can be easily shown for events where one of the tracks is charge mis-identified, that whereas the invariant mass calculated using the true Monte Carlo information peaks at around 91 GeV/c^2, the invariant mass distribution calculated using reconstructed kinematic variables is distorted towards higher values. That can be understood from the fact that charge mis-identified tracks are typically assigned much higher transverse momenta than what the particle's transverse momentum it has been generated with.

8.2.2 Shape of distributions in `PMCS`

Yet another way to obtain enough Monte Carlo $Z \rightarrow \mu\mu$ events that contain a track that was charge mis-identified is to use Fast Simulation Monte Carlo `PMCS` [138] with a parametrized response of the DØ detector. Whereas shapes of the invariant mass and acolinearity can be trusted, the rate for a charge

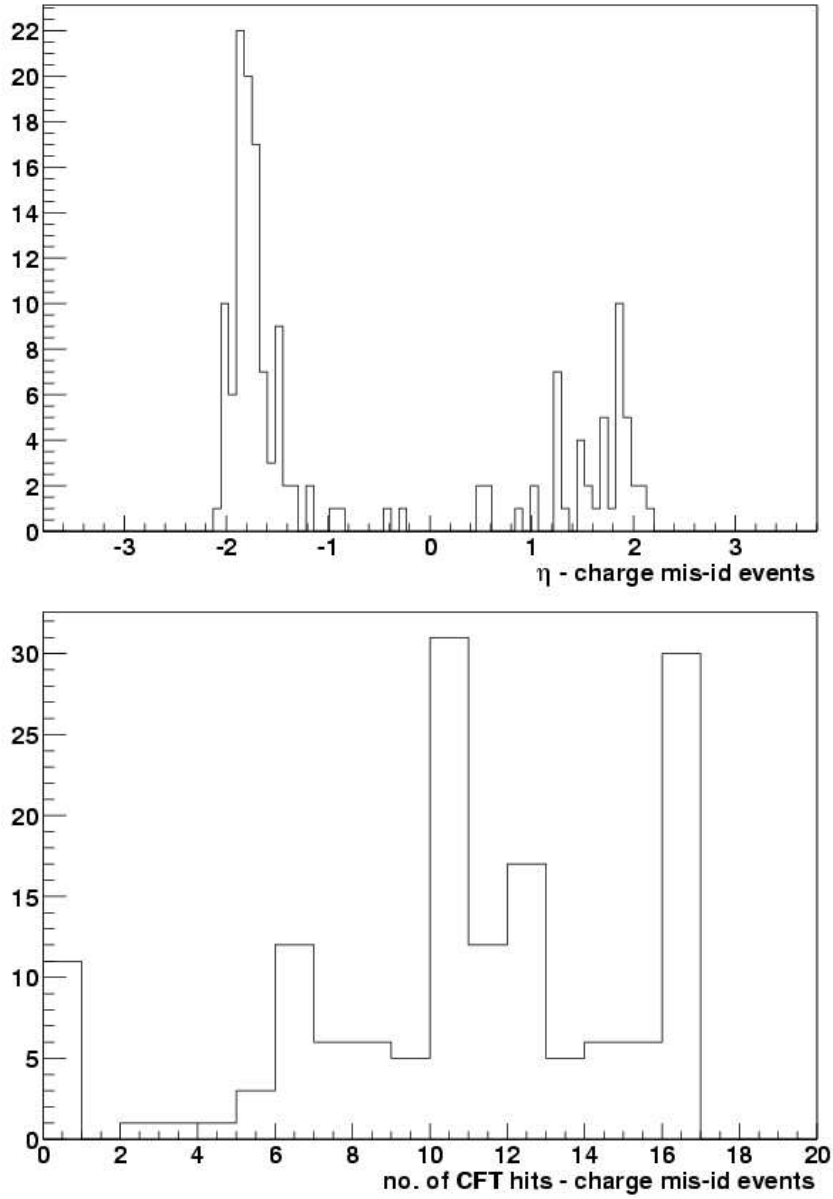

Figure 8.2: η (top) and number of CFT hits (bottom) distributions for leading transverse momentum tracks in Monte Carlo charge mis-identification events, η is calculated from the primary vertex position.

mis-identification cannot. There is no reason to think that a parametrized response of the detector could quantitatively describe such a rare effect as charge mis-identification. Despite of that, it is a common belief that the kinematic variables of reconstructed objects are, to the first order, described sufficiently. This is a reason why the fast Monte Carlos simulation was used to obtain shapes of invariant mass and acolinearity distributions of the $Z \to \mu\mu$ background after the last cut. The charge mis-identification rate is taken from the full-detector simulation.

8.2.3 Cosmic ray muon runs

To obtain the rate for charge mis-identification in the data, the usage of cosmic ray runs has been considered. There are more than 700k events available to be analyzed. Cosmic rays are an excellent tool for this kind of study, because the events are clean, all cosmic ray events must be opposite-charge (it follows from the CPT theorem) and there are many of them. Unfortunately, the entire sample is of a limited value because the CFT was not synchronized with the muon system and as a result, there are just a few events with muons matched to central tracks. This study should be repeated in the future on a new sample.

8.2.4 Comparison with the charge mis-identification rate from $Z \to ee$ events

An interesting check is to compare the charge mis-identification rate in the $Z \to \mu\mu$ and $Z \to ee$ data. This study was performed by the DØ Electroweak group [139]. The events are selected based on the following criteria:

- single EM trigger has to fire
- event must have a good primary vertex with 2 tracks
- there must be two EM objects satisfying:
  - object must be identified as a photon or electron/positron ($ID = 10, \pm 11$)
  - isolation < 0.15
  - EM fraction ≥ 0.9
  - H-matrix value must be less than 20.
  - an object is in the fiducial volume of the detector
  - it has a matched track
  - $p_{\mathrm{T}} > 25$ GeV/c
  - $CC : |\eta| < 1.1$
- the reconstructed invariant mass falls into a mass window 86 GeV/c^2 $< M_{ee} <$ 96 GeV/c^2.

The charge mis-identification rate using data diEM sample defined above is [139]

$$r_{mis-id} = \frac{N_{ss}}{N_{ss} + N_{os}} = 2.7 \times 10^{-2}. \tag{8.3}$$

This a very different result from what one obtains in the muon channel, 3×10^{-4}, almost two orders of magnitude different result. It is obvious that the charge mis-identification rate in $Z \rightarrow \mu\mu$ events cannot possibly be so

high. The difference between Equations 8.2 and 8.3 can be attributed to the following effects that are related to electrons:

- Bremsstrahlung - the track has a kink due to the p_{T} of the emitted photon, longitudinal momentum transfer is proportional to k/E^2 [129].
- and hard photon emission and a subsequent conversion into e^+e^- pair.

It is indeed hard to get an estimate on these two processes, both of them are closely related to a material budget inside the silicon and fiber tracker.

8.3 W+jets background

A further source of background at low dimuon masses is the production of a single W decaying into $\mu\nu$ in association with jets, where an additional muon may come for semi-leptonic decays in the jet, while failing the isolation criteria. Fake muons from hadron punch through and decays in flight are expected to be negligible [130].

This background needs to be studied using data. A $W \to \mu\nu$+jets data sample has been analyzed, requiring both muons to be isolated [131]. The main difference to the data set used in this analysis is a lower cut on the transverse momentum p_{T} of the lower p_{T} muon. The spectrum of this lower p_{T} muon is measured in the interval $3 < p_{\mathrm{T}} < 8$ GeV/c and then extrapolated to the region $p_{\mathrm{T}} > 15$ GeV/c. Using the ratio of the trigger efficiencies for the dimuon trigger and the single muon trigger used in the $W \to \mu\nu$ analysis, and the ratio of the muon reconstruction efficiencies, we obtain an estimate of (0.1 ± 0.1) for the number of events expected from $W \to \mu\nu$ events. To obtain an estimate for the background shape we use a PYTHIA simulation of

W+jets events, normalized to this background rate. A detailed description of this calculation is given in Section 5.2.5.

Chapter 9

Cut optimization

As it was pointed out earlier, the main idea of this analysis is to develop a set of selections that allow to reduce the Standard Model backgrounds significantly but at the same time do not change the signal efficiency too much. In other words, it is easy to apply cuts that reduce the amount of backgrounds practically to zero, but they might also represent an efficiency hit, i.e. reduce the signal sensitivity, on the other hand. That has to be avoided at any cost.

It is understood that there are selections that can hardly be changed or modified (preselection cuts or like-charge cut), but there are also cuts that can be optimized in order to improve the signal sensitivity and keep the level of backgrounds low at the same time. This is a purpose of the study that is presented in this chapter.

It is important to emphasize that any cut optimization should be performed 'blindly'. It means that one should never look on the candidate events and optimize selection criteria so that some of them are removed. It has to be done vice versa, looking at $S/\sqrt{S+B}$ ratio optimize the cuts, for

instance, and just then check whether the set of candidate events remains the same, or went through some changes.

The cut optimization is a very sensitive study, it can be also easily understood that there is a need for a long-term stability of the analysis in new particle searches. The reason for that is that it is a poor practice if cuts are change too dramatically from one iteration of the analysis to another. It immediately raises a question whether the selections are not suited to achieve higher limits too conveniently. The best way is to decided for a set of rather conservative, however needed and easily to be justified selections, and keep them unchanged for a long time. Indeed, the cut optimization is a must. Of course, later, when there is more statistics (luminosity), the cut optimization might be re-visited and newer values applied, it should not change the results significantly however.

And that is what has exactly been done in this analysis.

9.1 Preselection cut

This selection requires at least two loose muons, both with a matched central track, where each of the selected tracks has a transverse momentum greater than 15 GeV/c. The selected central track is required to have at least 2 SMT hits and more than 8 CFT hits. It is required that the invariant mass reconstructed in an event is above 30 GeV/c^2. This cut is intentionally made as loose as possible, so that no candidate events are rejected before any more specific selections are applied. Practically, the only candidates for a possible cut optimization are (a) the requirement on transverse momenta of central tracks matched to a muon, (b) the quality requirement on the number of

SMT and CFT hits associated with a central track, Figure 4.1.

It is a good idea to place the p_{T} cut as low as possible, however there is no need to require muons with p_{T} less than $10 - 12$ GeV/c, because the focus of this analysis is on high-p_{T} isolated muons, muons that have a harder transverse momentum spectrum than those observed in $Z \to \mu\mu$ events. A region above the Z mass peak is an interval of interest in this analysis. This is why any lowering of the transverse momentum requirement is actually contra-productive.

The same can be said about the quality criteria on tracks matched to muons. This criteria is very weak, in order to calculate the invariant mass of a high-mass dimuon system, a precise measurement of the transverse momentum is needed. It is essential to have good track, i.e. tracks with as many hits as possible, because this is where the momentum measurement and its precision comes from. The stereo tracks, tracks with hits both in axial and stereo CFT layers, are required. That directly translates into a requirement of more than 8 CFT hits (there are 8 CFT axial layers and 8 CFT stereo layers) on the track. Even for a high-p_{T} track, it is important to have a measurement in the silicon tracker, as a matter of fact, it is even more important for very high-p_{T} tracks because in order to do a good measurement, as large leverage as possible between the measurement closest to the beam pipe and the further-most measurement is needed. It is known that the transverse momentum resolution for tracks with the same p_{T} with and without the SMT measurement changes by factor of $2 - 3$ [140]. This is why it has been decide to require at least some measurement in the SMT, and 2 SMT hits is probably as low as one can get. In earlier days, the analysis

was performed without this requirement, but this cut was soon introduced because axial tracks matched to muons started to be a problem. The transverse momentum measurement for axial only tracks is poor, many events with high invariant masses have been therefore selected. What was common for them was that they all contained axial only tracks (at least one track per event). In this sense, it actually might be a good idea to tighten the selection a little bit, meaning to require more hits. On the other hand, it might not be such a good idea because of the hit to the signal efficiency that is affected by the cut. It is well known that an existing Monte Carlo does not describe the data all too well in terms of number of hits associated to tracks. In alternative language, the same requirement on number of hits on the track is much harder in Monte Carlo than in data. One has to be cautious about it. To conclude, introduction of loose requirements on the track quality seems to be the optimal way, and that is the approach taken in this analysis.

9.2 Isolation cut

The isolation selection requires that there are at least two isolated muons in an event. The definition of an isolated muon is given in Section 4.3. The definition of the isolation cut is not questioned in this study, the optimization was performed in [101]. However, the way isolation requirement has been applied is optimized. One can consider the following definitions of an isolation selection:

1. Any two muons in the event are isolated.

2. Two highest p_{T} muons must be isolated.

3. The two muons that enter to the calculation of an invariant mass and acolinearity must be isolated.

4. At least one muon in the event must be isolated.

Events that do not fulfill one of the criteria above, one at the time only, are rejected. Table 9.1 shows the number of events after the final selection (S4) in data, $Z \to \mu\mu$ Monte Carlo and signal Monte Carlo ($M_{\mathrm{H}^{\pm\pm}} = 120$ GeV/c^2) samples.

definition	data [events]	$Z \to \mu\mu$ MC [events]	signal MC [events]
(1)	3	0.31	3.02
(2)	3	0.31	2.70
(3)	3	0.00	2.67
(4)	4	0.42	3.22

Table 9.1: Number of events after the last selection (S4) in data, $Z \to \mu\mu$ Monte Carlo and signal Monte Carlo ($M_{\mathrm{H}^{\pm\pm}} = 120$ GeV/c^2). The expectation rate is normalized to the luminosity of the data sample.

The best results are achieved using definition (1) - any two muons in the event must be isolated. Definition (1) has been finally applied in this analysis. The differences between particular isolation cut definitions are marginal however. On the other hand, a few percentage point gain in the signal sensitivity represents $1 - 2$ GeV/c^2 improvement in the limit setting, in the region this analysis is searching through (it is going to be harder and harder to achieve such an improvement in the future).

9.3 Acolinearity cut

The $\Delta\varphi$ cut is the only one in the entire selection set that is not easy to understand immediately. In this analysis, the decision has been made to apply it at 2.51. This number comes from one σ limit around $\Delta\varphi = \pi$, i.e. muons are back-to-back in φ. This number can be understood from bottom (a) plots in Figures 9.1-9.3. A more quantitative justification for this cut is given in this Section. This cut is applied to remove back-to-back $Z \to \mu\mu$ events (85% of all $Z \to \mu\mu$ events are back-to-back) that could be potentially dangerous for the analysis if they happened to be charge mis-identified. This cut is therefore specifically tailored to be applied only to nearly back-to-back $Z \to \mu\mu$ events, i.e. it is applied only if there are exactly 2 muons in the event, otherwise it is dropped.

The real question is where in $\Delta\varphi$ should this cut be applied. The optimal way is to run the analysis for three different values of the acolinearity selection: $\Delta\varphi = 2.1$, $\Delta\varphi = 2.51$ and no cut at all, i.e. $\Delta\varphi = \pi$, and set mass limits for all three cases. The invariant dimuon mass and acolinearity distributions compared to Monte Carlo backgrounds for all three values of $\Delta\varphi$ are given in Figures 9.1, 9.2 and 9.3.

The signal efficiencies, mass limits, number of events in data, $Z \to \mu\mu$ and $b\overline{b}$ Monte Carlo after the final cut (S4) are given for all three values of $\Delta\varphi$ in Table 9.2. The $Z \to \mu\mu$ and $b\overline{b}$ Monte Carlo samples are chosen because they represent the largest contributions to the like-sign muon background in this analysis, and their rate and shape of the mass distributions play an important role in mass limit calculation. The exact procedure how to calculate a mass limit is described in Section 11. At this moment, the focus of the analysis is

on how does the final mass limit change when varying the $\Delta\varphi$ cut.

$\Delta\varphi$	signal efficiency (%)	mass limit (GeV/c^2)	data (events)	$Z \to \mu\mu$ MC (events)	$b\bar{b}$ MC (events)
2.10	43	117	3	0.22	0.00
2.51	45	118	3	0.22	0.90
π	47	99	5	0.56	3.36

Table 9.2: Signal efficiencies, mass limits, number of expected events in data, number of expected events in the two most important like-sign backgrounds, $Z \to \mu\mu$ and $b\bar{b}$, for three different $\Delta\varphi$ cuts at 2.1, 2.51 and π (no acolinearity cut is applied).

Confidence levels of the signal (top), $CL_S = CL_{S+B}/CL_B$, and confidence levels of the background CL_B (bottom) as a function of the mass $M(H^{\pm\pm})$ of a left-handed doubly-charged Higgs boson are calculated in Figures 9.4, 9.5 and 9.6 for $\Delta\varphi$ cuts set at 2.1, 2.51 and π.

If the $\Delta\varphi$ cut is applied at π, i.e. no acolinearity cut is applied at all. The dashed curve is the confidence level if no candidate events are taken into account. The mass limit is set at 99 GeV/c^2.

The $\Delta\varphi$ of 2.1 reduces the background by a factor of 5 as compared to the level of background in the analysis with $\Delta\varphi = 2.51$. The limit is only by about 1 GeV/c^2 better however. The background (mainly $b\bar{b}$) is far away from where one expects the signal, see Figures 9.1, 9.2 and 9.3 (upper plots, after preselection cut). The $b\bar{b}$ background invariant mass distribution after preselection is mainly concentrated at low masses, below the $Z \to \mu\mu$ peak. This is the reason why it almost does not affect the mass limit calculation in

a region where the competitive limit can be set in, i.e. at ≥ 115 GeV/c^2. The background contributing to the limit calculation is only $Z \rightarrow \mu\mu$ background which does not change between 2.1 and 2.51. What changes is the signal efficiency that drops by 2% when going from 2.1 to 2.51, that translates into a 1 GeV/c^2 difference in the mass limit. If no acolinearity cut is applied ($\Delta\varphi = \pi$), the mass limit calculation is governed only by number of candidate events and their distribution in the mass spectrum. This is why the $\Delta\varphi = \pi$ limit is by almost 10 GeV/c^2 worse than the other two alternatives, despite of a higher signal sensitivity.

From Figure 9.2 (bottom (d)) it might seem that a cut at $\Delta\varphi = 2.1$ eliminates one of the data events, and reduces the $Z \rightarrow \mu\mu$ backgrounds down to 0., likewise in case of the $b\overline{b}$ background. But Table 9.2 shows that there are 3 data events and 0.22 $Z \rightarrow \mu\mu$ events for $\Delta\varphi = 2.1$. Neither the data, nor the $Z \rightarrow \mu\mu$ background change when the cut is moved from 2.51 to 2.1. The explanation for that is simple, the $\Delta\varphi$ cut is applied only if there are exactly two muons in the event. If there are more than two muons, the cut is dropped. This explains why

- in data, there is one event between 2.1 and 2.51. It is the three-muon event though. One out of the 2 three-muon candidate events. The acolinearity cut does not reject it.

- in $Z \rightarrow \mu\mu$ Monte Carlo, events in question have three muons as well. They are $Z \rightarrow \mu\mu$+jet events, inside a jet, there is a muon with a matched track and transverse momentum greater than 15 GeV/c. This event is considered to be a three-muon event too, and the acolinearity cut is not applied either.

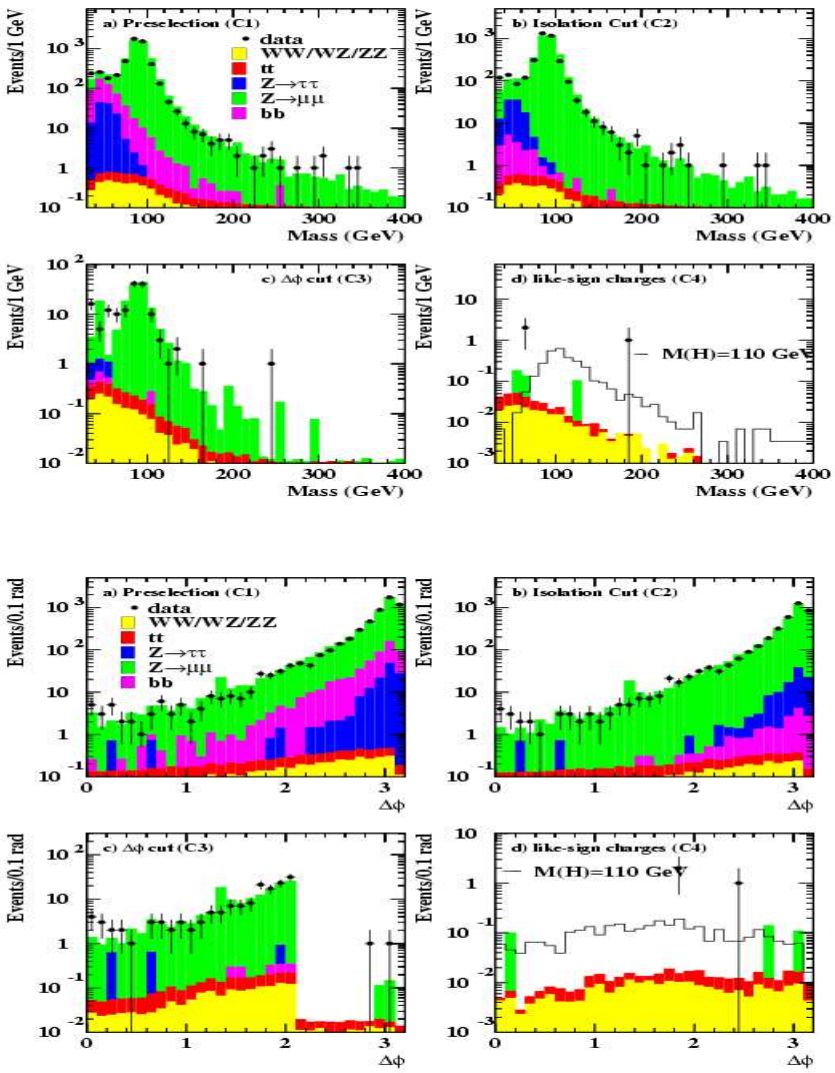

Figure 9.1: Distributions in the dimuon invariant mass (top) and $\Delta\varphi$ between the two muons (bottom) for data compared to the sum of Monte Carlo background processes: a) after preselection (S1); b) after the isolation requirement (S2); c) after the $\Delta\varphi$ requirement at 2.1 (S3); d) after the like-sign requirement (S4). The signal expected for a left-handed $H^{\pm\pm}$, with $M(H^{\pm\pm}) = 120$ GeV/c^2, is also shown by the open histogram.

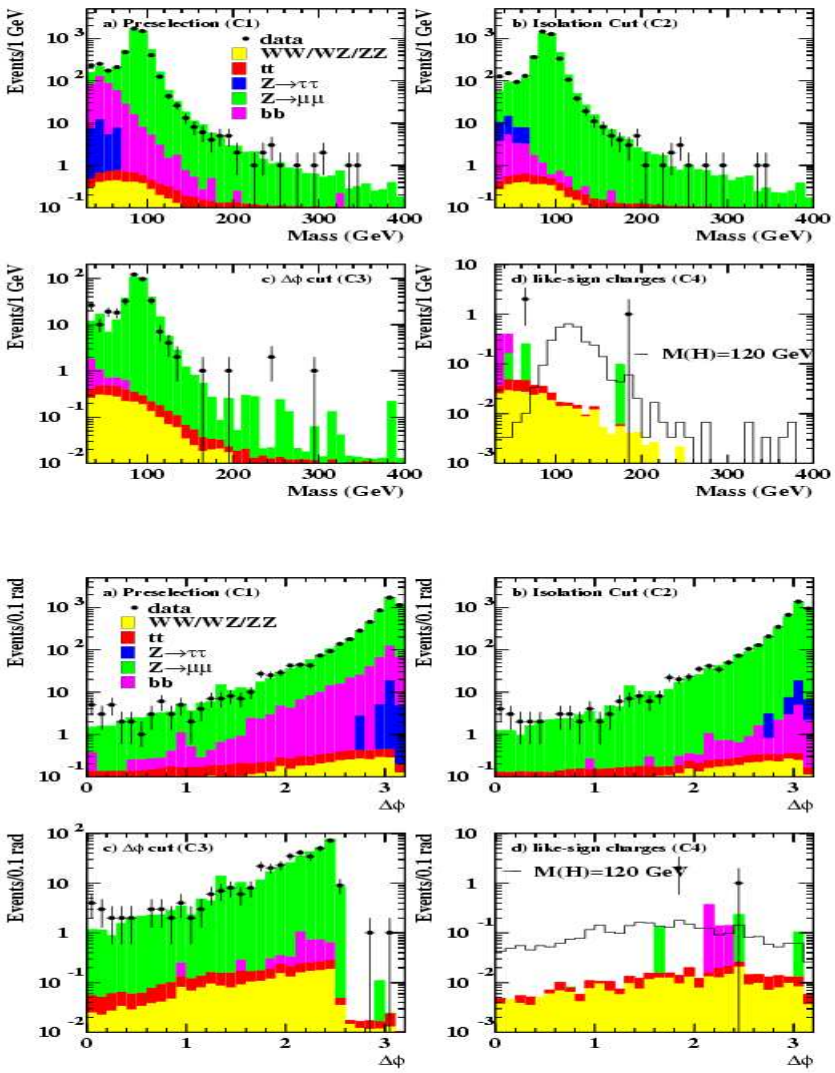

Figure 9.2: Distributions in the dimuon invariant mass (top) and $\Delta\varphi$ between the two muons (bottom) for data compared to the sum of Monte Carlo background processes: a) after preselection (S1); b) after the isolation requirement (S2); c) after the $\Delta\varphi$ requirement at 2.51 (S3); d) after the like-sign requirement (S4). The signal expected for a left-handed $H^{\pm\pm}$, with $M(H^{\pm\pm}) = 120$ GeV/c^2, is also shown by the open histogram.

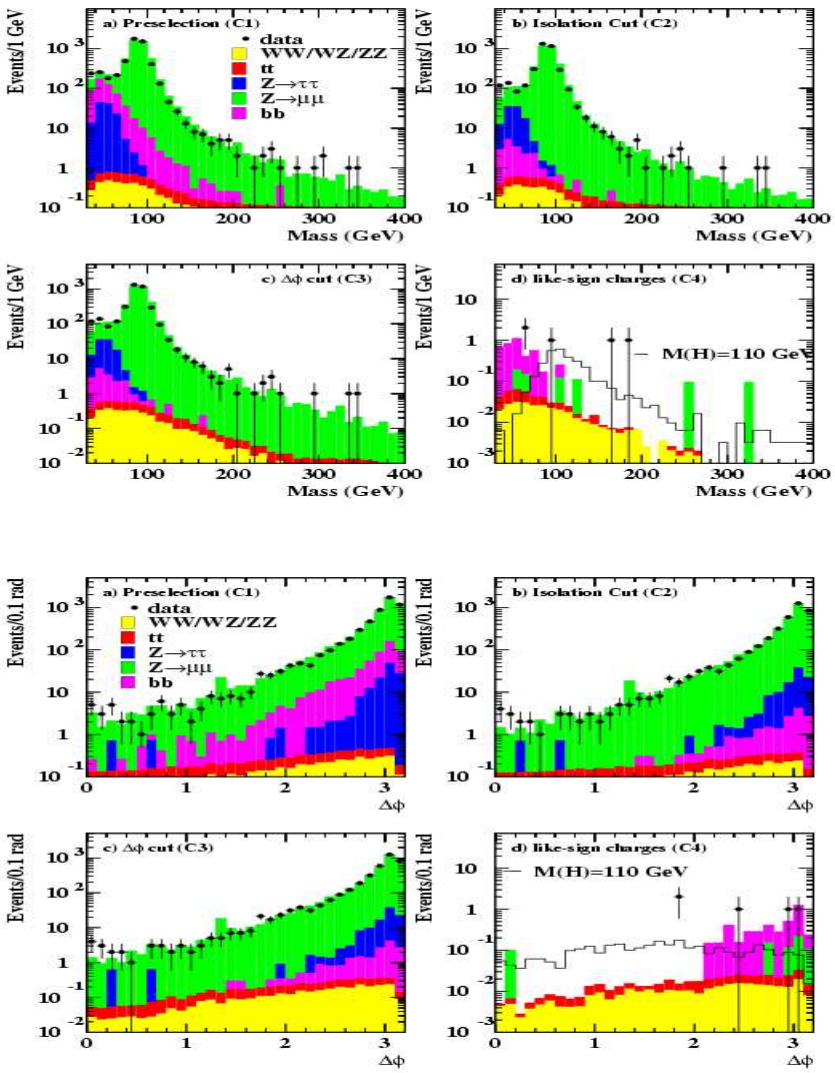

Figure 9.3: Distributions in the dimuon invariant mass (top) and $\Delta\varphi$ between the two muons (bottom) for data compared to the sum of Monte Carlo background processes: a) after preselection (S1); b) after the isolation requirement (S2); c) after the $\Delta\varphi$ requirement at π (no cut is applied) (S3); d) after the like-sign requirement (S4). The signal expected for a left-handed $H^{\pm\pm}$, with $M(H^{\pm\pm}) = 120$ GeV/c^2, is also shown by the open histogram.

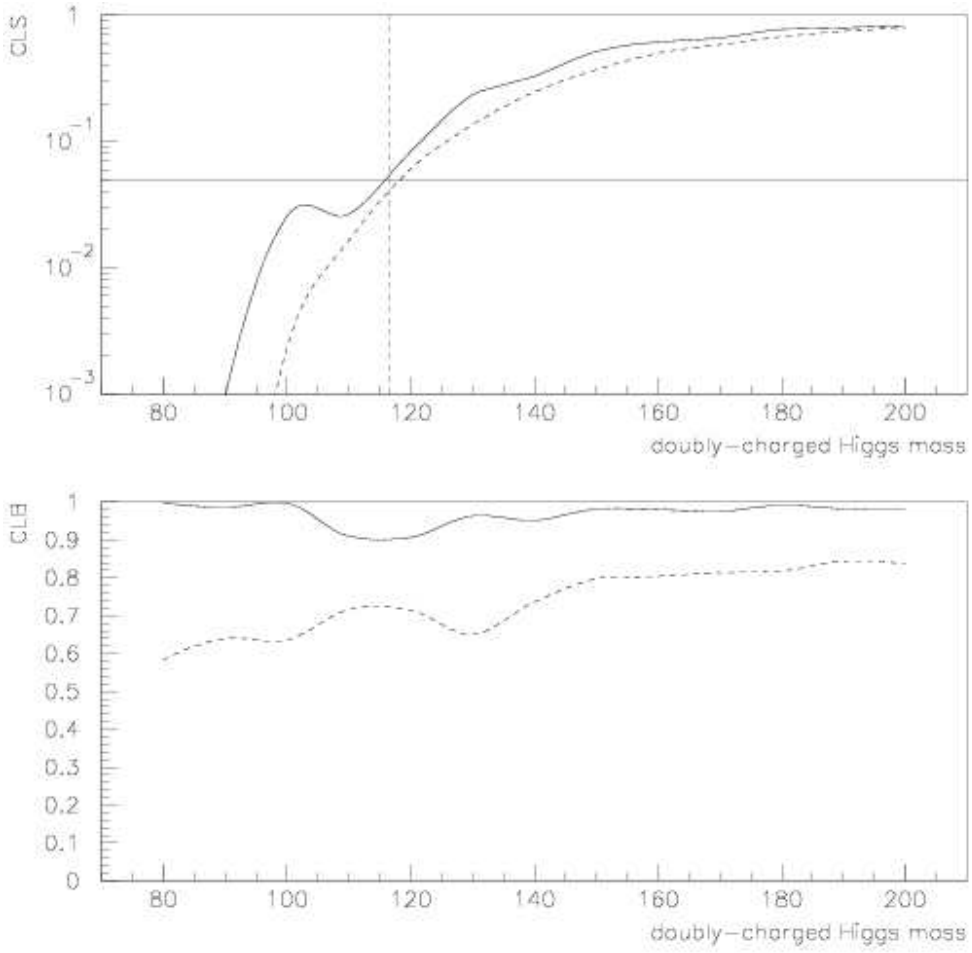

Figure 9.4: Confidence level of the signal (top), $CL_S = CL_{S+B}/CL_B$, and confidence level of the background CL_B (bottom) as a function of the mass $M(H^{\pm\pm})$ of a left-handed doubly-charged Higgs bosons, if the $\Delta\varphi$ cut is applied at 2.1. The dashed curve is the confidence level if no candidate events are taken into account. The mass limit is set at 117 GeV/c^2.

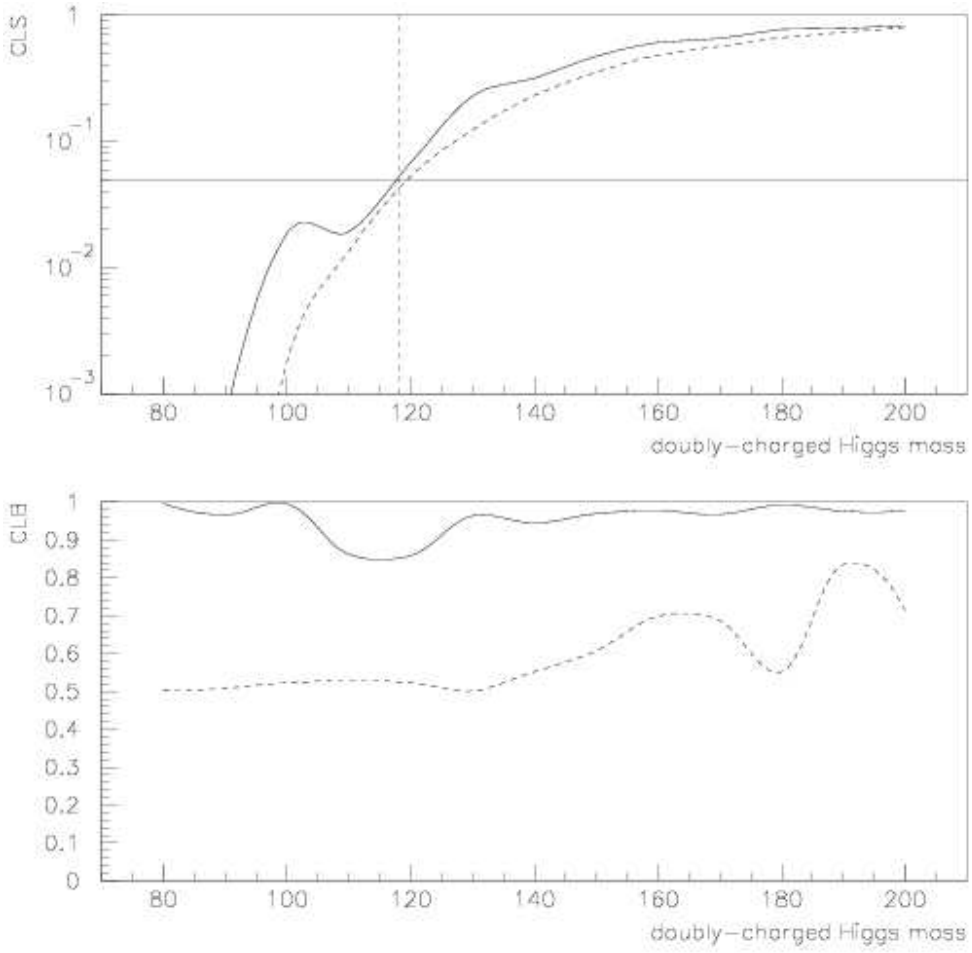

Figure 9.5: Confidence level of the signal (top), $CL_S = CL_{S+B}/CL_B$, and confidence level of the background CL_B (bottom) as a function of the mass $M(H^{\pm\pm})$ of a left-handed doubly-charged Higgs bosons, if the $\Delta\varphi$ cut is applied at 2.51. The dashed curve is the confidence level if no candidate events are taken into account. The mass limit is set at 118 GeV/c^2.

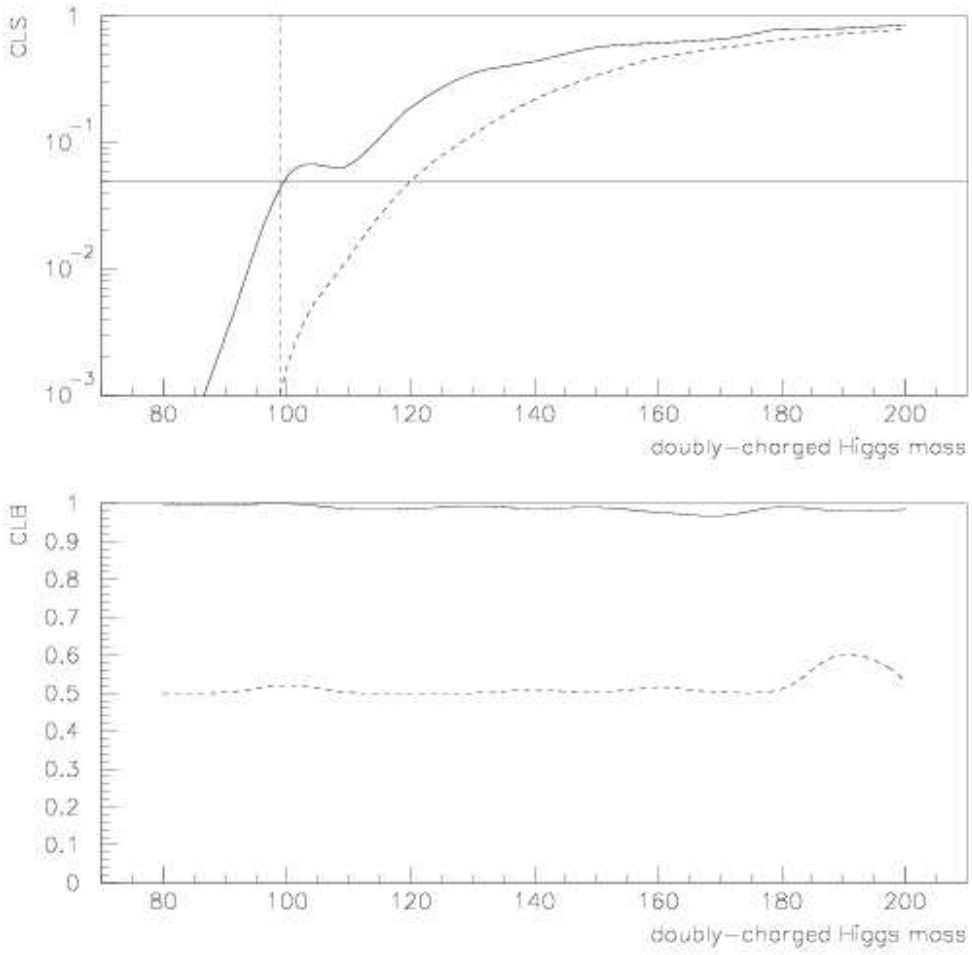

Figure 9.6: Confidence level of the signal (top), $CL_S = CL_{S+B}/CL_B$, and confidence level of the background CL_B (bottom) as a function of the mass $M(H^{\pm\pm})$ of a left-handed doubly-charged Higgs bosons, if the $\Delta\varphi$ cut is applied at π, i.e. no acolinearity cut is applied at all. The dashed curve is the confidence level if no candidate events are taken into account. The mass limit is set at 99 GeV/c^2.

Chapter 10

Candidate events

This chapter lists the kinematic parameters of all doubly-charged Higgs boson candidate events which pass the preselection, isolation, acolinearity and same-charge cuts. Each event is identified by a run and event number. The invariant mass $M(\mu_i\mu_j)$ is calculated based on kinematic properties of the dimuon pair $\{\mu_i, \mu j\}$, only muons that pass the selection criteria (Section 4.3) are considered. All analysis cuts and muon selection criteria have been discussed in Section 4.3.

10.1 Candidate details

Three candidates remain in the data after the final selection. The run and event numbers, as well as the invariant mass combinations between all muons in these events are given in

Table 10.1 and the kinematic properties of the individual muons in Table 10.2. Displays for these candidate events are given in Figures 10.1 - 10.3 in the transverse view ($r\phi$) and in the (rz) view.

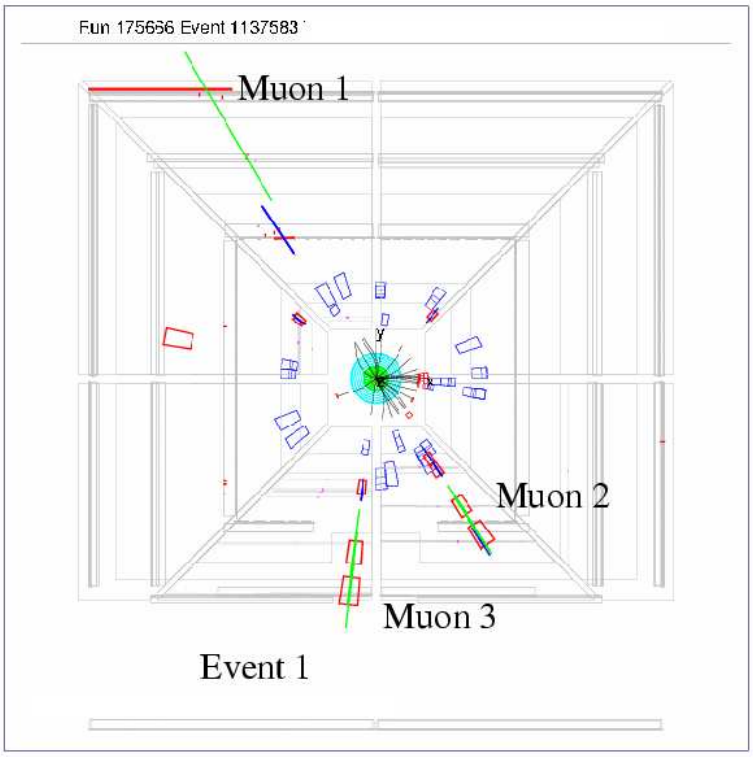

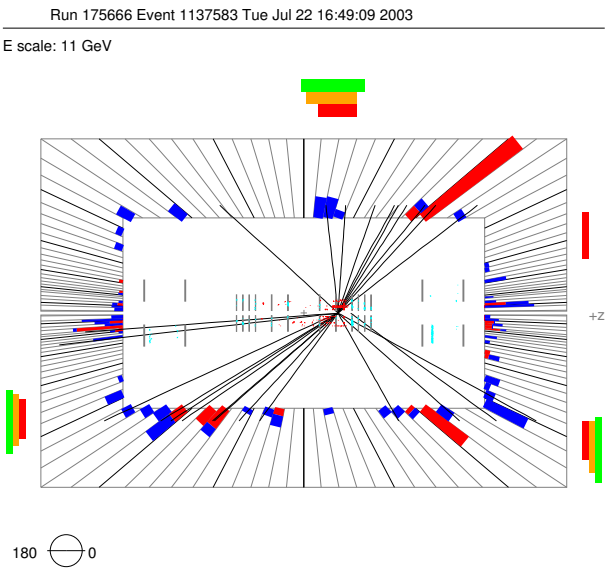

Figure 10.1: Display of candidate event (1) in the transverse (rϕ) view (top) and the (rz) view (bottom).

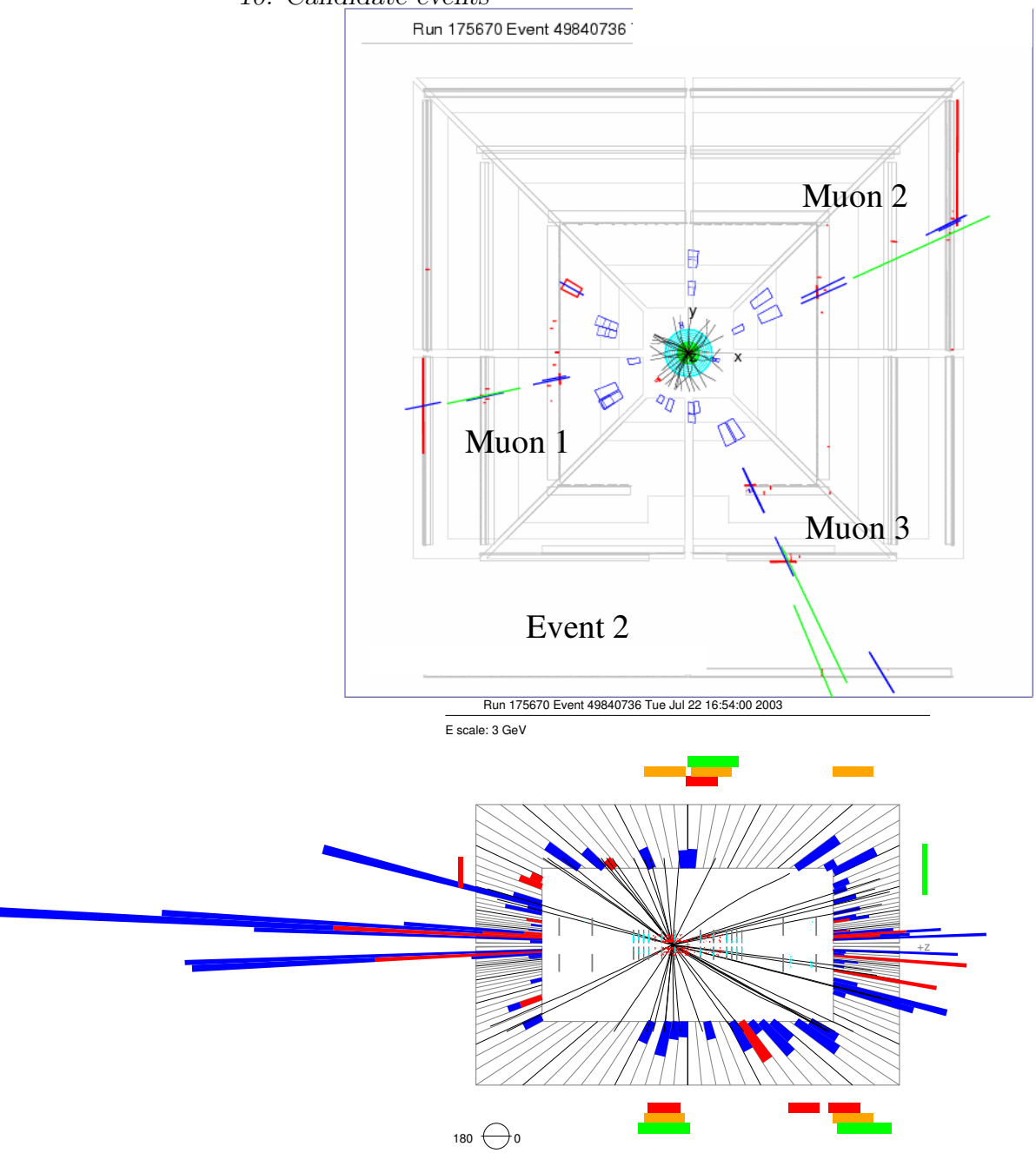

Figure 10.2: Display of candidate event (2) in the transverse (rϕ) view (top) and the (rz) view (bottom).

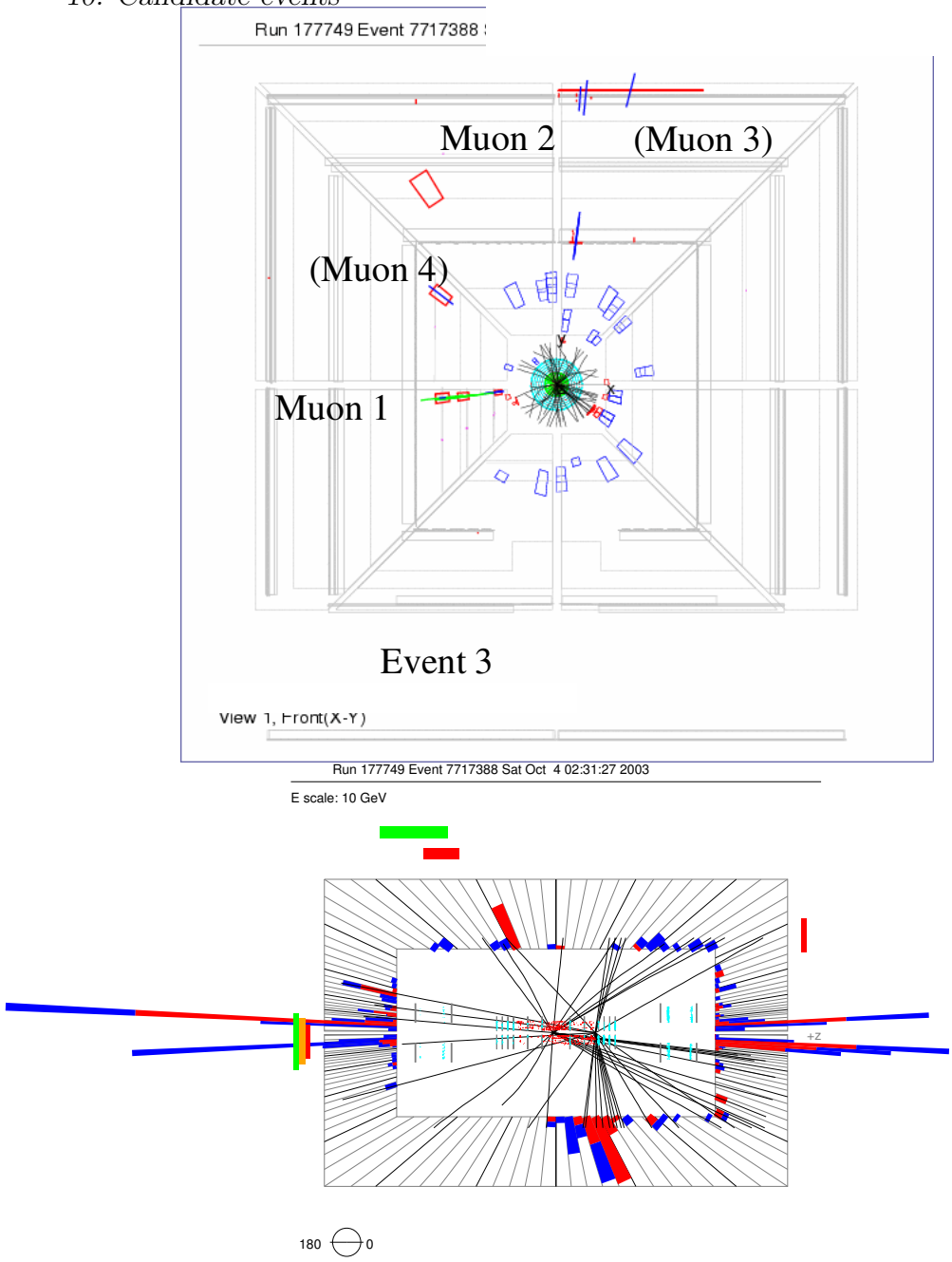

Figure 10.3: Display of candidate event (3) in the transverse (rϕ) view (top) and the (rz) view (bottom).

	Run	Event	$M(\mu_1\mu_2)$	$M(\mu_2\mu_3)$	$M(\mu_1\mu_3)$
(1)	175666	1137583	251(−+)	149(+−)	183(−−)
(2)	175670	49840736	91(−+)	45(+−)	63(−−)
(3)	177749	7717388	62(++)	–	–

Table 10.1: Run, event number and the invariant masses of the three possible pairings of muons for the candidate events. Muons are numbered clockwise in the (rϕ) plane, starting with the muon that is most to the left. The charges of the muons are given in parentheses (charges are calculated from the track curvature measurement in the central tracker's solenoid field).

10.2 Interpretation of candidate events

This section suggests a possible explanation of the candidate event nature. The reasoning is based on information listed in Tables 10.1 and 10.2, all three candidate events were reconstructed both with the p13 and p14 reconstruction version. That offers a new perspective in understanding the third candidate event. As far as the first two events are concerned, no major changes in kinematic variables obtained with the p13 and p14 `d0reco` reconstruction code are found.

10.2.1 First candidate event

Event (1) has two negatively charged muons and one positively charged muon, all with transverse momentum greater than 15 GeV/c. This event also contains a single jet with transverse energy of about 79 GeV/c^2, which deposits $\simeq$ 84% of its energy in the electro-magnetic compartment of the

Muon	Charge	p_{T}^{μ} (GeV/c)	η	ϕ	N_{SMT}	N_{CFT}	Quality
Event (1) Run 175666 event 1137583							
μ_1	-1	273	0.07	2.11	8	16	tight
μ_2	+1	45	-1.52	-0.99	4	16	loose
μ_3	-1	30	1.37	-1.70	3	16	loose
Event (2) Run 175670 event 49840736							
μ_1	-1	52	0.66	-2.95	6	16	loose
μ_2	+1	44	0.08	0.45	8	16	loose
μ_3	-1	24	-0.09	-1.09	6	16	tight
(μ_4)	+1	0.7	-0.62	-1.73	6	16	not selected
Event (3) Run 177749 Event 7717388							
μ_1	+1	36	-2.04	-3.03	7	10	tight
μ_2	+1	25	-0.84	1.44	7	16	tight
(μ_3)	+1	7	0.01	0.60	2	16	not selected
(μ_4)	+1	0.9	7.60	2.41	0	8	not selected

Table 10.2: Transverse momentum p_{T}, charge, pseudorapidity η, azimuthal angle ϕ and number of SMT and CFT hits for all muons in the candidate events. Muons which fail the selection criteria are put in parentheses.

calorimeter. The missing transverse energy in the event is very large, approximately 65 GeV/c^2 without correcting for muon transverse momentum. Table 10.1 gives calculated invariant masses for all dimuon permutations in this event. All three dimuon combinations are far away from the Z boson mass. This is why any explanation of this event by diboson production can be ruled out. All three muons are tight and isolated, they are associated with the same primary vertex (vertex position in the z-coordinate is 27.1 cm), only one primary vertex is reconstructed in this event. The measurement of charges using the muon system agrees with the measurement from the central tracker only for last two muons, the first muon is assigned opposite charges in the central tracker and the muon system. However, no conclusion can be drawn from this fact, since muons are assigned opposite charges in the muon system in roughly 34% of cases, this result is a conclusion of several mass resolution studies performed with $Z \rightarrow \mu\mu$ candidate events. Only about 11% of Monte Carlo muons are asigned a wrong charge in the muon system. Such a poor agreement in data is due to the transverse momentum resolution of the muon system. The hypothesis of a cosmic muon crossing the detector center at the time the event is actually being triggered on is not possible either, because none of the three dimuon permutations satisfies criteria listed in Section 6.6 for cosmic muon candidates. The transverse momentum of the first muon is about 273 GeV/c, that seems to be a little bit too high. Not many tracks are reconstructed with such a high transverse momentum, thus some kind of mis-reconstruction is possible. At this point, there is no satisfactory explanation of what the nature of this event is.

10.2.2 Second candidate event

Event (2) has two negatively charged muons and one positively charged muon. All three muons have transverse momenta well above 15 GeV/c. This event also contains a fourth, positively charged, muon that matches to a low-p_{T} central track. It is reasonable to believe however that this low-p_{T} track is matched to that muon by accident. The fourth muon is not considered in this analysis. All tracks are associated to the same primary vertex, with the z-coordinate at -15.0 cm. It also is the only primary vertex reconstructed in this event. The first muon is tight and the other two muons are loose. All selected muons pass the isolation criteria. There is a nice agreement between the central tracker and muon system measurement in terms of charges. No significant missing transverse energy is observed.

The second candidate event seems to be fully consistent with being a ZZ event, the first diboson event observed at DØ in Run II. The invariant mass calculation supports this idea. There is at least one Z candidate in this event, it does not help to use the muon system information to calculate the invariant mass of the other dimuon pair. The topology suggests that there is yet another dimuon pair consistent with Z boson decaying into muons. The invariant mass calculated for the second dimuon pair is small.

10.2.3 Third candidate event

Event (3) has two positively charged muons, both muons are tight and isolated. Additionally, there are two more muons, they do not pass the muon selection criteria, nor track quality cuts placed on the number of SMT and CFT hits associated with the track. Both tracks come from the same pri-

mary vertex, the z position of the primary (hard-scattering) vertex is 35.2 cm. There are two minimum bias vertices in this event, at -2.7 cm and -3.3 cm in z. Additionally, there is an EM cluster with a transverse momentum of 10.5 GeV/c, it is assigned to the minimum bias vertex at $z = -2.7$ cm, and two jets associated with the other minimum bias vertex at $z = -3.3$ cm. The p_{T} of the leading jet is 65 GeV/c, the p_{T} of the sub-leading jet is 24 GeV/c, approximately.

The highest p_{T} track in the event can be interpreted as a case of charge mis-identification. The η of this track, measured with respect to the primary vertex at $z = 35.2$ cm, is -2.0. This track traverses the CFT overlap region ($|\eta| > 1.63$) and has only 10 CFT hits, there are 7 SMT hits associated with this track. The position of the primary vertex is exactly on the edge of the silicon tracker, the barrels extend up to $|z| = 36$ cm. This track traverses the northern outermost barrel and several F-disks on the way to the fiber tracker. There is a big discrepancy between the transverse momentum measured in the central tracker and the muon system for this track, more than 100 GeV. It is possible due to the muon system resolution. It exceeds the expectation however. The main reason why this track is considered a candidate for a charge mis-identification is that it flips the charge when it is reconstructed with a better version of the `d0reco` code, i.e. with the p14. The kinematic variables of muons in this event reconstructed with p13, p14 reconstruction version, respectively, are given in Table 10.3.

The EM cluster is associated with the first minimum bias vertex in p13, i.e. the one at $z = -2.7$ cm, but with a different minimum bias vertex in p14, i.e. $z = -3.3$ cm. The jet energy does not change from one reconstruc-

Muon Number	Solenoid Charge	Toroid Charge	p_{T}^{μ} (GeV/c)	η	ϕ	N_{SMT}	N_{CFT}	Muon Quality
p13 : Event (3) Run 177749 Event 7717388								
μ_1	+1	+1	36.2	−2.04	−3.03	7	10	tight
μ_2	+1	+1	25.1	−0.84	1.44	7	16	tight
(μ_3)	+1	+1	7.4	0.01	0.60	2	16	not selected
(μ_4)	+1	+1	0.9	7.60	2.41	0	8	not selected
p14 : Event (3) Run 177749 Event 7717388								
μ_1	-1	+1	28.5	−2.04	−3.03	6	10	tight
μ_2	+1	+1	26.8	−0.84	1.44	7	16	tight
(μ_3)	+1	+1	6.8	0.01	−0.60	0	16	not selected
(μ_4)	+1	+1	1.2	0.10	2.34	4	13	not selected

Table 10.3: Transverse momentum p_{T}, central tracker charge, muon system charge, pseudorapidity η, azimuthal angle ϕ and number of SMT and CFT hits for both muons in Event (3), which is charge mis-identification candidate. Muons which fail the selection criteria are put in parentheses.

tion version to another, that is not surprising because there were almost no changes in p14 in terms calorimeter objects reconstruction.

The invariant mass of the dimuon pair is 62 GeV/c^2. It changes to 50 GeV/c^2 when the event is reconstructed with the p14 reconstruction version. Given the fact that the highest p_{T} track is suspected to be mis-reconstructed, one should not use its kinematic parameters to calculate the invariant mass. Instead, the invariant mass can be calculated using the muon system information only, it is 82 GeV/c^2. That is consistent with the Z boson mass. It gives an extra strength the hypothesis of a charge mis-identified $Z(\rightarrow \mu\mu)$+jet event.

Chapter 11

Limit setting

The final step is to take the Monte Carlo samples generated, the data and set the mass limit on doubly-charged Higgs boson mass. This chapter describes an efficient procedure for computing approximate confidence levels for searches for new particles where the expected signal and background levels are small enough to require the use of Poisson statistics. The limit calculations are performed using the programs MCLIMIT [141], it uses Monte Carlo experiments. The results have been cross-checked with the program CONFL10 [142], that uses an analytic approach based on fractional event counting. The strength of the approach used in this analysis is that observed candidates may be distributed over many decay channels with different preselection efficiencies, mass resolutions and different or poorly known background conditions. But they still might be combined, and the upper limits for production rates of particles, or, the probability for an upwards background fluctuation can be computed. Both programs are based on modified Frequentist approach and they provide consistent results. They were used by the CERN LEP Higgs working group. The method used in this analysis

is different from the Bayesian technique for setting of confidence intervals in various DØ Run I [143] searches.

11.1 Confidence Level computation for searches with small statistics

The confidence level computation for searches with small statistics are described in detail in [141] and [142]. The programs are developed to combine easily results of many independent searches for the same particle in different channels because most of the searches are found to be heterogeneous, i.e. many different techniques and different kind of results are reported. The method is independent of discriminating variables which are measured for the candidate events. Most of the model spaces are large, this is why the method needs to be rapid and efficient, so that all possibilities of the model can be explored fully. On the other hand, the method must be conservative, i.e. no spurious discoveries are acceptable.

Frequently, the signals are marginal, and it is therefore more convincing if several channels are combined. That improves the confidence level (CL) significantly, especially if the sensitivity is limited by the collected luminosity and not by the kinematic boundaries.

The method is based on binning the search results (invariant mass, acolinearity etc.) in their discriminant variables and treating each bin as a statistically independent counting search. This uniform representation is then easy to be combined. As it can be seen later in this chapter, this is a strong statement with profound consequences.

The effect of systematic uncertainties in the signal and background models is incorporated in the confidence levels.

11.2 Modified Frequentist Approach Confidence Levels

In this analysis we set the limit at 95 % confidence level (CL). Assuming two hypothesis 'signal+background' and 'background', the experiment should be able to distinguish between them. The 'signal+background' hypothesis is excluded at 95 % if: supposedly the 'signal+background' hypothesis is true, 95 % of experiments like the one performed must look more 'signal+background'-like than the one that was actually performed.

The problem is to find an estimator (also known as a test statistic) which orders the outcome of the experiments by their 'signal+background'- or 'background'-likeness. Such an estimator is a test statistics. In a more mathematical language, for the case of n independent counting search analyses, one may define a test statistic X which discriminates 'signal+background'-like outcomes from 'background'-like ones. An optimal choice for the test statistic is the likelihood ratio [145, 146, 147, 148].

If the estimated signal in the i^{th} channel is s_i, the estimated background is b_i, and the number of observed candidates is d_i, then the likelihood ratio can be written as

$$X = \prod_{i=1}^{n} X_i = \frac{P_{Poisson}\ (\ data \mid signal\ +\ background\ )}{P_{Poisson}\ (\ data \mid background\ )} \tag{11.1}$$

with

$$X_i = \frac{e^{-(s_i+b_i)}(s_i+b_i)^{d_i}}{d_i!} / \frac{e^{-b_i} b_i^{d_i}}{d_i!}. \quad (11.2)$$

The test statistics X has the following property: the joint test statistic for the outcome of two channels is the product of the test statistic of the two channels separately. The test statistics increases monotonically in each channel with the number of candidates d_i. The task of computing confidence levels for experimental searches with one or more discriminating variables measured for each event (e.g. invariant mass, acolinearity) reduces to the case of combining counting-only searches by binning each search analyses' results in the measured variables. Practically, it means that each bin becomes a separate search channel, and it is combined with others. The bottom line is that the expected signal in a given bin of a reconstructed invariant mass then depends on the hypothesized true mass of the doubly-charged Higgs boson and the expected mass resolution. The reconstructed invariant mass as well as the error on its measurement can be binned independently, so that the maximum of available information is preserved.

It is understood from what was said above that the word 'channel' could be freely replaced by the word 'bin' further in the text. Each bin is an independent search channel that can be combined with other channels/bins.

The confidence level for excluding the possibility of a simultaneous presence of new particle production and background is [148]

$$CL_{S+B} = P_{S+B}(X \leq X_{obs}) = \sum_{X(\{d_i'\}) \leq X(\{d_i\})} \prod_{i=1}^{n} \frac{e^{-(s_i+b_i)}(s_i+b_i)^{d_i'}}{d_i'!}, \quad (11.3)$$

where $P_{S+B}(X \leq X_{obs})$ is the probability, that the test statistics is less than or equal to the one observed in the data, under assumption of the

presence of both signal and background at their hypothesized level. The $X(\{d_i\})$ is the test statistics computed for the observed set of candidates in each channel $\{d_i\}$, and the sum runs over all possible final outcomes $\{d_i'\}$ which have test statistics less or equal to the one observed in the data.

The confidence level $(1 - \mathrm{C}L_{\mathrm{S}+B})$ could be used to quote exclusion limits. The disturbing problem are the downward background fluctuations, i.e. any signal, no matter of size, even the background itself (null hypothesis), can be ruled out.

Since the candidates are integers, only a discrete set of confidence levels is possible for a fixed set of s_i and b_i.

Limit calculation involves computing of the confidence level for the background itself,

$$CL_B = P_B(X \leq X_{obs}), \tag{11.4}$$

where the probability sum assumes the presence of the background only. It is the probability that the outcome of experiments would look 'background'-like assuming only 'background' is true.

The cure of downward background fluctuations is the Modified Frequentist Approach. The Bayes theorem [143]

$$P(Hypothesis|Data) = \frac{P(Hypothesis)P(Data|Hypothesis)}{P(Data)} \tag{11.5}$$

is used to rescue the method otherwise based on the Frequentist approach.

The Modified Frequentist confidence level $\mathrm{C}L_{\mathrm{S}}$ is then computed as a ratio [148]

$$\mathrm{C}L_{\mathrm{S}} = \frac{\mathrm{C}L_{\mathrm{S}+B}}{\mathrm{C}L_{\mathrm{B}}}. \tag{11.6}$$

The confidence level is an extension of the common single-channel $CL = 1 - \mathrm{C}L_{\mathrm{S}}$ [149, 150]. In case of a single channel, it actually is the same thing. The expected confidence level is actually a median of many hypothetical experiments. It gives a measure of an experimental sensitivity and it can be used as a tool to compare several experiments.

The confidence level calculation for n channels, each with m possible outcomes, is performed by computing the probability distribution function (PDF) for the test statistic for a set of channels, and iterative combining additional channels by convoluting with the PDFs of their test statistics [141]. The combination of channels is actually a 'channel' with many possible outcomes. The PDF must be sampled at discrete points so that the problem can be numerically solved. The idea is that the results are binned, and each bin is a separate search channel. That allows to have as many reconstruction variables as necessary, or in contrary none at all.

The possible discovery would be seen in $1 - \mathrm{C}L_{\mathrm{B}}$. It indicates the probability that the background could have fluctuated to produce a distribution of candidates similar in terms of signal-likeness to the one observed in the data. In alternative language, $1 - \mathrm{C}L_{\mathrm{B}}$ represents the probability for an upwards fluctuation of the background. This probability depends however on the signal hypothesis very much. Channels with a small s_i/b_i do not contribute to the calculation of $\mathrm{C}L_{\mathrm{B}}$ as much as those with large s_i/b_i. The computation of the reconstructed mass provides an excellent discrimination among competing signal hypotheses. The excess of candidates might be misleading in

this case.

Alternatively, we can work with event weights

$$ln(X) = -\sum_{n_{bins}} s_i + \sum_{n_{bins}} n_i \ (\ ln(1 + \frac{s_i}{b_i})\ ), \tag{11.7}$$

where

$$w_i = ln(\ 1 + \frac{s_i}{b_i}\ ) \tag{11.8}$$

can be understood as an event weight. Another example of an estimator (test statistics X) is the Weighted Event Counting used in CONFL10 program [142]

$$X = \sum_i \frac{d_i}{C + \frac{b_i}{s_i}} \tag{11.9}$$

where C is arbitrary, a value equal to one is chosen to optimize the expected limit. Yet another example of an estimator is the PDG Formula that has been frequently used in analyses before 1996:

$$CL = 1 - \frac{\sum_{i=1}^{n} \frac{e^{-(s+b)}\ (s+b)^i}{i!}}{\sum_{i=1}^{n} \frac{e^{-b}\ b^i}{i!}} = 1 - CL_S. \tag{11.10}$$

The systematic uncertainties on signal and background are accommodated by a generalization of the method of Cousins and Highland [141, 144]. The idea is to choose randomly s and b within their uncertainties. The outcome under each chosen s and b is treated as a separate possible outcome of the experiment, it is weighted by its probability to happen, and it is combined using the PDFs for the test statistics for a set of channels. The PDF of the data estimator is found under varying s and b assumptions, and folded in with the outcome PDF.

Both programs (MCLIMIT and CONFL10) have a feature that allows to include systematical uncertainties. The limits become worse, on the other hand, assuming that probability distributions are Gaussian, with the lower tail cut off at zero, so that negative s and b are not allowed, leads in general to small changes in the limits.

11.3 Calculation of limits

Both programs discussed in the previous section provide the confidence level for the background hypothesis, CL_{B}, and the confidence level for the signal with background hypothesis, CL_{S+B}, taking into account the expected mass distribution for the signal and for the background and the mass resolution [151].

The expected signal rate as a function of the Higgs mass is given by the NLO cross section [55], the signal efficiencies (Section 7), and the measured luminosity (Section 4).

Since the mass dependent confidence levels are determined in mass intervals of 1 GeV/c^2, whereas the NLO cross sections are given in 10 GeV/c^2 intervals, the logarithmic interpolation is used to obtain the cross sections for each mass interval. The logarithmic interpolation is applied because the shape of the NLO production cross section as a function of the doubly-charged Higgs mass is described by the falling exponential rather well. That can be inferred from Figure 2.7.

In order to parametrize the mass resolution, the sum of two Gaussian distributions (g_i)

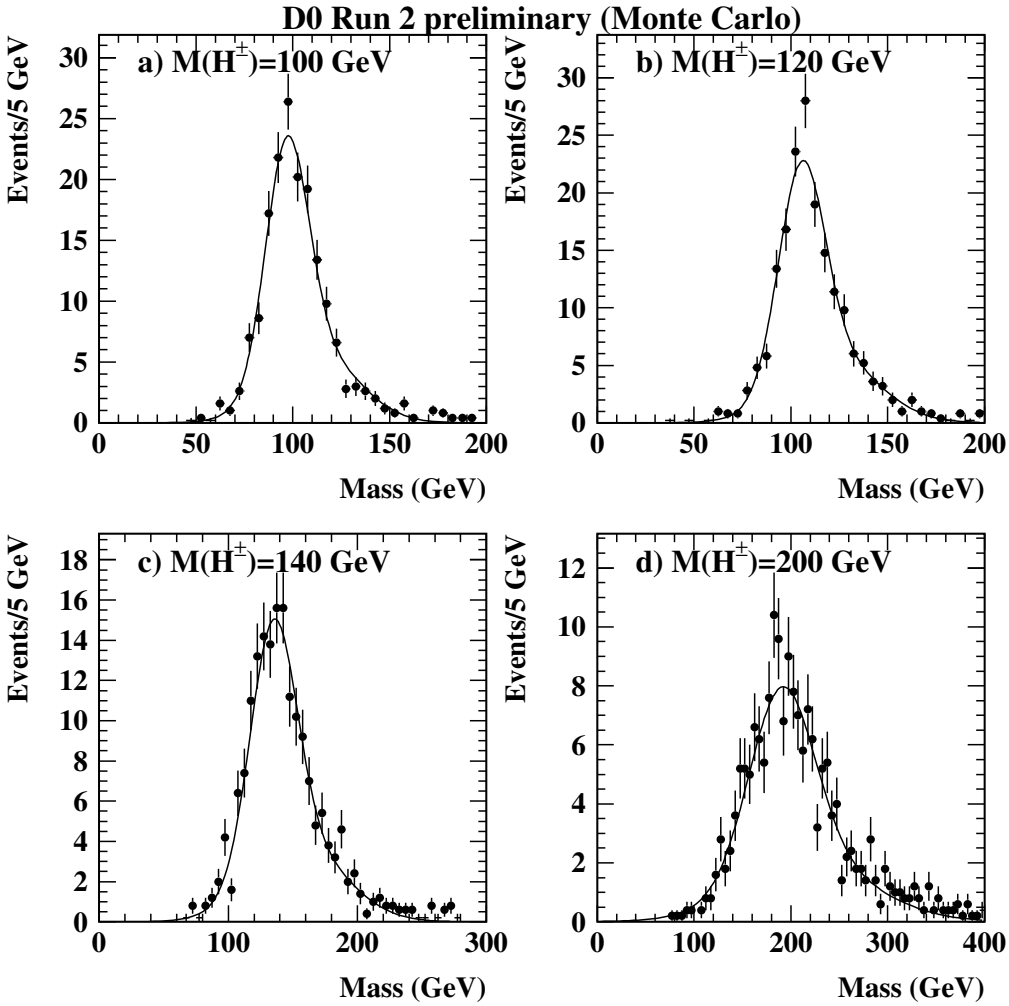

Figure 11.1: The reconstructed dimuon invariant mass after the full detector simulation for events with doubly-charged Higgs bosons generated at masses of a) $M(\mathrm{H}^{\pm\pm}) = 100$ GeV/c^2, b) $M(\mathrm{H}^{\pm\pm}) = 120$ GeV/c^2, c) $M(\mathrm{H}^{\pm\pm}) = 140$ GeV/c^2, and d) $M(\mathrm{H}^{\pm\pm}) = 200$ GeV/c^2.

$$f(M) \propto g_1(\overline{M}_1, \hat{\sigma}_1) + r g_2(\overline{M}_2, \hat{\sigma}_2) \tag{11.11}$$

is chosen for simplicity. This function is fitted to the reconstructed mass M for the signal same-charged dimuon combinations, where $\overline{M}_1 = M(\mathrm{H}^{\pm\pm})$, $\overline{M}_2 = 1.15\ M(\mathrm{H}^{\pm\pm})$, $r = 0.3$, and $\hat{\sigma}_2 = 2\hat{\sigma}_1$. $M(\mathrm{H}^{\pm\pm})$ is the generated mass for the doubly-charged Higgs boson. To facilitate the interpolation of the resolution function between different mass points, only $\hat{\sigma}_1$ is fitted as a function of $M(\mathrm{H}^{\pm\pm})$. The result of the fit is given in Table 7.7 and the distributions are shown in Figure 11.1.

The 95% confidence level upper limit is determined from the confidence level of the signal, $\mathrm{C}L_{\mathrm{S}}$, which is defined by Equation 11.6. The mass limit is given by requiring $\mathrm{C}L_{\mathrm{S}} = 0.05$.

By definition the hypothesis of having a signal plus background is excluded at the 95% confidence level if $\mathrm{C}L_{\mathrm{S}+B} < 0.05$. Statistical downward fluctuations of the background can lead to a deficit of observed events, which can be inconsistent with the expected background. This can cause the signal+background hypothesis to be excluded even when the expected signal rate is below the sensitivity of the experiment.

The confidence level $\mathrm{C}L_{\mathrm{S}}$ is defined to regulate this behavior of $\mathrm{C}L_{\mathrm{S}+B}$. Since $\mathrm{C}L_{\mathrm{B}} \leq 1$, the resulting limit using $\mathrm{C}L_{\mathrm{S}}$ is always more conservative than for $\mathrm{C}L_{\mathrm{S}+B}$.

Chapter 12

Systematic uncertainties

The sources of systematic uncertainties are discussed in this chapter. The sources can be divided into two categories: (a) systematic uncertainties that are related to the normalization of Monte Carlo to data, (b) systematic uncertainties contributing from other sources, e.g. fits and interpolations. Both contributions have to be taken into account to set the correct limit on the mass of a doubly-charged Higgs boson in this analysis. The mechanism of systematic error implementation in the limit calculation programs is described in Section 11.2.

12.1 Systematic uncertainty of normalization

The following sources of systematic uncertainty affecting the normalization of the signal are taken into account in this analysis:

- The integrated luminosity $\int \mathcal{L}$ is calculated in two different ways. First, $\int \mathcal{L} = 113$ pb^{-1} is obtained using the DØ luminosity system. The systematic uncertainty on this luminosity is estimated to be 6.5% [152].

In addition, the data can be normalized to the inclusive cross section for $Z \to \mu^+\mu^-$ production using the dimuon data after selection S3, i.e. without requiring both muons to have same charge. This cross section is within 10% of the NLO prediction. The measured value of $BR \times \sigma\ (Z \to \mu^+\mu^-)$ is given in Equation 6.23, and its time dependence is shown in Figure 6.15.

- The theoretical uncertainty on the NLO $H^{\pm\pm}$ production cross section originates from the choice of parton distribution functions and variations of the renormalization and factorization scales. The total contribution is about 10% [55]. The details are given in Section 2.2.2.

- The efficiencies determined using the $Z \to \mu^+\mu^-$ data are applied in the Monte Carlo to obtain the signal and background efficiencies. The total uncertainty on the efficiency is derived from the uncertainties given in Section 6. It is dominated by the uncertainties on the efficiency to reconstruct an isolated muon and on the trigger efficiency. The total uncertainty amounts to 5%. The effect from choosing different parton distribution functions is found to be negligible.

- The statistical uncertainty on the Monte Carlo background rate is 27%. Statistical uncertainties for every Monte Carlo sample are given in Table 8.1. Adding the systematic uncertainty of 25% on the measured $b\overline{b}$ cross section [127] yields a total uncertainty on the background rate of 50%.

As it has been mentioned in Section 11, the systematic uncertainties on signal and background are taken into account in the limit calculation

by averaging over possible values of signal and background, given by their probability distributions, which are assumed to be Gaussian [141]. This procedure weakens the limit on the mass by about 1 GeV/c^2.

12.2 Other systematic uncertainties

In addition, the following sources of systematic uncertainties were examined. However their contribution to the limit setting was found to be negligible:

- A linear interpolation between mass points was used for the NLO cross sections of signal instead of a logarithmic interpolation. The differences are of the order of a few percent, which is negligible as compared to other systematical errors.

- The width of the two Gaussian distributions used to parametrize the mass resolution was increased by 20%. This is a conservative estimate for the difference in mass resolution between the data and Monte Carlo observed in $Z \rightarrow \mu^+\mu^-$ events. A good agreement between the data and Monte Carlo $Z \rightarrow \mu^+\mu^-$ sample in terms of mass resolution is demonstrated in Figure 7.1a. Indeed, it does not necessarily have to be the case for higher doubly-charged Higgs masses. Here the agreement might be much worse. This test shows however that the effect of mass resolution is not crucial in this analysis and that other sources of systematic uncertainties are going to be dominant.

Chapter 13

Results and Conclusions

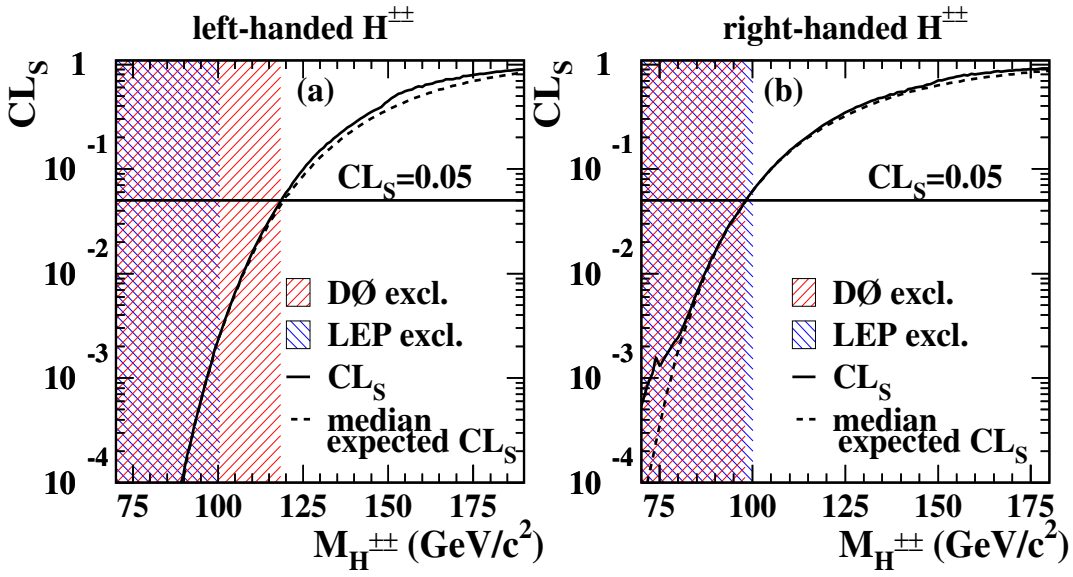

Figure 13.1: Confidence level of the signal, $CL_{S} = CL_{S+B}/CL_{B}$, as a function of the mass $M(H^{\pm\pm})$ of a) left-handed and b) right-handed doubly-charged Higgs bosons. The mass region below 100.5 (100.1) GeV/c^2 is excluded by LEP. The impact of systematic uncertainties is included in the limits. The dashed curve shows median expected CL_{S} for no signal.

In Figure 13.1 (a) and (b) the confidence level for signal, $CL_S = CL_{S+B}/CL_B$, is shown as a function of the doubly-charged Higgs boson mass $M(H^{\pm\pm})$. The median expected CL_S given the data sample luminosity indicates the sensitivity of the experiment under assumption there is no signal.

Due to the experimental resolution and the mass dependent signal production cross section, the higher mass candidate affects the shape of the CL_S result near the mass of 150 GeV/c^2 and the lower mass candidates the shape around 80 GeV/c^2. At the same time it can be observed from Figure 13.1 that the contribution of both candidates does not peak at around their invariant mass value, but much lower. This is the consequence of the doubly-charged Higgs boson production cross section dependence on the mass of a doubly-charged Higgs, it can be described nearly as a falling exponential. The limit setting program tends to shift the contribution of each candidate in the direction of a higher cross section, i.e. shift it to the left in Figure 13.1. As a result, the contribution from candidate events is not symmetric, but not only that, it is skewed to one side.

Figure 13.1 also demonstrates that none of the candidates affects the measurement in the mass region $100 - 120$ GeV/c^2. That is not surprising because the mass resolution is too small for both $H^{\pm\pm}$ candidates to contribute significantly in that interval. As soon as the larger data sample is collected, the higher mass candidate event, i.e. Event (1) in Section 10, Table 10.1, is going to affect the measurement. The expectation for the end of the year 2004, in terms of integrated luminosity, is $\int \mathcal{L} > 0.5$ fb^{-1}. The charge mis-identified $Z \rightarrow \mu^+\mu^-$ events are reconstructed with higher invariant mass because one of the track's transverse momentum is reconstructed

wrong, and the muon transverse momentum is then much larger than what the particles's momentum actually has been. These events represent an eminent danger for this analysis because they most likely will contribute in a region where one desires to set a competitive limit in. This issue has been discussed in Section 7.

Taking into account the systematic uncertainties described in Section 12, a lower mass limit of 118.6 GeV is obtained for a left-handed and a mass limit of 98.1 GeV/c^2 for a right-handed doubly-charged Higgs boson. This significantly extends the current limit of $M(\mathrm{H}^{\pm\pm}) > 100.5$ GeV for left-handed doubly-charged Higgs bosons from OPAL [32] assuming 100% branching into muons, hypercharge $Y = |2|$, and Yukawa couplings[1] $h_{\mu\mu} > 10^{-7}$. Both mass limits are related to the production cross section of a doubly-charged Higgs boson. The production cross section limits are ≤ 60 fb for a left-handed, and ≤ 59 fb for a right-handed doubly-charged Higgs boson.

[1]This limit is calculated from the decay width of $\mathrm{H}^{\pm\pm}$ into leptons given in Equation 2.5 in Chapter 2, for $M_{\mathrm{H}^{\pm\pm}} > 100$ GeV/c^2 and under assumption that the $\mathrm{H}^{\pm\pm}$ decays less than 1 cm away from the primary vertex.

Appendix A

SMT cluster efficiencies

The ability of the DØ detector to examine a large number of physics channels relies on high performance tracking. The precise coordinate measurement provided by the silicon vertex detector is essential for many physics processes. Physics of the silicon tracker is quite complex and understanding of its performance is a very involved subject. It is important however to understand all possible aspects in a great level of detail. In our study of the SMT cluster efficiencies, we pursue several goals: (a) devise a method to calculate cluster efficiencies precisely, (b) map out all the problematic devices, (c) understand dependence of SMT cluster efficiencies on a broad scale of parameters, such as HV biases, noise levels, SVXIIe chip parameters settings, radiation dose, number of dead and noisy strips, etc.

A.1 Method of SMT cluster efficiency calculation

All clusters used in this study are 1-dimensional, i.e. cluster efficiencies for p- and n-side can be calculated separately. The method can be described as follows:

- CFT only tracks are propagated to SMT, these tracks are stored in chunk 201 [155].
- one layer of the silicon tracker is skipped at the time
- good tracks are selected, they serve as a tool to measure SMT cluster efficiency, even a hard quality cut can be applied without biasing the measurement
- a window inside the conture around the track position is searched for presence of the cluster
- cluster efficiency is equal to the number of tracks with a matched cluster divided by the total number of all selected tracks

To select good isolated tracks, in order to have an unbiased measurement, this set of criteria is applied:

- number of hits (SMT+CFT) is more than 16
- $DCA < 300$ microns. DCA is corrected for the beam position.
- $p_{\mathrm{T}} > 1$ GeV/c

- the 'road method' is applied to chose isolated tracks, i.e. no more than one hit is allowed within the 11 σ_{track} window around the track, where σ_{track} is the uncertainty calculated by the tracking algorithm code on each surface, i.e. its value is different for each tested device.

- size of the window, where the efficiency is defined, is 5 σ_{res}, the value σ_{res} is different for the p-side and for the 2° and 90° devices on the n-side. The resolutions obtained in this data sample are: (55 ± 2) μm on the p-side, (257 ± 11) μm on the 2° n-side and (55 ± 1) μm on the 90° n-side. The choice of the 5 σ_{res} window was carefully decided based on the following study: dependence of cluster efficiency on the size of the n σ_{res} window, where n is varies from one to ten. The dependence is nearly tangents hyperbolic. The 5 σ_{res} window is the point on the curve where the cluster efficiency starts to saturate, and is almost independent of the size of the window.

The data used in this study are from run 162049 (3k events) for barrel cluster efficiency studies, and run 163493, no layers are skipped (30k events) for F-disk cluster efficiency studies. It is possible to calculate cluster efficiency only for the inner F-disks, i.e. for disks 5, 6, 7 and 8, because only there is a sufficient number of tracks crossing barrels. Outer F-disks (disks 1 to 4 and 9 to 12) do not have enough tracks crossing barrels, this is why a measurement is nearly impossible given the number of events we can reconstruct on `clued0`. It takes 8 hours of reconstruction.

A.2 Estimation of uncertainties on cluster efficiency measurements

It is important to understand uncertainty on the cluster efficiency measurement. The uncertainty is going to be smaller with increasing number of tracks that are selected to calculate the cluster efficiency. The errors must be binomial. We are using the following formula to estimate cluster efficiency uncertainties

$$err^2 = \frac{(\epsilon + err) \cdot (1 - \epsilon + err)}{n}, \tag{1.1}$$

where err is the uncertainty on the cluster efficiency ϵ, cluster efficiency $\epsilon = m/n$ is the ratio of the number of tracks with a matched cluster m and the total number of all selected tracks n. By solving this quadratic equation, one obtains a formula that prescribes how to estimate uncertainties on cluster efficiencies:

$$err = \frac{-1 + 2\epsilon \pm \sqrt{(2\epsilon - 1)^2 - 4(n+1)(\epsilon^2 - \epsilon)}}{2(n+1)}. \tag{1.2}$$

Indeed, only positive roots are considered as uncertainties on cluster efficiency measurements.

There are two important effects that contribute to cluster efficiency calculation:

- 'fake tracks' - tracks found by the tracking algorithm, they are typically a product of the instrumental noise in the tracker. These tracks are not real, hits that are associated to those tracks only create a pattern that resembles a real track.

- 'fake clusters' - clusters built by the clustering tool from the instrumental noise in the detector. These are not the real hits. The ADC information read out from some fibers only exceeds a threshold downloaded to the readout chips for the sparse readout. Such a fiber is 'fired' and thus considered as a candidate for the hit.

The fake tracks contribute to cluster inefficiency, i.e. they lower cluster efficiency. A fake track does not necessarily need to have a hit associated to it on every layer. Different situation is with the noise clusters. In contrary, they contribute to cluster efficiency. If there is a fake (= noise) cluster in the vicinity of the track, it is considered to be a hit, and it is immediately associated to a track by the tracking algorithm.

It was estimated earlier that the amount of fake tracks in the data is of the order of one percent [156]. This number is significantly reduced by requiring a larger number of SMT and CFT hits associated to selected tracks. As a result, the contribution to a cluster efficiency measurement from fake tracks, is less than 0.2%. This number is typically smaller than the uncertainty on the measurement, see Figures 1.1 or 1.2.

The contribution of 'fake clusters' (= noise clusters) to cluster efficiency can be estimated as

$$inefficiency \simeq (1-\epsilon) \times \frac{size\ of\ the\ window}{width\ of\ the\ device} \times \langle no.\ of.\ clusters\ per\ device \rangle \tag{1.3}$$

On average there are about $4-5$ clusters per device, which is about 2 cm wide. This effect can be approximated by less than 0.2%, which is safely under the precision of the method.

A.3 SMT cluster efficiencies

SMT cluster efficiencies for barrels 2 and 5, both for p- and n-side, are shown in Figures 1.1 and 1.2. Values are shown with errors (in brackets) on the last digit for each device that was read out. The devices that are disabled from the read out are black, the ones with cluster efficiency less than 80% are high-lighted in blue and devices with high cluster efficiencies are painted in red.

Generally speaking, cluster efficiencies for ladders (devices in barrels are also called 'ladders') are very high, above 95%. Cluster efficiency distribution can be seen in Figure 1.3. This statement is valid both for p-side and n-side. Only a few devices show a low cluster efficiency. It is fairly likely that these devices did experience some kind of readout problem.

SMT cluster efficiency measured with F-disk wedges (devices in disks are also called 'wedges') is much worse. Approximately 30% of all F-wedges have cluster efficiency lower than 20%. The rest has efficiency higher than 80%. However, even for the well performing wedges is the cluster efficiency lower than expected. Cluster efficiencies measured in F-disks should be comparable to the ones obtained for ladders. It can be inferred from Figure 1.4 that this is not the situation.

The explanation is an effect called microdischarges. It was already noticed during the initial testing [164] that number of devices exhibited breakdown sensitive to the voltage applied on the p-side of the device. The breakdown is due to the avalanche breakdown of the p-n junction when the potential between the negatively biased p-implant and grounded AC pad increases the junction field. This was in fact confirmed by measuring the temperature

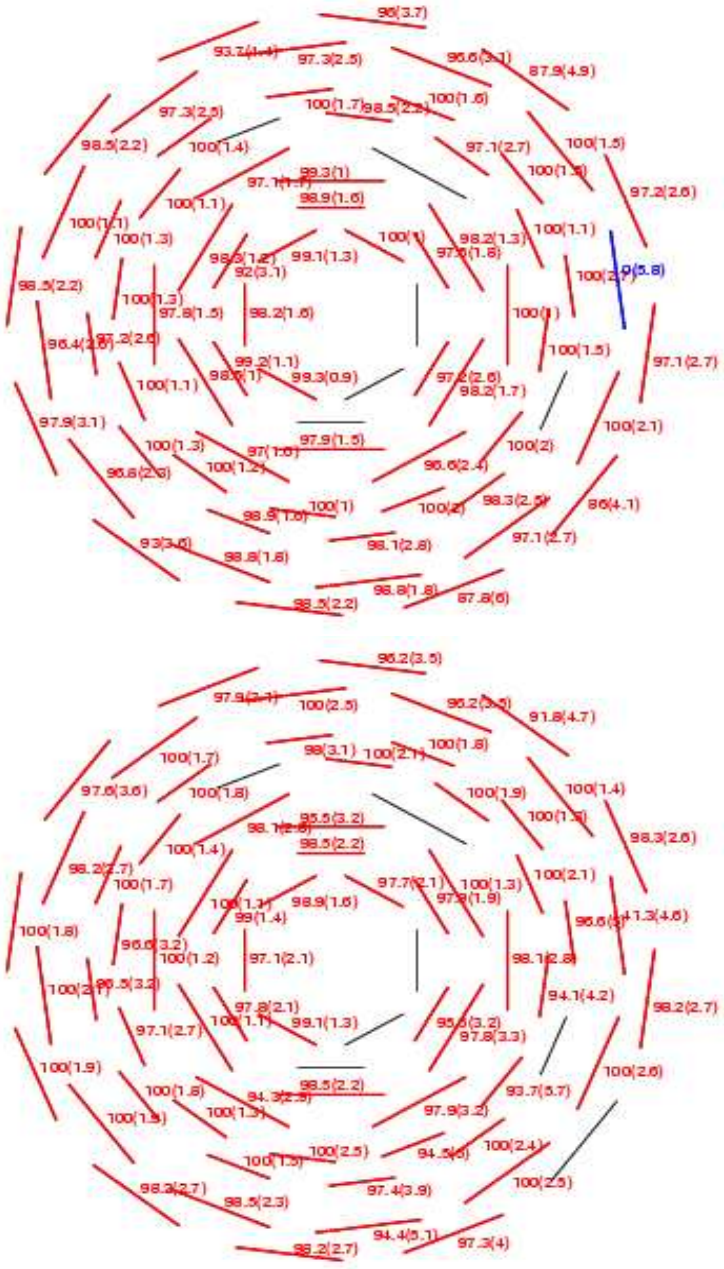

Figure 1.1: SMT cluster efficiencies for devices in barrel 2, p-side (top) and n-side (bottom).

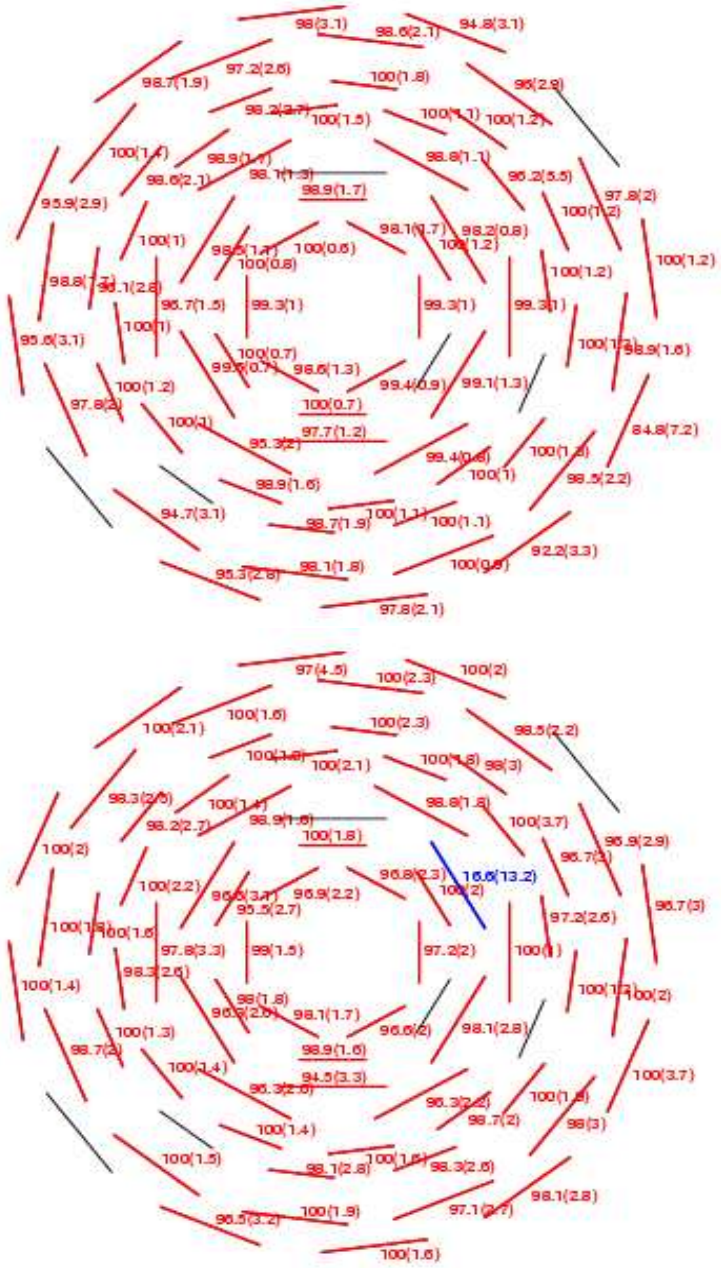

Figure 1.2: SMT cluster efficiencies for devices in barrel 5, p-side (top) and n-side (bottom).

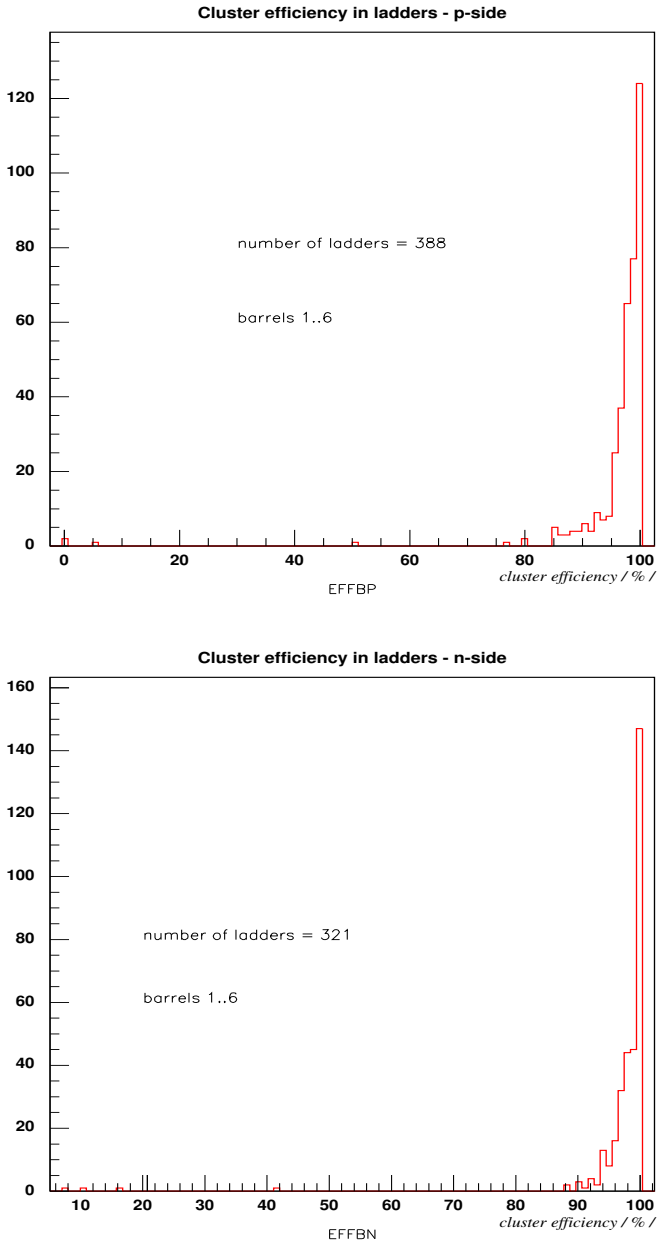

Figure 1.3: Distribution of cluster efficiencies for devices in SMT barrels 1 to 6, p-side (top) and n-side (bottom).

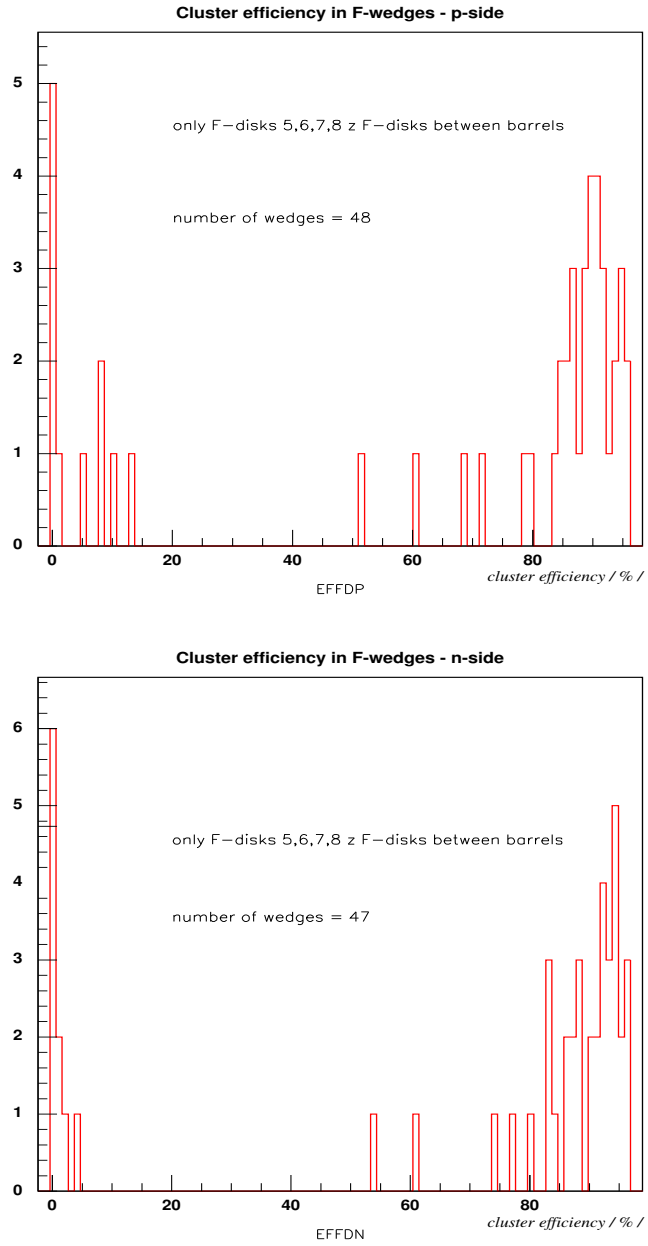

Figure 1.4: Distribution of cluster efficiencies for inner F-disks (disks 5, 6, 7 and 8), p-side (top) and n-side (bottom).

dependence of the associated current. The current increases with the temperature due to the increasing mobility of carriers. The breakdown is worst for devices which have misaligned implants and AC coupling strips.

Central disks are double-sided devices, their pitch is 50 microns on the p-side and 62.5 microns on the n-side. They were manufactured by two companies: Micron and Eurisys. Detectors produced by Micron were tested at the Micron factory by DØ personnel and Eurisys were tested by the company. In-process testing of n-side strips at Micron was introduced to identify problem described above at early stages of the processing.

Table 1.1 lists cluster efficiencies measured for F-wedges. The two innermost disks (disks 6 and 7) are made by Eurisys, outer central F-disks (disks 5 and 8) are made by Micron. Eurisys devices have a better performance than Micron devices in terms of cluster efficiency. That can be also seen in the Table.

A.4 Readout abort feature ON in crate 0×61

Readout abort feature was accidentally turned ON for the VRB readout crate 0×61 in run 165795. It means that if the signal occupancy was higher than some preset threshold, the chip ignored the rest of the readout. If the threshold is set correctly, it would not make any difference, however if the threshold was incorrect, for some devices, it would inevitably mean the loss of data. This feature might represent a hit to cluster efficiency. Unfortunately, this mistake meant loss of the data, on the other hand, it represents a unique opportunity for understanding of how is the readout affected.

There are two scenarios of how the cluster efficiency behavior:

F-disk number	wedge	efficiency (%)	error (%)	F-disk number	wedge	efficiency (%)	error (%)
5	1	85.2	2.1	7	1	93.8	0.8
5	2	88.3	1.5	7	2	94.4	0.8
5	3	79.8	2.1	7	3	95.1	0.7
5	4	84.8	1.8	7	4	93.9	0.9
5	5	72.1	1.6	7	5	90.6	1.4
5	6	91.3	1.3	7	6	94.8	0.7
5	7	86.8	1.6	7	7	96.0	0.7
5	8	90.0	1.5	7	8	92.3	1.0
5	9	92.8	1.1	7	9	95.3	0.7
5	10	10.0	1.6	7	10	88.4	2.0
5	11	88.2	1.8	7	11	86.1	1.7
5	12	86.6	2.3	7	12	90.6	1.1
6	1	60.9	1.3	8	1	8.7	1.6
6	2	86.3	1.2	8	2	88.5	1.8
6	3	8.5	2.5	8	3	0.0	50.0
6	4	13.6	3.1	8	4	91.8	1.5
6	5	78.7	1.6	8	5	0.0	50.0
6	6	51.5	1.8	8	6	0.0	50.0
6	7	91.6	1.1	8	7	91.0	1.4
6	8	68.5	1.2	8	8	89.9	1.6
6	9	0.0	50.0	8	9	89.6	1.5
6	10	0.0	16.7	8	10	89.3	1.5
6	11	0.9	0.6	8	11	84.0	1.2
6	12	5.2	1.1	8	12	85.9	2.2

Table 1.1: Cluster efficiencies for inner F-disks (disks 5 - 8), p-sides only.

- **Pessimistic scenario:**

  If the occupancy exceeds the preset threshold, part of the readout is going to be dropped, clusters could be lost. As a result, cluster efficiency drops significantly.

- **Optimistic scenario:**

  If the occupancy is lower than the threshold, nothing happens. There is no difference in cluster efficiency between the sector affected and other parts of the detector.

- **Realistic scenario:**

  The occupancy is relatively low, but sometimes it is above the threshold. Most of devices are not affected, majority of the time. However, there are noisy devices and additionally, the coherent noise effect has been observed. The coherent noise demonstrates as a collective jump of pedestals. This is why the efficiency drop is not going to manifest strongly and only a moderate drop in cluster efficiencies is observed. For noisy devices, the readout is dropped only occasionally, in some events. The difference in cluster efficiencies could be of the order of a few percent.

We have reconstructed about 3k events from run 162049, where the readout abort feature was OFF in all crates, and run 165795, where the readout abort feature was ON for the VRB readout crate 0×61, the rest was OFF. The affected sector is $-60° < \varphi < 0°$. Barrels 1, 2 and 3 are not affected by the readout abort ON feature. They can serve as an independent measurement for both runs.

The reconstructed beam position is $(x, y) = (-280\ \mu m, 360\ \mu m)$.

There seems to be an apparent drop of $2-3\%$ in the affected crate Ø $\times 61$. However, it is of the same order as the error on the measurement, and hence no strong conclusion can be made. Nevertheless, we believe that the 'realistic scenario' is an explanation for the observed drop in cluster efficiencies in the crate affected by the abort feature ON.

A.5 Selection of the optimal ADC cut applied on a per strip and per cluster basis

SMT cluster efficiency studies performed above can also help to choose the optimal ADC cut applied on a per strip and per cluster basis. The values considered are: 4/8, 8/8, 4/10 and 4/12 ADC cuts. These cuts are applied in the offline event reconstruction code. This study was performed only for devices in inner barrels, i.e. barrels 2 to 5 are considered, in layers 1 and 2, on the p-sides only, in order not to bias the measurement. The results are shown in Table 1.2.

Cluster efficiencies differ only marginally, given the size of the error, there hardly is any difference. However, it has been observed that the ADC cut applied at 8/8 per strip/cluster gives the highest cluster efficiency among those considered. The variation of the contribution from noise clusters to cluster efficiency is negligible, it can hardly give an explanation for a change of cluster efficiency. Even such a small change in cluster efficiency as the one observed, must be a consequence of the change of the ADC cut applied to readout strips and reconstructed clusters.

ADC cut	efficiency (%)	avg. no. of clusters per device	fake cluster contribution (%)
4/8	97.3(2)	4.13	0.17
4/10	97.1(2)	4.08	0.18
4/12	96.8(2)	3.95	0.15
8/8	97.6(2)	4.25	0.19

Table 1.2: SMT cluster efficiencies for several ADC cuts applied on a per strip/cluster basis. Average number of clusters per device is calculated and the contribution of noise cluster to the efficiency is estimated. Only inner barrels (barrel 2 to 5), layers 1 and 2, p-sides, are used in this calculation in order not to introduce any bias to the measurement.

When applying the harder ADC cut 4/12, as compared to the 8/8 cut, we loose about 2.4% of all selected tracks. This is perfectly consistent with the observed decrease of cluster efficiency, by approximately 0.7% ($= \sqrt[3]{0.976^3 - 0.969^3}$), on each SMT layer.

Appendix B

CFT cluster efficiencies

This chapter describes a method of calculating CFT cluster efficiencies. Clusters are building blocks for a tracking algorithm, tracking code uses them to find and fit tracks. The better are their properties, i.e. cluster positions and uncertainties on their positions, known and understood, the better is the performance of the track reconstruction code. It is important to know and monitor periodically cluster efficiencies, because they can serve as an important tool of understanding performance of the detector, finding hidden problems and possible biases of the tracking algorithm, and debug the detector. This study turned out to be successful, since many problems were found and understood, both on the hardware and software level. The performance of the tracker has been also improved using results of this study, e.g. cluster efficiencies are compared for runs before and after the change in timing.

B.1 Method of CFT cluster efficiency calculation

The cluster efficiency method starts with choosing CFT stereo tracks, which are kept in chunk 201 [155]. One layer of CFT, one out of 16 CFT layers, is skipped at the time. This is the layer, the efficiency is going to be calculated for. Tracks are refitted without a measurement, if there is any, in this layer. After that, tracks are propagated to the silicon tracker. Selected tracks must have an uncorrected $DCA < 300$ microns, transverse momentum greater than 15 GeV/c and more than 8 CFT hits (stereo tracks). In order to have an unbiased measurement, only the 'isolated tracks' are used, i.e. every hit associated to a selected track must be isolated. In other words, that there cannot more than one cluster in a window of 11 σ_{track} around the track position (for definition of σ_{track} see below). Finally, the cluster efficiency is defined as follows: a cluster either is, or it is not, found inside the 6 σ_{res} window around the track on a given surface. If it is found, it is called an efficiency, if it is not, it is an inefficiency.

In the cluster efficiency calculation we operate with two different σ:

- σ_{track} is the uncertainty on the track position on a given surface. It comes both from the fit of the track, as well as from uncertainties of other hits that are associated to the track.

- $\sigma_{resolution}$ is the resolution of the tracker on a given surface. It is a value that is obtained for each CFT layer from the Gaussian fit to track residuals. The best resolution is indeed in cylinders four and five. The worst is in cylinder eight, due to the extrapolation of a fit.

The cluster efficiency is estimated for the first 14 layers only. It is not possible to calculate the cluster efficiency for last the two CFT layers (cylinder 8) because of the internal implementation of the `GTR` tracking algorithm. This tracking algorithm has the feature of starting track finding from the outermost axial layer. If we intentionally skip the outermost axial layer, the fit might not converge and hence there are going to be very few tracks found. On the top of that, these tracks will have ill fitted track parameters. No serious calculation can be done with them.

The size of the window which actually defines the cluster efficiency is adjusted for each CFT layer, so that no bias due to the size of the window can be present. The optimization of the size of the window is shown in Figure 2.4.

The dimuon sample is used to perform cluster efficiency studies. The sample is selected based on the following criteria:

- 2 loose muons are required (it is the same definition of a loose muon as in the rest of the analysis, Section 4),
- both with $p_{\mathrm{T}} > 15$ GeV/c,
- each of them must be matched to a central stereo track, i.e. (number of CFT hits is required to be more than 8, and number of SMT hits is more than 2),
- the isolation cut described in Section 4 is applied to both muons,
- it must be an opposite-sign muon pair.

This sample corresponds to 104 pb^{-1} of data, and it was taken between August 2002 and June 2003.

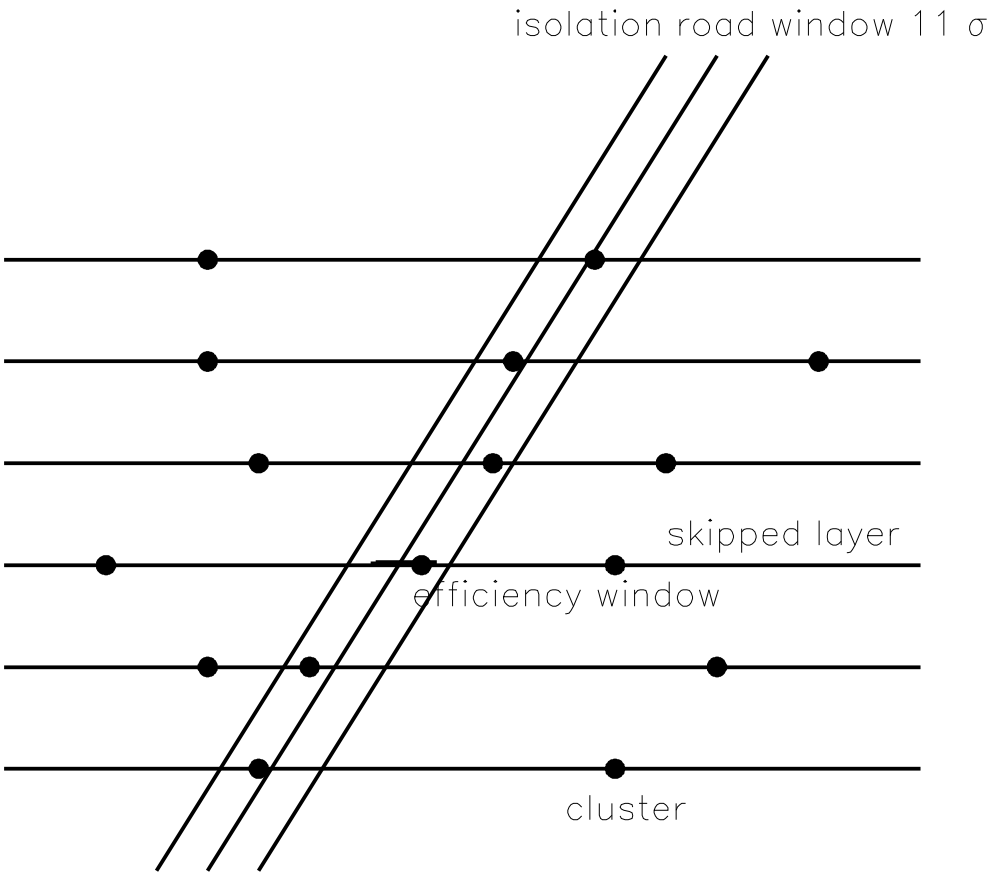

Figure 2.1: The 'road method' is used to obtained isolated tracks for an unbiased measurement of cluster efficiencies.

The cluster efficiency measurement can also give answer to a question: why there is a dip in the track reconstruction efficiency as a function of track pseudorapidity at around $\eta \sim 0$, where track η is measured from the vertex, not from the detector center. The cluster efficiency is in high nineties, and the `GTR` tracking algorithm allows at least two misses. The track reconstruction efficiency should be therefore close to 100%, and no dip at $\eta \sim 0$ should be present. The track reconstruction efficiency as a function of track η is given in Figure 2.2.

B.2 Beam position measurement

In order to obtain an unbiased measurement, this is mostly important for the silicon vertex detector studies, it is important to subtract the beam position from the DCA. In our case, it is hard because for the results shown in this chapter, we did not use a single run, but many runs. It is known that the beam position changes time-to-time. The change in the beam position is not dramatic, but it is large enough to introduce all kinds of biases in a precision measurement as the one described here. The changes in the beam position are shown in Figure 2.3. The beam position is displayed for each run in x and y coordinate system which is an alternative description of the $(r,\ \varphi)$ plane.

The CFT cluster efficiency has been calculated with respect to the size of the window, which defines the cluster efficiency. It goes without saying that the cluster efficiency should not depend on the selection of the window. The way to select the correct value is to look for the point when the cluster efficiency saturates. At the beginning, when the window is small, it raises

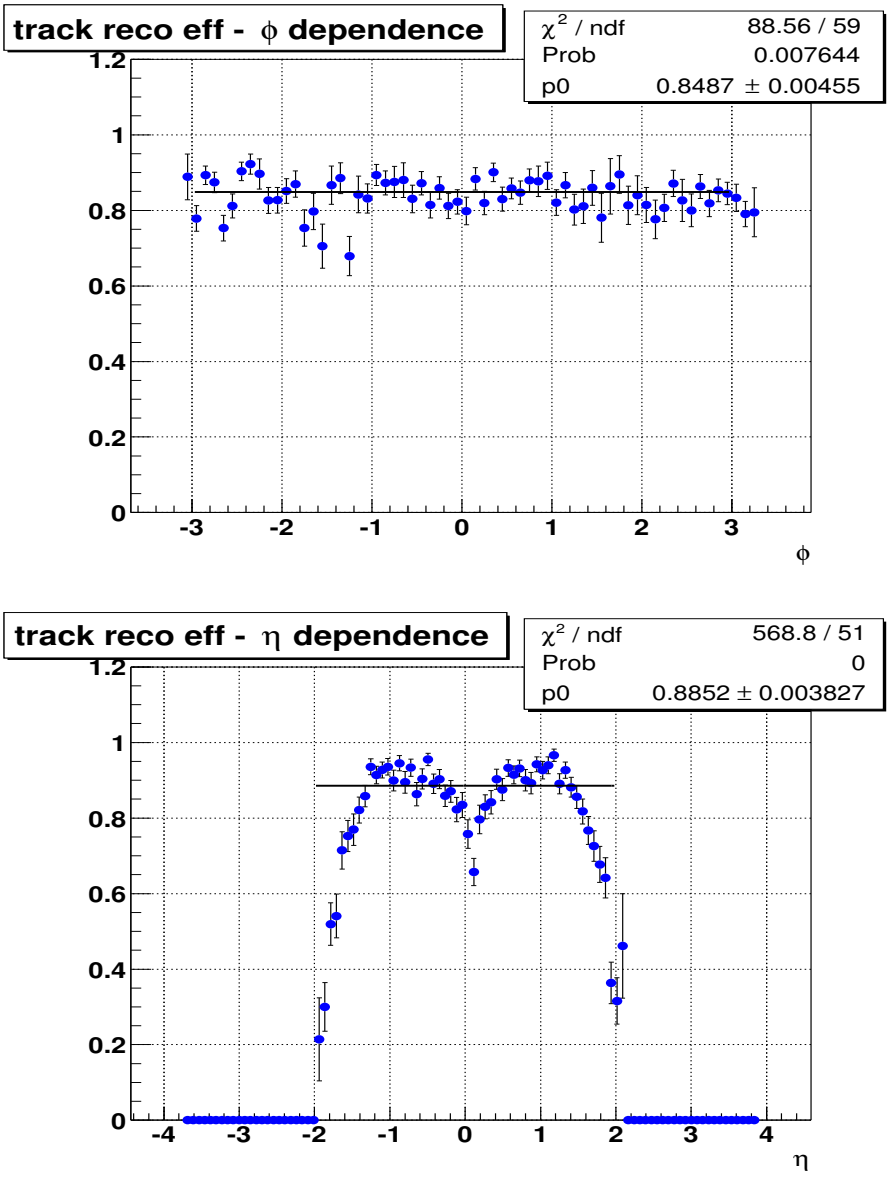

Figure 2.2: Track reconstruction efficiency as a function of azimuth angle φ (top) and track η (bottom). A clear dip in the track η distribution can be observed at around $\eta = 0$.

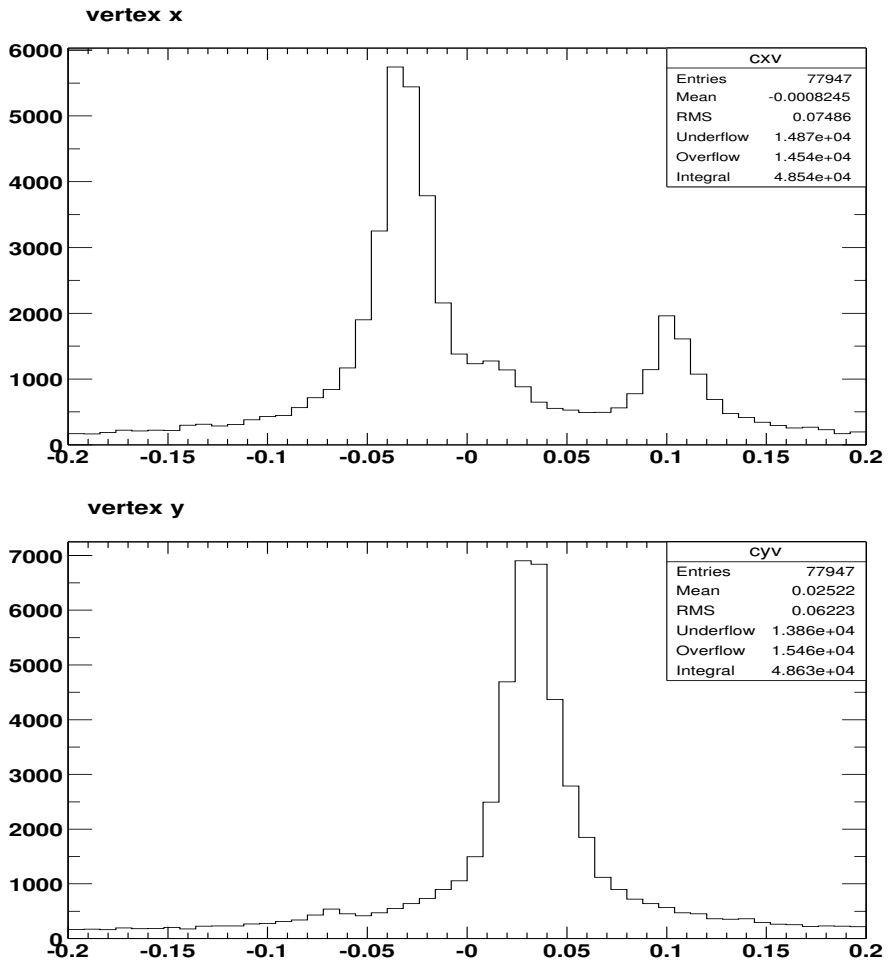

Figure 2.3: Beam position in x and y coordinate, which is an alternative description of the (r, φ) plane. The vertical axis is given in centimeters. The data sample spans over several runs, this is why the distribution is not a symmetrical Gaussian. It also shows that the beam position does not change too frequently and too radically. One can safely assume that the there are two Gaussians only, one with beam coordinates [-324 μm, 322 μm] and the other with [103 μm, 322 μm].

quickly until it starts to slow down and eventually saturates. Of course, due to the noise in the detector which creates fake clusters, it never saturates. The cluster efficiency gets slowly higher and higher as the size of the window increases. The chosen size of the window is 6 σ_{res}. Any bias of cluster efficiency is believed to be negligible. The amount of noise cluster contribution to the cluster efficiency can be derived from the slope of a continuous increase in the area of cluster efficiency saturation, i.e. region above $5 - 6\ \sigma_{res}$.

B.3 Cluster efficiencies and the 20 ADC cut

The cluster efficiency measurement is sensitive to all cuts that affect cluster building, such as the 20 ADC cut applied on per fiber basis. The cut is defined a pedestal value calculated for a particular readout channel plus 20 ADC counts on the top of that. This cut was introduced to lower the rate of the so-called long events that take too long to get reconstructed [140]. The decision was based on the distribution of signal ADC for all channels readout in the CFT. No larger optimization has been made. This cut removes all events that take too long (minutes) to reconstruct, but it also alters the efficiency of the tracker at the times when application of such a cut is not necessary. The effect of the 20 cut can be investigated in full by plotting the cluster efficiency as a function of the azimuth angle φ and pseudorapidity η before the cut is applied, and after it has been removed.

There is no clear difference in azimuth angle distributions shown in Figures 2.5 and 2.7. However, there is a difference in pseudorapidity distributions shown in Figures 2.6 and 2.8. A well-pronounced dip in a distribution of cluster efficiency as a function of pseudorapidity in a region at $\eta \sim 0$ is

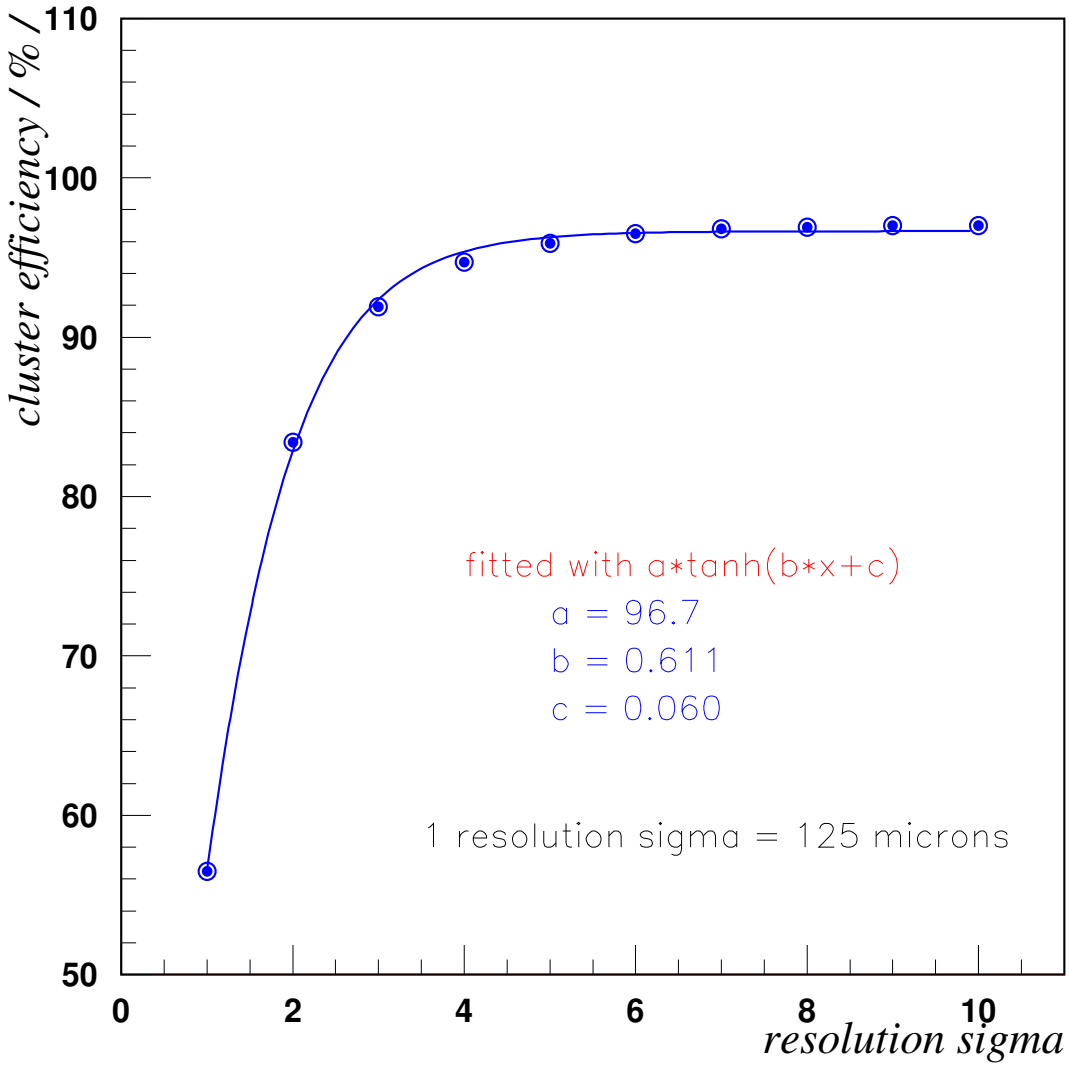

Figure 2.4: Cluster efficiency as a function of the size of the window where the cluster is searched for. This plot shows cluster efficiency for the CFT layer 10 only (5^{th} cylinder, stereo layer). The 6 σ_{res} has been chosen to define the cluster efficiency window.

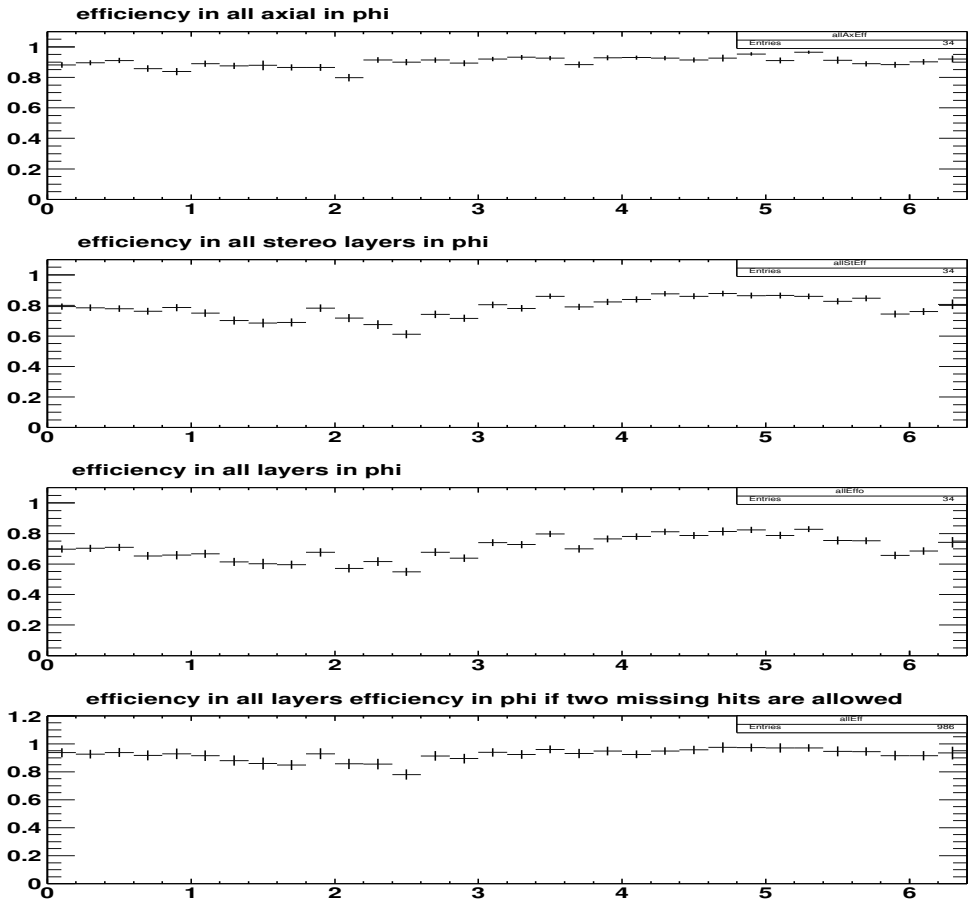

Figure 2.5: Cluster efficiency as a function of the azimuth angle φ when the 20 ADC cut is applied. The upper plot shows a multiplicative product of cluster efficiencies in all axial layers, the second plot from the top shows the same for stereo layers, the third plot from the top shows a multiplicative product of cluster efficiencies in all measured layers (layers 1 to 14). The bottom plot is a prediction of what the final cluster efficiency of the CFT would be if one assumes two misses to be allowed in the tracking algorithm. The algorithm of calculating cluster efficiency for the entire tracker, when two missing hits are allowed, is described in Equation 2.1.

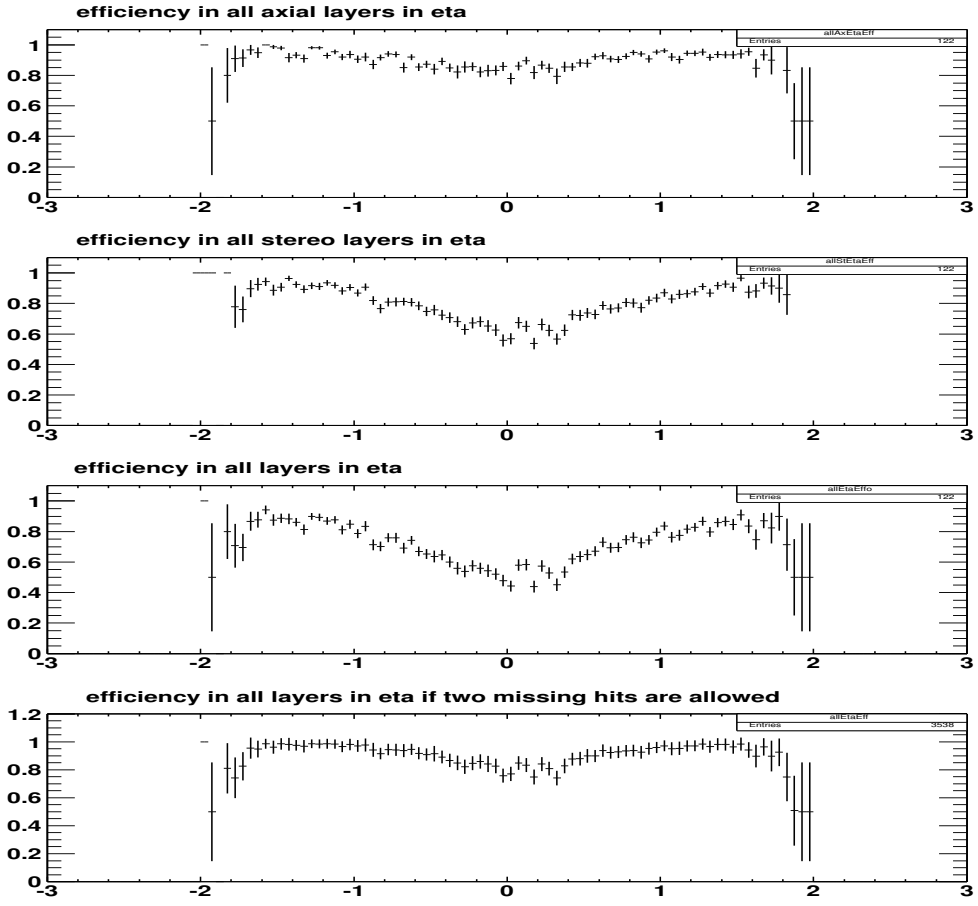

Figure 2.6: Cluster efficiency as a function of the pseudorapidity η when the 20 ADC cut is applied. The upper plot shows a multiplicative product of cluster efficiencies in all axial layers, the second plot from the top shows the same for stereo layers, the third plot from the top shows a multiplicative product of cluster efficiencies in all measured layers (layers 1 to 14). The bottom plot is a prediction of what the final cluster efficiency of the CFT would be if one assumes two misses to be allowed in the tracking algorithm. The algorithm of calculating cluster efficiency for the entire tracker, when two missing hits are allowed, is described in Equation 2.1.

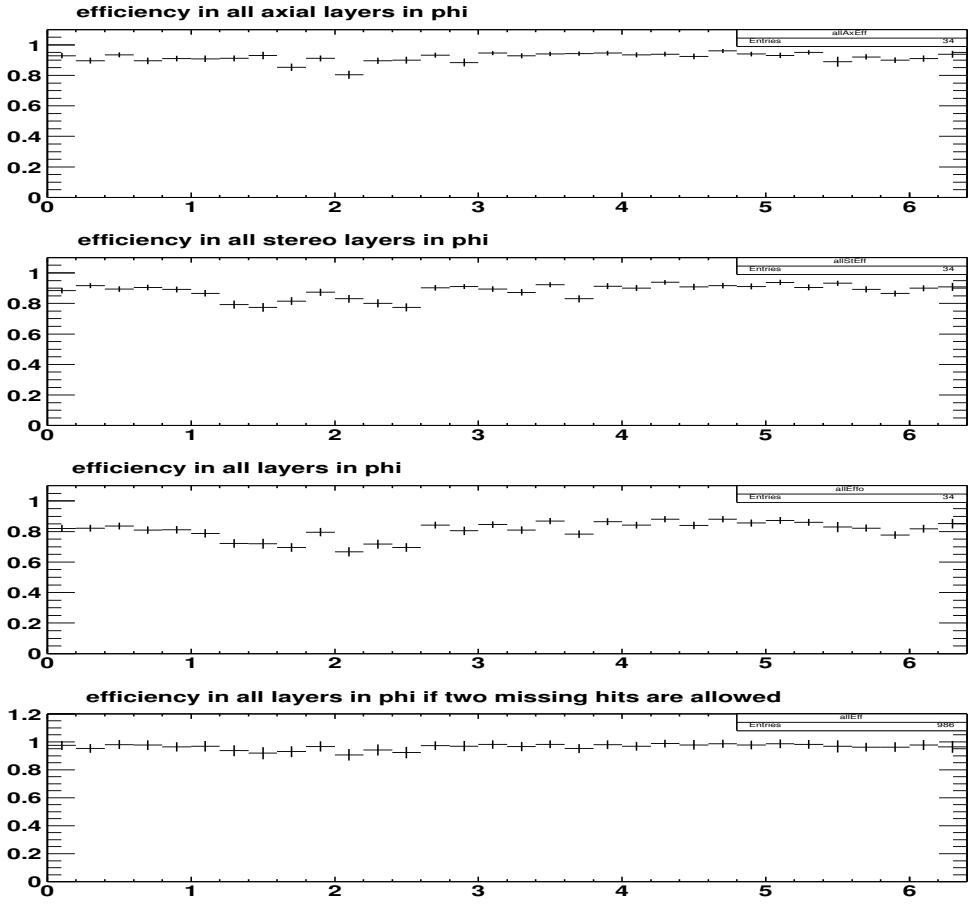

Figure 2.7: Cluster efficiency as a function of the azimuth angle φ when the 20 ADC cut is removed. The upper plot shows a multiplicative product of cluster efficiencies in all axial layers, the second plot from the top shows the same for stereo layers, the third plot from the top shows a multiplicative product of cluster efficiencies in all measured layers (layers 1 to 14). The bottom plot is a prediction of what the final cluster efficiency of the CFT would be if one assumes two misses to be allowed in the tracking algorithm. The algorithm of calculating cluster efficiency for the entire tracker, when two missing hits are allowed, is described in Equation 2.1.

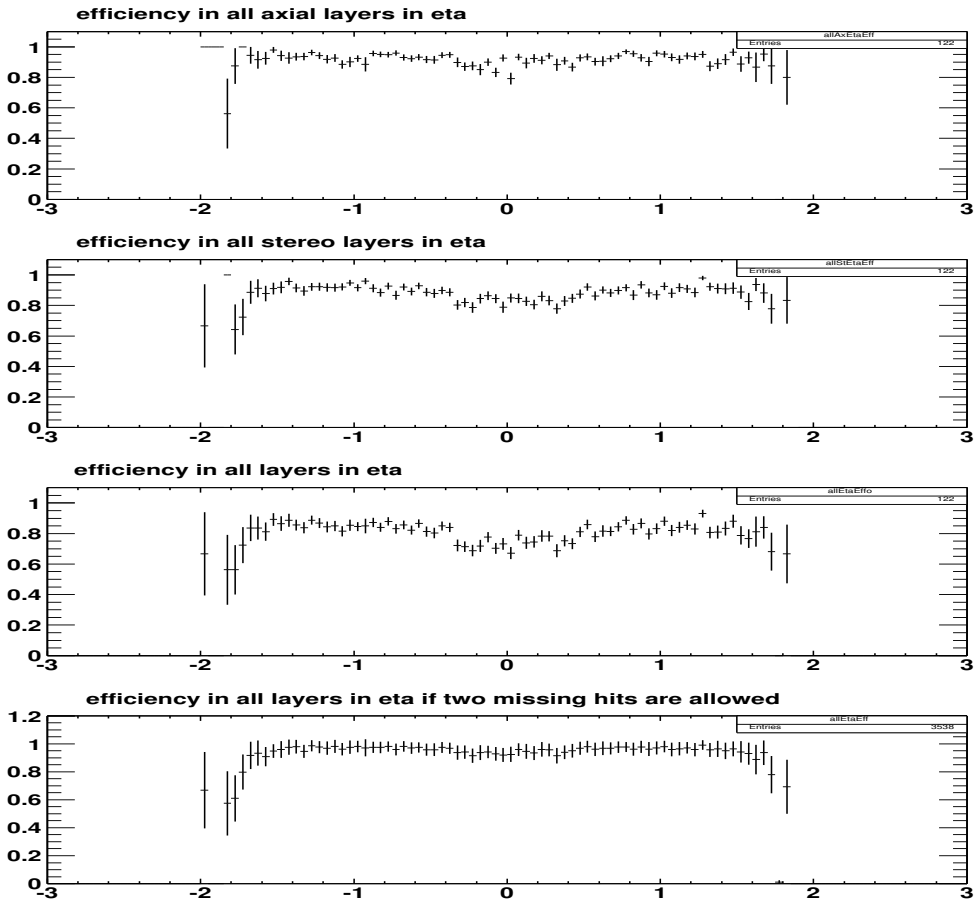

Figure 2.8: Cluster efficiency as a function of the pseudorapidity η when the 20 ADC cut is removed. The upper plot shows a multiplicative product of cluster efficiencies in all axial layers, the second plot from the top shows the same for stereo layers, the third plot from the top shows a multiplicative product of cluster efficiencies in all measured layers (layers 1 to 14). The bottom plot is a prediction of what the final cluster efficiency of the CFT would be if one assumes two misses to be allowed in the tracking algorithm. The algorithm of calculating cluster efficiency for the entire tracker, when two missing hits are allowed, is described in Equation 2.1.

present. This effect is more pronounced in stereo layers than in axial layers. A pure multiplicative product of cluster efficiencies in η therefore shows a well pronounced dip at $\eta = 0$ (the third plot from the top in all figures).

As soon as two misses (=missing hits) are allowed in the tracking code, which is implemented in the `GTR` tracking algorithm, the cluster efficiency calculated for the entire tracker, both in φ and η, improves. Nevertheless, it never disappears completely. Only after the 20 ADC cut is removed from the cluster building algorithm, cluster efficiencies improve. The dip is not there any more. The algorithm of calculating cluster efficiency for the entire tracker, when two missing hits are allowed, can be described by

$$\epsilon \;=\; \prod_{i=1}^{14} \epsilon_i + \sum_{i=1}^{14}(1-\epsilon_i)\prod_{j\neq i}\epsilon_j + \sum_{i=1}^{14}\sum_{j\neq i}(1-\epsilon_i)(1-\epsilon_j)\prod_{k\neq i\neq j}\epsilon_k, \qquad (2.1)$$

where ϵ_i is the cluster efficiency in layer i, and ϵ is the total cluster efficiency of the CFT.

There are several conclusions that can drawn from this study:

- **about the origin of the dip:**

  The origin of the dip is clear. It is related to the dependence of the light yield on pseudorapidity. Tracks with a larger pseudorapidity cross fibers that are (almost) parallel to the beam axis for (stereo) axial layers under a larger angle. This is why they have a larger opportunity to deposit energy in the scintillating fiber and more light can be collected by the VLPC. In contrary, tracks that are almost perpendicular to the fiber (beam axis) will cross the fiber on a shorter path. Less light is going to be read out and thus these fibers are more susceptible to

be rejected by the 20 ADC cut. Doublet clusters will turn to singlet clusters, singlet cluster might be removed completely. The result is that the cluster efficiency is going to be lower for those tracks and a dip at around $\eta = 0$ shows up in the pseudorapidity distribution.

- **where does it come from:**

  It is clear from Figures 2.5 to 2.8 that most of the inefficiency comes from stereo layers. During the CFT commissioning, stereo layers were equipped with a lower-grade electronics and they were the last layers to be installed. Generally speaking, stereo layers have a worse performance than the axial layers. It is a known fact that the worse electronics, namely AFE boards, has built in VLPC's (visible light photon counter) with lower gains. A lower gain translates into lower light yield. This is a reason why for the same tracks (particles), the cluster efficiency in stereo layers is going to be lower compared to axial layers.

- **what is the source of the inefficiency:**

  The source of the inefficiency are effects described above that are magnified by the unnecessarily hard ADC cut applied on fiber-by-fiber basis. When it is removed, the cluster efficiency and thus track reconstruction efficiency improve a great deal. A chance that this cut is going to be removed is not high, because it serves as protection from a much serious problem - existence of long running events that are a serious hit to the speed of data reconstruction on the farms.

- **and what is the solution:**

  The solution could be to design a special set of cuts that are applied

on layer-by-layer basis. In other words, they are different for each geometrical segment of the detector. Regions that have lower gains could be affected by this cut much less and regions with traditionally high gains, i.e. axial layers, could preserve this cut as is without degrading cluster efficiency.

The measurement obtained is fully consistent with other measurements presented in this thesis, e.g ratio of number of singlets and doublets as a function of pseudorapidity. This plot is shown in Figure 5.3 and details are discussed in Appendix E.

CFT cluster efficiencies for each layer, except the two outermost layers, with the 20 ADC cut applied are listed in Table 2.1. The same is done in Table 2.2 when the 20 ADC cut is removed.

B.4 Cluster efficiency and a timing change

The aim of this chapter is to demonstrate how useful can be cluster efficiency study for optimization of the CFT performance. Cluster efficiencies before and after the timing change are compared.

In this study we use the same data sample defined earlier, it contains two isolated high-p_{T} muons with matched tracks. The data sample is broken into two pieces: (a) before the timing change has been made on April 11, 2003 (it corresponds to run 175626), and (b) after it was made. The integrated luminosity of the data sample with an implemented timing change is approximately 39 pb^{-1}.

Additionally, the high-p_{T} di-EM sample is available, it contains 11,915

layer	efficiency (%)	occupancy (clus/cm)	fake rate (%)
1	98.2(2)	1.76	0.24
2	95.8(2)	1.66	0.56
3	98.5(2)	1.38	0.16
4	97.1(2)	1.25	0.27
5	98.3(2)	1.51	0.19
6	96.9(2)	1.38	0.35
7	98.8(2)	1.25	0.11
8	96.8(2)	1.17	0.28
9	98.4(2)	1.05	0.13
10	96.5(2)	0.99	0.26
11	98.6(2)	0.91	0.10
12	96.5(2)	0.83	0.21
13	98.9(2)	0.71	0.06
14	96.5(2)	0.71	0.18

Table 2.1: CFT cluster efficiencies in all measured layers, the 20 ADC cut is applied. Occupancies and fake rates are given.

layer	efficiency (%)	occupancy (clus/cm)	fake rate (%)
1	98.6(2)	2.0	0.21
2	97.5(2)	1.9	0.39
3	98.5(2)	1.6	0.19
4	98.3(2)	1.5	0.20
5	98.5(2)	1.7	0.20
6	98.3(2)	1.6	0.25
7	99.0(2)	1.5	0.12
8	98.5(2)	1.4	0.16
9	98.6(2)	1.3	0.14
10	98.3(2)	1.3	0.17
11	98.8(2)	1.2	0.12
12	98.3(2)	1.1	0.15
13	99.2(2)	1.0	0.06
14	98.3(2)	1.0	0.13

Table 2.2: CFT cluster efficiencies in all measured layers, the 20 ADC cut is removed. Occupancies and fake rates are given.

events. These events are mainly $Z \rightarrow ee$ events, however purity of this sample is much lower than the one of the dimuon sample.

Track reconstruction efficiency as a function of time is given in Figure 2.9. Total track reconstruction efficiency is $(77.7 \pm 3.4)\%$. Track reconstruction efficiency before the timing change is $(77.9 \pm 3.5)\%$, and after the timing change $(77.3 \pm 3.4)\%$.

Cluster efficiencies before and after the timing change are given in Tables 2.3 and 2.4, respectively.

The conclusion of this study is that there does not seem to be any statistically significant difference in track reconstruction efficiency before and after the timing change has been implemented. No significant difference actually has been expected however, because the change is very small and the tracking code allowing two missing hits should be able to accommodate for the difference.

Cluster efficiency as a function of a layer number, before and after the timing has changed, is shown in Figure 2.10. There is a small systematical shift in cluster efficiencies of all layers after the timing cut change, it is a marginal effect though. There is almost no difference observed for axial layers (odd layer numbers). Unlike axial layers there seems to be a non-negligible difference in stereo layers. This can be understood in the following way: due to using electronics with lower gain in stereo layers, the light yield is lower. Any change, not only the timing change, increases the probability to reject the fiber from reconstruction when applying the ADC cut. That is going to lower the cluster efficiency.

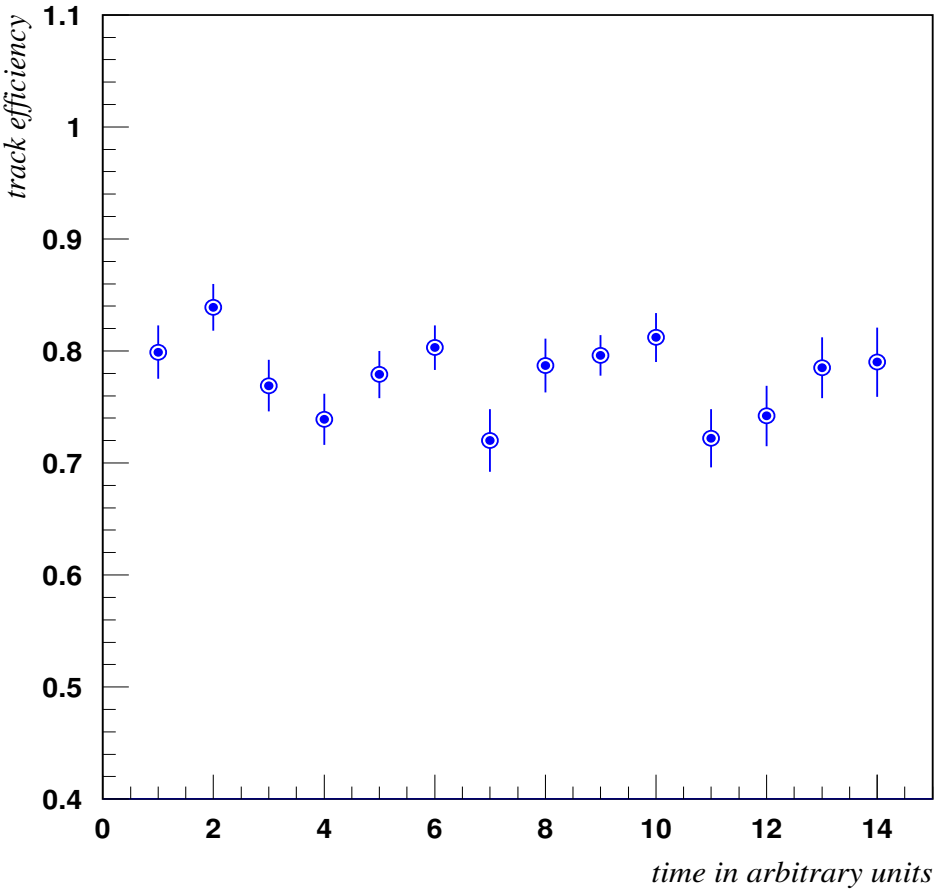

Figure 2.9: Track reconstruction efficiency as a function of time. Track reconstruction efficiency is about the same before and after the timing change has been made. The change takes place after the measurement number 10.

layer	efficiency (%)	occupancy (clus/cm)	fake rate (%)
1	98.1(2)	2.4	0.2
2	95.9(2)	1.7	0.6
3	98.4(1)	1.6	0.1
4	96.8(2)	1.2	0.3
5	98.2(2)	1.5	0.2
6	96.7(2)	1.4	0.4
7	98.8(1)	1.2	0.1
8	96.6(2)	1.2	0.3
9	98.3(1)	1.0	0.1
10	96.3(2)	1.0	0.2
11	98.6(2)	0.9	0.1
12	96.3(2)	0.8	0.2
13	98.7(2)	0.7	0.06
14	96.3(2)	0.7	0.02

Table 2.3: CFT cluster efficiencies in all layers before the timing change has been made.

layer	efficiency (%)	occupancy (clus/cm)	fake rate (%)
1	98.4(3)	1.8	0.2
2	95.8(4)	1.6	0.6
3	98.8(2)	1.4	0.1
4	98.0(3)	1.3	0.2
5	98.6(2)	1.5	0.2
6	97.6(3)	1.4	0.3
7	99.0(2)	1.3	0.1
8	97.5(3)	1.2	0.2
9	98.5(2)	1.0	0.1
10	97.0(3)	1.0	0.2
11	98.7(2)	0.9	0.1
12	97.2(3)	0.8	0.2
13	99.2(3)	0.7	0.04
14	97.1(4)	0.7	0.2

Table 2.4: CFT cluster efficiencies in all layers after the timing change has been made.

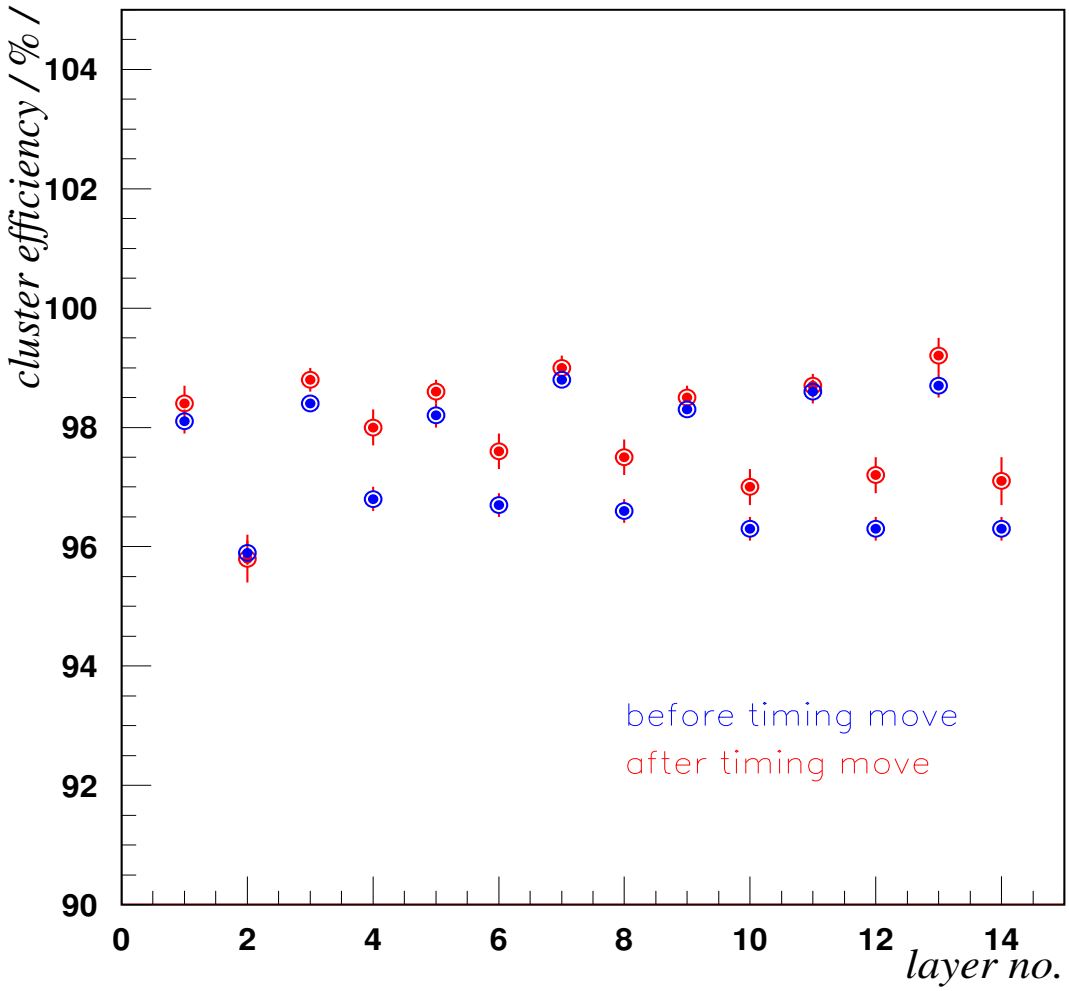

Figure 2.10: Cluster efficiency as a function of the layer number, before and after the timing change is introduced.

Appendix C

CFT cluster positions and errors

This chapter describes the development and maintenance of the `cft_trf_clus` package. This package is part of the offline event reconstruction code. It was developed to calculate prediction of the track position and its uncertainty on a given surface in the Central Fiber Tracker. The factors which determine the track position prediction and the uncertainty are the multiplicity of the cluster and the track parameters, namely azimuth angle φ and dip angle α angles.

C.1 Geometry of the CFT clusters

The Central Fiber Tracker design is described in Section 3.1.2.

The CFT geometry parameters for each cylinder, layer and fiber can be obtained from the `cft_geometry` package, the `rcp` directory contains all values of geometry.

Based on the track parameters on a given surface there can be clusters of different multiplicities. There are only two physical possibilities: only singlet and doublet clusters are geometrically allowed. There are various explanations for clusters of higher multiplicities. For instance, there might a delta electron emitted from the charged particle in the material of the fiber. The electron might escape the fiber and cause the neighboring fiber to be fired. In such a case, the triplet or quadruplet is observed. The nature of clusters with high multiplicities might be either noise (with a high probability), or the fact that two tracks might cross (or be very close to each other on this surface, usually the underlying physics is a reason). The clustering algorithm is simple. It adds fibers to the cluster until there are no more fired neighboring fibers to be added. In case of a noise or underestimated pedestal values this can cause higher average fiber multiplicity of clusters in the data.

In this analysis, we have taken into account only three scenarios:

- singlet - only one fiber is fired by the track
- doublet - two fibers build a cluster, track crosses both of them
- all higher multiplicity clusters - the position has to be estimated. These clusters are assigned a large uncertainty.

The first two possibilities are pictured in Figure 3.1. The track is painted in red. The blue lines show how is the error calculated for singlets and doublets. The α parameter of the track can be viewed as an angle between the vertical axis and the direction of the track on the nominal surface of the doublet layer. The α parameters is rigorously defined as:

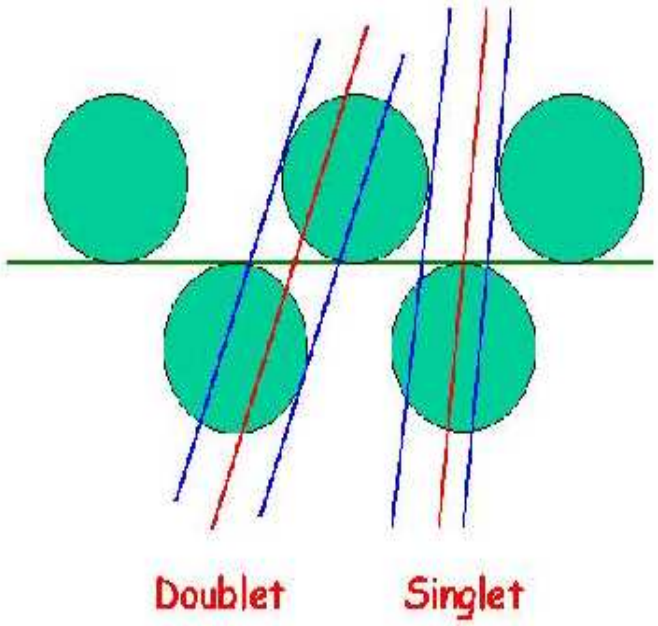

Figure 3.1: CFT Clusters - doublets (left) and singlets (right).

$$\alpha = \varphi - \varphi_d \tag{3.1}$$

where φ is the azimuth angle of the track and φ_d is the tangent direction to the track on the given surface.

C.2 Calculation of track position predictions and uncertainties for the new CFT clusters

This section explains how to calculate track predictions for the CFT clusters on a given surface and how to evaluate uncertainties of each position. The calculation is different for each of the three possible scenarios. The aim of the package also is to calculate properly the derivatives of the hit position with respect to track parameters and pass these values to the tracking algorithm.

C.2.1 Singlet clusters

The track position for the singlet cluster, see Figure 3.1, is calculated as an average between the track curvature projected on the surface of the left unhit fiber and the track curvature projected on the right unhit fiber (both positions are measured in φ and also the track position prediction is an azimuth angle). It is obvious, that the position strongly depends on the α parameter of the track. An example is the situation when the track parameter α is equal to zero. In such a case, the difference between both projections will be equal to the fiber pitch minus diameter of the fiber. The predicted

track position is exactly in the middle of the pitch, in the midway between both unhit fibers, located on the nominal surface. Should the α parameter be positive, the track predicted position shifts toward the left because the lines projected on the surface of neighboring unhit fibers are parallel to the track trajectory and cross the nominal surface of the doublet layer under the angle α.

The errors are calculated as a difference between points on the nominal surface, where both projections cross the nominal surface, divided by square root of twelve.

$$\sigma_{\varphi} = \frac{\varphi_{left} - \varphi_{right}}{\sqrt{12}} \tag{3.2}$$

where φ_{left} and φ_{right} can be viewed as the azimuth angles of the points where the blue line (the line projected on the surface of the neighboring unhit fiber, it is parallel to the track) crosses the nominal surface of the doublet layer.

C.2.2 Doublet clusters

The track position for the doublet cluster, see Figure 3.1, is calculated as an average between the track curvature projected on the surface of the left/right hit fiber and the track curvature projected on the surface of the right/left unhit fiber. Whether the track curvature is projected on the left or right hit fiber in order to calculate φ_{left} depends on the angle α. If the angle α is less than 45°, the track is projected on the left edge of the right hit fiber in order to calculate φ_{left} and on the right edge of the left hit fiber to get φ_{right}. In case the α parameter is larger than 45°, the φ_{left} is obtained from

the track projection on the left edge of the left hit fiber and φ_{left} from the track projection on the right edge of the right hit fiber.

The predicted track position is calculated exactly the same as in the previous section. It also strongly depends on the α parameter of the track.

The errors calculated for the doublet are smaller as compared to singlets or clusters of higher multiplicities. The reason is that the prediction is constrained by the geometrical overlap of two adjacent fibers. The road where the particle crossed the layer is rather narrow. This is why the predicted position of the track on a given surface is know with a much smaller uncertainty.

The effect which complicates this picture is a so-called *spoiled doublets*. What happens is that a singlet is misidentified as a doublet. The reason for that might be that there was an δ-ray electron which deposited all its energy in the neighboring fiber or the neighboring fiber crossed the pedestal and it was read out. A smaller error is assigned to a predicted track position. That is a danger for the track reconstruction because the hit might be lost completely. This effect is small, but not negligible (about 6%).

C.2.3 Clusters with fiber multiplicity higher than two

The track position prediction for these cluster is calculated as a difference between the track projection on the right edge of the left unhit fiber and the track projection on the left edge of the right unhit fiber. The predicted position is in the middle of the cluster. Nothing more can be done in this case. In the future, it could be possible to make a use of the ADC cluster charge information to devise a better track position prediction. The ADC

information could also help to split these unphysical clusters into smaller clusters. The tracking algorithm could then decide which of the cluster is the best for the track, based on the lowest track χ^2 for instance.

The error assigned to these clusters is the maximal. It is calculated the same way as in previous sections. Because we do not have more information about the nature of this cluster and do not know where the track crossed the surface, we assign it the largest error we can.

C.3 Improvement of track position measurement

In this study we are using a Monte Carlo single muon sample with $p_{\mathrm{T}} = 0.5$ GeV/c and 1.0 GeV/c. This sample is ideal to understand the effect of α-dependent corrections to the predicted track position and their uncertainties.

The effect of the newly calculated track predictions and their uncertainties is demonstrated on the pulls between the predicted track position and the Monte Carlo position of the track. The difference between the predicted and the true Monte Carlo position is then divided by the predicted position uncertainty. The expected pull should be flat because the track might be equally probably within the error ranges in φ. The pull is supposed to be in the interval $-\sqrt{3}$ to $\sqrt{3}$ because the farthest distance the track can be from a predicted position is exactly the uncertainty on the position.

The pulls of the track position in the axial and stereo layer can be viewed separately for singlets and doublets in Figures 3.4-3.11 in more detail. The important factor is the transverse momentum of a track, the lower is the p_{T}

of the track, the more likely it is that the track has a large α parameter. The low-p_{T} tracks are more curved. The α correction to the track prediction is a large effect. There is an improvement between applying α-dependent corrections and $\alpha = 0$ track prediction calculation, for low-p_{T} tracks mainly.

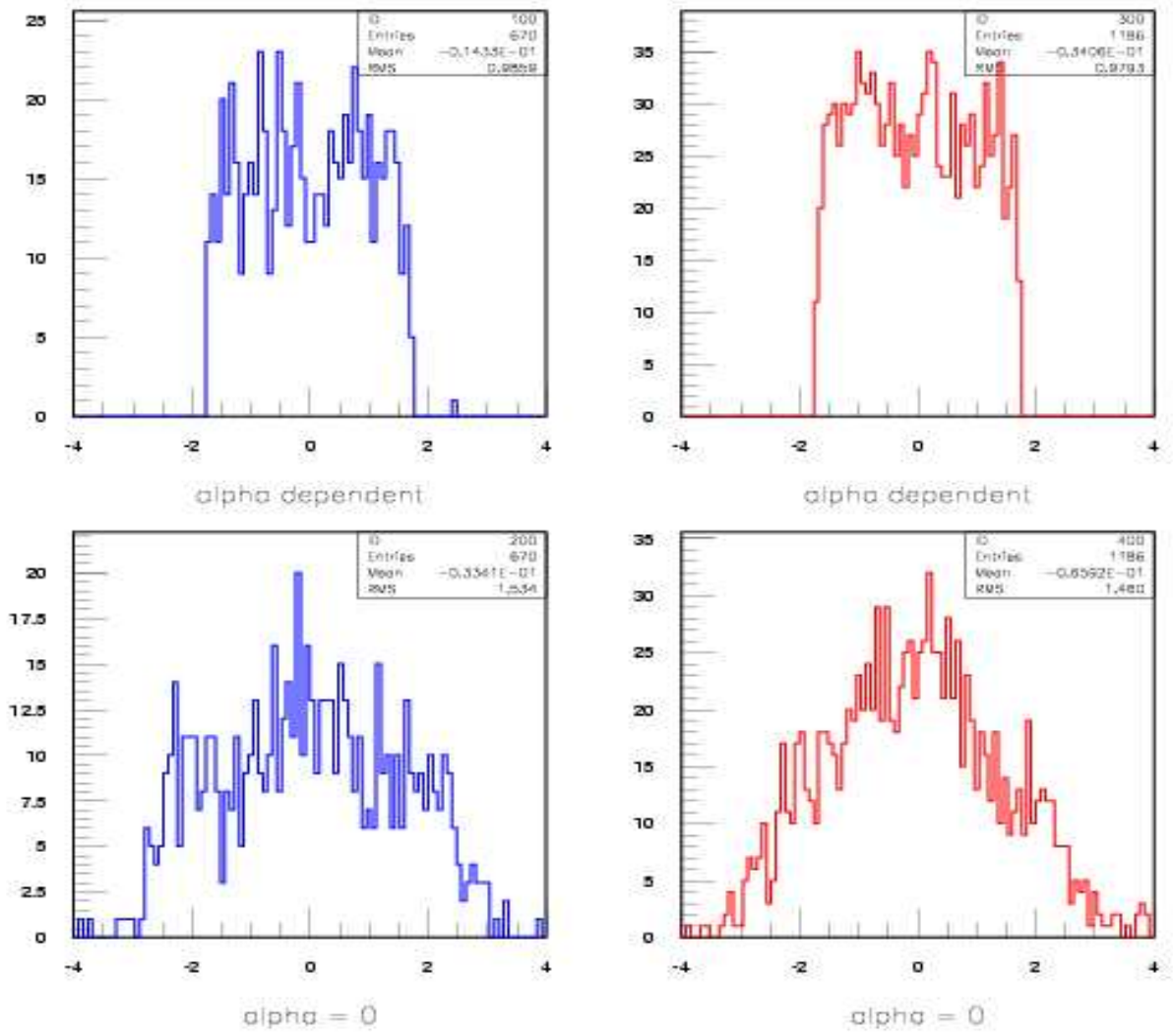

Figure 3.2: The predicted position pulls for tracks with p_T = 1.0 GeV/c - singlets (left) and doublets (right) in axial layers, α-dependent (top) and α=0 (bottom).

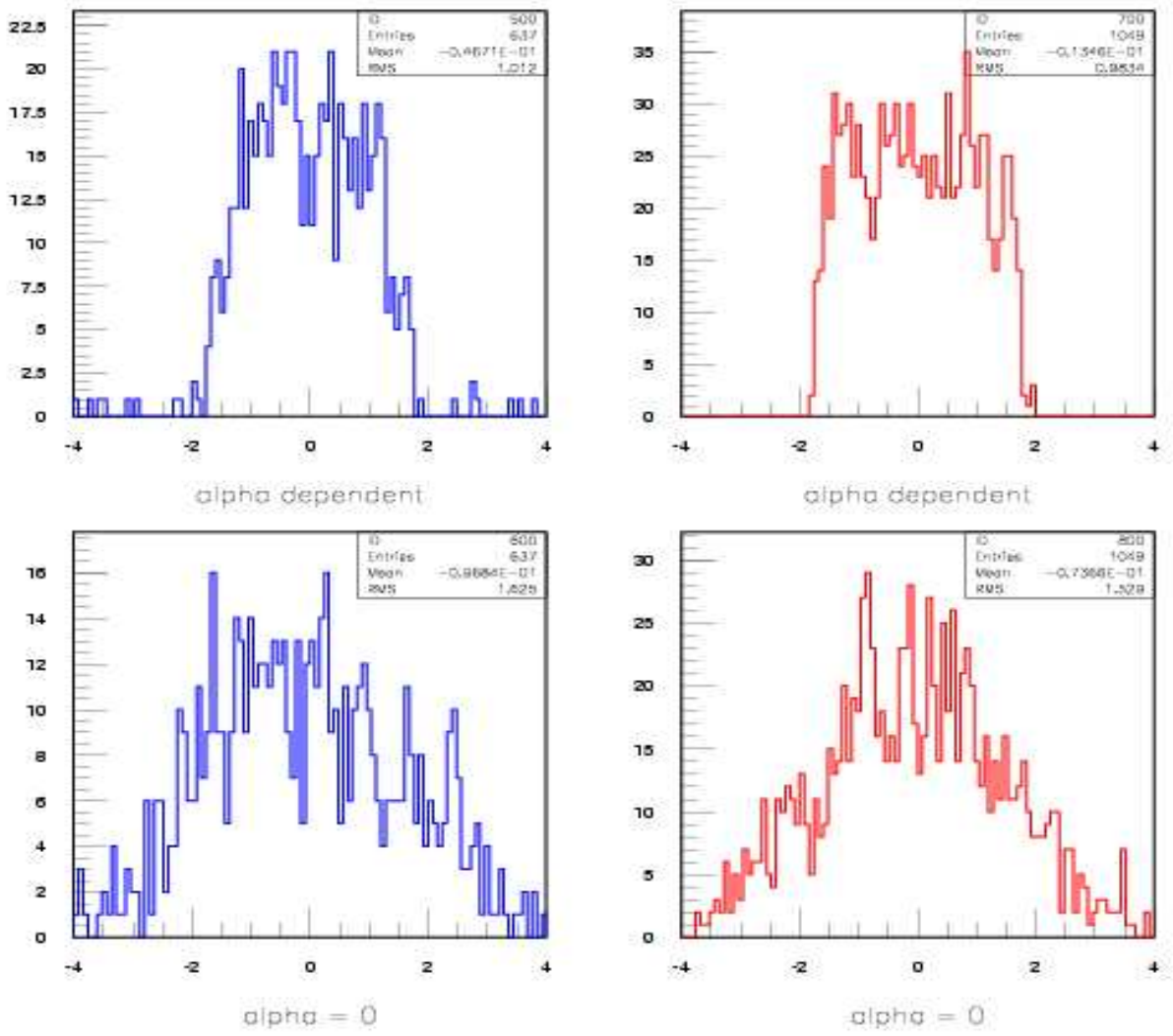

Figure 3.3: The predicted position pulls for tracks with p_T = 1.0 GeV/c - singlets (left) and doublets (right) in stereo layers, α-dependent (top) and $\alpha = 0$ (bottom).

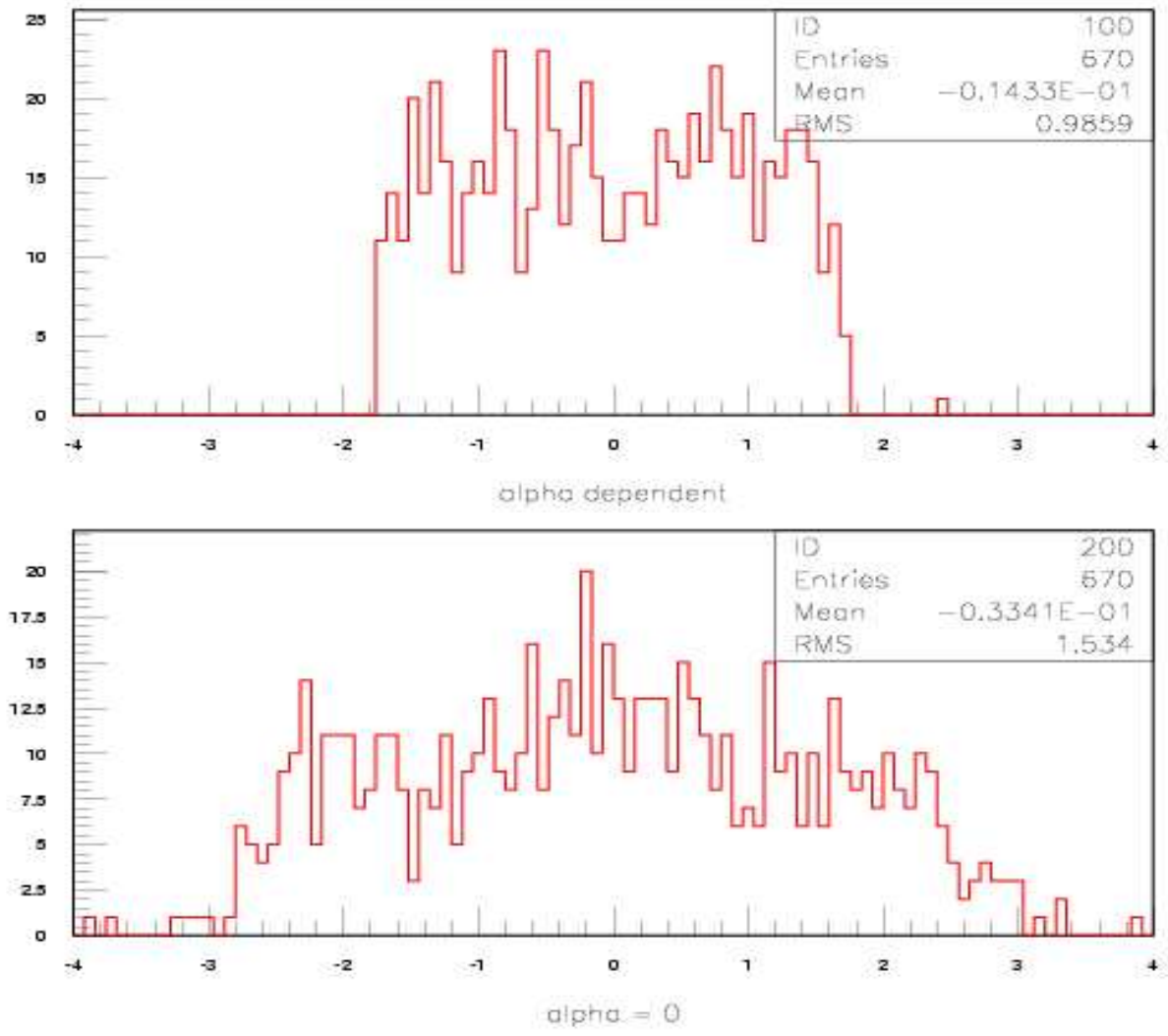

Figure 3.4: The predicted position pulls for tracks with $p_T = 0.5$ GeV/c for singlet clusters in axial layers only, α-dependent (top) and $\alpha = 0$ (bottom).

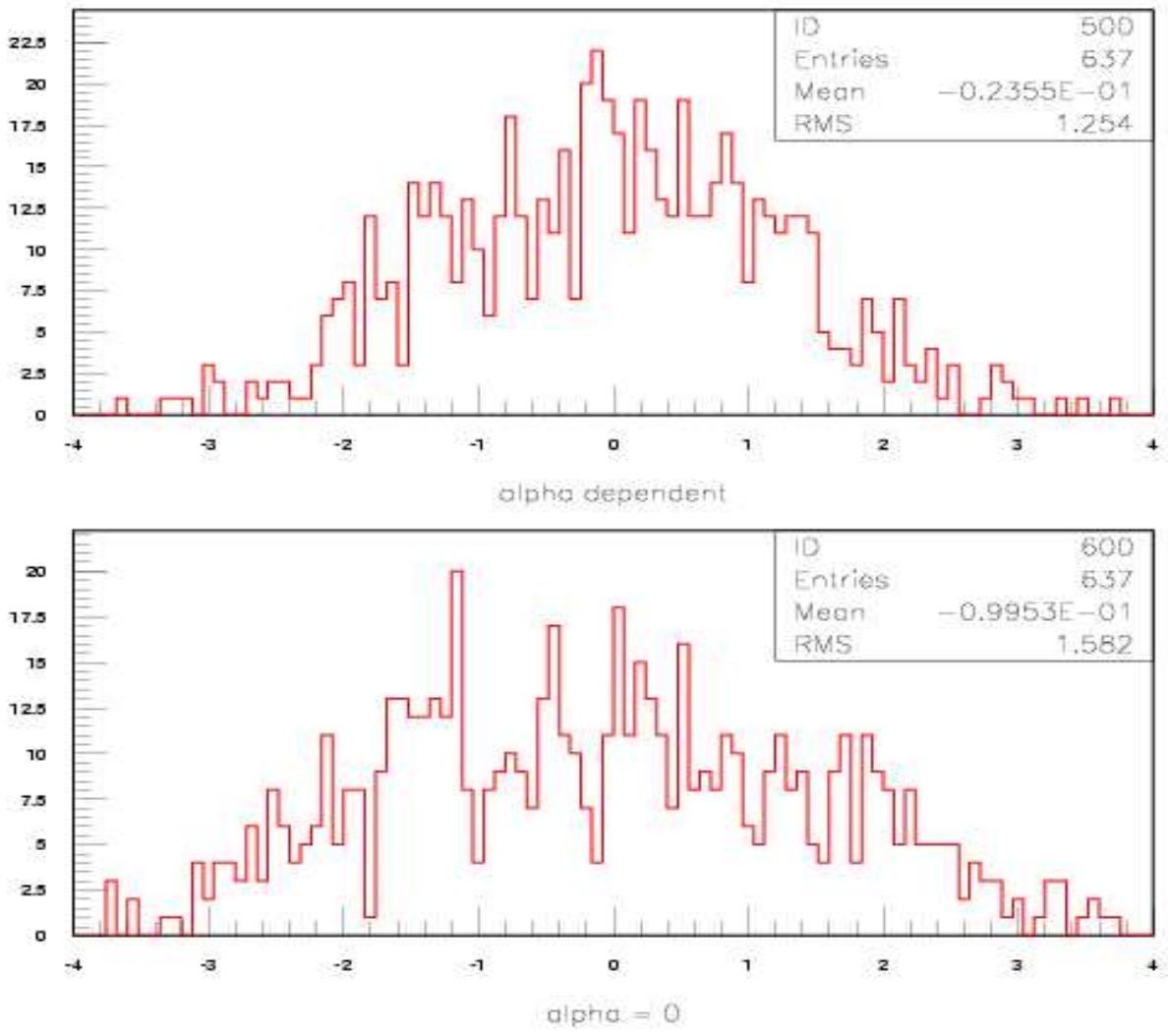

Figure 3.5: The predicted position pulls for tracks with $p_{\mathrm{T}} = 0.5$ GeV/c for singlet clusters in stereo layers only, α-dependent (top) and $\alpha = 0$ (bottom).

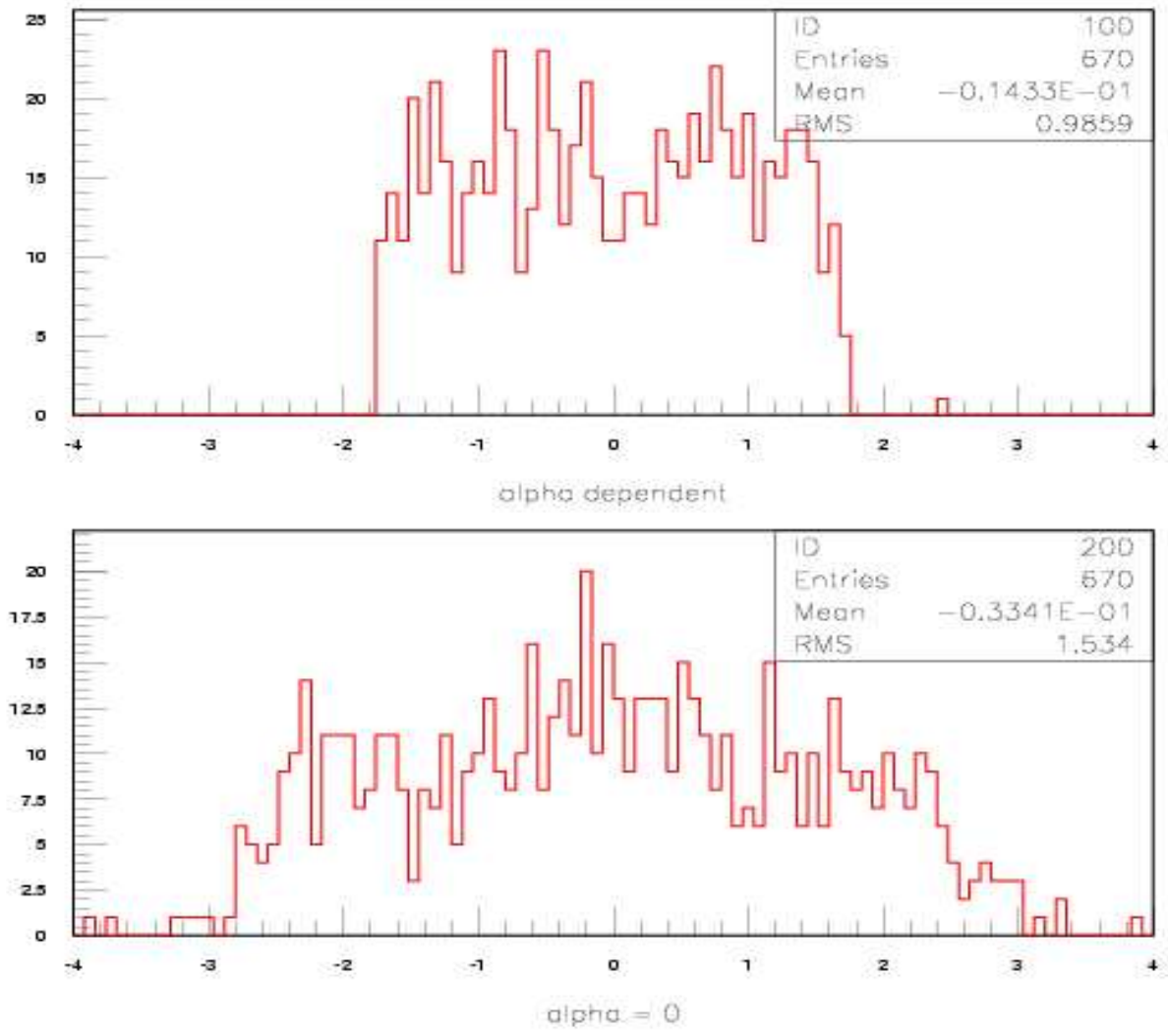

Figure 3.6: The predicted position pulls for tracks with $p_T = 1.0$ GeV/c for singlet clusters in axial layers only, α-dependent (top) and $\alpha = 0$ (bottom).

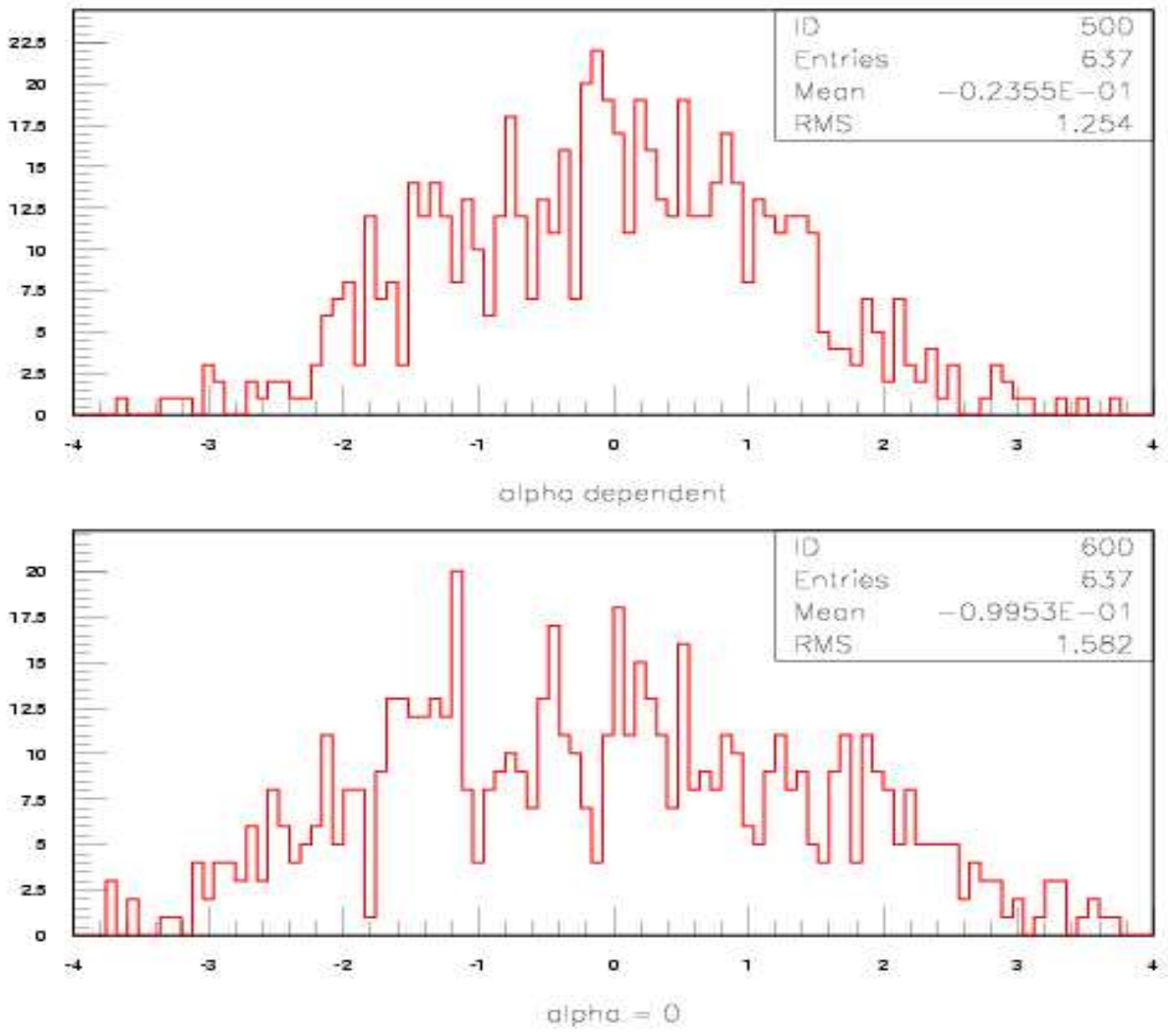

Figure 3.7: The predicted position pulls for tracks with $p_T = 1.0$ GeV/c for singlet clusters in stereo layers only, α-dependent (top) and $\alpha = 0$ (bottom).

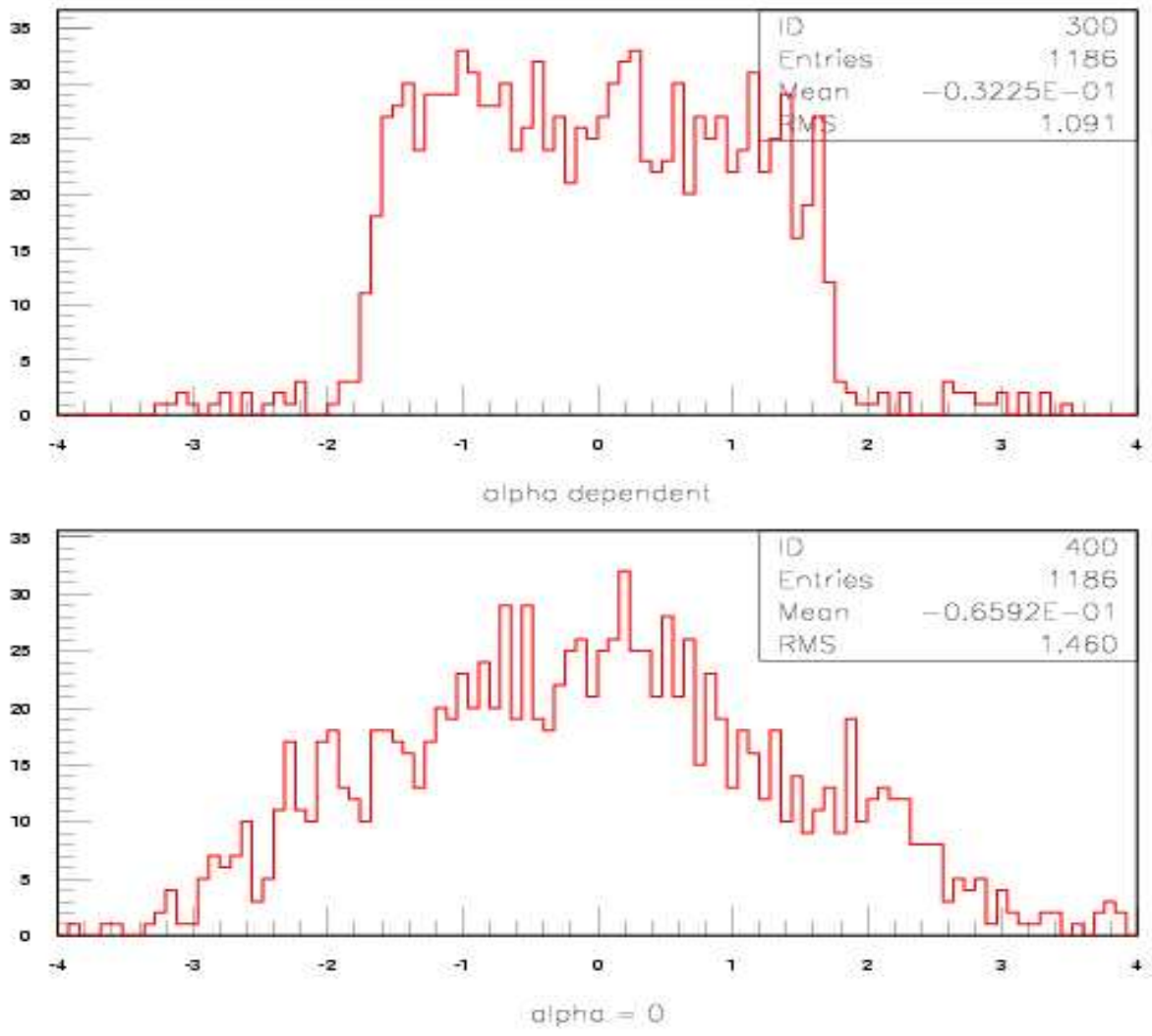

Figure 3.8: The predicted position pulls for tracks with $p_T = 0.5$ GeV/c for doublet clusters in axial layers only, α-dependent (top) and $\alpha = 0$ (bottom).

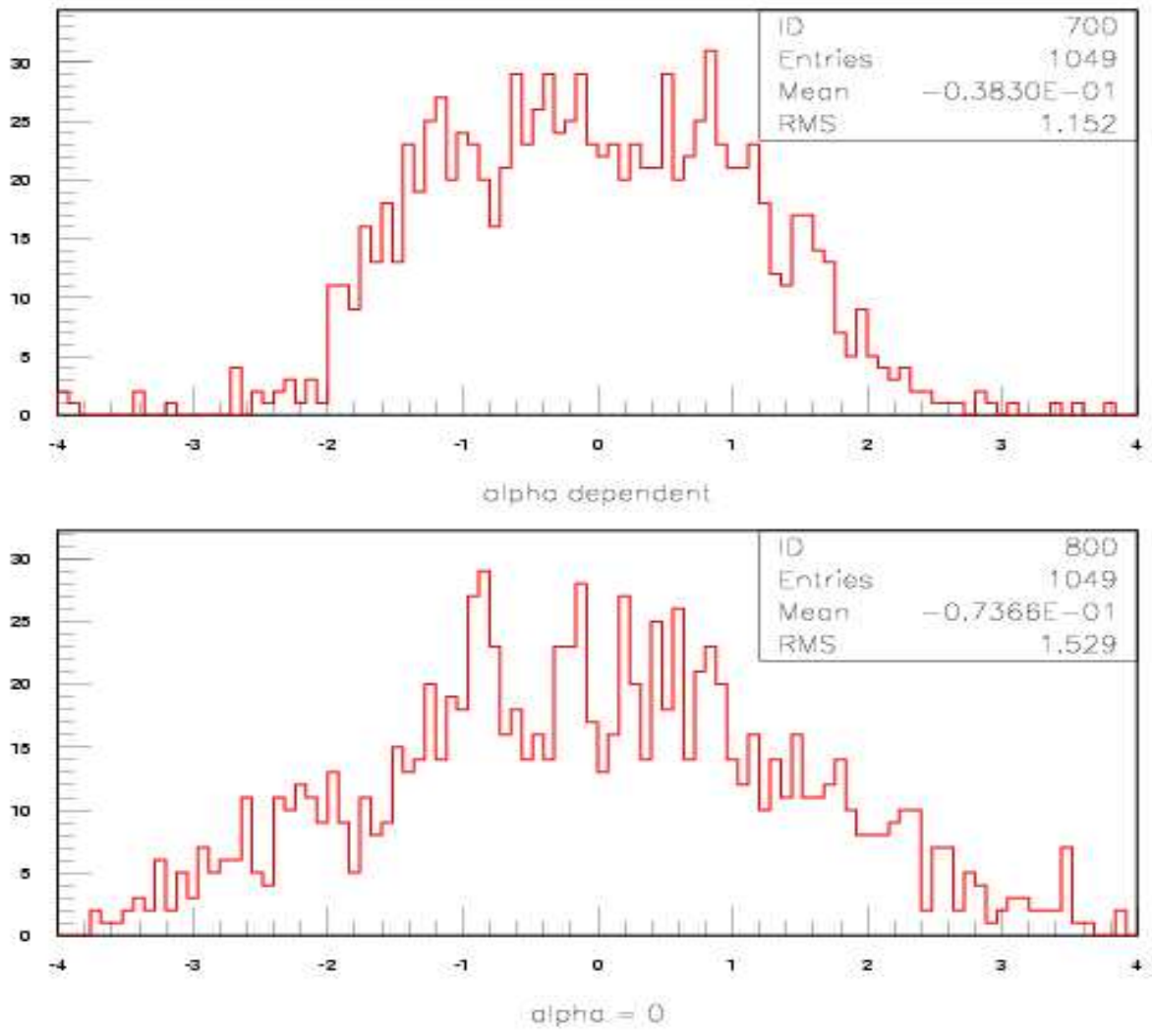

Figure 3.9: The predicted position pulls for tracks with $p_T = 0.5$ GeV/c for doublet clusters in stereo layers only, α-dependent (top) and $\alpha = 0$ (bottom).

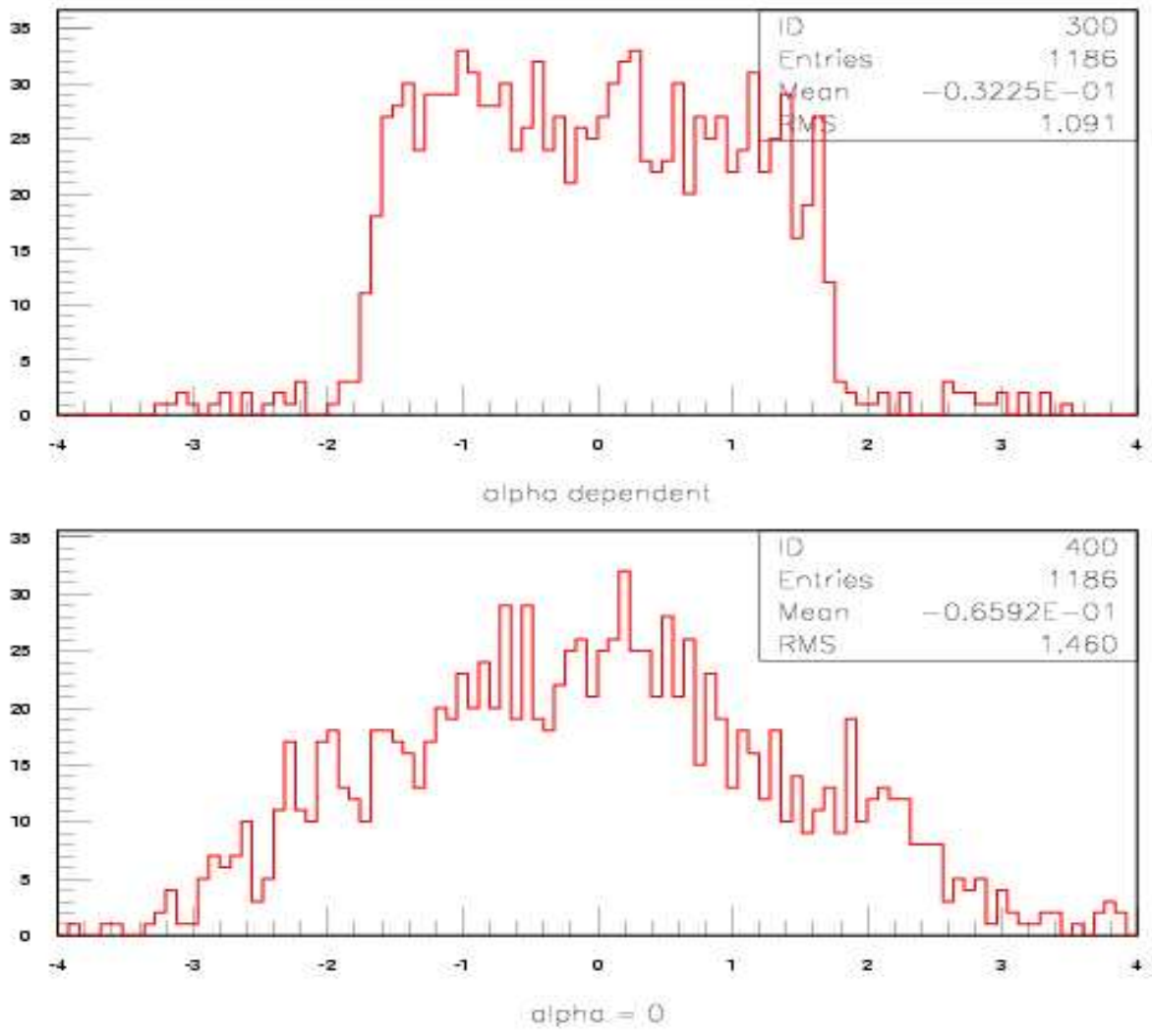

Figure 3.10: The predicted position pulls for tracks with $p_T = 0.5$ GeV/c for doublet clusters in axial layers only, α-dependent (top) and $\alpha = 0$ (bottom).

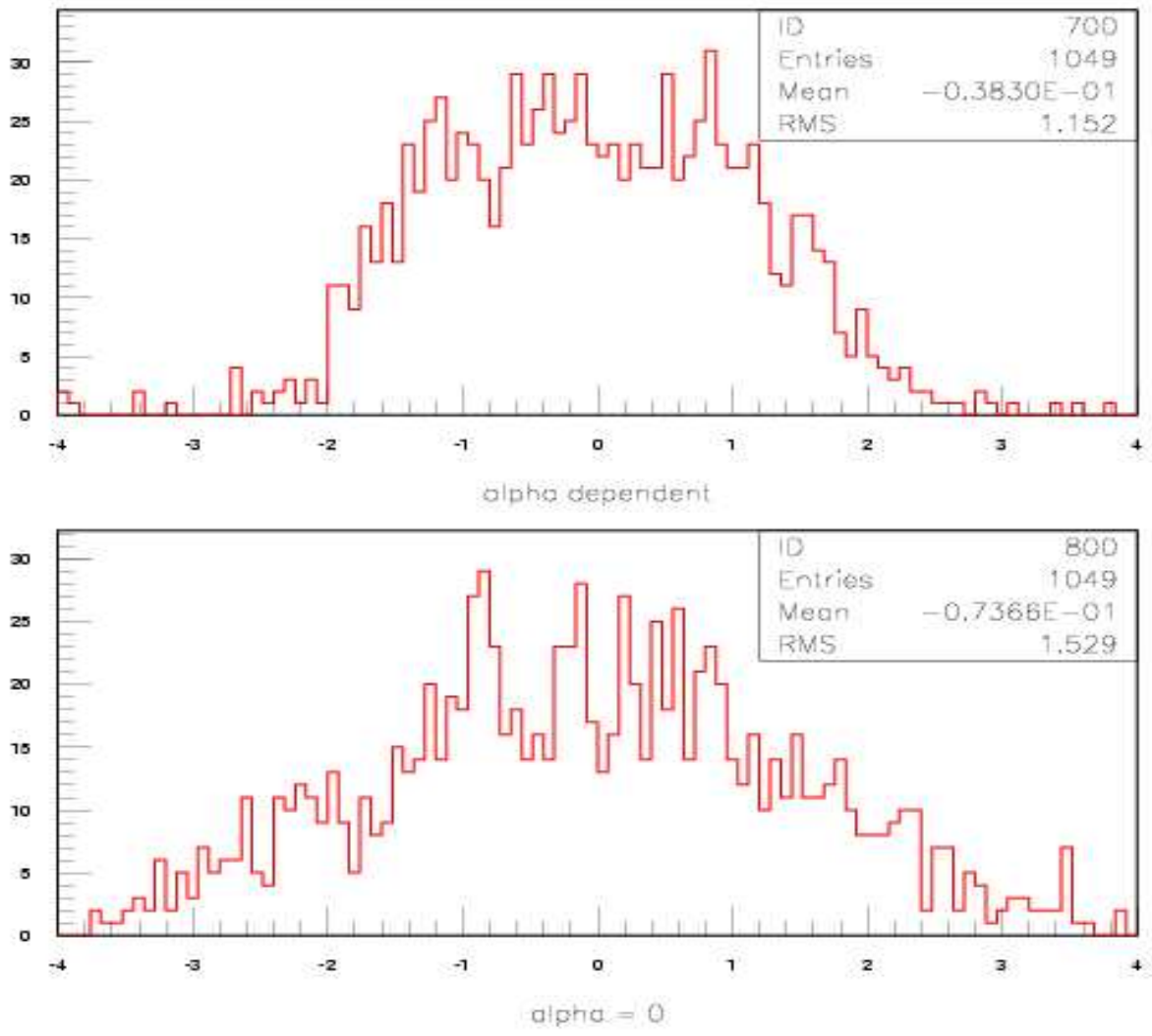

Figure 3.11: The predicted position pulls for tracks with $p_T = 0.5$ GeV/c for doublet clusters in stereo layers only, α-dependent (top) and $\alpha = 0$ (bottom).

Appendix D

SMT Offline calibration database

This chapter describes the Silicon Microstrip Tracker (SMT) Offline Calibration Database at the DØ . The essential part of the database is the C++ access code based on the `dOomCORBA` (DØ Object Model `CORBA`) code. This code provides an access to the offline calibration database via `PYTHON` database server with an advanced caching mechanism. The list of available access methods to the database and the detailed description of how to turn on the database access in the reconstruction code are given at the end of this chapter.

D.1 Introduction

The SMT offline calibration database stores the calibration constants such as pedestal values, gains, drifts, channel statuses and uncertainties on all calibration constants. These constants are calculated by the front end pro-

cessors of the power PCs in the sequencer crates during the Secondary Data Acquisition (SDAQ) run in the silent period between data taking. The calibration constants are calculated based on the measurement of 500 events. The run might be taken for all VRB readout crates and/or one VRB readout crate at the time. The quiet time for the SDAQ is currently required every $2-3$ days and data taking itself can be finished in about an hour. After evaluation of the run, the constants are stored in the SMT online calibration database [158] together with down-load parameters for the SVX chips. The calibration constants are going to be transfered by the SMT Calibration Data Transfer code to the SMT offline calibration database which holds calibration constants from good calibration runs. Unlike the online database, it holds only the calibration constants. To retrieve calibration constants from the offline calibration database for purposes of the offline event reconstruction, each individual channel is looked-up by the database access code for each run taken. The set of calibration constants will be different from run to run. Thus each calibration set has to be created based on the run number. At the beginning of the offline reconstruction, the reconstruction code requests a set of calibration constants based on the run number. This is going to be repeated for each and every event in the input file. The top-level calibrator is responsible for making a decision which set of calibration constants to pull out from the database. This decision is made by checking the validity range for a given calibration constant set. It passes the information about the calibration set to be used to the SMT Calibrator. The SMT calibrator is technically responsible to access the database using provided accessors and create a set of calibration constants that can be used by the reconstruction

code.

The design of the SMT Offline Calibration Database, its content and relation between tables is illustrated in the Entity Relation Diagram (ERD) in Figure 4.1.

D.2 SMT offline calibration database access code

The `smt_calibration package`, contains the C++ access code to access the SMT Offline Calibration Database. It provides methods to retrieve calibration constant values of pedestals, gains, drifts and their uncertainties from the offline calibration database. All values are extracted based on the following set of ID's: calibration ID, chip ID and channel ID. Every High Density Interconnect (HDI) in the SMT has a unique and distinct number, called the calibration ID. The ladder and layer numbers are coded in the calibration ID numbers. This makes it relatively easy to look up in what part of the SMT this channel is situated in. The calibration ID is combined with the chip and strip information to provide a channel identification number [161]. This set of IDs is unique for each channel. Only the channel ID is necessary to access calibration constants for each channel however. The other two IDs (calibration ID and the chip ID) can speed up the information retrieval from the database significantly. The code is simplified to find the HDI first with a given calibration ID, then to find the chip with a given chip ID on that HDI and finally loop through 128 channels to find the channel with a unique channel ID. That naturally makes the access code more efficient in terms of

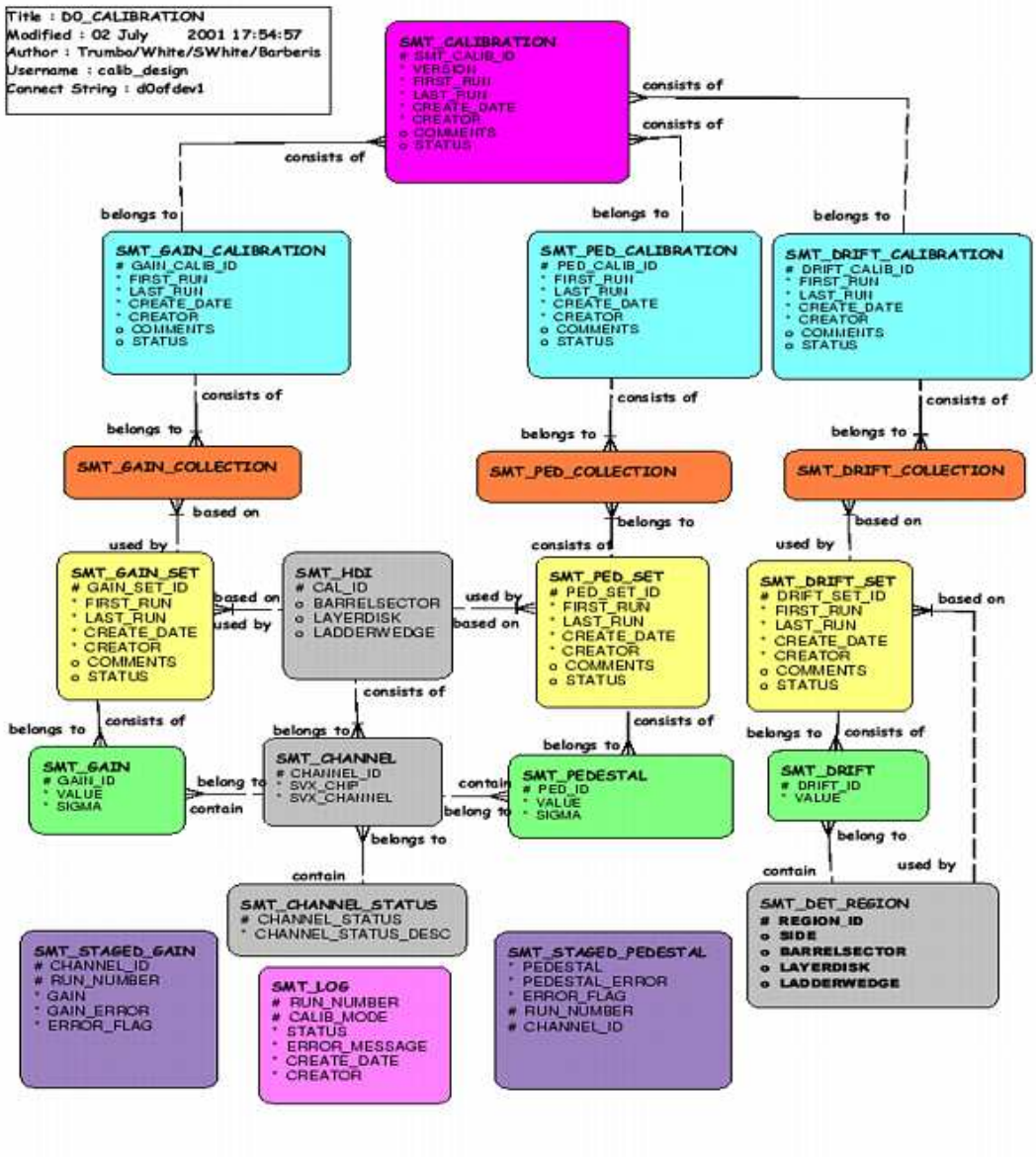

Figure 4.1: The Entity Relation Diagram of the SMT Offline Calibration Database [159].

time consumption.

After the information is retrieved from the database, calibration constants are stored in the container class `SmtDetector` which provides a set of methods to apply those values in the offline reconstruction. This step is performed before the reconstruction starts. There are some issues connected with this step which are subject of a further discussion in Section D.6.

The package contains classes for each table in the Offline Calibration Database and additionally it holds the framework based SmtCalibrater class that has all the methods needed to access the database.

SMT offline calibration database represents an offline calibration system with a direct connection to the `ORACLE` database. There are two levels:

- top level: `d0_calibration` [160]
- subdetector: `smt_calibration` (this package)

SMT Offline Calibration involves:

- Tree of objects: they correspond to `ORACLE` tables
- User(`d0reco` package) interface: to access the elements of the tree (refreshed and updated by the calibration manager). The access is through the handle methods.
- Framework management package: (`calibration_management`) initialize tree and calls to top level calibration.

Beneath the database access code are:

- calibration data model:

  `dOom, dOomCORBA, dOstream` to describe the database objects, pointers and collections based on the query objects.

- C++ to ORACLE mapping dictionaries

- client/server structure

The `smt_calibration` code has its own documentation that can be view at the URL address in [162].

D.3 SMTCalibrator access methods

There are access methods to access gains, pedestals and drifts. They are listed in what follows:

GAINS :

const GainMap& gains();

const ToGains gain(int channel);

PEDESTALS :

const PedMap& pedestals();

const ToPeds pedestal(int channel);

DRIFTS :

const DriftMap& drifts();

const ToDrifts drift(int region);

Methods to access the packed channel ID created from CalID, SVX Chip ID and SVX Channel ID are:

int packedChId(int calId, int svxChip, int svxChannel);

where the channel ID is packed as follows:

(calId << 12) + (svxChip << 8) + svxChannel

There are direct access methods to the calibration constants for each channel, where each channel is identified by the calibration ID, SVX Chip ID and SVX Channel ID:

float getPedestal(int calId, int svxChip, int svxChannel);

float getGain(int calId, int svxChip, int svxChannel);

float getPedestalSigma(int calId, int svxChip, int svxChannel);

float getGainSigma(int calId, int svxChip, int svxChannel);

long getStatus(int calId, int svxChip, int svxChannel);

Possible CHANNEL STATUS values are :

OK ... channel is OK

DEAD ... channel is marked as dead

NOISY ... channel is marked as noisy

BELOW ... pedestal for this channel is below the threshold

DnN ... channel is marked as dead and noisy at the same time

DnB ... channel is marked as dead and the pedestal is below the threshold

NnB ... channel is noisy and below the threshold at the same time

DnNnB ... channel is dead, noisy and below the threshold

SATURATED ... channel is saturated

DnS ... channel is dead and saturated at the same time

NnS ... channel is noisy and saturated at the same time

DnNnS ... channel is marked as dead, noisy and saturated

UNKNOWN ... status of the channel is unknown

D.4 SMT calibration data transfer process

During the SMT calibration data transfer process, the calibration constants are transferred from the online to the offline calibration database. The following steps describe the process for building the database on the offline side and the related data flow depict the processes for populating the SMT offline calibration tables `SMT_CALIB`. It is shown in Figure 4.2.

1. Online detector data is transferred to the offline calibration database and placed in temporary Staging tables.

2. Offline calibration data can be added to the same Staging tables allowing for application of the same filtering and consolidation rules as applied to online collected constants.

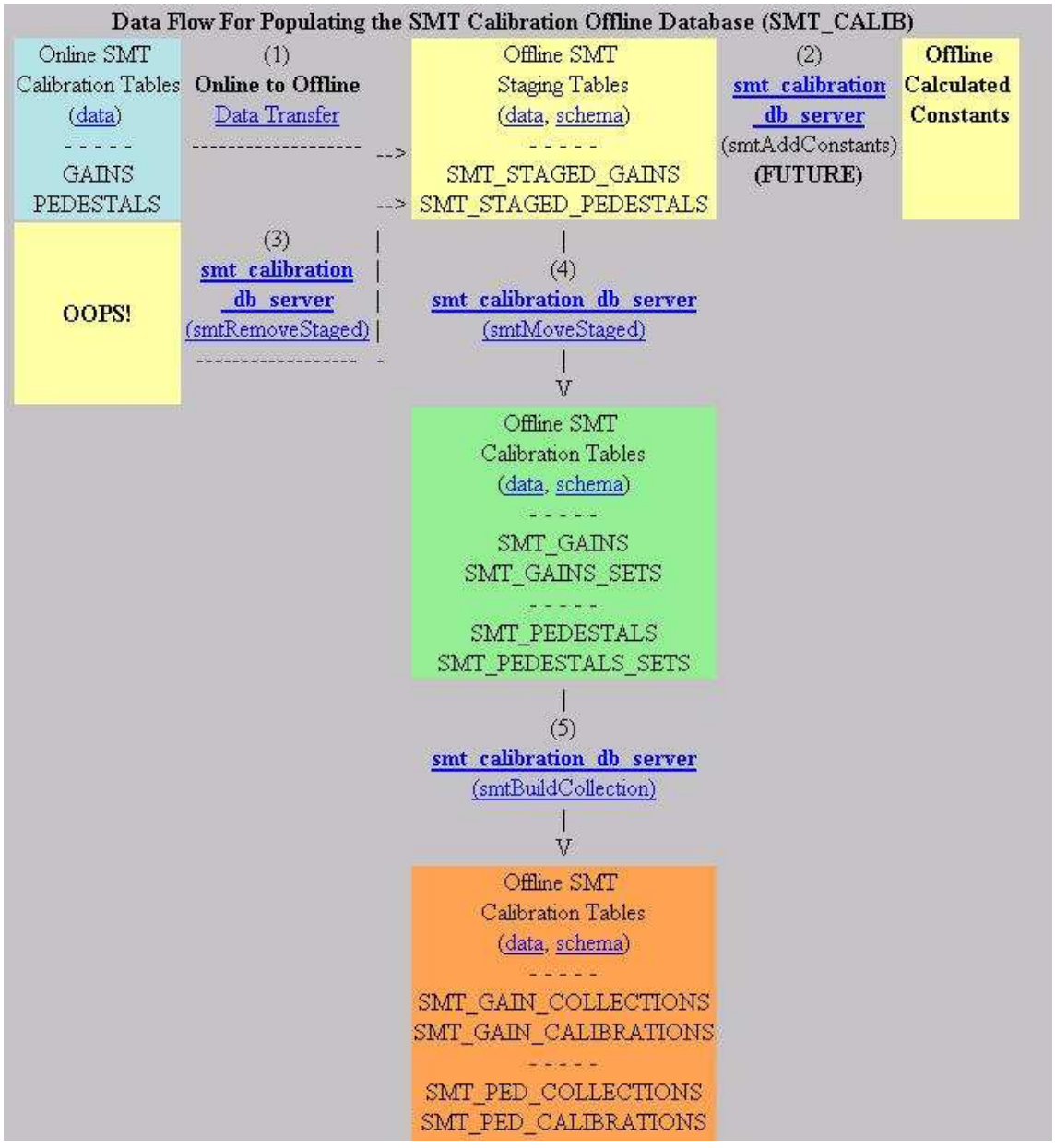

Figure 4.2: The SMT Calibration data transfer process flow.

3. This process removes data from the staging tables that had inadvertently been transferred.

4. Data is moved from the Staging tables into the appropriate offline tables allowing for filtering and consolidation.

5. This process builds the appropriate collections (top level offline tree) for the detector data populated in step (4).

D.5 SMT Calibration database space estimate

This section is intended to provide the rationale used for table row estimates used in the Oracle Designer space reports for the `SMT_CALIB` tables.

The total space requirements for the SMT Calibration database using these estimates are given in Table 4.1.

	Initial	End
Tables	13.6 Gb	29.39 Gb
Indexes	11.4 Gb	23.62 Gb

Table 4.1: The total space requirements for the SMT Calibration Database.

It should be noted that 2 tables (`SMT_GAINS` and `SMT_PEDESTALS`) require 12 Gb of the 'Initial' 13.6 Gb. They would consume a proportionate share of the 'End' table-space and index table-spaces.

The estimated number of rows for each of these 2 tables is a significantly wild guess. This is due to the nature of the process. On a run by run basis, only those rows that have changed from the previous run will be maintained

in the database. The wild card is knowing what this percentage is. As data is collected this might become better defined.

If these 2 tables had their individual table-space, fragmentation issues will be avoided and, hopefully, growth can be more easily accommodated.

We have listed in what follows the initial and max extents for each table based on the row estimates. This is followed by the algorithms/rationale for those row estimates.

D.5.1 Preliminary space estimates for `SMT_CALIB` table

The preliminary space estimates for the `SMT_CALIB` table are given in Table 4.2.

D.5.2 Rationale used to estimate number of rows per table

These are stagnant tables, almost administrative in the nature. Once populated they will be updated on a very infrequent basis.

The initial rows estimate is based on the current known configuration of the SMT detector.

Max rows is arbitrarily set at twice the initial to allow for the periodic updates, twice a week supposedly.

`SMT_CHANNEL_STATUS` is a validation type table which contains a small, limited number of rows.

`SMT_DET_REGIONS` is estimated to be similar to the `SMT_HDIS` (for the moment `SMT_DRIFT` branch is not used).

Table space	Table	Initial Rows	Max Rows	Initial Extent	Max Extents
SMT_CALIB_DATA	SMT_CALIBRATIONS	300	600	139.26 Kb	278.53 Kb
SMT_CALIB_DATA	SMT_CHANNELS	800,000	1,600,000	72.82 Mb	145.64 Mb
SMT_CALIB_DATA	SMT_CHANNEL_STATUSES	20	20	16.38 Kb	16.38 Kb
SMT_CALIB_DATA	SMT_DET_REGIONS	1,000	2,000	73.73 Kb	139.26 Kb
SMT_CALIB_DATA	SMT_DRIFTS	60,000	120,000	6.73 Mb	13.47 Mb
SMT_CALIB_DATA	SMT_DRIFT_CALIBRATIONS	300	600	122.88 Kb	237.57 Kb
SMT_CALIB_DATA	SMT_DRIFT_COLLECTIONS	55,000	110,000	3.79 Mb	7.58 Mb
SMT_CALIB_DATA	SMT_DRIFT_SETS	55,000	110,000	22.53 Mb	45.06 Mb
SMT_CALIB_DATA	SMT_GAINS	45,000,000	90,000,000	6.04 Gb	12.09 Gb
SMT_CALIB_DATA	SMT_GAIN_CALIBRATIONS	300	600	122.88 Kb	237.57 Kb
SMT_CALIB_DATA	SMT_GAIN_COLLECTIONS	55,000	110,000	3.24 Mb	6.49 Mb
SMT_CALIB_DATA	SMT_GAIN_SETS	55,000	110,000	21.46 Mb	42.92 Mb
SMT_CALIB_DATA	SMT_HDIS	1,000	2,000	40.96 Kb	73.73 Kb
SMT_CALIB_DATA	SMT_LOGS	1,000	2,000	353.3 Kb	712.7 Kb
SMT_CALIB_DATA	SMT_PEDESTALS	45,000,000	90,000,000	6.04 Gb	12.09 Gb
SMT_CALIB_DATA	SMT_PED_CALIBRATIONS	300	600	122.88 Kb	237.57 Kb
SMT_CALIB_DATA	SMT_PED_COLLECTIONS	55,000	111,000	3.24 Mb	6.55 Mb
SMT_CALIB_DATA	SMT_PED_SETS	55,000	110,000	21.46 Mb	42.92 Mb
SMT_CALIB_DATA	SMT_STAGED_GAINS	800,000	8,000,000	126.03 Mb	1.26 Gb
SMT_CALIB_IDX	SMT_STAGED_PEDESTALS	800,000	8,000,000	126.03 Mb	1.26 Gb

Table 4.2: The preliminary space estimate for the SMT_CALIB table.

The rationale to estimate number of rows in SMT_HDIS, SMT_CHANNELS, SMT_CHANNEL_STATUSES, and SMT_DET_REGIONS tables is given in Table 4.3.

Table	barrels	F-disks	H-disks	total	initial rows	max rows
SMT_HDIS	432	288	192	912	1,000	2,000
SMT_CHANNELS	387,072	258,048	147,456	7,925,768	800,000	1,600,000
SMT_CHANNEL_STATUSES					20	20
SMT_DET_REGIONS					1,000	2,000

Table 4.3: Rationale used to estimate number of rows in SMT_HDIS, SMT_CHANNELS, SMT_CHANNEL_STATUSES and SMT_DET_REGIONS tables.

These are the three major space hogs. These tables will only contain data that has changed from one run to the next one. Therefore the biggest factor in determining is in knowing how the data changes from run to run and this is the big unknown.

These are insert only tables. There are no updates or deletions in these tables. The initial rows estimate is based on half of the max rows required in total.

Consideration should be given to creating a separate table-space for each of these tables. This should provide some flexibility in managing growth. It will also eliminate the fragmentation that is likely to occur if they are in the same table-space with smaller tables.

The rationale to estimate number of rows in SMT_GAINS, SMT_PEDESTALS and SMT_DRIFTS tables is given in Table 4.4.

The _SETS tables are the parent tables to the 3 major space hogs men-

Table	# channels	runs/week	weeks/year	years	% of changed records		init rows	max rows
SMT_GAINS	800,000	× 3	× 52	× 3	×25%	= 93,600,000	45,000,000	90,000,000
SMT_PEDESTALS	800,000	× 3	× 52	× 3	×25%	= 93,600,000	45,000,000	90,000,000
SMT_DRIFTS	1,000	× 3	× 52	× 3	×25%	= 117,000	60,000	120,000

Table 4.4: Rationale used to estimate number of rows in SMT_GAINS, SMT_PEDESTALS and SMT_DRIFTS tables.

tioned above. The difference in their estimates is that they are driven by the number of SMT_HDIS and SMT_DET_REGION table rows rather than the number of SMT_CHANNELS. The rationale used to estimate number of their rows is given in Table 4.5.

The _COLLECTIONS tables are parents of the _SETS tables. The maximum number of rows is a factor of the number of SMT_HDI/SMT_DET_REGION table and the number of runs. They are affected by the percentage of channel sets that have changed. So the calculation is the same as for the _SETS tables.

This is probably an overstatement since many of the _SETS combinations will be combined in these tables, but since the space requirements are so small it is probably not worth the guess.

The rationale used to estimate number of rows in _COLLECTIONS tables is given in Table 4.6.

Each of these tables has the potential to transfer $800,000$ rows of channel data per run between the online database and the offline database.

These tables are transient in nature, in that after the data is transferred, an offline SMT database server process is initiated that will move the data from these tables into their permanent home (SMT_GAINS and SMT_PEDESTALS), deleting the data from the respective SMT_STAGED_GAINS and SMT_STAGED_PEDESTALS tables.

Based on 3 runs/week transferred from online to offline, this will hold about 3 weeks data.

Periodic coalescing of these tables is important, which should be handled by the toolman or OEM [163].

The rationale to estimate number of rows in staged tables is given in

Table	# *cal_id* # *region_id*	runs/week	weeks/year	years	% of changed records		init rows	max rows
SMT_GAIN_SETS	1,000	× 3	× 52	× 3	×25%	= 117,000	55,000	110,000
SMT_PED_SETS	1,000	× 3	× 52	× 3	×25%	= 117,000	55,000	110,000
SMT_DRIFT_SETS	1,000	× 3	× 52	× 3	×25%	= 117,000	55,000	110,000

Table 4.5: The rationale used to estimate number of rows in SMT_GAIN_SETS, SMT_PED_SETS and SMT_DRIFT_SETS tables.

Table	initial rows	max rows
SMT_GAIN_COLLECTIONS	55,000	110,000
SMT_DRIFT_COLLECTIONS	55,000	110,000
SMT_PED_COLLECTIONS	55,000	111,000

Table 4.6: The rationale used to estimate number of rows in SMT_GAIN_COLLECTIONS, SMT_PED_COLLECTIONS and SMT_DRIFT_COLLECTIONS tables.

Table	number channels	max number of runs to be held		initial rows	max rows
SMT_STAGED_GAINS	800,000	× 10	= 8,000,000	800,000	8,000,000
SMT_STAGED_PEDESTALS	800,000	× 10	= 8,000,000	800,000	8,000,000

Table 4.7: The rationale used to estimate number of rows in staged tables.

Table 4.7.

The maximum number of rows these _CALIBRATIONS tables can contain is one per run transferred from offline to online. There is some consolidation that potentially takes place, but since the amount of space need is relatively minimal, refinement should not be necessary.

Table	runs/week	weeks/year	years		initial rows	max rows
SMT_CALIBRATIONS	3	× 52	× 3	= 468	300	600
SMT_DRIFT_CALIBRATIONS	3	× 52	× 3	= 468	300	600
SMT_GAIN_CALIBRATIONS	3	× 52	× 3	= 468	300	600
SMT_PED_CALIBRATIONS	3	× 52	× 3	= 468	300	600

Table 4.8: The rationale used to estimate number of rows in SMT_CALIBRATIONS, SMT_DRIFT_CALIBRATIONS, SMT_GAIN_CALIBRATIONS and SMT_PED_CALIBRATIONS tables.

The rationale to estimate number of rows in _CALIBRATIONS tables is given in Table 4.8.

The SMT_LOGS table should contain 1 row for every run with entries indicating if the data has moved from the staging to the database and if the top level tree has been built (2 states).

Table	runs/week	weeks/year	years	# of states # of states		initial rows	max rows
SMT_LOGS	3	× 52	× 3	× 2	= 936	1,000	2,000

Table 4.9: The rationale used to estimate number of rows in SMT_LOGS table.

The rationale to estimate number of rows in `SMT_LOGS` table is provided in Table 4.9.

D.6 SMT Offline Calibration database status

The SMT Offline Calibration database is currently fully functioning. The calibration constants can be used for the offline calibration. It is possible to pull out all calibration constants for the SMT and CFT at the same time with a standard p11.10.00 `d0reco` version (main offline reconstruction package). The number of tracks reconstructed increased by about 10%.

D.6.1 Instructions to turn on the database access code

In order to turn on the database access code in d0reco, the user has to add these lines to the framework RCP file, e.g. to `runD0reco_data.rcp`.

```
RCP calib = <calibration_management calibration_management>
RCP smtconfig = <smt_config SmtConfiguration_db>
```

and have the following initialization packages

```
string Packages = "calib init read cfgm unpack det ... smtconfig"
```

And the user has to modify the *calibration_management/rcp/calibration_management.rcp* file to include

```
string d0CalibDB = "CORBA:D0DbServer.prd"
string SmtCalibDB = "CORBA:SmtDbServer.prd"
```

This functionality has been enabled in p11.11.00 (selected with rcp), and

the farms group has been asked to test it. There is a memory usage problem however. Using standard measurements, the job used 635 Mb. That could be a serious problem for regular users in the clued0 batch system. The timing is also an issue. It takes about 15 minutes to pull out calibration constants for $800,000$ channels from the SMT offline calibration database and about 3 minutes to get all constants for the CFT. The database access happens at the beginning of the offline reconstruction. That will not represent a problem for farm jobs but might be unacceptable for DØ users who run their reconstruction code locally. The optimal way is to write a new database server in C++ so that the task can be handled much faster.

D.7 SMT Offline Calibration database access code tests

We have tested thoroughly the access code requiring a comparison between flat files calibration constants (obtained with the simple python script directly from the online database) for each channel to be identical with the constants retrieved from the database by the access code. These values are for majority of the channels identical (both for barrels and disks), identical means that they differ only on the second decimal digit. That is a precision of pedestal values in the offline calibration database. There are some minor discrepancies which are caused by the update method during the online-to-offline transfer, the flat file did not have the same tree build for all channels. The result is satisfactory. It means that for a given run we have obtained the calibration set that has been requested. This test is a comprehensive test of

the offline calibration database because it not only tests the access code but also the transfer mechanism and the top-level calibrator as well.

As a result, the number of tracks reconstructed was close to the number obtain with calibration constants from a flat file. The track parameters in terms of pulls, DCA resolution, φ track distributions were similar for the reconstructed files with and without the database access.

The goal is to reconstruct more tracks keeping the same fake rate, and observe the improvement of track parameters on run-by-run basis. That is an ultimate test of the access code.

D.8 Trailor

The top level RCP file for the `smt_calibration` package is the `SmtCalibrater.rcp` file. The most important RCP file for the offline calibration DB access code is `calibration_management_t.rcp` where all the calibration DB servers are defined. The default calibration set can be defined there as well. Figure 4.3 shows what the default RCP parameters are set to.

```
// The next three items are used by the calibration_management framework
// package.  The remaining items are read by the CalibrationManager class.

string PackageName = "calibration_management"  // Used only by framework
bool   forceInit = false                       // true $==>$ init even for MC
bool   disable = false                         // true $==>$ never init

//-------------------------------------------------------------------------------
//
//  RCP for the CalibrationManager initialization in calibration_management
//
//-------------------------------------------------------------------------------

// Override the default (initial) calibration by specifying a valid ID.

int default_calib_id = -1

// The following are the DB names for each subdetector.  Duplicate names are
// allowed, but only one stream will be opened for duplicates.  An empty
// string implies no database will be opened.  The database name is of the
// form "tag:dbname".   The tag identifies the access method(CORBA, ORACLE
// EVPACK, DSPACK or DBFILE), and the dbname is the database name.  If ORACLE
// access is used, the DB must be of the form "username/password@db". For
// EVPACK (or DSPACK) the name must be a file whose top level class is the
// top level of the  requested detector's calibration tree.
//
// The type DBFILE indicates a flattened oracle database.  The flattening
// produces three types of files, by default all in the same directory tree. The
// three files are: top.db which contains the top-level tables, [xxxCalib.db
// (xxx=subdet) which contains the individual subdetector top-level tables] and
// $xxx/xxxCalibration_nnnnnn.db$ which contains the full calibration tree for
// each subdetector calibration with nnnnnn specifying the calibration id. The
// possible formats of the DBFILE specifier are:
//
//   DBFILE:directory/          - specifies full directory path.
//   DBFILE:subdir              - specifies subdirectory relative to top level
//   DBFILE:                    - uses defaults or top level(if DBFILE)
//
string d0CalibDB  = "$CORBA:D0DbServer.user_prd$"
string SmtCalibDB = "$CORBA:SmtDbServer.user_prd$"
string CftCalibDB = "$CORBA:CftDbServer.user_prd$"
string CalCalibDB = ""
string CpsCalibDB = "$CORBA:CpsDbServer.user_prd$"
string FpsCalibDB = ""
string MdtCalibDB = "$CORBA:MuonMDTDbServer.user_prd$"
string PdtCalibDB = "$CORBA:MuonPDTDbServer.user_prd$"
string MscCalibDB = "$CORBA:MuonMSCDbServer.user_prd$"
string FpdCalibDB = ""

// The automatic version control can be overridden to a fixed calibration
// version for all events subdetector-by-subdetector. The ID must be a valid
// ID entry in the top level table for the appropriate subdetector.

int d0CalibForceID  = -1
int SmtCalibForceID = -1
int CftCalibForceID = -1
int CalCalibForceID = -1
int CpsCalibForceID = -1
int FpsCalibForceID = -1
int MdtCalibForceID = -1
int PdtCalibForceID = -1
int MscCalibForceID = -1
int FpdCalibForceID = -1

// An untracked debugging flag

bool debug = false
}
```

Figure 4.3: Names of all database servers needed to access calibration databases must be specified in `calibration_management_t.rcp` file.

Appendix E

$Z \to \mu^+\mu^-$ mass resolution

In the p13 data, the resolution of Z mass has been by factor of $2-3$ worse than in the $Z \to \mu\mu$ Monte Carlo sample reconstructed with the same version of the `d0reco` package (event reconstruction code). This chapter describes, what is the cause of this effect, how can the data be corrected with a simple correction to the transverse momentum, and which effects are responsible for the residual discrepancy in the resolution between Monte Carlo and data.

E.1 Discrepancy between Monte Carlo and data

Figure 5.1 shows the invariant mass calculated in Monte Carlo $Z \to \mu\mu+$ Drell-Yan sample (top) and the data (bottom). The invariant mass has been fitted in the same mass region by a Gaussian plus the exponential background. The calculated resolutions are $\sigma = 6.5$ GeV/c^2 in Monte Carlo and $\sigma = 11.5$ GeV/c^2 in the data. Ideally, both values should be close, except

for some little difference, supposedly less than 1 GeV/c^2 or so. That is not what we have observed. As a matter of fact, the discrepancy is more than factor of $2-3$. The data has a much worse resolution than expected.

This discrepancy means that there is some problem with the high-p_{T} tracking. The same problem was observed in $Z \to ee$ channel, i.e. that this effect can be completely decoupled from the muon system or the calorimeter. Only the central tracking system is responsible for this problem.

There could be many possible effects involved:

- misalignment (there are 2 CFT alignment geometries available at that time)
- magnitude of the magnetic field is wrong
- magnetic field is shifted
- geometry is wrong (e.g. it can be shifted, rotated, shifted+rotated etc.)
- cluster residuals in CFT and SMT are much worse in data than in Monte Carlo, difference in cluster size
- primary vertex constraint is not taken into account
- ADC cuts applied on the CFT cluster charge information, are killing some clusters, or at least changing cluster positions so that track parameters are measured worse, see Section C.
- geometrical effect, e.g. Z events reconstructed in a forward region have a different resolution than those reconstructed in the central part; Z events reconstructed out of the fiducial volume of SMT barrels have worse resolution than those decaying inside SMT barrels, etc.

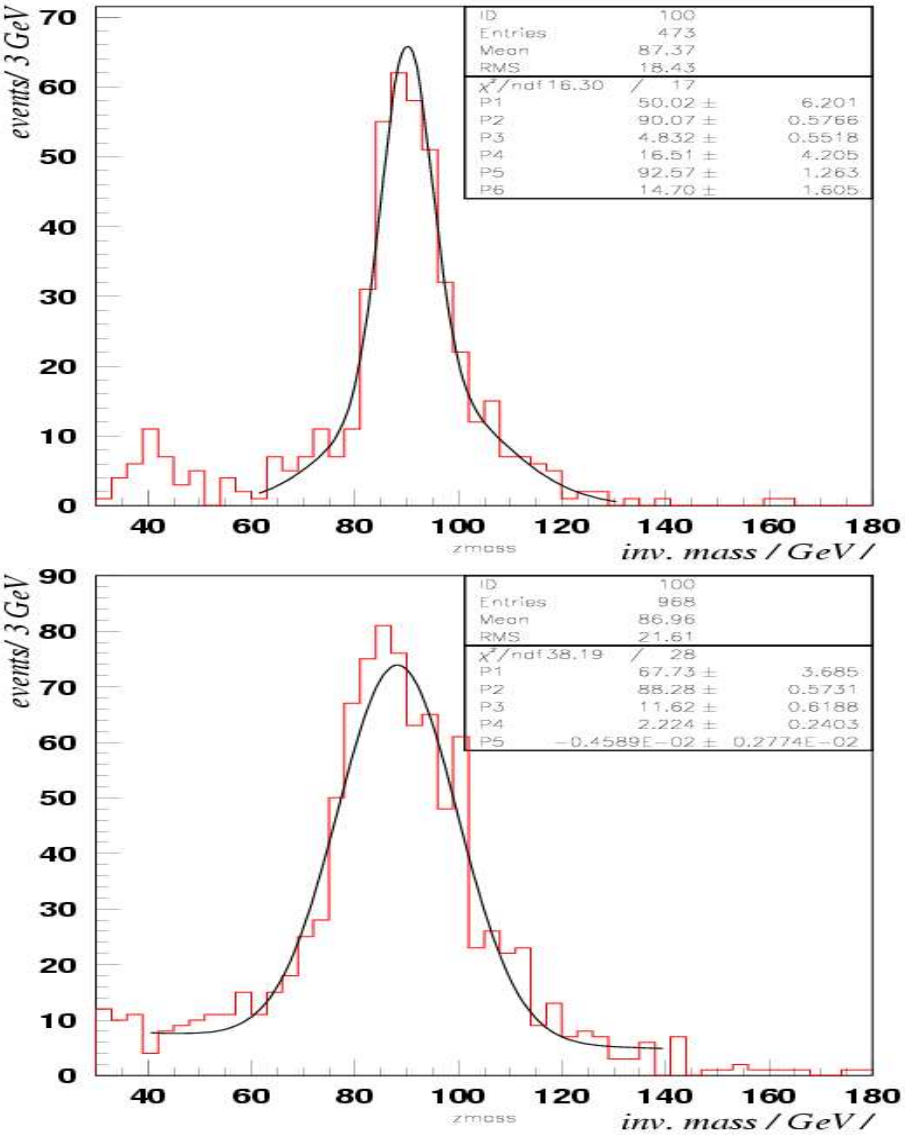

Figure 5.1: Reconstructed dimuon mass in Monte Carlo $Z \to \mu\mu$ + Drell-Yan (top) and the data (bottom). The resolution in Monte Carlo is $\sigma = 4.8$ GeV/c^2, whereas in data it is $\sigma = 11.6$ GeV/c^2. This represents a factor of more than two. Only information from the central tracker is used to calculate the invariant mass.

- active radius of the CFT fiber might not be implemented correctly
- some dependence on a particular version of the track reconstruction code

All these effects, were taken into account and investigated closely. Unfortunately, at the time this study has started, there was only a small sample of high-p_{T} dimuon events available. Not every study can be performed into detail. Some of the checks performed gave us a hint, but given the size of the sample, they were not conclusive. This is why we had to wait we collected a larger dimuon sample by skimming a single muon Electroweak group stream.

E.2 SMT and CFT cluster residuals

It is well known that the residuals observed in the data are worse than those in Monte Carlo. This is mainly true for high-p_{T} tracks. It is obvious, that most of the track resolution comes from the central tracker, and it is generally accepted, that the silicon tracker is less important for high-p_{T} tracking. Whereas this is true for track finding, it is not true for track fitting. It can be understood that the larger is the leverage between the first and the last hit, the better is known the transverse momentum. As a matter of fact, it can be proven that the first and the last couple of hits are the most important ones for a precise measurement of the transverse momentum. The importance of the silicon tracker for high-p_{T} tracking is demonstrated on the Z mass resolution in this chapter.

A good understanding of SMT and CFT clusters is a necessity for a precise momentum measurement. A huge difference in terms of hit resolution, both

detector	cluster type	$Z \to \mu\mu$ MC (μm) hit included	$Z \to \mu\mu$ MC (μm) hit not included	data (μm) hit included	data (μm) hit not included
CFT	singlets	64(1)	72(1)	95(2)	108(2)
	doublets	80(1)	88(2)	88(2)	96(2)
SMT	p-side	10.4(2)	–	15.1(2)	–
	n-side (2°)	302(10)	–	379(15)	–
	n-side (90°)	75(2)	–	127(3)	–

Table 5.1: The SMT and CFT residuals, i.e. the difference between the track and cluster position on a given surface, in $Z \to \mu\mu$ Monte Carlo and data. The measurement is done separately for singlet and doublet clusters in the CFT, for clusters on the p-side, and the 2° and 90° n-side in the SMT. For CFT, the measurement is also done for clusters that are included in the track fit and for clusters that are intentionally skipped from a track fit in order to obtain an unbiased measurement of residuals.

in SMT and CFT, is an evidence of problems in the track reconstruction in the data.

The residuals measured in Monte Carlo and data, both in SMT and CFT, are given in Table 5.1. There were $1,047$ $Z \to \mu\mu$ candidate events available in the data, and $2,500$ $Z \to \mu\mu$ + Drell-Yan Monte Carlo events with the cross section of 776 pb.

It is critical to understand that the light yield from CFT fibers (ADC cluster charge information) depends strongly on the η of the track. That is shown in Figure 5.2 for Monte Carlo (top) and

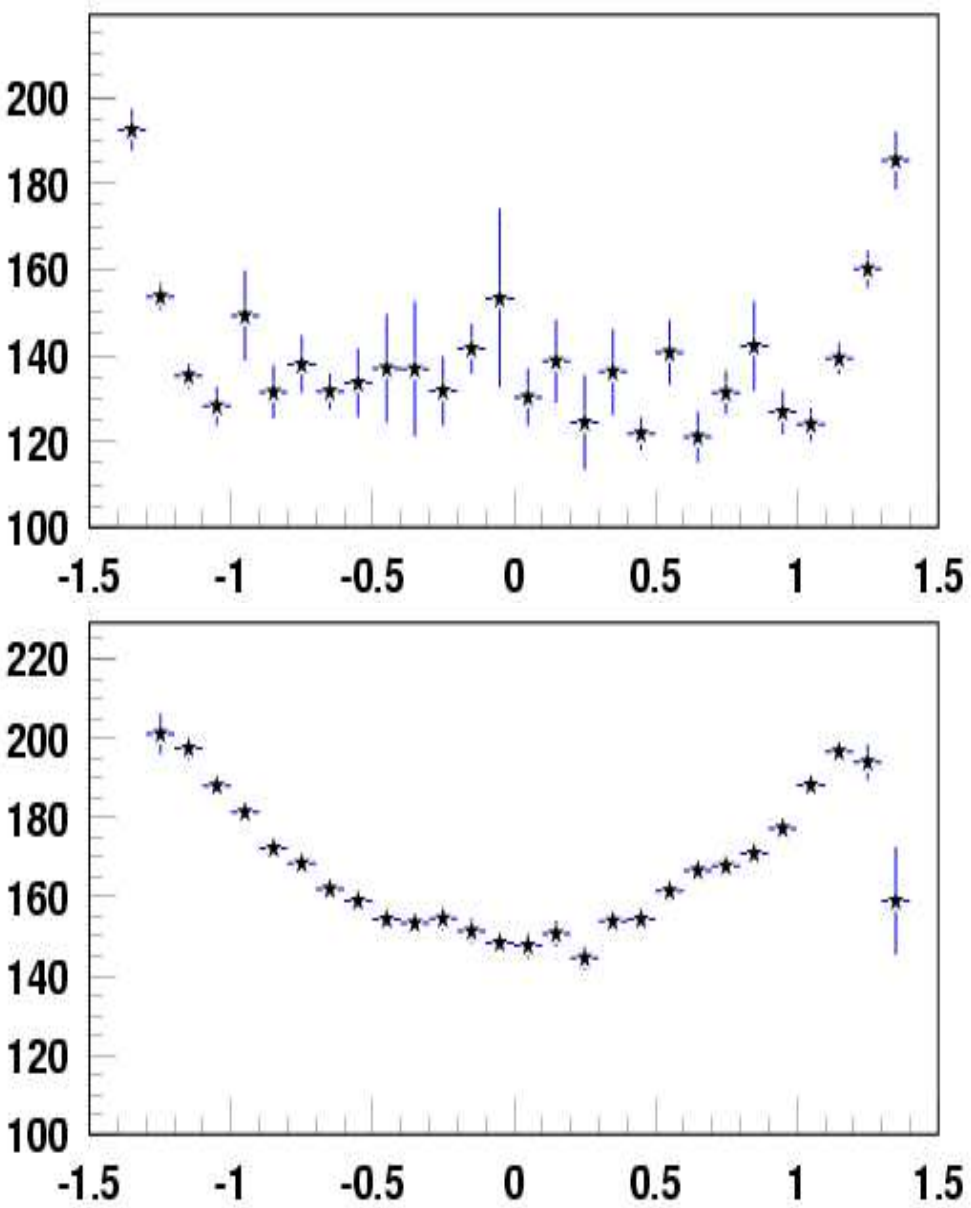

Figure 5.2: The ADC information from singlet clusters (only one fiber) as a function of track η in Monte Carlo (top) and the data (bottom). The vertical axis is in ADC counts. The distribution for doublet clusters is similar.

the data (bottom) for singlet clusters only, the distribution is very similar for doublet clusters. The larger is the η, the longer is the path of the particle inside the fiber (fibers are parallel to the beam axis in axial layers, and under the 2° angle with the beam axis in stereo layers), and the more light is detected, converted into ADC counts and read out from the detector. The light yield is the smallest for $\eta = 0$, i.e. tracks that are perpendicular to fibers, no matter what their position along the z-axis is. In contrary, tracks that hit fibers under a large η benefit from the large light yield. There are several issues related to the light yield dependence on the pseudorapidity that are going to be discussed in this section: (a) dependence of the noise on η and its influence on the fiber multiplicity in clusters, and (b) the dependence of track residuals and cluster size on η and on the ADC cut applied in the CFT unpacker on a per strip basis.

E.2.1 Dependence of noise on pseudorapidity

Unlike the light yield, the noise does not depend on track η, i.e. it is flat in η. It is know for some time already, that the amount of noise in Monte Carlo is underestimated and it does not describe the data correctly. The noise affects the size of clusters. It increases the fiber multiplicity in a cluster higher, i.e. some singlet clusters turn to be doublets, some doublets turn to be triplets. Triplets, and higher multiplicity clusters, are unphysical. Track residuals are more than half-a-fiber wide for these clusters. They can spoil the track momentum resolution and the particle charge measurement by pulling the track fit away from particle's true path and altering the momentum measurement.

E.2.2 Dependence of cluster size and residuals on η and the ADC cut

The size of the cluster should not depend on track η. That can be verified in Monte Carlo. However, this is not what is seen in the data. There is a dependence of cluster size on η. Number of singlet clusters decreases with η, on the other hand, number of doublet clusters increases towards small η. A scissor effect is observed. It means that the ratio of number of singlets to doublets as a function of η looks like a parabola with a maximum at $\eta = 0$. This behavior is shown in Figures 5.3 and 5.5.

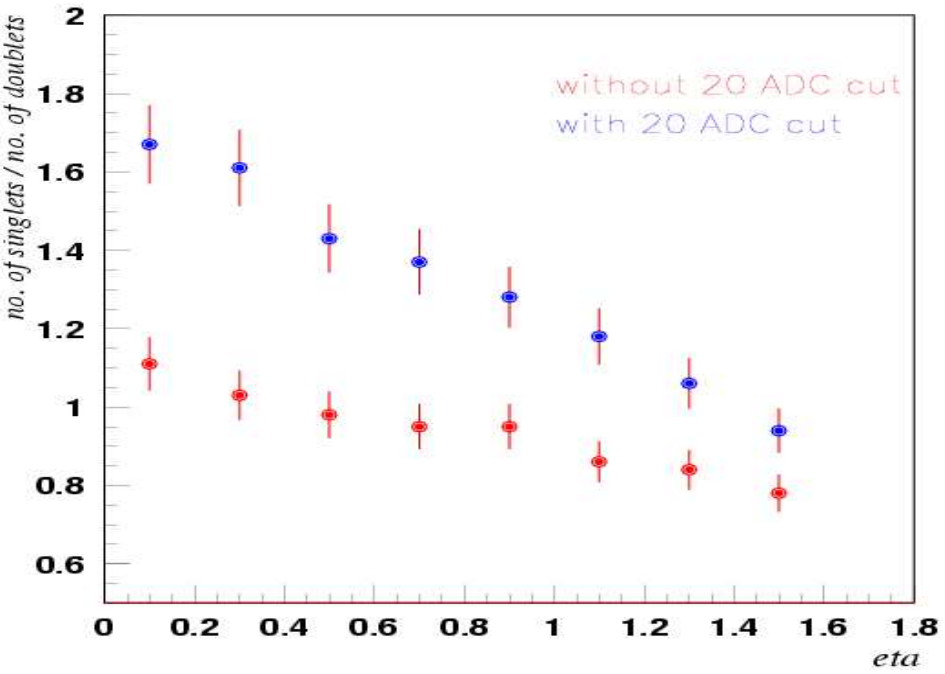

Figure 5.3: The ratio of number of singlet and doublet CFT clusters as a function of track η, with and without the 20 ADC cut applied on a per cluster basis. The ratio observed in Monte Carlo is flat, it is approximately 0.78.

The scissor effect can be easily understood, it is related to the light yield dependence on η. In the data, there are two kinds of ADC cuts that affect the cluster size. It is the software cut (20 ADC cut per fiber) and a hardware cut. What happens is that some of the fibers that do not pass the ADC cuts, no matter if they are applied in the event reconstruction or on the hardware level, are lost from the read out, reconstruction respectively. When the clusters are build offline, in the reconstruction, see Section C, the fibers with low light yield are not considered to be part of the cluster, i.e. some doublet clusters by nature turn to be singlets in the reconstruction code. In the worst case, a singlet cluster (= one fiber), is lost completely. As a result, multiplicity of fibers in clusters changes due to the ADC cut applied. Some doublets are converted into singlets, some singlets are lost completely. The base line is the dependence of the light yield on η. From a flat distribution in η, a nearly parabolic behavior with a maximum at $\eta = 0$ is obtained. Most of the doublets are converted into singlets. In the forward region, the ratio is about what it should be thanks to the large light yield. It is obvious that the residuals are directly related to cluster sizes, i.e. they are η dependent too. This dependence is demonstrated in Figure 5.4.

If a doublet fiber converts into a singlet, the residual are not going to stay unchanged, it will get much worse. Indeed, the residual is not going to be worse by half-a-fiber, because during refitting, the track is naturally pulled towards the cluster center. But the residuals for singlets get worse. It would be nice to do clustering without any ADC cut, but it is not possible. The software cut at 20 ADC can hardly be removed because there are events for which a collective jump of pedestals is observed and many fibers are read

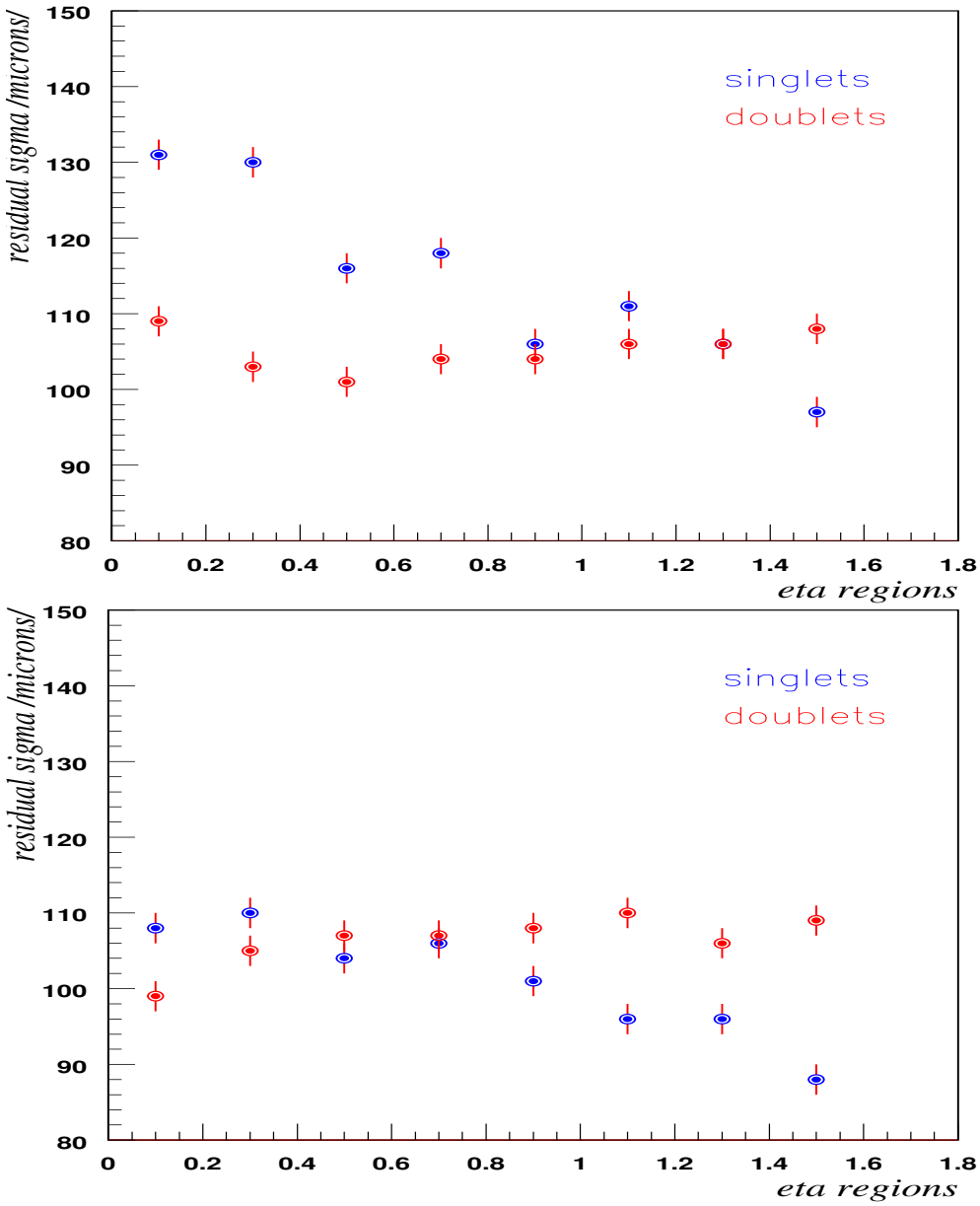

Figure 5.4: Track residuals for singlet and doublet clusters in the data as a function of track η, with (top) and without (bottom) the 20 ADC cut applied on a per fiber basis.

out at once. It is hard to do tracking with events like that because the combinatorics increases exponentially, and this kind of events slows down the entire event reconstruction. These events are called 'long events' and it can take up to several minutes to reconstruct them. This cut should be optimized however. Further consequences of this cut on the tracking efficiency as a function of η have been discussed in Appendix B. This cut is also responsible for a dip at around zero in η. The hardware ADC cut cannot be removed either, it is related to various thresholds in read-out electronics that cannot be removed. Figure 5.3 shows the ratio of number of singlet and doublet CFT clusters *versus* track η, with and without the 20 ADC cut applied.

The CFT cluster size distributions in Monte Carlo and data do not differ significantly however. There are more 'spoiled' doublets, i.e. clusters with a multiplicity three and higher, in the data than in the Monte Carlo.

In order to understand the SMT residuals, the following information about pitches between strips on silicon sensors is necessary. For barrels, the pitch on:

- p-side is 50 μm
- n-side (2° devices) is 62.5 μm
- n-side (90° devices) is 153.5 μm

The two outermost barrels have no 90° devices on the n-side, and hence they are only single-sided. The four inner barrels have both 2° and 90° n-sides. The first superlayer (layers one and two) has 90° n-side, the second superlayer (layers three and four) has a 2° n-side, the third superlayer (layers

five and six) has a 90° n-side again, and finally the fourth superlayer (layers seven and eight) has a 2° n-side. The 90° n-side is the best for a 3-dimensional resolution, but it has way too many ghosts. This is why a compromise between 2° and 90° devices on the n-side has been opted for.

For the F-disks, the pitch on the p-side is 50 microns and on the n-side 62.5 microns.

The resolution of the silicon detector goes roughly speaking as a pitch/$\sqrt{12}$, but thanks to the electron/hole charge sharing on several neighboring strips in a depleted area of the silicon sensor, it is much better than that. A method of weighting the charge collected from several neighboring strips has been developed to tell the position of a particle passing through the silicon sensor more precisely.

E.3 Role of the SMT in high-p_{T} tracking

As it has been discussed earlier, the importance of the silicon tracker is usually underestimated when talking about high-p_{T} tracking. This is a rather common misunderstanding. It is the goal of this section, to explain the opposite, it means, how important is the SMT for the transverse momentum resolution of high-p_{T} tracks.

The inner-most layer of the silicon vertex detector is only 2.7 cm away from the interaction point. There are four super-layers, i.e. eight layers of silicon sensors. They are equally spaced in radii from $2.7 - 10.$ cm. Every track therefore crosses at least four silicon sensors. The details can be found in [100, 164] as well as in Section **??**.

The central fiber tracker consists of 8 cylinders, on each cylinder, there

is an axial and stereo layer. The first cylinder is about 20 cm away from the beam axis. The distances between cylinders is 5 cm, with an exception of cylinder seven and eight. The last two cylinders are intentionally only 2 cm apart, i.e. the seventh cylinder is 50 cm and the eight 52 cm away from the beam axis in the (r, φ) plane. The intention was to put them as close to each other as possible in order to get the best resolution [140]. The best resolution comes from the two furthermost measurements, because they have the largest leverage. Indeed, the closer they are to each other, the more precisely is known the position of the track on those two surfaces. The 2 cm distance between CFT7 and CFT8 (CFT cylinders 7 and 8) is the smallest technically achievable separation, given the overall design of the tracker, see Section 3.1.2. The same could be done for the first two layers, but it was not, since unlike the last two hits, there are silicon measurements closer to the interaction point. The tracking algorithm does not extrapolate for the two inner-most CFT hits, but in contrary, it interpolates. That makes a big difference. It is obviously much easier and more precise to interpolate than extrapolate. It also means that the most important hits from the point of view of the tracking will not be the outermost CFT measurements, i.e. CFT1, CFT2, CFT7 and CFT8, but the outer-most measurements in the entire central tracking system - SMT1, SMT2, CFT7 and CFT8. In other words, the two nearest hits to the interaction point, most probably silicon hits, and the two most distant hits from the interaction point, probably hits in the last few CFT layers.

This reasoning puts the role of the silicon vertex detector into a whole different perspective. It still holds that the silicon detector is not critical for

sample	tracking system used	Z mass resolution ($\mathrm{GeV/c^2}$)
data	SMT+CFT	(12 ± 1)
	CFT only	(28 ± 2)
Monte Carlo	SMT+CFT	(6 ± 1)
	CFT only	(21 ± 5)

Table 5.2: Z mass resolution calculated using (a) both SMT and CFT measurement to find and fit tracks, (b) CFT measurement only.

track finding, the track reconstruction efficiency would be not much worse if silicon hits were not used. However, the resolution of high-p_{T} tracks would be significantly worsened, were the silicon hits not used in track refitting. Moreover, one can say that not only the central tracker problems should be blamed for the discrepancy in Z mass resolution, the SMT could be responsible for the difference too.

Table 5.2 gives the Z mass resolutions in Monte Carlo and data, for the two situations: (a) SMT and CFT are used to find and fit tracks, (b) only CFT is used to perform tracking. The difference is striking, there is almost factor of $2-3$ difference in mass resolution when using fiber tracker information only.

Given the information above, it is obvious that one should also compare number of hits (SMT and CFT) in the data and Monte Carlo. But not only that, compare distributions of the inner-most and outer-most hits in Monte Carlo and data, to see whether there is any difference. Both comparisons have been made, however no significant difference has been found. In Monte

Carlo, 79% of high-p_{T} tracks have the innermost hits in the two first silicon layers ($r < 4$ cm), in the data, 72%. The uncertainty on both values is couple of percent.

E.4 Smearing of SMT and CFT cluster positions

The large discrepancy between Monte Carlo Z mass resolution and the one observed in the data, could be explained by the difference in SMT and CFT track residuals in Monte Carlo and the data. That has been demonstrated in Table 5.1. The question is whether smearing of cluster positions, both for silicon and fiber tracker clusters, changes the momentum resolution so much that the resolution of the calculated invariant mass changes by a factor of more than 2.

The following smearing of cluster positions has been implemented in the tracking code:

- SMT cluster smearing:

  It is well known from earlier studies [165, 166], that the silicon cluster errors are underestimated in Monte Carlo. The uncertainties are wrong by a factor of two. The cluster position has to be Gaussian smeared as $\sqrt{3}\times$ error, where the error is calculated by the tracking algorithm from the track fit, for every track on a given silicon sensor surface. The modifications have been implemented to `trfxyp` and `trfzp` packages, the corresponding classes are HitXYPlane2 and HitZPlane2. The SMT residuals after the smearing agree very nicely with those observed in

the data. That is demonstrated in Tables 5.1 and 5.3.

- CFT cluster smearing:

  The smearing has to be performed inside the `cfttrf_clus` package, in CftTrfHitPhi and CftTrfHitPhiZ classes. The smearing factors are introduced based on the following formula for singlets

$$(\sigma_{smeared})^2 = (\sigma_{not\ smeared})^2 + (\sigma_{smearing})^2 + (\sigma_{track})^2 \quad (5.1)$$

$$(163\ \mu m)^2 = (75\ \mu m)^2 + (135\ \mu m)^2 + (52\ \mu m)^2 \quad (5.2)$$

  and for doublets

$$(\sigma_{smeared})^2 = (\sigma_{not\ smeared})^2 + (\sigma_{smearing})^2 + (\sigma_{track})^2 \quad (5.3)$$

$$(117\ \mu m)^2 = (98\ \mu m)^2 + (35\ \mu m)^2 + (54\ \mu m)^2 \quad (5.4)$$

  where the additional factor $\sigma_{track} = 54\ \mu m$, $52\ \mu m$ respectively, comes from the uncertainty of a track position on a given surface. Indeed, it should be about the same number for singlet and doublet clusters, because the track does not know about the multiplicity of a cluster, the error comes from the fit of a track to measured hits. The factors introduced to smear the CFT singlets and doublets are 135 microns and 35 microns, respectively. Both values tend to over-smear the Monte Carlo a little bit, singlets by almost 50 microns and doublets by 15 microns. The comparison of measured values is given in Tables 5.1 and 5.3.

detector	cluster type	$Z \to \mu\mu$ MC no smearing (μm)	$Z \to \mu\mu$ MC smearing (μm)
CFT	singlets	75(1)	163(6)
	doublets	98(1)	117(3)
SMT	p-side	10.1(2)	14.5(3)
	n-side (2°)	311(11)	350(12)
	n-side (90°)	71(2)	124(4)

Table 5.3: The SMT and CFT cluster residuals before and after smearing are presented. CFT cluster positions are randomly smeared as follows: singlets by 135 μm and doublets by 35 μm. SMT cluster positions are randomly smeared by a factor $\sqrt{3}\times$ error, where the error comes from the track measurement.

If only the SMT cluster positions are smeared, the mass resolution changes from 4.6 GeV/c^2 to 6.0 GeV/c^2. The additional smearing of CFT cluster positions results in the Z mass resolution of (7.2 ± 0.6) GeV/c^2. It means that the additional random smearing of cluster positions is able to explain some of the worse mass resolution observed in the data. It can only explain an effect of a few GeV/c^2, but not more than that. The smearing is a random effect. It means that uncertainties on the fitted tracks increase, they also tend to cancel, since they are random. It means that the final effect cannot be large.

On the other hand, any systematic effect, e.g. shifted ribbons, misalignment, magnetic field etc., could be held responsible for a larger effect.

There is another interesting aspect that has been investigated in this study. It is an effect of the 20 ADC cut on the CFT cluster residuals in the data. With the 20 ADC cut applied, singlet cluster residuals are worse than doublet cluster residuals. When the 20 ADC cut is dropped, i.e. only hardware cuts are applied, the situation reverts. The singlet clusters have a better resolution now. The nature of this effect has been already discussed in Section E.2, Table 5.4.

E.5 Model describing the CFT residuals

This section describes the dependence of CFT residuals on the efficiency, which is defined as a probability that the fiber has been hit by the particle is going to be read out and eventually considered part of the CFT cluster. This definition is a little bit vague, however, it has a great predictive power and it provides an opportunity to formulate a simple model that quantitatively

detector	cluster type	data with 20 ADC cut applied (μm)	data without 20 ADC cut applied (μm)
CFT	singlets	106(4)	97(3)
	doublets	95(3)	101(4)

Table 5.4: CFT cluster residuals measured in the data, with and without the 20 ADC cut applied.

describes the behavior of singlet cluster residuals.

A good starting point for this model is the track η dependence of ratio of number of singlets divided by number of doublets (in a given η region) in the data. This dependence is shown in Figure 5.3, the dependence has been discussed in previous sections. It is shown that even after removing the 20 ADC cut, the dependence does not get flat, as it has been observed in Monte Carlo. The ratio of number of singlet and doublet clusters in Monte Carlo is flat and the average value is close to $(78\pm5)\%$. In the data, the slope of the dependence is greater when the 20 ADC cut is applied, because more doublets are converted into singlets due to this cut. When it is removed, the slope is much smaller. The reason why it is not flat is because there always is some residual hardware cut that kills some fired fibers and some doublets are therefore converted into singlets, or some singlets disappear completely, and the track observes a 'miss' on that layer. The ratio is greater for smaller track η than for the larger ones due to less light yield, when track traverses the fiber under a smaller angle.

An interesting observation can be made: all three lines, i.e. both lines

with and without the 20 ADC cut applied and an imaginary flat line at approximately 0.78, cross in one point, at about $\eta = 1.9 - 2.0$. That is not trivial fact. There is not enough light read out, neither software nor hardware ADC cut affects sizes of clusters and in consequence residuals. In the ideal situation, under the circumstances that are similar to present Monte Carlo, the ratio is going to be flat in η. The residuals must be therefore flat in η too. No 'scissor effect', i.e. dependence of track residuals on η for singlets and doublets, is observed in Monte Carlo.

This also means that we should be able to describe the dependence of CFT track residuals on η, or some other variable that depends on track η, from the first principles. An attempt to create a model to do that for singlet clusters is described further. One can define a set of equations that describe the dynamics of the system, each of them determines how does the number of singlets N^{sing}, doublets N^{doub} and triplets N^{trip}, depends on the number of singlets N_{MC}^{sing}, doublets N_{MC}^{doub} and triplets N_{MC}^{trip} observed in Monte Carlo. In order to give a realistic model of this effect, the probability ϵ, that a given fiber is going to pass the ADC cut, and the probability n, that the detector noise converts a singlet cluster into a doublet, are introduced:

$$N^{sing} = (\epsilon - n)N_{MC}^{sing} + (1 - \epsilon)N_{MC}^{doub} \tag{5.5}$$

$$N^{doub} = \epsilon N_{MC}^{doub} + n(N_{MC}^{sing} - N_{MC}^{doub}) \tag{5.6}$$

$$N^{trip} = nN_{MC}^{doub} \tag{5.7}$$

$$R = \frac{N_{MC}^{sing}}{N_{MC}^{doub}} = 0.78 \tag{5.8}$$

Equation 5.5 predicts the number of singlet clusters. Each singlet Monte Carlo [1] cluster has a probability to pass the ADC cut, however neighboring fiber fired by the noise might convert the Monte Carlo singlet into a doublet cluster. At the same time, some Monte Carlo doublets might be converted due to the ADC cut, into a singlet which is expressed by the $(1 - \epsilon)$ term.

Equation 5.6 gives the number of doublets. Some doublets might pass the ADC cut, some doublets might be converted into triplets (they are unphysical) and some singlets might turn into doublets if some neighboring fiber is fired by the detector noise.

Equation 5.7 gives the number of unphysical triplet clusters. There is no other explanation for their existence other than the noise effect. Some fibers might be read out just because the level of noise exceeds the threshold calculated for the operation in a sparse mode. Such a fiber is considered in the clustering algorithm as a candidate for a singlet or doublet. The cluster multiplicity is spoiled. The clusters might have a multiplicity that is much higher than three, it all depends on thresholds chosen in the clustering algorithm.

The last equation, Equation 5.8, gives the ratio between singlet and doublet clusters observed in Monte Carlo. It is assumed that the number of triplets, and higher multiplicity clusters, is zero in Monte Carlo, i.e. $\epsilon_{MC}^{trip} = 0$.

The probability ϵ, that the fiber passes the ADC cut applied, can be expressed from the set of Equations 5.5-5.8. It depends only on number of

[1] The singlet Monte Carlo cluster means a true singlet cluster

singlets, doublets, triplets in the data, and on the ratio of number of singlets and doublets in Monte Carlo.

The following study can be made: all tracks can be divided into nine groups, based on their η. The probability ϵ can be calculated for each group, and the residuals for singlet clusters are fitted. Each of the nine track groups represents one bin now, it is represented by the probability ϵ and an average singlet cluster residual σ. The dependence of the singlet cluster residual on the probability ϵ is given in Figure 5.5. The dependence is shown both with and without the 20 ADC cut applied in the reconstruction code. Both dependencies fall onto the same line. That is not a trivial observation and it only demonstrates strength of the model. The dependences could be shifted from one another. The linear dependence is observed. The important result of this fit is the value of singlet residuals (vertical axis, expressed in microns) at $\epsilon = 1$, it is (79 ± 4) microns. The probability $\epsilon = 1$ means that no doublet can be converted into a singlet and that there is no noise at all (n=0). This is the situation observed in current Monte Carlo. It does not come as a surprise, that the CFT singlet residuals in Monte Carlo are (75 ± 2) microns, which is a striking agreement.

This result means that not only is the model described above valid, but it also has a predictive power. One can calculate what the singlet residuals should be, given a certain ADC cut. The model developed using the data is able to predict, in the limit case of an infinite light yield and negligible noise, what the residuals are in Monte Carlo, or vice versa.It means that we understand the nature of CFT clusters and their dependence on track η, and/or light yield.

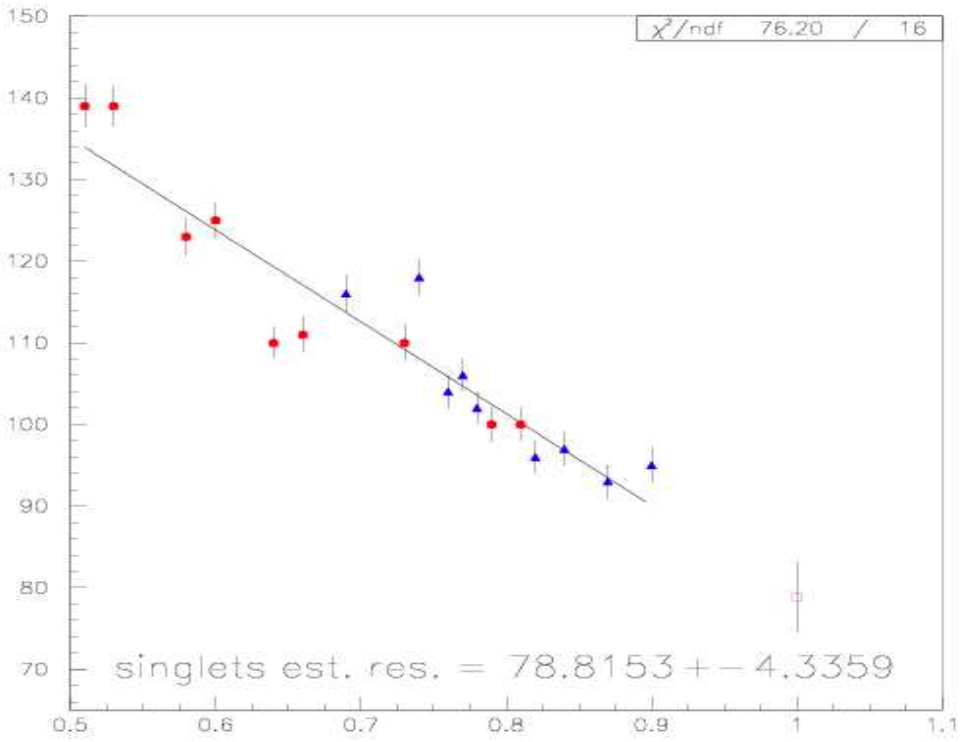

Figure 5.5: The dependence of singlet cluster residuals (vertical axis, in microns) in a given track η region (there are nine of them) as a function of the probability ϵ (horizontal axis) for a fiber to pass the ADC cut. The ideal situation similar to current Monte Carlo ($\epsilon = 1$) predicts residuals for singlet clusters to be (79 ± 4) μm. That is in a very good agreement with previous results from Monte Carlo, given in Table 5.3. The Monte Carlo value for singlets is 75 microns. The dependence is shown with (red circles) and without (blue triangles) the 20 ADC cut, both dependences fall onto the same line. That is not a trivial fact. It demonstrates the strength of the model.

E.6 Primary vertex constraint

Yet another explanation for a larger mass resolution observed in data, could be that in this analysis, one does not use the information about the primary vertex. When the invariant mass is calculated, two isolated tracks with the highest transverse momenta are used. The helix track parameters are taken at their DCA's (distance of the closest approach to the coordinate system center in (r,φ) plane). They might come from the same primary vertex or not. It is possible that the two highest p_{T} tracks are from two different vertices, far apart in the z coordinate. The Z boson decays promptly into muons, practically at the primary vertex. The primary vertex is therefore one more constraint that could be used to calculate the invariant mass of a dimuon system. The best way to obtain a good dimuon mass resolution is to find the primary vertex, make sure that both muons are associated to that vertex, and re-calculate track parameters of both tracks at the primary vertex position, by using the primary vertex constraint. This should improve the mass resolution. On the other hand, realistically speaking, by constraining tracks to the same vertex, only a small (a few GeV/c^2) improvement in the mass resolution is expected. Definitely not a factor of two or more. Nevertheless, this study is worth to perform in order to see whether one can benefit from constraining tracks to the same vertex in the doubly-charged Higgs analysis.

The reason, why we are so certain about a smallness of the primary constraint impact on the mass resolution, can be understood from the error analysis of the invariant mass formula. The invariant mass formula can be written as follows

$$M_Z^2 = p_1^2 + p_2^2 + 2p_1p_2 = 2M_\mu^2 + 2\ (E_1E_2 - \vec{p_1} \cdot \vec{p_2}), \tag{5.9}$$

and after neglecting mass of the muon M_μ as

$$M_Z^2 = 2E_1E_2\ (1 - \cos\ \vartheta). \tag{5.10}$$

An error analysis of Equation 5.10 gives

$$2M_Z\frac{\Delta M_Z}{M_Z^2} = \frac{2\Delta M_Z}{M_Z} = \frac{\Delta E_1}{E_1} + \frac{\Delta E_2}{E_2} + \frac{\Delta(1 - \cos\ \vartheta)}{1 - \cos\ \vartheta}, \tag{5.11}$$

which can be expressed as

$$\frac{2\Delta M_Z}{M_Z} = \frac{\Delta E_1}{E_1} + \frac{\Delta E_2}{E_2} + \frac{sin\vartheta}{1 - \cos\ \vartheta}\ \Delta\vartheta. \tag{5.12}$$

The $Z \rightarrow \mu\mu$ events are 85% of the time back-to-back, i.e. $\vartheta = \pi$ most of the time. Due to the specific topology, the last term vanishes:

$$\lim_{\vartheta \rightarrow \pi} \sin\ \vartheta = 0, \tag{5.13}$$

and only the first two terms in Equation 5.12 - track momentum resolution terms - contribute to the mass resolution. The primary vertex constraint does not help with momentum resolutions, but it helps with an angular measurement. The angular resolution of tracks improves. In this specific situation, due to the topology of $Z \rightarrow \mu\mu$, the contribution to the mass resolution from constraining tracks to the primary vertex almost vanishes.

The silicon vertex detector resolution is about 10 microns. It is also clear that the direction of a track is given by the silicon measurement. Suppose, that a track with $p_{\mathrm{T}} = 45$ GeV/c is measured, and it deflects from its true

direction in the last silicon layer ($r = 10$ cm) by 10 microns, which is what happens in the reality. It means that the uncertainty on the measurement in the last layer of the fiber tracker ($r = 52$ cm) is roughly 50 microns. It can be easily calculated that a track with $p_{\mathrm{T}} = 1$ GeV/c deflects from a straight line in the last layer of the CFT ($r = 52$ cm) by 1.8 mm, i.e. track with $p_{\mathrm{T}} = 45$ GeV/c deflects from a straight line by 330 microns. That is of the order of the central tracker resolution on that layer, approximately 150 microns. The following simple relation, based on the numbers that have been just presented

$$\frac{\Delta p}{p} \sim \frac{\Delta x}{x} = \frac{50\ \mu m}{330\ \mu m} \sim 15\% \tag{5.14}$$

On the other hand, using mass resolution measured in data, the momentum resolution is

$$\frac{\Delta p}{p} \doteq \frac{10\ GeV/c^2}{90\ GeV/c^2} \sim 10\%. \tag{5.15}$$

These are two comparable results, given the fact that this is only a guess. From this perspective, it does not seem to be surprising that the dimuon invariant mass has such a bad resolution in the data.

The primary vertex constraint is implemented in the following way:

- The list of primary vertices in the event is obtained, and the list of tracks associated to them is available.
- Tracks with the highest transverse momenta are found, and it is checked that they are associated to the same primary vertex.

sample	no constraint (GeV/c^2)	vertex constraint (GeV/c^2)
Monte Carlo	4.6(5)	4.1(3)
data	10.4(6)	9.6(5)

Table 5.5: Mass resolution in Monte Carlo and data, with and without constraining tracks to the same vertex.

- These two tracks are passed to the vertexing code. If the common vertex is found, tracks are refitted with the topological constraint of the found vertex. These tracks are called V-tracks, because their track helix parameters are recalculated at the position of a found vertex.

- Finally, the invariant mass of dimuons is calculated using V-track parameters.

This method has been tested in Monte Carlo and the data. Table 5.5 gives the comparison.

There is a very small improvement in Monte Carlo, which is expected, since there are no problems with the mass resolution. But there is not a big effect in the data, either. Moreover, the draw back of this method is that the primary vertex is not always found, and the two highest p_{T} tracks are not necessarily associated to the primary vertex. That represents a hit to reconstruction efficiency. A better vertexing method can be devised to perform the primary vertex constraint. The vertexing code has also improved in p14.

E.7 Reconstructed dimuon mass in φ sectors

The ultimate break-through in understanding the mass resolution has been made possible by breaking the invariant mass into azimuth angle φ sectors. Figure 5.6 shows the invariant mass in 10 φ sectors, starting from $\varphi = 0$ going to $\varphi = 2\pi$ with a step of $\pi/5$. The fiber tracker is divided on the hardware level into five supersectors, each of them has a size of $2\pi/5$.

The invariant mass is narrower in some sectors than in others. The distribution breaks into two independent Gaussians. The invariant mass distribution breaks into two plots, the invariant mass calculated for the positive and negative curvatures of the leading track.

The invariant mass in a sector $\varphi \, \epsilon \, (\, 0, \, \pi/5 \,)$ is shown in Figure 5.7. The curvature of the track is defined as a solenoid field polarity times the charge of a track, and the invariant mass calculated is divided according to the curvature of the leading track into a plot with a positive leading track curvature (center) and a negative leading track curvature (bottom). The figure shows that there are two Gaussians in the invariant mass distribution, one for a positive curvature and the other one for a negative curvature. They are both shifted with respect to each other. The positive curvature peak is in higher masses, the negative one in lower masses.

The invariant mass is fitted by a Gaussian with an exponential background, both for a positive and negative curvature. The second and third sectors, i.e. $\varphi \, \epsilon \, (\, \pi/5, \, 3\pi/5 \,)$, seem to be preferred by the alignment because the resolution is only about 7.6 GeV/c^2 in the (r, φ) plane. This can be seen in Figure 5.8. There is only one peak in the upper plot, positive and negative curvature mass distributions are aligned at about 84 GeV/c^2.

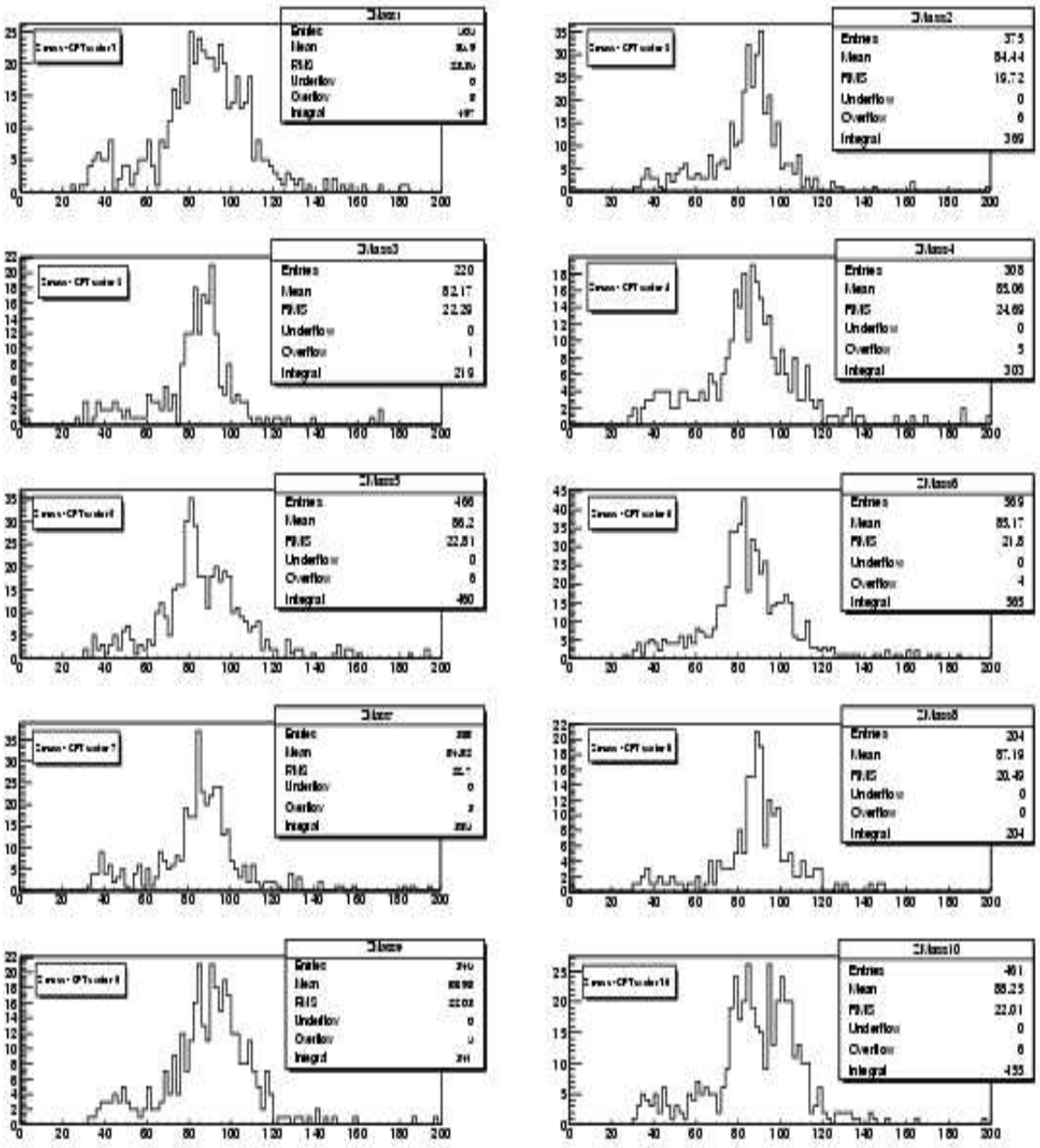

Figure 5.6: The dimuon mass is divided into 10 sectors in φ, the sector it belongs to is decided based on the leading track's azimuth angle φ. The horizontal axis is expressed in GeV/c^2.

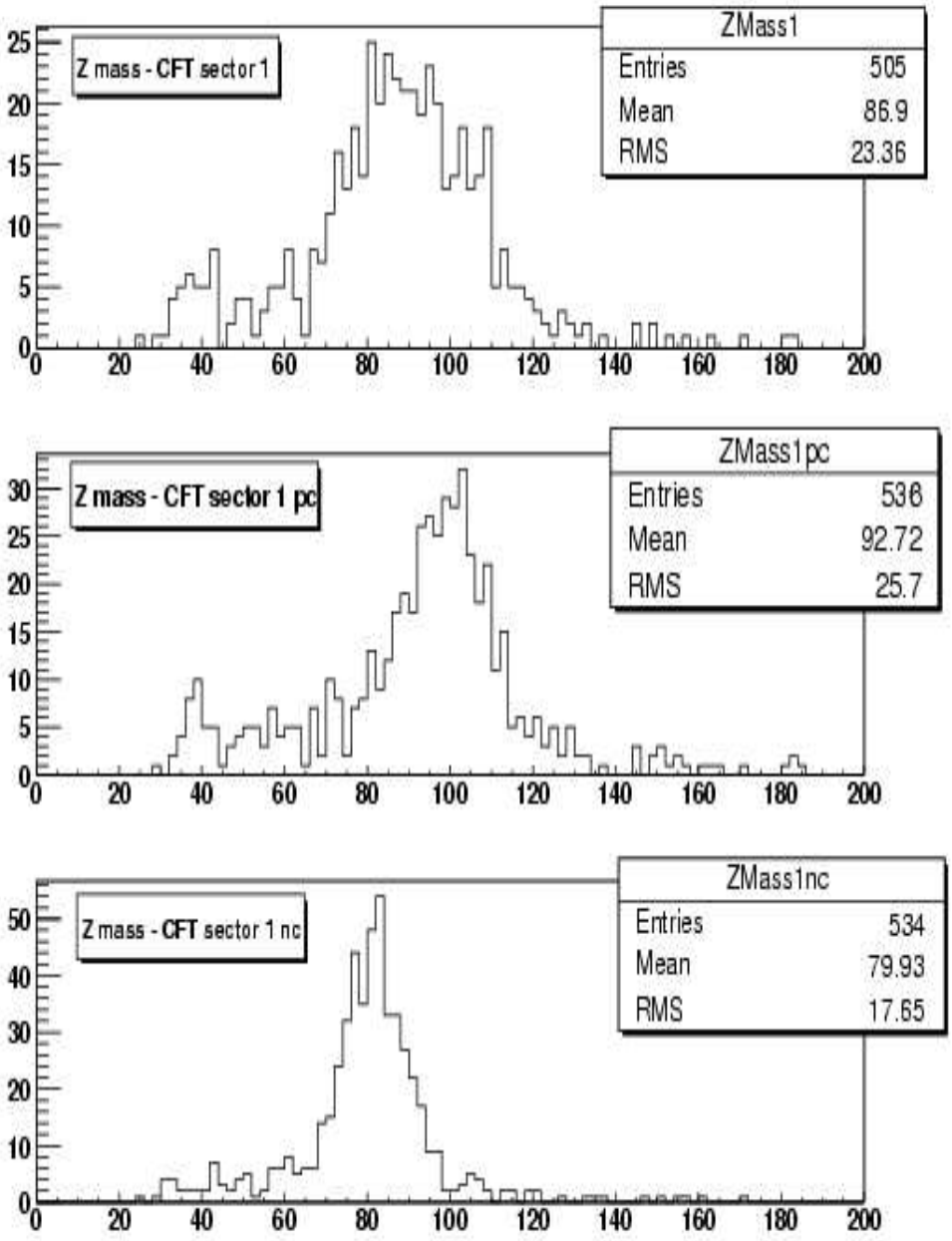

Figure 5.7: Invariant mass in the sector $\varphi\,\epsilon\,(\,0,\,\pi/5\,)$. Dimuon mass is shown for both curvatures (top), positive curvature (center) and negative curvature (bottom). The horizontal axis is expressed in units of GeV/c^2.

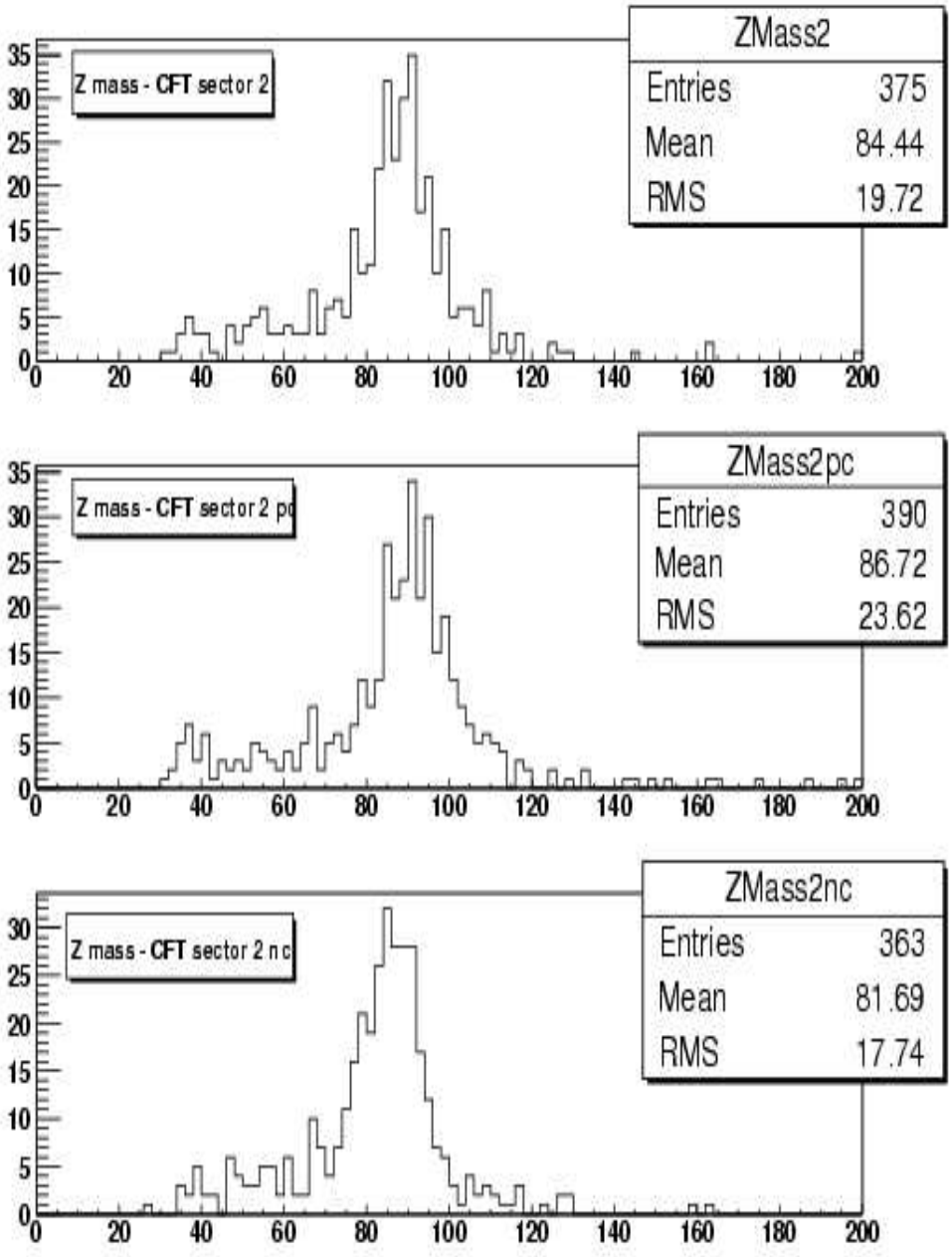

Figure 5.8: Invariant mass in the sector $\varphi \epsilon$ ($\pi/5$, $2\pi/5$). Dimuon mass is shown for both curvatures (top), positive curvature (center) and negative curvature (bottom). The horizontal axis is expressed in units of GeV/c^2. The horizontal axis is expressed in units of GeV/c^2.

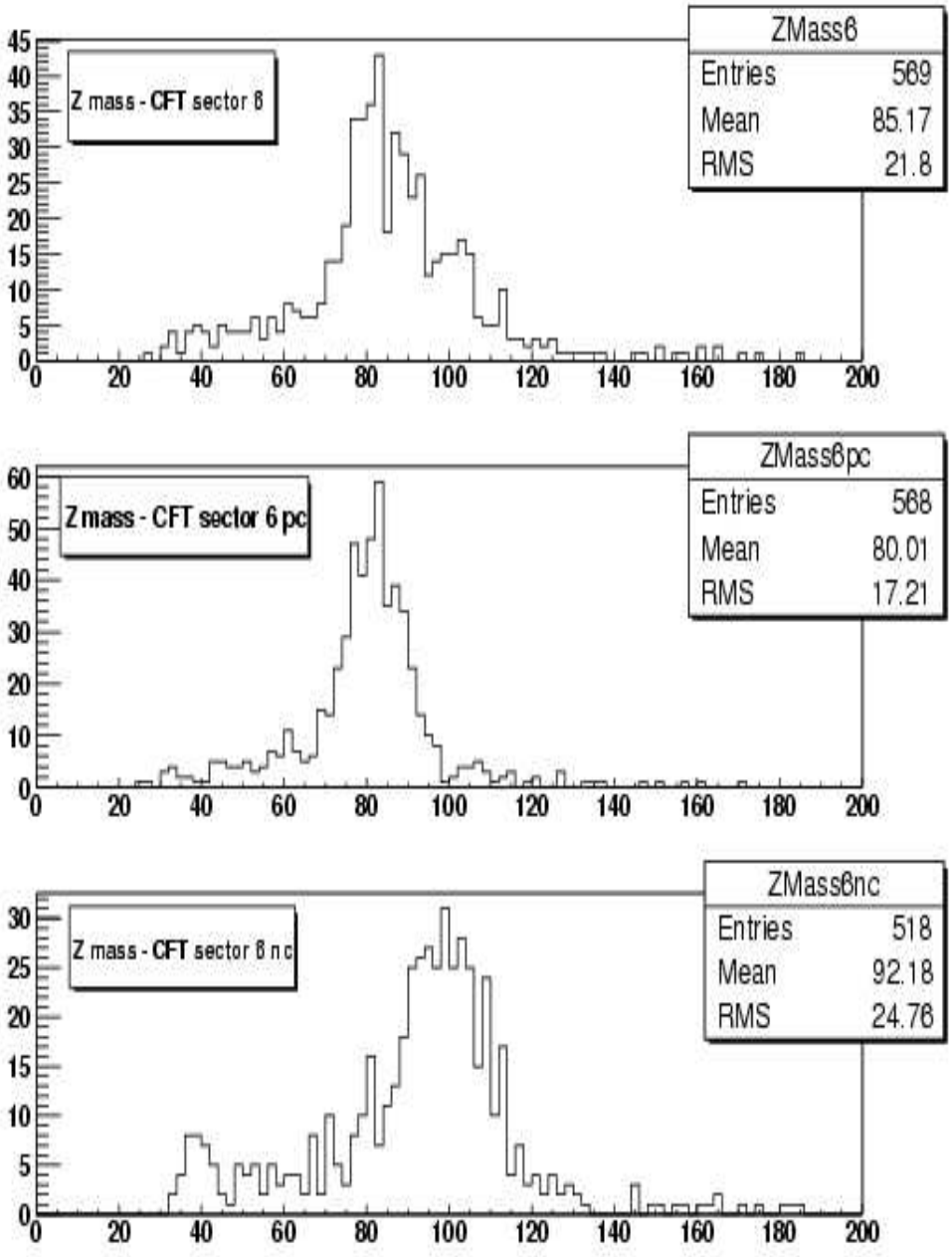

Figure 5.9: Invariant mass in the sector $\varphi \in (\ \pi,\ 6\pi/5\ )$. Dimuon mass is shown for both curvatures (top), positive curvature (center) and negative curvature (bottom). The horizontal axis is expressed in units of GeV/c^2. The horizontal axis is expressed in GeV/c^2.

Figure 5.9 shows the invariant mass distribution in a sector $\varphi \, \epsilon \, (\, \pi, \, 6\pi/5 \,)$. It is on the opposite side of the first sector in φ. There are again two peaks in the mass distribution, one is in the positive curvature distribution, the other one in the negative curvature mass distribution. Unlike the first sector, they are shifted with respect to each other in the opposite sense. The positive curvature Gaussian is on the low mass side and the negative curvature Gaussian is on the high mass side.

The invariant mass calculated for the same sign of leading track's curvature depends on the azimuth angle φ. It can be approximated by the following fit:

$$A \ \sin(\varphi + B) + C, \tag{5.16}$$

where the coefficients obtained from the fit are, for a positive curvature:

$$A = 9.03 \ GeV/c^2, \ B = 1.773, \ C = 89.73 \ GeV/c^2 \tag{5.17}$$

and negative curvature:

$$A = 9.08 \ GeV/c^2, \ B = -1.36, \ C = 89.67 \ GeV/c^2. \tag{5.18}$$

The dependence of the Gaussian mean value on φ is shown in Figure 5.10, for a positive and negative curvatures of leading tracks.

The best mass resolution can be achieved if $\varphi = 101^\circ$, i.e. it is pointing down. It immediately raises the question whether the SMT could be shifted downwards with respect to the CFT by as much as 300 microns, due to the gravity for instance. If the geometry of the silicon tracker is shifted by 300 microns in the opposite direction (upwards), the amplitude of of a

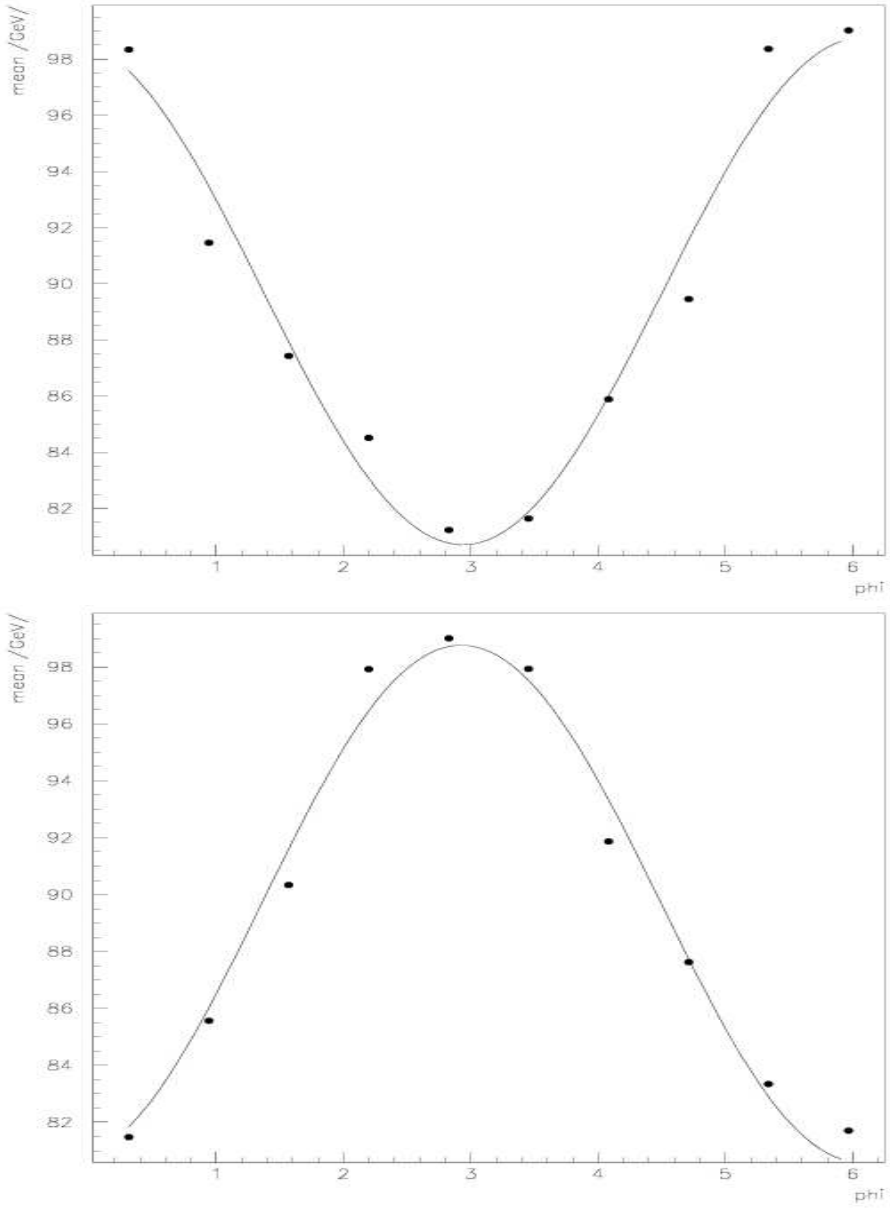

Figure 5.10: The mean value of the fitted Gaussian (the Gaussian plus an exponential background is fitted to the dimuon mass distribution) as a function of leading track's φ, for a positive (top) and negative (bottom) curvature of leading tracks.

sin wave observed in Figure 5.10 decreases by a factor of two, it is about 4 GeV/c^2 now. This result can be observed in Figure 5.11.

In order to calculate the correction to the average transverse momentum $\langle q/p_{\mathrm{T}} \rangle$, a zero magnetic field run 175897, has been analyzed. There cannot be any dependence of $\langle q/p_{\mathrm{T}} \rangle$ on the azimuth angle φ, i.e. it must be flat in φ and $\langle q/p_{\mathrm{T}} \rangle = 0$. That is not the situation however, the dependence resembles a sin wave. The average transverse momentum of all global tracks (SMT+CFT) $\langle q/p_{\mathrm{T}} \rangle$ as a function of the azimuth angle φ fitted with a sin wave

$$\langle q/p_{\mathrm{T}} \rangle = A \ \sin(\varphi - B) + C, \tag{5.19}$$

where the fitted values are

$$\begin{aligned} A &= (\ 2.216 \pm 0.029 \ ) \times 10^{-3} \ c/GeV \\ B &= (\ 1.341 \pm 0.012 \ ) \\ C &= (\ -3.18 \pm 0.20 \ ) \times 10^{-4} \ c/GeV. \end{aligned} \tag{5.20}$$

The misalignment originates mainly from the CFT, the same dependence can be calculated for CFT only tracks, i.e. for tracks with CFT hits only. The results of a fit is

$$\begin{aligned} A &= (\ 2.352 \pm 0.041 \ ) \times 10^{-3} \ c/GeV \\ B &= (\ 1.333 \pm 0.016 \ ) \\ C &= (\ -2.61 \pm 0.28 \ ) \times 10^{-4} \ c/GeV. \end{aligned} \tag{5.21}$$

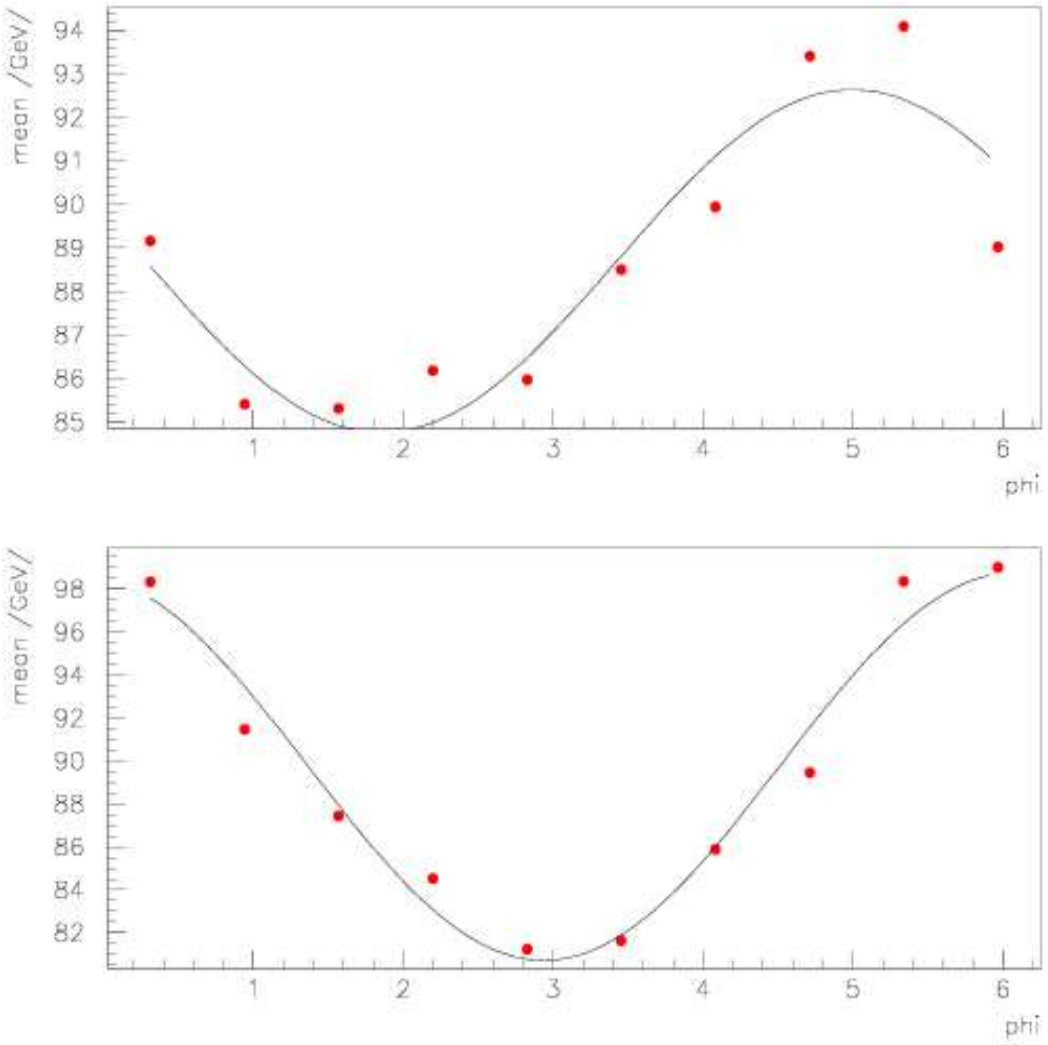

Figure 5.11: The mean value of the fitted Gaussian (the Gaussian plus an exponential background is fitted to the dimuon mass distribution) as a function of leading track's φ, for positive curvature leading tracks, when the silicon tracker's geometry is shifted by 300 microns upwards. The amplitude of a sin wave observed in Figure 5.10 decreases by a factor of two (upper plot). The bottom plot shows the mean of the Gaussian fit as a function of φ before the CFT geometry has been shifted.

The fit of $\langle q/p_{\mathrm{T}} \rangle$ as a function φ looks very similar to the one obtain for global tracks. This is an indication, that the main contribution to the misalignment originates from the CFT geometry.

The amplitude of a sin wave then gives the size of the shift of the SMT with respect to the CFT by 113 microns downwards.

The corrections given in Equations 5.19 and 5.21 should be applied for a positive solenoid field polarity as

$$q/p'_{\mathrm{T}} = q/p_{\mathrm{T}} - \langle q/p_{\mathrm{T}} \rangle, \tag{5.22}$$

and for a negative polarity as

$$q/p'_{\mathrm{T}} = q/p_{\mathrm{T}} + \langle q/p_{\mathrm{T}} \rangle. \tag{5.23}$$

The result can be seen in Figure 5.12.

The mass resolution obtained after this correction is 7.5 GeV/c^2. There still is a residual difference of about 1 GeV/c^2 between Monte Carlo and the corrected data. This remaining discrepancy can be explained by the difference of track residuals observed in Monte Carlo and the data. The additional smearing of SMT and CFT clusters in Monte Carlo increases the mass resolution by approximately 1 GeV/c^2.

The remaining question to be answered is: How is it possible that the CFT geometry is misaligned, and is it time dependent misalignment ? The answer to the first part has been already given earlier. It probably is due to the gravity, because the preferred direction of misalignment is pointing downwards. The cylinders of the fiber tracker are probably sagging due to the gravity. The misalignment is not big, it is of the order of 125 microns.

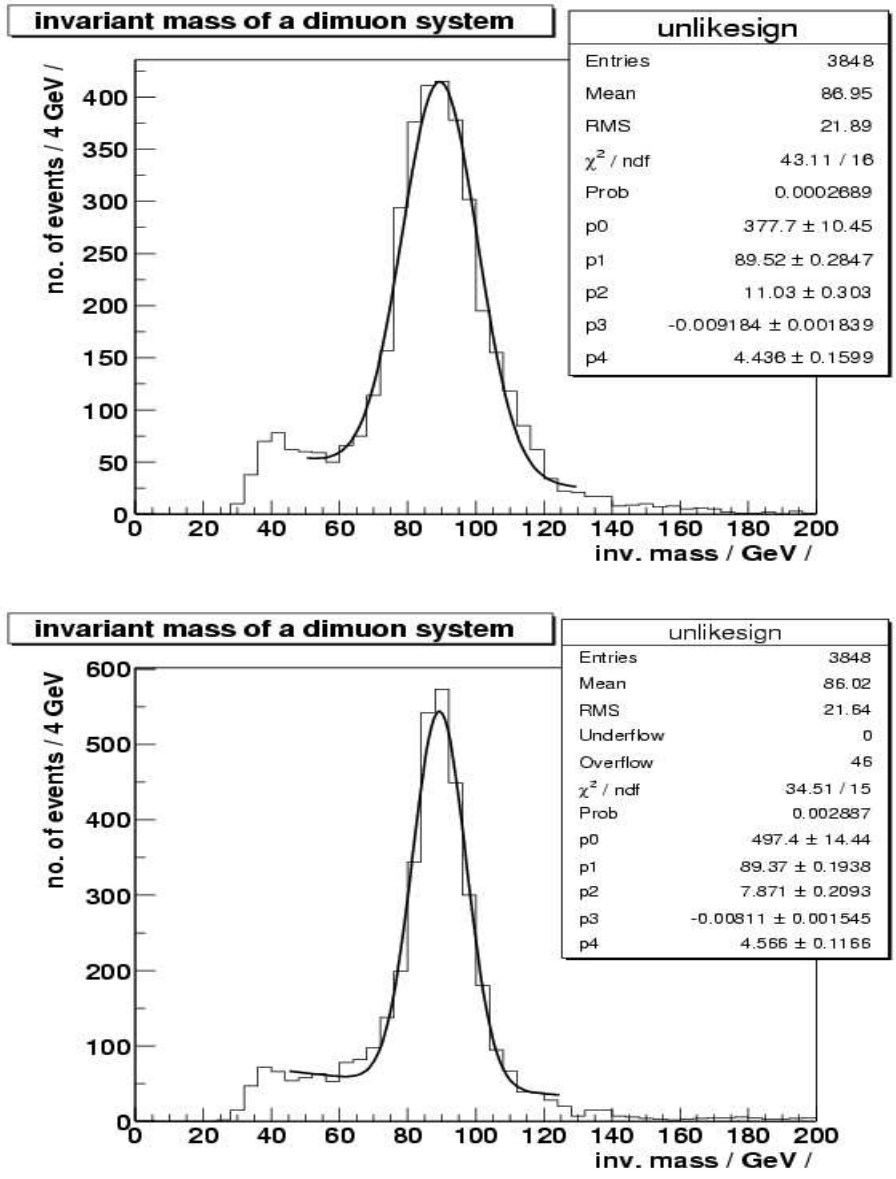

Figure 5.12: The comparison of invariant mass with (bottom) and without (top) the average $\langle q/p_{\mathrm{T}} \rangle$ correction calculated from the zero magnetic field run.

job	first run	last run	no. of events
1	153441	165717	1,222
2	165717	168656	1,278
3	169201	172568	751
4	172577	175058	951
total	153441	175058	4,202

Table 5.6: The statistics of the time-ordered data sample, which serves as a tool to investigate the time dependence of the CFT misalignment.

In order to study the time dependence of the misalignment, the data sample has been order on an event-by-event basis, and broken into four pieces. The statistics of each sample is given in Table 5.6.

The total integrated luminosity of this sample is 76 pb^{-1} if the `2MU_A_L2M0` dimuon trigger is used. The fitted results for each sample are summarized in Table 5.7.

There is no time dependence of the misalignment observed in this sample. If there was any change in the detector geometry, one could not correct q/p_{T} properly in earlier runs (jobs 1 and 2). As a matter of fact, a correction derived from later runs must increase the width of the Z mass peak. It means that the shift of the SMT with respect to the CFT probably happened before the tracker has been aligned.

Low-p_{T} tracks have been used to align the CFT. The alignment program probably found some local minimum that suits the low-p_{T} tracks, but it is wrong for the high-p_{T} tracks.

This study is also described in [93] in a great level of detail. Plots made

		job 1 (GeV/c^2)	job 2 (GeV/c^2)	job 3 (GeV/c^2)	job 4 (GeV/c^2)
uncorrected	Z mass	89.23(55)	88.27(46)	89.82(65)	89.83(57)
	σ	12.68(55)	11.53(48)	12.25(62)	11.36(55)
corrected	Z mass	89.74(38)	88.72(34)	89.82(74)	90.20(42)
	σ	9.42(46)	8.73(41)	8.64(54)	8.67(42)

Table 5.7: The fitted Z mass and the Z mass resolution σ of the time-ordered data sample. Both values are given for a corrected and uncorrected transverse momenta. No time dependence has been observed in this sample.

with a new aligned geometry are shown there.

Appendix F

Massive neutrinos and Left-right symmetric model

Neutrinos play a key role in our understanding of particles, forces and create a natural step in exploring physics beyond the Standard Model [175, 176, 177]. Unfortunately, there is an absence of solid experimental results, except the solar neutrino experiments. This builds a basis for theoretical hypothesis concerning the massive neutrinos and neutrino oscillations [178]. A brief introduction to the neutrino oscillations is given in the first section. Several models giving a mass to neutrinos and explaining the smallness of neutrino mass are discussed in this appendix.

F.1 Introduction to the neutrino oscillations

Although neutrino mass is predicted to be zero within the minimal Standard Model, the solar and atmospheric neutrino observations may have non-zero masses and oscillate. A variety of massive neutrino scenarios have been

proposed to accommodate the experimental observations. Most attention have attracted the works using mass matrix ansatz based on the principles of symmetry.

F.1.1 Neutrino oscillations in vacuum

Neutrino created in a charged current interaction (together with lepton l) is called ν_l and it is given by

$$|\nu_l\rangle \;=\; \sum_\alpha U_{l\alpha}\;|\nu_\alpha\rangle, \tag{6.1}$$

where U is a unitary matrix that is going be discussed in the next section, which summarizes various models of neutrinos.

After a time t, the evolution of the initial beam gives

$$|\nu_l\;(t)\rangle \;=\; \sum_\alpha e^{-iE_\alpha t}\;U_{l\alpha}\;|\nu_\alpha\rangle \tag{6.2}$$

The amplitude of finding a $\nu_{l'}$ in the original ν_l beam is

$$\langle\;\nu_{l'}\;|\;\nu_l(t)\;\rangle \;=\; \sigma_{\alpha,\beta}\langle\;\nu_\beta\;|\;U^\dagger_{\beta l'}\;e^{-iE_\alpha t}\;U_{l\alpha}\;|\;\nu_\alpha(t)\;\rangle \tag{6.3}$$

using the orthonormality of the mass ϵ-states, one obtains the probability

$$P_{\nu_l\nu_{l'}}(t) \;=\; |\langle\nu_{l'}|\nu_l(t)\rangle|^2 \;=\; \sum_{\alpha,\beta}|\;U_{l\alpha}U^\star_{l'\alpha}U^\star_{l\beta}U_{l'\beta}\;|\;\cos[(E_\alpha-E_\beta)t-\phi_{ll'\alpha\beta}], \tag{6.4}$$

where

$$\phi_{ll'\alpha\beta} \;=\; arg(\;U_{l\alpha}U^\star_{l'\alpha}U^\star_{l\beta}U_{l'}\beta\;). \tag{6.5}$$

Because neutrinos are extremely relativistic particles we can replace t by the distance x traveled by the beam, so one gets [19]

$$P_{\nu_l\nu_{l'}}(t) \;=\; \sum_{\alpha,\beta} \mid U_{l\alpha}U^{\star}_{l'\alpha}U^{\star}_{l\beta}U_{l'\beta} \mid \cos(\frac{2\pi x}{L_{\alpha\beta}} - \phi_{ll'\alpha\beta}), \tag{6.6}$$

where

$$L_{\alpha\beta} \;=\; \frac{4\pi|\vec{p}|}{\Delta_{\alpha\beta}}, \tag{6.7}$$

with

$$\Delta_{\alpha\beta} \;=\; m^2_{\alpha} \;-\; m^2_{\beta} \tag{6.8}$$

and *oscillation lengths* - distance over which the oscillation effects take place.

F.1.2 Oscillation with unstable neutrinos

The interesting picture of oscillation gives the possibility of unstable neutrinos. The mass eigenstates are related to the flavour states through

$$\begin{pmatrix} \nu_1 \\ \nu_2 \end{pmatrix} \;=\; \begin{pmatrix} \cos\vartheta & -\sin\vartheta \\ \sin\vartheta & \cos\vartheta \end{pmatrix} \begin{pmatrix} \nu_e \\ \nu_\mu \end{pmatrix} \tag{6.9}$$

If the ν_2 is the heavier of the two neutrinos, and it decays via $\nu_2 \longrightarrow \nu_1 X$ with the lifetime of the decay Γ^{-1}.

The initial beam is

$$|\nu_{in}\rangle \;=\; \cos\alpha|\nu_e\rangle \;+\; \sin\alpha|\nu_\mu\rangle, \tag{6.10}$$

and the beam at the time t is

$$|\nu(t)\rangle \;=\; e^{-iE_1 t}\cos(\vartheta+\alpha)|\nu_1\rangle \;+\; e^{-iE_2 t-\Gamma t/2}\sin(\vartheta+\alpha)|\nu_2\rangle \;+\; \sum_l |\nu_l(k)X\rangle. \tag{6.11}$$

The probability of finding the electron neutrino in the beam can be expressed as

$$P_{\nu_{in}\nu_e}(t) \;=\; \cos^2(\vartheta+\alpha)\,\cos^2\vartheta + e^{-\Gamma t}\sin^2(\vartheta+\alpha)\,\sin^2\vartheta + \frac{1}{2}e^{-\Gamma t/2}\sin 2\vartheta\,\sin 2(\vartheta+\alpha)\,\cos\frac{t\,\Delta}{2|\vec{p}|}, \tag{6.12}$$

and of the muon neutrino as

$$P_{\nu_{in}\nu_\mu}(t) \;=\; \cos^2(\vartheta+\alpha)\,\sin^2\vartheta + e^{-\Gamma t}\sin^2(\vartheta+\alpha)\,\cos^2\vartheta - \frac{1}{2}e^{-\Gamma t/2}\sin 2\vartheta\,\sin 2(\vartheta+\alpha)\,\cos\frac{t\,\Delta}{2|\vec{p}|}. \tag{6.13}$$

None of these probabilities is zero. Even for fast decays a non-zero probability (first terms) is obtained.

Since the probability must be equal to unity, we get

$$\sum_k P_{\nu_{in}\longrightarrow\nu_1 X} \;=\; (1-e^{-\Gamma t})\sin^2(\vartheta+\alpha). \tag{6.14}$$

The ν_1's produced in the decay of ν_2 are incoherent with respect to the ν_1's in the original beam. Therefore, one can say [19]

$$\sum_k P_{\nu_{in}\longrightarrow\nu_e X} \;=\; (\;1-e^{-\Gamma t}\;)\;\sin^2(\vartheta+\alpha)\;\cos^2\vartheta \tag{6.15}$$

$$\sum_k P_{\nu_{in}\longrightarrow\nu_\mu X} \;=\; (\;1-e^{-\Gamma t}\;)\;\sin^2(\vartheta+\alpha)\;\sin^2\vartheta \tag{6.16}$$

.

F.1.3 Neutrino oscillations in the matter

The patterns of neutrino oscillations [179] might be significantly different when passing through the material because the electron neutrinos interact with electrons of the medium via both neutral and charged current interactions. However, the muon and tau neutrino interact with the neutrino only via the neutral current. This is why their interaction is different in magnitude [180].

Of course, the interactions modify the effective mass that a particle exhibits while traveling through a medium. The effective masses of neutrinos are modified in a medium by the interactions. This has dramatic consequences if the neutrinos mix in the vacuum. Physical eigenstates will have components of $\nu_e,\ \nu_\mu,\ \nu_\tau$. This fact causes changes in the oscillation probabilities compared to their values in the vacuum.

- Vacuum oscillations:

$$i\frac{d}{dt}\begin{pmatrix}\nu_1(t)\\ \nu_2(t)\end{pmatrix} = \begin{pmatrix}E_1 & 0\\ 0 & E_2\end{pmatrix}\begin{pmatrix}\nu_1(t)\\ \nu_2(t)\end{pmatrix} \tag{6.17}$$

As the neutrinos are relativistic we can approximate energies E_1 and E_2 as

$$E_{1,2} = |\vec{p}| + \frac{m_{1,2}^2}{2|\vec{p}|}, \tag{6.18}$$

and now we have to mix the flavor states in order to get weak eigenstates

$$i\frac{d}{dt}\begin{pmatrix}\nu_e(t)\\ \nu_\mu(t)\end{pmatrix} = UHU^\dagger\begin{pmatrix}\nu_e(t)\\ \nu_\mu(t)\end{pmatrix} \tag{6.19}$$

where

$$H' \;=\; UHU^{\dagger} \;=\; |\vec{p}| + \frac{m_1^2 + m_2^2}{4|\vec{p}|} + \frac{\Delta}{4|\vec{p}|} \begin{pmatrix} -\cos\ 2\vartheta & \sin\ 2\vartheta \\ \sin\ 2\vartheta & \cos\ 2\vartheta \end{pmatrix} \quad (6.20)$$

- Passing through the matter:

  Under assumption the density of the background matter is uniform, the scattering off the particles of the matter affects the effective masses of the neutrinos.

  – If we consider scattering via CC, the only contribution is going to be $\nu_e e$ scattering.

$$L_{eff} \;=\; \frac{4\ G_F}{\sqrt{2}} \{\bar{e}(p_1)\gamma_\lambda P_L \nu_e(p_2)\}\{\bar{\nu}_e(p_3)\gamma^\lambda P_L e(p_4)\} \qquad (6.21)$$

  and using the Fierz transformation (from the s-channel to the t-channel), and for forward scattering where $p_2 \;=\; p_3 \;=\; p$ one gets

$$L_{eff} \;=\; \sqrt{2}\ G_F\ \bar{\nu}_{eL}(p)\gamma_\lambda \nu_{eL}(p) \langle \bar{e}\gamma^\lambda (\ 1 - \gamma_5\ ) e \rangle. \qquad (6.22)$$

  In the non-relativistic approximation, the axial current reduces to spin and that is negligible. The spatial component of the vector current is negligible as well, it gives only the average velocity. The only non-zero part average is

$$\langle\ \bar{e}\ \gamma^0\ e\ \rangle \;=\; \langle\ e^{\dagger}\ e\ \rangle \;=\; n_e. \qquad (6.23)$$

and finally the effective Lagrangian is

$$L_{eff} \;=\; \sqrt{2}\; G_F\; n_e\; \bar{\nu}_{eL}\gamma_0\nu_{eL}, \tag{6.24}$$

which contributes to the energy of the neutrino with a factor: $\sqrt{2}G_F n_e$.

– If we consider scattering via the neutral currents (NC):

$$L_{eff} \;=\; \sqrt{2}G_F \sum_f n_f[\; I_{3L}^{(f)} \;-\; 2\;\sin^2\vartheta_w\; Q^{(f)}\;] \tag{6.25}$$

as for the usual matter the contribution of the electrons and protons is the same, they will cancel each other. This is why only neutron contribution

$$L_{eff} \;=\; -\sqrt{2}\; G_F\; n_n/2 \tag{6.26}$$

is significant.

To the NC contribution contribute all flavors, nevertheless one can use the same evolution equation with H':

$$H' \;=\; UHU^\dagger \;=\; |\vec{p}| \;+\; \frac{m_1^2 \;+\; m_2^2}{4|\vec{p}|} \;-\; \sqrt{2}\; G_F\; n_n/2 \;+$$
$$\begin{pmatrix} -\frac{\Delta}{4|\vec{p}|}\;\cos\;2\vartheta \;+\; \sqrt{2}\; G_F\; n_e & \frac{\Delta}{4|\vec{p}|}\sin\;2\vartheta \\ \frac{\Delta}{4|\vec{p}|}\;\sin\;2\vartheta & \frac{\Delta}{4|\vec{p}|}\;\cos\;2\vartheta \end{pmatrix} \tag{6.27}$$

one can easily see that the mixing angle changes inside the matter as the H' has changed.

F.2 Neutrino mass in $SU(2)_L \times U(1)_Y$ models

The Standard Model of electroweak interactions is based on the gauge group $SU(2)_L \times U(1)_Y$, which fixes only gauge bosons of this model [181]. This is why all fermions and Higgs boson have to be chosen arbitrarily. The neutrinos are chosen to be massless in the SM. The way to give masses to neutrinos is to introduce some new fermions or Higgs bosons in the model. There are several models on the market that are able to predict the mass of neutrinos in such a case [182]:

- Models with new fermions

  The crucial point is to add the right-handed neutral fields N_{lR} corresponding to each charged lepton l, unlike the SM which contains only left-chiral projections of neutrinos. They are thought of to be the singlets of $SU(2)_L$, i.e. $T_{3L} = 0$, and they fulfill the Gell-Mann & Nishijima formula:

  $$Q = T_{3L} + \frac{Y}{2} \tag{6.28}$$

  This formula implies that they have $Y = 0$ which makes them to be singlets of $SU(2)_L \times U(1)_Y$ as well.

  There are several models with new fermions [19], for instance:

  - Simple models with Dirac neutrinos

    The presence of the new right-handed field imply new gauge-invariant interactions in the Yukawa part of the SM Lagrangian:

$$-\mathcal{L}'_Y = \sum_{\ell,\ell'} f_{\ell\ell'} \bar{\psi}_{\ell L} \phi^c N_{\ell' R} + \text{h.c.} \tag{6.29}$$

where $f_{\ell\ell'}$ are new coupling constants, Higgs doublet is the same and $\psi_{\ell L}$ is the lepton doublet. This equation conserves the total leptonic charge $\sum_\ell N_\ell$ ($L_e + L_\mu + L_\tau$).

– The complete model with right-handed Majorana neutrinos using see-saw mechanism [183]

- Models with expanded Higgs sector

  In each generation there are two degrees of freedom in case no new particle is added to the particle content of the SM. It corresponds to the uncharged fermions. The mass must always be Majorana type which means that the mass terms must violate $B - L$. The idea is to introduce new Higgs bosons which can violate $B-L$ symmetry in their interactions [184].

  The SM can be expanded by:

  – Introduction of the triplet

  One of the possible extentions of the SM Higgs sector is the following triplet Δ

$$\mathbf{\Delta} = \begin{pmatrix} \Delta_1 \\ \Delta_2 \\ \Delta_3 \end{pmatrix}. \tag{6.30}$$

  For an isotriplet, with $T = 1$ and the hypercharge $Y = 2$, the

components of the triplet Δ are the neutral, singly- and doubly-charged Higgs boson:

$$\mathbf{\Delta} = \begin{pmatrix} \Delta^{++} \\ \Delta^{0} \\ \Delta^{+} \end{pmatrix}, \tag{6.31}$$

where

$$\begin{aligned} \Delta^{++} &= \tfrac{1}{\sqrt{2}}(\Delta_1 - i\Delta_2) \\ \Delta^{0} &= \tfrac{1}{\sqrt{2}}(\Delta_1 + i\Delta_2) \\ \Delta^{+} &= \Delta_3. \end{aligned} \tag{6.32}$$

There are three independent generators of $SU(2)$, which form the basis of $SU(2)$ algebra and satisfy the well-known commutation relations

$$[T_i, T_j] = i\epsilon_{ijk}T_k \tag{6.33}$$

The lowering and rising operators $T_\pm$ can be defined as:

$$T_\pm = T_1 \pm T_2, \tag{6.34}$$

that satisfy

$$[T_+, T_-] = 2T_3; \;\; [T_\pm, T_3] = \mp T_\pm. \tag{6.35}$$

Recall that the generators of $SU(2)$ can be written by means of Pauli bidimensional matrices $\tau_i, \;\; i = 1, 2, 3$ as $\tau_i/2, \;\; i = 1, 2, 3,$ where

$$\begin{aligned}
\tau^+ &= \frac{1}{\sqrt{2}}(\tau_1 + i\tau_2) = \begin{pmatrix} 0 & \sqrt{2} \\ 0 & 0 \end{pmatrix}, \\
\tau^- &= \frac{1}{\sqrt{2}}(\tau_1 - i\tau_2) = \begin{pmatrix} 0 & 0 \\ \sqrt{2} & 0 \end{pmatrix}, \\
\tau^0 &= \tau_3 = \begin{pmatrix} 1 & 0 \\ 0 & -1 \end{pmatrix}
\end{aligned} \tag{6.36}$$

This representation can be used to construct all other multiplets of $SU(2)$. After an easy calculation, one obtains

$$\tau\cdot\mathbf{\Delta} = \Delta_1\tau_1+\Delta_2\tau_2+\Delta_3\tau_3 = \Delta^{++}\tau^+ + \Delta^0\tau^- + \Delta^+\tau^0 = \begin{pmatrix} \Delta^+ & \sqrt{2}\Delta^{++} \\ \sqrt{2}\Delta^0 & -\Delta^+ \end{pmatrix}. \tag{6.37}$$

– Introduction of the charged singlet and a new doublet

Suppose we introduce a new $SU(2)_L$ singlet particle h_- in the Higgs sector. The Yukawa coupling of this particle is given by

$$-\mathcal{L}'_Y = \sum_{\ell,\ell'} f_{\ell\ell'}\bar{\psi_{\ell L}}\psi^c_{\ell' L}h_- + \text{h.c.} \tag{6.38}$$

As in previous model, we can assign a B - L quantum number of 2 to the field h_-. The h has the electric charges and hence its *v.e.v.* must vanish in a physically acceptable ground state, because otherwise gauge symmetry would be spontaneously broken. This is why there must be some other source of $B - L$ violation - the Higgs potential.

The situation dramatically changes if there are two doublets in the theory. If ϕ' couples to quarks and leptons in the same way as ϕ does, it must have a vanishing $B-L$ quantum number and so

$$\phi^T i\tau_2 \varphi h_- + \text{h.c.} \tag{6.39}$$

violates $B-L$ by two units. Such a coupling cannot exist.

There are 3 different singly charged scalars in the theory: ϕ^+, φ^+ and h^+. The physical spectrum contains two charged scalars S and S' (each of them is a mixture of ϕ^+, φ^+ and h^+). Hence these are not eigenstates of $B-L$. Thus, neutrinos will obtain Majorana masses at the one-loop level from the self-energy diagrams.

The diagram seems to give infinite contribution to neutrino masses. All infinities arising in the calculation are absorbed into the definitions of the parameters in the classical Lagrangian. The theory is renormalizable. The tree-level Lagrangian does not have any neutrino mass term, however, the renormalizability of the theory is guaranteed by the general proof of 'tHooft.

The mass terms are simple assuming that only one of the Higgs doublets couples to leptons.

$$M_{\ell\ell'} = A f_{\ell\ell'}(m_\ell^2 - m_{\ell'}^2) \tag{6.40}$$

where A is a constant. Matrix $M_{\ell\ell'}$ is symmetric because it is a mass matrix in the Majorana basis.

The advantage of this model is that it gives pattern of neutrino masses and mixings. Defining parameters:

$$\begin{aligned} \tan\alpha &= \frac{f_{\mu\tau}}{f_{e\tau}}\left(1-\frac{m_\mu^2}{m_\tau^2}\right) \\ \sigma &= \frac{f_{e\mu}}{f_{e\tau}}\frac{m_\mu^2}{m_\tau^2}\cos\alpha \end{aligned} \tag{6.41}$$

and neglects the electron mass which is small compared to the masses of the muon and the tau, the mass matrix is given by

$$M = m_0 \begin{pmatrix} 0 & \sigma & \cos\alpha \\ \sigma & 0 & \sin\alpha \\ \cos\alpha & \sin\alpha & 0 \end{pmatrix} \tag{6.42}$$

where $m_0 = Am_\tau^2 f_{\tau e}/\cos\alpha$. Under assumption $\sigma \ll 1$, $m_\mu \ll m_\tau$ ($f_{e\mu} \geq 10^4 f_{e\tau}$). The diagonalization of the matrix M gives the eigenvalues

$$\begin{aligned} m_1 &= -m_0\sigma\sin 2\alpha \\ -m_2 &= m_0\left(1-\frac{1}{2}\sigma\sin 2\alpha\right) \\ m_3 &= m_0\left(1+\frac{1}{2}\sigma\sin 2\alpha\right) \end{aligned} \tag{6.43}$$

correct up to first order terms in σ. In order to eliminate negative $-m_2$, we can again choose a matrix K, so that m_2 is the mass of the physical eigenstate. Previous equation clearly shows that there are two physical neutrinos with very close masses whereas the other mass m_1 is significantly smaller.

F.3 Neutrino mass in L-R symmetric models

All these models are based on the left-right symmetry that is prior to symmetry breaking. In the symmetric phase, these models lead to parity conserving weak interaction. That is different from the SM and makes this theory appealing for unified theories.

The requirement is that all left handed fermions must have a right handed partner. The consequence is the presence of the new particle - right handed neutrino (ν_R or N_R). The theory gives masses to neutrinos and obeys the left-right symmetry.

The smallest gauge group that contains the hypothesis of L-R symmetry of weak interactions is $SU(2)_L \times SU(2)_R \times U(1)_{B-L}$. Originally, the $U(1)$ was not identified with $B - L$. It turned out later when people introduced a formula similar to Gell-Mann Nishijima relation in case of strong interactions:

$$Q = T_{3L} + T_{3R} + \frac{B - L}{2} \tag{6.44}$$

This formula introduced several fundamental facts, e.g. if $SU(2)_L$ is unbroken, $SU(2)_R$ is broken. One finds that

$$\Delta I_{3R} \ = \ -\frac{1}{2}\Delta(\ B \ - \ L\ ) \tag{6.45}$$

Moreover, for baryon number conserving interactions $\Delta B = 0$, this equation implies that $|\Delta L| = 2|\Delta I_{3R}|$. If $\Delta I_{3R} = 1$, we find $\Delta L = 2$. This implies Majorana neutrinos and neutrino-less double beta decay. Similarly, for lepton number conserving interactions, processes like neutron-antineutron oscillation appear.

F.3.1 Higgs and gauge sectors; symmetry breaking

In the L-R symmetric models, the quarks and leptons are assigned to the following irreducible representations of the gauge group $SU(2)_L \times SU(2)_R \times U(1)_{B-L}$:

$$\begin{aligned} q_{\ell L} = \begin{pmatrix} u_\ell \\ d_\ell \end{pmatrix}_L &\sim \left(\mathbf{2}, \mathbf{1}, \frac{1}{3}\right) \\ q_{\ell R} = \begin{pmatrix} u_\ell \\ d_\ell \end{pmatrix}_R &\sim \left(\mathbf{1}, \mathbf{2}, \frac{1}{3}\right) \\ \psi_{\ell L} = \begin{pmatrix} \nu_\ell \\ \ell \end{pmatrix}_L &\sim (\mathbf{2}, \mathbf{1}, -1) \\ \psi_{\ell R} = \begin{pmatrix} N_\ell \\ \ell \end{pmatrix}_R &\sim (\mathbf{1}, \mathbf{2}, -1) \end{aligned} \tag{6.46}$$

This representation is logically associated with 3 numbers. The first number means a dimension of $SU(2)_L$ representation (i.e. it is equal to $2\,T_L + 1$), the second means the same for $SU(2)_R$, and the third number is a value of $B - L$. T_{3L} and T_{3R} components are derived from Equation 6.44 using the electric charge of a particle (or vice-versa using third isospin component to derive the charge).

The right handed neutrino is assigned with a different symbol than his left partner for the case it is part of two different Majorana neutrinos.

The gauge invariant Lagrangian for the quarks and leptons leads to

$$\mathcal{L}_{\text{gauge}} = g_L \left[\bar{q}_L \gamma_\mu \frac{\tau}{2} q_L + \bar{\psi}_L \gamma_\mu \frac{\tau}{2} \psi_L\right] \cdot W_L^\mu$$

$$+g_R\left[\bar{q}_R\gamma_\mu\frac{\tau}{2}q_R+\bar{\psi}_R\gamma_\mu\frac{\tau}{2}\psi_R\right]\cdot W_R^\mu$$
$$+g'\left[\frac{1}{6}\bar{q}\gamma_\mu q-\frac{1}{2}\bar{\psi}\gamma_\mu\psi\right]\cdot B^\mu \tag{6.47}$$

where W_L^μ, W_R^μ, B^μ are gauge bosons and g_L, g_R, g' are corresponding coupling constants to the group $SU(2)_L, SU(2)_R, U(1)_{B-L}$.

Let's assume that the theory is parity invariant which makes the field to transform as

$$q_L \leftrightarrow q_R\ ,\ \psi_L \leftrightarrow \psi_R\ ,\ W_L \leftrightarrow W_R. \tag{6.48}$$

That clearly requires $g_L = g_R = g$, the number of coupling constants is the same as in the SM. We can parameterize g and g' in terms of two parameters: electric charge of the electron and the Weinberg angle as

$$\sin\vartheta_W \ = \ e/g, \tag{6.49}$$

which gives

$$g' \ = \ \frac{e}{\sqrt{\cos 2\vartheta_W}} \tag{6.50}$$

Breaking of the gauge symmetry means that in order to maintain left-right symmetry we have to choose the Higgs multiplets to be left-right symmetric. One of the possible multiplets is

$$\Phi = \begin{pmatrix} \phi^0 & \phi'^+ \\ \phi^- & \phi'^0 \end{pmatrix} \sim (\mathbf{2},\mathbf{2},0) \tag{6.51}$$

which can couple to the fermion bilinears $\bar{\psi_L}\psi_R$ and $\bar{q_L}q_R$. In our convention, a neutral field ϕ^0 is written in terms of correctly normalized real and

imaginary components as $\phi^0 = 1/\sqrt{2}(\phi^{0r} + i\phi^{0i})$. After symmetry breaking, non-zero *v.e.v.*s of the neutral components of Φ are

$$\langle \Phi \rangle \equiv \begin{pmatrix} \frac{\kappa}{\sqrt{2}} & 0 \\ 0 & \frac{\kappa'}{\sqrt{2}} \end{pmatrix} \tag{6.52}$$

give masses to quarks and leptons. This is not enough to break the gauge symmetry. Since Φ is neutral under $B - L$, $U(1)_{B-L}$ is not broken by the *v.e.v.*s of Φ.

Electrically neutral components of Φ have $T_{3L} + T_{3R} = 0$. The gauge symmetry is broken to $U(1)_{T_{3L}+T_{3R}} \times U(1)_{B-L}$ in contrary to the experimentally observed $U(1)_Q$.

The breaking of the gauge symmetry was implemented by choosing the Higgs multiplets [185]

$$\chi_L \sim (\mathbf{2}, \mathbf{1}, 1) \ , \ \chi_R \sim (\mathbf{1}, \mathbf{2}, 1) \tag{6.53}$$

In order to understand the smallness of neutrino masses, it is reasonable to introduce (considering $SU(2)$ and its decomposition $\mathbf{2} \bigotimes \mathbf{2} = \mathbf{3} \bigoplus \mathbf{1}$, the direct tensor product of two doublets decomposes a singlet and a triplet) [186]

$$\Delta_L \sim (\mathbf{3}, \mathbf{1}, 2) \ , \ \Delta_R \sim (\mathbf{1}, \mathbf{3}, 2) \tag{6.54}$$

The gauge symmetry breaking proceeds in two stages. First, the neutral electrical components Δ_R require *v.e.v.*:

$$\langle \Delta_R \rangle \equiv \begin{pmatrix} 0 & 0 \\ \frac{v_R}{\sqrt{2}} & 0 \end{pmatrix} \tag{6.55}$$

and breaks the gauge symmetry down to $SU(2)_L \times U(1)_Y$ with

$$\frac{Y}{2} = T_{3R} + \frac{B-L}{2}. \tag{6.56}$$

The parity symmetry breaks down now. Secondly, the neutral components of Φ breaks the symmetry down to $U(1)_Q$.

Experimental constraints force the relation that

$$\kappa, \kappa' \ll v_R \tag{6.57}$$

In the first stage, the charged right handed gauge bosons $W_R^{\pm}$ and a neutral gauge boson called Z' acquire masses proportional to v_R and become much heavier than the normal left handed partners which pick-up masses proportional to κ and κ' only in the second stage. In general the different gauge bosons mix and lead to a 2×2 mass matrix describing the W_L, W_R system and 3×3 mass matrix describing the neutral gauge bosons W_{3L}, W_{3R} and B. The charged gauge boson mass matrix turns out to be

$$\begin{pmatrix} \frac{1}{2}g^2(\kappa^2 + \kappa'^2 + 2v_L^2) & g^2\kappa\kappa' \\ g^2\kappa\kappa' & \frac{1}{2}g^2(\kappa^2 + \kappa'^2 + 2v_R^2) \end{pmatrix} \tag{6.58}$$

The mixing angle ξ fulfills

$$\tan 2\xi = \frac{2\kappa\kappa'}{v_R^2 - v_L^2} \tag{6.59}$$

In what follows we assume that

$$\kappa' \ll \kappa \tag{6.60}$$

In this case, the physical charged gauge bosons W_1 and W_2 are the same as W_L and W_R to a good approximation. The masses give

$$\begin{aligned} m_{W_L} &= \frac{1}{\sqrt{2}} g\kappa \\ m_{W_R} &= g v_R \end{aligned} \tag{6.61}$$

The *v.e.v.* of Δ_L^0 is assumed to be much smaller than $\kappa,\ \kappa'$

$$v_L \ll \kappa' \ll \kappa \ll v_R. \tag{6.62}$$

For $\kappa' = 0$ we find

$$\begin{aligned} m_{W_L}^2 &\simeq \frac{1}{4}(\kappa^2 + 2v_L^2) \\ m_Z^2 &\simeq \frac{1}{4}\frac{g^2(g^2+2g'^2)}{g^2+g'^2}(\kappa^2 + 4v_L^2) \end{aligned} \tag{6.63}$$

The appropriate definition of the Weinberg angle for the left-right symmetric model is such that

$$\cos^2\vartheta_W = \frac{g^2 g'^2}{g^2 + 2g'^2}, \tag{6.64}$$

so that we have [1]

$$\rho_{EW} \equiv \frac{m_{W_L}^2}{\cos^2\vartheta_W m_Z^2} = \frac{\kappa^2 + 2v_L^2}{\kappa^2 + 4v_L^2} \tag{6.66}$$

[1] generally speaking, if there are several Higgs scalar multiplets, the ρ parameter is defined as [19]:

$$\rho = \frac{\sum_{T,Y} |v(T,Y)|^2 [T(T+1) - Y^2/4]}{2\sum_{T,Y} |v(T,Y)|^2 Y^2/4}, \tag{6.65}$$

where $v(T,Y)$ is are the corresponding *v.e.v.*'s. The Higgs scalar bidoublet Φ is $\kappa(1/2,1)$ and the Higgs triplet $\Delta_{L,R}$ is $v_L(1,2)$.

We know experimentally that $|1 - \rho_{EW}| \leq 0.01$, implying that

$$v_L \leq 0.07 \cdot \kappa. \tag{6.67}$$

In particular, it is clearly always safe to neglect effects of order v_L/v_R, since $v_R \gg \kappa$. We also note at this time the formulas for the W_R and Z' masses:

$$\begin{aligned} m^2_{W_R} &\simeq \frac{1}{4} g^2(\kappa^2 + 2v_R^2) \\ m^2_{Z'} &\simeq v_R^2(g^2 + g'^2). \end{aligned} \tag{6.68}$$

Of the twenty real degrees of freedom (d.o.f.) contained in this Higgs sector, six are absorbed in giving mass to the left- and right-handed gauge bosons, $W_L^{\pm}$, $W_R^{\pm}$, Z ($\simeq Z_L$), and Z' ($\simeq Z_R$). According to the Goldstone theorem, there must be 14 physical Higgs bosons, and 20 Goldstone bosons. These 20 d.o.f. break into 3 (Δ triplet) $\times$ 2 d.o.f. (real and imaginary component) $\times$ 2 (left- and right-handed Higgs triplet Δ) + 4 (Φ bidoublet) $\times$ 2 d.o.f. (real and imaginary component).

F.3.2 Majorana neutrinos; see-saw mechanism

The way of giving masses to Majorana neutrinos is the see-saw mechanism. The main components of the theory are Φ - Higgs multiplets and triplets Δ introduced in Section F.2. We introduce matrices

$$\delta_{L,R} = \epsilon\tau \cdot \Delta_{L,R} \tag{6.69}$$

where $\epsilon = i\tau_2$ is a antisymmetric matrix (Levi-Civita). And corresponding charged terms δ_{LR} are

$$\delta_{L,R} = \begin{pmatrix} \frac{1}{\sqrt{2}}\Delta^+ & \Delta^{++} \\ \Delta^0 & -\frac{1}{\sqrt{2}}\Delta^+ \end{pmatrix}_{L,R} \tag{6.70}$$

The general Yukawa mass term involving leptons is [19]

$$\begin{aligned} -\mathcal{L}_{\rm Y} &= \sum_{a,b} h^{\ell}_{ab}\bar{\psi_{aL}}\Phi\psi_{bR} + \widetilde{h^{\ell}_{ab}}\bar{\psi_{aL}}\widetilde{\Phi}\psi_{bR} \\ &+ f_{ab}\left[\psi^T_{aL}C\delta_L\psi_{bL} + \psi^T_{aR}C\delta_R\psi_{bR}\right] + \text{h.c.} \end{aligned} \tag{6.71}$$

where

$$\widetilde{\Phi} = \tau_2\Phi^*\tau_2 = \begin{pmatrix} \phi^{0*} & -\phi^{-*} \\ -\phi'^{+*} & \phi'^{0*} \end{pmatrix}$$

and a, b label different generations. First, we have $v_L = 0$ and $v_R \neq 0$. This leads to heavy Majorana mass for right-handed neutrinos.

$$m_{Nab} = f_{ab}v_R \tag{6.72}$$

and the mass matrix gives :

$$m^{\ell}_{ab} = h^{\ell}_{ab}\kappa' + \widetilde{h^{\ell}_{ab}}\kappa \tag{6.73}$$

In the second stage, the neutral components in Ψ develop non-zero *v.e.v.*s and we obtain the mass matrix of the neutrinos

$$\begin{pmatrix} 0 & m_D \\ m_D^T & fv_R \end{pmatrix} \tag{6.74}$$

where

$$m_{Dab} = h^{\ell}_{ab}\kappa + \widetilde{h^{\ell}_{ab}}\kappa' \tag{6.75}$$

For N generations of fermions, eq. (6.74) gives a $2N \times 2N$ matrix where all the elements shown are $N \times N$ blocks. We can diagonalize this matrix using the orthogonal matrix:

$$\begin{pmatrix} 1 - \frac{1}{2v_R} m_D f^{-1} & \frac{1}{v_R} m_D f^{-1} \\ -\frac{1}{v_R}(f^{-1})^T m_D^T & 1 - \frac{1}{2v_R} m_D f^{-1} \end{pmatrix}_{L,R}$$

This diagonalization is all right for terms smaller than ρ^2 and one obtains the mass matrix for light neutrinos

$$m_\nu = \frac{1}{v_R} m_D f^{-1} m_D^T. \tag{6.76}$$

We need to diagonalize this matrix further to obtain the light neutrino eigenvalues and eigenstates. Ignoring mixing between generations in the first approximation and assuming $m_D \sim m_\ell$, where m_ℓ is the mass of the charged lepton, we get a very important relation (equivalently $h^\ell \sim \widetilde{h^\ell}$):

$$m_{\nu\ell} \sim \frac{m_\ell^2}{m_{N\ell}} \tag{6.77}$$

where $m_{N\ell}$ is the mass of the heavy right-handed neutrino. If M_{N_l} is generation independent, there is a mass formula for neutrino masses:

$$m_{\nu_e} \ : \ m_{\nu_\mu} \ : \ m_{\nu_e} \ = \ m_e^2 \ : \ m_\mu^2 \ : \ m_\tau^2 \tag{6.78}$$

The smallness of the neutrino mass is connected to the suppression of $V + A$ currents in this theory.

Bibliography

[1] DØ Run II Collaboration, V. M. Abazov *et al.*, *Search for Doubly-charged Higgs Boson Pair Production in the Decay to $\mu^+\mu^+\mu^-\mu^-$ in $p\bar{p}$ Collisions at $\sqrt{s} = 1.96$ TeV*, hep-ex/0404015, FERMILAB-Pub-04/045-E, submitted to Phys. Rev. Letters on April 13, 2004.

[2] N.G. Deshpande, J.F. Gunion, B. Kayser, Phys. Rev. **D44** (1997) 837.

[3] J. F. Gunion, J. Grifols, A. Mendez, B. Kayser, and F. Olness, Phys. Rev. **D40** (1989) 1546.

[4] J.F. Gunion, C. Loomis, K.T. Pitts, *Searching for Doubly Charged Higgs Bosons at Future Colliders*, hep-ph/9610237;
T. Rizzo, Phys. Rev. D25 (1982) 1355 and Addendum-ibid **D27** (1983) 657;
J.F. Gunion, H.E. Haber, G. Kane, S. Dawson, *The Higgs Hunter's Guide*, Frontiers in Physics.

[5] N. Arkani-Hamed *et al.*, JHEP 0208 (2002) 021.

[6] J. F. Gunion, R. Vega, J. Wudka, Phys. Rev. **D42** (1990) 1673.

[7] M. Bando, T. Sato and T. Takahashi, Phys. Rev. **D52** (1995) 3076.

[8] B. Brahmachari, Phys. Rev. **D52** (1995) 1.

[9] B. Brahmachari and R. N. Mohapatra, Phys. Lett. **B357** (1995) 566.

[10] E. Ma, Phys. Rev. **D51** (1995) 236.

[11] D.-G. Lee and R. N. Mohapatra, Phys. Rev. **D52** (1995) 4125.

[12] J. C. Pati and A. Salam, Phys. Rev. **D10** (1974) 275.

[13] R. N. Mohapatra and J. C. Pati, Phys. Rev. **D11** (1975) 566, 2558.

[14] G. Senjanovic and R. N. Mohapatra, Phys. Rev. **D12** (1975) 1502.

[15] R. N. Mohaatra, R. E. Marshak, Phys. Lett. **91B** (1980) 222.

[16] K. Huitu et al., Nucl. Phys. **B487** (1997) 27.

[17] M. L. Schwartz, Phys. Rev. **D40** (1989) 1521.

[18] T. Yanagida, in Proceedings of *Workshop on Unified Theory and Baryon Number in the Universe*, eds. O. Sawada and A. Sugamoto (KEK 1979)

[19] R. Mohapatra, P. Pal, *Massive Neutrinos in Physics and Astrophysics*, World Scientific Lecture Notes in Physics - Vol. 41, World Scientific Publishing Co. Pte. Ltd., Singapore, ISBN 981-02-0434-5, p. 96-122, (1991).

[20] M. Gell-Mann, P. Ramond and R. Slansky, in *Supergravity*, eds. P. van Niewenhuizen and D. Z. Freedman (North Holland 1979)

[21] Muon (g-2) Collaboration, BNL, *Measurement of the Negative Muon Anomalous Magnetic Moment to 0.7 ppm*, hep-ex/0401008, submitted to Phys. Rev. in January 2004.

[22] DELPHI Collab., J. Abdallah *et al.*, Phys. Lett. **B552** (2003) 127.

[23] OPAL Collab., G. Abbiendi *et al.*, Phys. Lett. **B577** (2003) 93.

[24] J. S. Hagelin, Nucl. Phys. **B193** (1983) 123,
A. J. Buras, W. Slominski, and H. Steger, *ibid* **B245** (1984) 369.

[25] A. Halprin, Phys. Rev. Lett. **48** (1982) 1313.

[26] T. M. Huber *et al.*, Phys. Rev. Lett. **61** (1988) 2189.

[27] F. Cuypers, S. Davidson, *Bileptons: Present Limits and Future Prospects*, PSI-PR-96-21, MPI-PhT/96-45, hep-ph/9609487.

[28] TASSO Collaboration, M. Althoff *et al.*, Zeitschrift für Physik, **C22** (1984) 13,
W. Braunschweig *et al.*, *ibid.* **37** (1988) 171.

[29] PLUTO Collaboration, C. Berger *et al.*, Zeitschrift für Physik, **C27** (1985) 341.

[30] HRS Collaboration, M. Derrick *et al.*, Phys. Lett. **B166** (1986) 463,
M. Derrick *et al.*, Phys. Rev. **D34** (1986) 3286.

[31] MAC Collaboration, E. Fernandez *et al.*, Phys. Rev. **D35** (1987) 10.

[32] OPAL Collab., G. Abbiendi *et al.*, Phys. Lett. **B577** (2003) 93;
OPAL Collab., G. Abbiendi *et al.*, Phys. Lett. **B526** (2002) 221;
OPAL Collab., P. D. Acton *et al.*, Phys. Lett. **B295** (1992) 347.

[33] L3 Collab., P. Achard, Phys. Lett. **B576** (2003) 18.

[34] See for example, R. Engfer and H. K. Walter, Annu. Rev. Nucl. Part. Sci. **36** (1986) 327,
R. E. Shrock, *Report No. ITP-SB-88-28* (1988) (unpublished)

[35] G. K. Leontaris, K. Tamvakis, and J. D. Vergados, Phys. Lett. **B162** (1985) 153.

[36] R. N. Mohapatra, *Quarks, Leptons and Beyond*, proceedings of the NATO Advanced Study Institute, Munich, Germany, 1983. Edited by H. Fritzsch *et al.* (NATO ASI Series B, Vol. 122) (Plenum, New York,1985), p. 219.

[37] U. Bellgardt *et al.*, Nucl. Phys. **B299** (1988) 1.

[38] A. J. Davies, Xiao-Gang He, Phys. Rev. **D43** (1991) 225.

[39] J. P. Leveille, Nucl. Phys. **B137** (1978) 63.

[40] M. L. Schwartz, Phys. Rev. **D40** (1989) 1521,
M. Lusignoli and S. Petrarca, Phys. Lett. **B226** (1989) 397.

[41] R. Mohapatra, Phys. Rev. **D46** (1992) 2990.

[42] A. Zee, Phys. Lett. **B93** (1980) 389.

[43] G. K. Leontaris, K. Tamvakis, J.D. Vergados, Phys. Lett. **B162** (1985) 153.

[44] J. A. Coarasa, A. Mendez, J. Sola, Phys. Lett. **69** (1992) 2475.

[45] J. D. Bjorken, S. Weinberg, Phys. Rev. Lett. **38** (1977) 622.

[46] R. D. Bolton *et al.*, Phys. Rev. **D38** (1988) 2077.

[47] G.W. Bennett, *et al.*, Phys. Rev. Lett. **89**, (2002) 101804. Result published on 2000 data.

[48] A. Yamamoto *et al.*, Nucl. Instrum. Methods Phys. Res. **A491** (2002) 23.

[49] X. Fei, V. W. Hughes and R. Prigl, Nucl. Instrum. Methods Phys. Res. **A394** (1997) 349.

[50] J. Ouyang *et al.*, Nucl. Instrum. Methods Phys. Res. **A374** (1996) 215, S. A. Sedykh *et al.*, Nucl. Instrum. Methods Phys. Res. **A455** (2000) 346.

[51] E. Efstathiadis *et al.*, Nucl. Instrum. Methods Phys. Res. **A496** (2003) 8.

[52] Y. K. Semertzidis *et al.*, Nucl. Instrum. Methods Phys. Res. **A503** (2003) 458.

[53] M. Davier, S. Eidelman, A. Höcker, Z. Zhang, Eur. Phys. J. **C3** (2003) 503.

[54] S. Ghozzi and F. Jegerlehner, hep-ph/0310181, Phys. Lett. **B**, in Press (2004)

[55] M. Mühlleitner, M. Spira, Phys. Rev. D68 (2003) 117701 and private communications.

[56] W. Furmanski and R. Petronzio, Zeitschrift für Physik **C11** (1982) 293.

[57] V. N. Gribov and L. N. Lipatov, Yad. Fiz. **15** (1972) 781,
G. Altarelli and G. Parisi, Nucl. Phys. **B126** (1977) 298,
Y. L. Dokshitzer, Sov. Phys. JETP **46** (1977) 641.

[58] William Joseph Thompson, *Search for the Top Quark in the Muon + Jets channel at DØ*, PhD Thesis, State University of New York at Stony Brook, Stony Brook, New York, February 1994.

[59] Scott Stuart Snyder, *Measurement of the Top Quark Mass at DØ*, PhD Thesis, State University of New York at Stony Brook, Stony Brook, New York, May 1995.

[60] V. Abazov, *et al.*, in preparation for submission to Nucl. Instrum. Methods Phys. Res. A, and T. LeCompte and H.T. Diehl, *The CDF and DØ Upgrades for Run II*, Ann. Rev. Nucl. Part. Sci. **50** (2000) 71.

[61] R. Yarema *et al.*, *A Beginners Guide to the SVXIIe*, Fermilab-TM-1892, October 1996.

[62] M. Utes, *SVX Sequencer Board*, DØ Engineering Note 3823.110-EN-480, November 1997.

[63] S. Abachi, *et al.*, Nucl. Instrum. Methods Phys. Res. **A338** (1994) 185.

[64] *R&D and Optimization Progress Report*, DØ Note 1322 (1992).

[65] *Step 1 and Beyond*, DØ Note 1421 (1992).

[66] *D0$_\beta$*, DØ Note 1733 (1992).

[67] *Magnetic Tracking*, DØ Note 1933 (1993).

[68] *Electron ID*, DØ Submission to the PAC (January, 1994).

[69] S. Mishra and P. McBride, *B Physics at Hadron Colliders*, Proceedings of the 1993 Snowmass Workshop (1993).

[70] DØ Note 1846 (1993).

[71] C. W. Fabjan, ed. Thomas Ferbel, *Experimental Techniques in High-energy Nuclear and Particle Physics,*"*Second Edition*", World Scientific, Singapore, (1991)

[72] C. W. Fabjan, T. Lundlam, *Calorimetry in High Energy Physics,* Ann. Rev. Nucl. Part. Sci. **32**, (1982)

[73] C. W. Fabjan, *Detectors for Elementary Particle Physics,* CERN-PPE/94-61, (1996)

[74] C. W. Fabjan *et al.*, *Nucl. Inst. and Meth. 141,* (1977)

[75] S. Abachi *et al.*, Nucl. Instr. Meth., **A338** (1994) 185-253.

[76] S. Hagopian, *The Run II DØ Muon System at the Fermilab Tevatron*, submitted to World Scientific, January 2002.

[77] DØ Collaboration, S. Abachi *et al.*, *The DØ Upgrade - the Detector and its Physics*, FERMILAB-PUB-96-357-E, October 1997.

[78] T. LeCompte and H. T. Diehl, Annu. Rev. Part. Sci. **50**, 71 (2000).

[79] DØ Collaboration, S. Abachi *et al.*, *The DØ Upgrade - Forward Preshower, Muon System and Level 2 Trigger*, DØ Note 2894, FERMILAB-FN-641.

[80] DØ Collaboration, S. Abachi *et al.*, Nucl. Instrum. Methods **A338**, 185 (1994).

[81] DØ Collaboration, B. Baldin *et al.*, *Technical Design of the Central Muon System*, DØ Note 3365.

[82] DØ Collaboration, G. Alexeev *et al.*, *Technical Design of the Forward Muon Tracking Detector Based on Mini-drift Tubes*, DØ Note 3366.

[83] DØ Collaboration, V. Abramov *et al.*, *Technical Design of the DØ Forward Trigger Scintillation Counters*, DØ Note 3237.

[84] DØ Collaboration, G. C. Blazey *et al.*, *The DØ Run II Trigger*, Xth IEEE Real Time Conference, Beaune, France, 22-26 September 1997, Editor C. E. Vandoni, 83-87.

[85] N. Parashar *et al.*, *Real-Time Data Processing in the Muon System of the DØ Detector*, IEEE Trans. Nucl. Sci., **47**, 276, (2000), FERMILAB-Conf-01-083-E (July 2001).

[86] C. Leonidopoulos, *The Muon Trigger at DØ* , Proceedings of CHEP 2001 Conference, Beijing, China, Sept 2001.

[87] WZ Group,
http://www-d0.fnal.gov/Run2Physics/wz/d0-private/wzskim/

[88] Run Quality Database,
http://d0db.fnal.gov/qualitygrabber/qualQueries.html

[89] Luminosity ID group,
http://www-d0.fnal.gov/d0dist/dist/packages/lm_access/devel/doc/
Luminosity Measurement, DØ Note 4328.

[90] Trigger Meister web site,
http://www-d0online.fnal.gov/www/groups/tm/tm_main.html

[91] `2MU_A_L2M0` trigger description,
http://d0db.fnal.gov/trigdb/cgi/tdb_report_element.py?function=
Trigger+Name&intnname=2MU_A_L2M0&intnversion=3

[92] Terry Toole, private communications.

[93] G. Borissov *et al.*, *The p14 Tracker Realignment,* DØ Note 4161.

[94] Peter Tamburello - *higgs_skim* package,
http://www-d0.fnal.gov/Run2Physics/higgs/

[95] Muon-ID Group,
http://www-d0.fnal.gov/phys_id/muon_id/d0_private/certif/p13/index.html

[96] Muon-ID Group,
http://www-d0.fnal.gov/computing/algorithms/muon/muon_algo.html

[97] Global Tracking Group,
http://www-d0.fnal.gov/global_tracking/

[98] T. Christiansen, *The D-Zero L2-Muon Trigger Performance for p11*,

[99] DØ Upgrade Collaboration, *DØ Central Fiber Tracker Technical Design Report*, DØ Note 3551, Fermilab, (1994);
S. Abachi *et al.*, *The DØ Upgrade*, Fermilab-Conf-**95/177-E**

[100] DØ Upgrade Collaboration, *DØ Silicon Tracker Technical Design Report*, DØ Note 2169, Fermilab, (1994);
R. Yarema *et al.*, *A Beginners Guide to the SVX II Chip*, Fermilab-TM-1892, (1994);
DØ Collaboration, *The DØ Silicon Microstrip Vertex Detector*, NIM paper in preparation.

[101] D. Whiteson and M. Kado, *Muon Isolation Studies*, DØ Note 4070.

[102] T. Sjöstrand, Comp. Phys. Comm. **82** (1994) 74.

[103] CERN. `GEANT` Detector Description and Simulation Tool, 1993. CERN Program Library Number Q123.
(URL:http://www.hep.net/cernlib/docs/www.dir/geant/GEANTMAIN.html)
(URL:http://wwwcn.cern.ch/ascdoc/geant/GEANTMAIN.html)

[104] R. Raja, Q. Li-Demarteau, and S. Kunori, `DOGEANT`, DØ Note 1007, July 1990.

[105] D. Evans, `mc_runjob` development group,
http://www-clued0.fnal.gov/runjob/current/

[106] ALPGEN generator,
have to find some reference

[107] F. A. Berends, H. Kuijf, B. Tausk, and W. T. Giele, Nucl. Phys. **B357**, 32-64 (1991).

[108] CTEQ Collab., H.L. Lai *et al.*, Phys. Rev. **D55** (1997) 1280.

[109] T. Wyatt, plenary talk given at LP2003, Fermilab, and references therin.

[110] N. Kidonakis, Phys. Rev. **D64** (2001) 014009;
N. Kidonakis, E. Laenen, S. Moch, R. Vogt, Phys. Rev. **D64** (2001) 114001.

[111] Higgs Group,
http://www-d0.fnal.gov/Run2Physics/higgs/d0_private/tools/higgs_prod.html,
and references therein.

[112] R. Hamberg, W. L. van Neerven, and T. Maatsuura, Nucl. Phys. **B359**, 343 (1991), Erratum ibid. **B644**, 403 (2002).

[113] http://www-d0.fnal.gov/Run2Physics/higgs/docs/Spring_2003/higgs_spring03.html

[114] G.C. Blazey, *et al.*, *Run II Jet Physics: Proceedings of the Run II QCD and Weak Boson Physics Workshop"*, hep-ex/0005012.

[115] JES group, http://www-d0.fnal.gov/phys_id/jes/d0_private/certified/v4.1/note.ps

[116] M. Zdražil, *Understanding the dimuon data,*, DØ Note 4218.

[117] D. Evans, `d0_mess` development group,
http://www-clued0.fnal.gov/d0_mess/

[118] Rick Field, `Fermilab Monte Carlo Workshop presentation`
http://www.phys.ufl.edu/ rfield/cdf/rdf_talks.html

[119] X. Zhang, *Opposite Side Jet Charge Tagging and Measurement of CP Asymmetry Parameter sin(2β) at DØ* , PhD Thesis, Oklahoma University, Norman, Oklahoma, 2004.

[120] A. Kharchilava, M. Zdražil, S. Söldner-Rembold, DØ Note in preparation.

[121] In the Proceedings *Z Physics at LEP*, ed. R. Kleiss, CERN Yellow Report 89-08, vol. 3.

[122] In the Proceedings *Physics at HERA*, ed. W. Buchmüler, G. Ingelman, vol. 3.

[123] Frank Paige and Serban Protopopescu, ISAJET. BNL Report 38034, Brookhaven, 1986. Release v6.49. (Unpublished)

[124] G. Marchesini *et al.*, Comp. Phys. Comm., **67**, 465-508 (1992).

[125] A. Kupco et al., *Measurement of Inclusive Jet and Dijet Cross Sections in $\bar{p}p$ collisions at $\sqrt{s} = 1.96\,\mathrm{TeV}$*, DØ Note 4382.

[126] A. Kupco et al., *Measurement of dijet azimuthal angle distribution in $p\bar{p}$ collisions at $\sqrt{s} = 1.96\,\mathrm{TeV}$*, DØ Note 4384.

[127] DØ Collab., S. Abachi et al., Phys. Rev. Lett. **74** (1995) 3548.

[128] J. Elmsheuser *et al.*, *Search for the Higgs boson in $H \to WW \to \mu\nu\mu\nu$ decays at DO in Run II,* DØ Note 4223.

[129] G. Hesketh, *In-flight Decays ?*, DØ Workshop 2004, Fresno, GTR Group session.

[130] G. Hesketh, F. Deliot, B. Tuchming, P. Telford, E. Nurse, *Measurement of $\sigma\times$ BR for $W \to \mu\nu$ in $p\bar{p}$ collisions at $\sqrt{s} = 1.96\ TeV$*, DØ Note in preparation.

[131] P. Tamburello, *Search for* $WH \to l\nu b\bar{b}$, DØ Note in preparation.

[132] Run Database Query,
http://www-d0online.fnal.gov/run/runQuery.html

[133] Trigsim documentation,
http://www-d0.fnal.gov/computing/trigsim/general/docs.html

[134] J. Kotcher, *Response of the Calorimeter to Cosmic Ray Muons*, PhD thesis, New York University, New York, New York, October 1992.

[135] H. T. Diehl, *Cosmic Ray Muon Rejection in the Level 2 filter at DØ* , DØ Note 1517, (1992).

[136] Barger, Lopez and Putikka, Int. J. Mod. Phys. **A3** (1988) 2181.

[137] R. Brun and F. Carminati, CERN Program Library Long Writeup W5013, 1993 (unpublished)

[138] `PMCS` documentation,
http://www-d0.fnal.gov/sceno/pmcs_doc/pmcs.html

[139] R. Gelhaus, `WZ group meeting presentation`, pages 2-12, October 9, 2003.

[140] G. Gutierrez, private communications.

[141] T. Junk, Nucl. Inst. and Meth., A434 (1999) 435;
see also http://thomasj.home.cern.ch/thomasj/searchlimits/ecl.html.

[142] P. Bock, *CONFL10: A statistics program to compute confidence levels for exclusion or discovery of a signal over background*, June 2001.

[143] I. Bertram, G. Landsberg, J. Linnemann, R. Partridge, M. Paterno and H. B. Prosper, *A Recipe for the Construction of Confidence Limits*, DØ Note 3476.

[144] R. D. Cousins and V. L. Highland, Nucl. Instr. and Meth. **A320**, 1992, 331.

[145] A. G. Frodesen, O. Skeggestad *et al.*, *Probability and Statistics in Particle Physics*, Universitetsforlaget, 1979, ISBN 82-00-01906-3.

[146] W. T. Eadie, D. Drijard, F. E. James, M. Roos, and B. Sadoulet, *Statistical Methods in Experimental Physics*, North-Holland, 1971, ISBN 0 7204 02395.

[147] M. G. Kendall and A. Stuart, *The Advanced Theory of Statistics*, vol. 2, 2^{nd} ed., ch. 24., Ch. Griffen & Company Limited, London, 1967, SBN 85264 011 0.

[148] A. L. Read, *Optimal Statistical Analysis of Search Results based on the Likelihood Ratio and its Application to the Search for the MSM Higgs Boson at* $\sqrt{s}$ *= 161 and 172 GeV*, DELPHI 97-158 PHYS 737 (1997).

[149] B. Escoubes, S. De Unamuno, and O. Helene, Nucl. Instr. and Meth. **A257** (1987) 346.

[150] Particle Data Group, R. M. Barnett, *et al.*, Phys. Rev. **D54** 1, (1996), and earlier editions.

[151] ALEPH, DELPHI, L3 and OPAL Collaborations and the LEP Working Group for Higgs Boson Searches, *Search for the Standard Model Higgs Boson at LEP*, CERN-EP/2003-011, submitted to Phys. Lett. B.

[152] M. Begel, private communications.

[153] John Hobbs, private communications.

[154] Tom Ferbel, private communications.

[155] Tracking and Vertexing Group web page, *http://www-d0.fnal.gov/global_tracking/algorithms.html*.

[156] Slava Kulik, private communications.

[157] The DØ Upgrade Central Fiber Tracker, *Technical Design Report*, (1999).

[158] I. Bertram, *Online Calibration Requirements* , DØ Note 3660 (1999).

[159] E. Barberis, H. Greenlee, V. White, *Database Access Using d0om*, DØ Note 3123 (2001).

[160] I. Bertram, J. Hobbs, H. Melanson, *Calibration and Alignment WG1 Report*, DØ Note 3509 (1998).

[161] F. Bleckman, *Numbering schemes for the DØ SMT*, DØ Note 3899 (2001).

[162] M. Zdražil, SMT Offline Calibration documentation, (2001). *http://www-d0.fnal.gov/d0dist/dist/releases/p14.01.00/smt_calibration/doc/*

[163] J. Weigand, *http://d0ora3.fnal.gov:8539/smt_calibration/*, web page with the SMT Offline Calibration Database Transfer documentation, (2001).

[164] B. Asman *et al.* [DØ Silicon Group] "DØ RunIIa Silicon Microstrip Tracker", to be submitted to Nucl. Instr. and Meth. . For DØ Collaborators available at http://www-d0.fnal.gov/ asman/d0_private/nim.ps

[165] A. Khanov *et al.*, *Charge distribution in SMT Clusters*, DØ Note 3981 (2002).

[166] G. Gutierrez, H. Melanson, Y. S. Kulik, A. Khanov, G. Borrisov, H. Greenlee, *Tracking Task Force Group*

[167] K. Anikeev *et al*, *B Physics at the Tevatron: RunII and Beyond*, Fermilab-Pub-01/197 (2001); hep-ph/0201071

[168] http://www-d0.fnal.gov/phys_id/emid/d0_private/emid_docs.html

[169] http://www-d0.fnal.gov/ sch/d0_private/d0root/d0root.html

[170] http://www-d0.fnal.gov/ sch/d0_private/btag_certification/secvertex_v1.html

[171] A. Schwartzmann, private communications.

[172] K. A. Burkett, *Measurement of the Lifetime of the B_s^0 Meson and the Width Difference in the B_s^0-$\bar{B}_s^0$ System in $p\bar{p}$ Collisions at $\sqrt{s} = 1.8$ TeV*, Ph.D. Thesis, 1997.

[173] O. R. Long, *A proper time dependent measurement of ΔM_D using jet charge and soft lepton flavor tagging*, Ph.D. Thesis, 1998.

[174] M. Paulini, *B Lifetimes, Mixing and CP Violation at CDF*, CDF/PUB/BOTTOM/PUBLIC/484, Fermilab-Pub-99/014-E (1999); hep-ex/9903002

[175] W. Greiner, *Gauge Theories of Weak Interactions*, Springer Verlag, 2nd edition, (1996).

[176] C. Itzykson, *Quantum Field Theory*, McGraw-Hill, (1980).

[177] F. Halzen and A. D. Martin, *Quarks and Leptons: An Introductory Course in Modern Particle Physics*, Wiley, (1984).

[178] G. Altarelli, *Models of Neutrino Masses from Oscillations with Maximal Mixing*, CERN-TH/98-310, DFPD-98/TH/46, hep-ph/9809096, (1998).

[179] Y. Fukuda *et. al.*, *Evidence for oscillation of atmospheric neutrinos*, The Super-Kamiokande Collaboration, (1998).

[180] E. J. Chun, *Three neutrino Δm^2 scales and the singular seesaw mechanism*, Phys. Rev. D **58**,093003, (1998).

[181] Ta-Pei Cheng and Ling-Fong Li, *Gauge Theory of Elementary Particle Physics*, Oxford University Press, (1994).

[182] B. Kayser, *Neutrino mass: Where do we stand, and where are we going ?*, hep-ph/9810013, (1998).

[183] Y. Chikira, *The Singular Seesaw Mechanism with Hierarchical Dirac Neutrino Mass*, TIT-HEP-397, KEK-TH-582, hep-ph/9808254, (1998).

[184] K. Kang, *Neutrino Oscillations and Lepton Flavour Mixing*, hep-ph/9808419, KIAS-P98018, YUMS 98-016, SNUTP 98-094, (1998).

[185] R. N. Mohapatra and D. P. Sidhu, Phys. Rev. Lett. **38** (1977) 667. R. N. Mohapatra, F. E. Paige and D. P. Sidhu, Phys. Rev. **D17** (1978) 2462.

[186] R. N. Mohapatra and G. Senjanović, Phys. Rev. Letter **44** (1980) 912. Phys. Rev. **D23** (1981) 165.